Microfluidics to characterize and manipulate biomimetic membranes

Marianne Elias

THÈSE

En vue de l'obtention du

DOCTORAT DE L'UNIVERSITÉ DE TOULOUSE

Délivré par l'Université Toulouse 3 - Paul Sabatier

Cotutelle internationale : Université de Florence

Présentée et soutenue par

Marianne ELIAS

Le 25 mai 2021

Microfluidique pour manipuler et étudier des membranes biomimétiques

---

Ecole doctorale : **GEETS - Génie Electrique Electronique,Télécommunications et Santé : du système au nanosystème**

Spécialité : **MicroNano Systèmes**

Unité de recherche :
LAAS - Laboratoire d'Analyse et d'Architecture des Systèmes

Thèse dirigée par
Pierre JOSEPH et Debora BERTI

Jury

M. Tom ROBINSON, Rapporteur
Mme Stephanie MANGENOT, Rapporteure
M. Nicolas DESTAINVILLE, Examinateur
M. Jean-Christophe BARET, Examinateur
Mme Francesca BALDELLI BOMBELLI, Examinatrice
M. Pierre JOSEPH, Directeur de thèse
Mme Debora BERTI, Co-directrice de thèse

On-chip micropipette: a tool to characterize mechanical properties of model membranes

Marianne Elias

A thesis submitted for the degree of Doctor of Philosophy

Université Toulouse 3 – Paul Sabatier

and

University of Florence

May 2021

Acknowledgement

After spending 3 years and a half in LAAS and the University of Florence for my PhD project, I would like to express my sincere gratitude for all the people who have helped and participated in this project directly or in other ways. First, I would like to thank both my PhD directors, Debora Berti and Pierre Joseph for giving me the opportunity to conduct my research in their team. Thank you for the trust you have placed in me during these three years as well as for your kindness and enthusiasm. It was a real pleasure to work with you every day on this project.

I would like to deeply thank Morgan Delarue, for introducing me to the Tigette world and the spheroid world. It was a real pleasure working, discussing and conducting experiments with you. Thank you for teaching to me how to "research" when I was focused on just getting results.

Costanza and Lucrezzia, thank you for all the scientific discussions in Florence and for all the help you provided during my staying there and for working side by side with me and coming with me on Saturdays to the lab to conduct experiments.

I would like to also thank all the previous and current members of Mile team of LAAS. It has been super fun to have met you and worked with some of you. Zack, Tiphaine, Baptiste, Lucie, Lyn, Marion, Paul, Jeffrey and Amani, thank you again. My copineta de bureau Inga, Anais and Bayan, a special thanks to you for all the long conversations we had. You were a very nice support system. I also want to thank Adrien Dutoya and Hajar Ajiyel, for being enthusiastic and hardworking interns.

I would like also to thank the characterization platform members, for your devotion and efficiency. Life would have been very hard without you in the lab. Charline, Sandrine and Julien thank you so much.

I also would like to thank the clean room platform members, for all the help and development. Specially Aurelie Lecestre, thank you for all the work to etch the B33 type glass. Adrian, thank you for your sense of humor and your every single day good mood. Thank you for being my number one call, facebook, WhatsApp etc. when I was panicking inside the clean room (and sorry for that). Jean Baptiste, Samuel, Laurent, Fabien, Tom, Demba and Benjamin, thank you for all the help you provided. A special thanks also to Remi Courson, for being always available when needed and for all the help and advises for the 3D printing.

Roberto, there are no words that could express my gratitude for having you by my side for the last almost 6 years. You have been my main support system even though you were writing and preparing your defense at the same time as me. Thank you for being present whenever I needed you.

Thank you for my friends and family, the ones that are close and the ones I haven't seen in more than a year due to the pandemic. You have been my support system.

Table of Contents

Table of abbreviations

2D	Two-dimensional
3D	Three-dimensional
AFM	Atomic Force Microscopy
AuNP	Gold Nanoparticles
BARC	Bottom Anti-Reflecting Coating
BODIPY	2-(4,4-Difluoro-5,7-Dimethyl-4-Bora-3a,4a-Diaza-*s*-Indacene-3-Dodecanoyl)-1-Hexadecanoyl-*sn*-Glycero-3-Phosphocholine
BSA	Bovine Serum Albumin
Chol	Cholesterol
DF	Dry Film
DI	Deionized
$DiIC_{20}$	1,1'- dieicosanyl-3,3,3',3'-tetramethylindocarbocyanine perchlorate
DLPC (12:0)	1,2-dilauroyl-sn-glycero-3-phosphocholine
DMPC (14:0)	1,2-dimyristoyl-sn-glycero-3-phosphocholine
DOPC (18:1)	1,2-dioleoyl-sn-glycero-3-phosphocholine
DPPC (16:0)	1,2-dipalmitoyl-sn-glycero-3-phosphocholine
DPPG (16:0)	1,2-dipalmitoyl-*sn*-glycero-3-phospho-(1'-*rac*-glycerol) (sodium salt)
DSPC (18:0)	1,2-distearoyl-sn-glycero-3-phosphocholine
GUV	Giant Unilamellar Vesicles
HMDS	Hexamethyldisilazane
ITO	Indium tin oxide
K_A	Direct Stretching modulus
K_b	Bending modulus
k_B	Boltzmann constant
K_c	Bending modulus
K_{dir}	Direct Stretching modulus
Liss Rhod PE	1,2-dipalmitoyl-sn-glycero-3-phosphoethanolamine-N-(lissamine rhodamine B sulfonyl) (ammonium salt)
L_d	Liquid disordered
L_o	Liquid ordered
NPs	Nanoparticles

PBS	Phosphate Buffered Saline
PC	Phosphatidylcholine
PDMS	Polydimethylsiloxane
PEB	Post Exposure Bake
PEO-PCL	Poly(ethylene oxide)-*block*-poly(caprolactone)
POPC (16:0/18:1)	1-palmitoyl-2-oleoyl-glycero-3-phosphocholine
SEM	Scanning Electron Microscopy
Si	Silicon
SM	Sphingomyelins
SOPC (18:0/18:1)	1-stearoyl-2-oleoyl-sn-glycero-3-phosphocholine
T_m	Temperature phase transition
UV	Ultra-Violet
w/o	Water in oil
Wt %	Weight percentage
αHL	α-hemolysin

Lipid structures

DLPC (12:0)

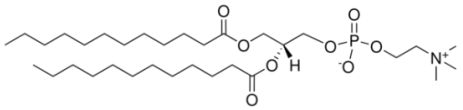

DMPC (14:0)

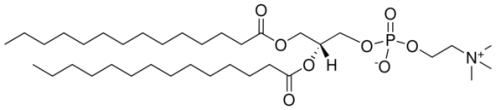

DPPC (16:0)

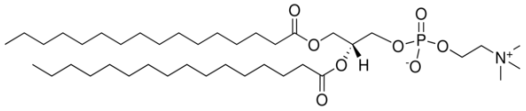

DPPG (16:0)

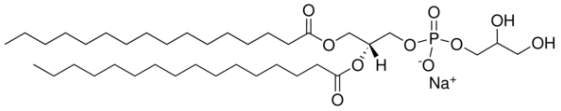

DSPC (18:0)

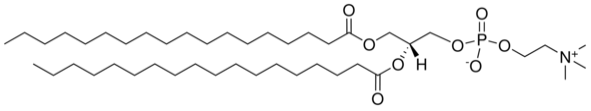

DOPC (18:1)

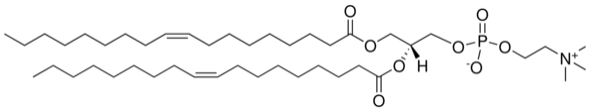

POPC (16:0/18:1)

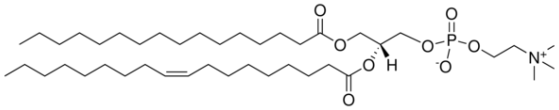

SOPC (18:0/18:1)

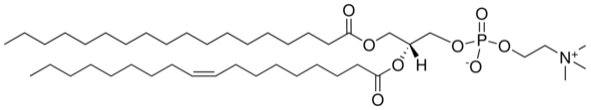

Brain SM

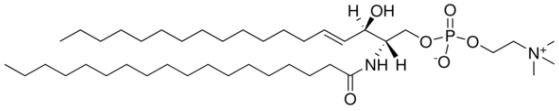

Cholesterol

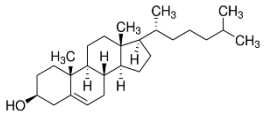

Liss Rhod PE 16:0

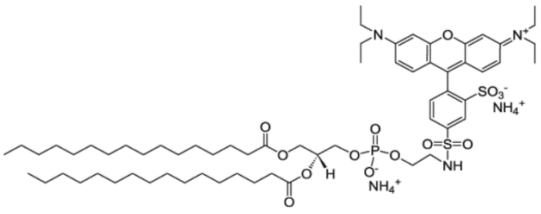

BODIPY C12

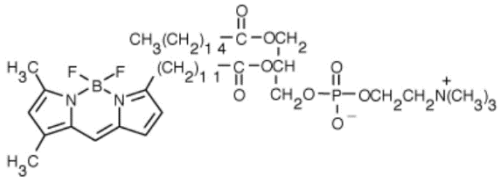

General introduction

The plasma cellular membrane is the envelope that enwraps the cell and is the main barrier between the interior and the outside environment of the cell. Many biological processes, such as endocytosis and exocytosis are controlled by the plasma membrane, mostly made by lipids and proteins, and which undergoes various physico-chemical changes in order to allow or not such passages to happen. Any disturbances happening in the membrane could lead to dysfunctional biological processes and could cause many pathologies. Therefore, understanding the different properties (physical, mechanical and chemical) of the cellular membrane is a must. The cellular membrane has thus been one of the main field of study for many biologists, biophysicists and especially pharmacologist. In fact, a lot of drugs need to first cross the cellular membrane in order to reach a specific target inside the cell. Nevertheless, cellular membrane is too complex to be fully studied and understood without decomposing into compartmentalized parts. Therefore, over the years, scientists have developed biomimetic model membranes, which aim is to reproduce and mimic parts of the cellular membrane. Biomimetic membranes are many, however Giant unilamellar vesicle s (GUVs) are the most common used models due to their architecture, which is the closest to the cell, and because they are easy to manipulate and visualize under optical microscopy. Many are the techniques which have been developed to characterize the GUVs, however micropipette aspiration became the gold standard technique. It gave access to determine several properties of the model membranes such as the mechanical properties (bending and stretching modulus), the thermal transition and thermomechanical behavior as well as the line tension and the molecular exchange and interactions between vesicles. However, this technique suffers from low experimentation throughput, heavy equipment, and long experimentation.

Microfluidics, which is the science of manipulating and controlling fluids at small scales, has been increasingly applied over the years on biomimetic models. In fact, thanks to this technology, scientist have been able to: generate GUVs, characterize several properties of the membranes and finally to investigate membrane-molecules or membrane-nanoparticles (NPs) interactions, for drug delivery targets. In MILE team in LAAS, we generally focus on developing Lab on Chips systems based on microfluidic platform to address health and environmental applications. Therefore, the first main objective of my Ph.D project is to use microfluidics in order to manipulate and characterize different properties of Giant unilamellar vesicles.

The parallel axis of this project is to use model membranes as tools to investigate membrane-molecule or membrane-NPs interactions in order to understand what is the effect of nanoparticles on

membranes, and if they are able to cross the membrane and penetrate inside the cell. These are relevant questions related to drug-delivery and nanomedicine topics. To do so, we worked with CSGI lab (Center of Colloid and Surface Science) and the University of Florence in Italy as part of my cotutelle. They have developed expertise in model membranes and their interactions with nano-objects, as well as in synthesizing different nanoparticles.

The aim of the work is to first, develop an on-chip micropipette aspiration in order to characterize the mechanical properties of Giant unilamellar vesicles. Our goal is to overcome the limitations of the traditional micropipette aspiration technique, by offering a high throughput microfabrication and microfluidic experimentation. Secondly, as an interesting application of microfluidics and model membranes combination, we wanted to investigate the effect of different nanoparticles on model membranes, by characterizing the mechanical properties of GUVs that are challenged with nanoparticles.

This manuscript will be divided in 5 chapters, 3 of them are necessary introductions followed by the main works and results that were done during the Ph.D. The first chapter will introduce the main components and characteristic of the plasma cellular membranes, followed by the model membranes types and their fabrication techniques. In the second chapter, the different method of characterizing the mechanical properties (such as the bending and the stretching modulus) of the model membranes are introduced, however only the micropipette aspiration technique will be fully elaborated. As there is a significant variability in the literature on the elastic moduli of the lipid membranes measured by different techniques, the reasons behind the differences are discussed, as well as other parameters that could affect the elasticity of the model membranes. The third chapter will be dedicated to microfluidics and the main concepts used. Moreover, I will go into the details of how microfluidics has been a great tool to investigate different properties of the model membranes, such as the permeability, the mechanical properties and the interaction of GUVs with molecules and particles.

The results part is divided into two chapters based on two different microfluidic approaches to build an on-chip micropipette. In chapter 4, the first microfluidic platform was made of three level microchannels, with a hanging channel in between which represents the trap in which the GUV would be deformed. The final chip was made by assembling etched silicon and glass wafers. An important technological development of glass etching was made. The second microfluidic platform, which will be detailed in the final chapter (chapter 5), is a novel technique and is made on an assembly of polydimethylsiloxane (PDMS) microfluidic chip and a sliding element which contains all the function, in our case, the on-chip micropipette. Using both of the platforms, the objective is to characterize GUVs with simple lipid composition, GUVs that are made with a mixture of lipids and GUVs that are

challenged with nanoparticles. The large advantages that offers the second microfluidic platform provides many possible applications of the on-chip micropipette. Therefore, micropipette aspiration was also tested on biological objects, such as 3D aggregates of cancer cells.

Chapter I

1 Cellular and Model membranes

Cells are very complex systems. They have multiple structures and functions, and understanding specific mechanisms can be a difficult task. The cellular membrane is the barrier between the interior of the cell and the outside environment. In mammalian cells, a cellular membrane, also called plasma membrane, is made of a bilayer of mostly phospholipids with embedded proteins. The plasma membrane's primary function is to protect the cell from its surrounding by being selectively permeable. It also plays a role in anchoring the cytoskeleton to provide the shape of the cell and maintaining cellular potential.

"In short, if the cell is represented by a castle, the plasma membrane is the wall that provides structure for the buildings inside the wall, regulates which people leave and enter the castle, and conveys messages to and from neighboring castles. Just as a hole in the wall can be a disaster for the castle, a rupture in the plasma membrane causes the cell to lyse and die" [1].

Artificial cellular membranes present a basic model solution to mimic cellular membranes. Scientists often use them to understand biological processes that happen on/to the membrane. Model membranes are many, but Giant unilamellar Vesicles are commonly used models because of their large sizes and because they can be easily manipulated and visualized under a fluorescence microscope. They are compartments of aqueous solution enveloped with a lipid bilayer, and their fabrication techniques have been growing ever since the first electroformation technique in 1986.
In this chapter, I will discuss the structure of the biological plasma membrane, the different types of lipids that constitute it, and their different characteristics and effect on the plasma membrane. I will then discuss the different model membranes and their applications, specifically the Giant unilamellar vesicles and their fabrication techniques.

1.1 Cellular membrane

A cell is the basic unit of life. The different structure and elements that constitute it are grouped in separate compartments which interact with each other and form complex networks and molecular machinery on scales ranging from nanometers to micrometers [2]. The role of a cell consists in transporting nutrients to use in the chemical processes that go on inside them, producing energy through respiration, creating metabolic reactions, and aiding in reproduction. 70% of the cell is made of water, 18% of proteins, 5% of phospholipids, and other kinds of lipids, and the rest is divided between numerous things, among them the RNA and DNA, which carry the genetic information ***(Figure I-1)***

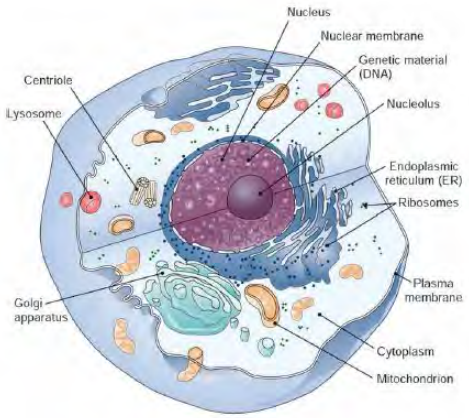

Figure I-1 : Composition of a eukaryotes cell enveloped by a plasma membrane [3].

In biology, compartmentalization is a universal expression that is the organization of all living cells that are encapsulated by a biological membrane that encloses and maintains a highly regulated state dissimilar from the surrounding environment [3].

1.1.1 Biological membrane and its main components in mammalian cells

The cellular membrane, sometimes called the plasma membrane, is the envelope that groups all cell's compartments. It separates the inside of the cells from the outside environment. The cellular membrane is mainly made of lipids and proteins, which due to their characteristics, avoid any leakage from inside to outside the cell and vice-versa and therefore maintaining the different concentrations of solutes on the two sides [4]. The bilayer lipid membrane is 3 - 5 nm thickness in animal cells and 7-9 nm in bacterial cells. Though all cells have membranes, their lipid and protein composition and changes in their composition are essential characteristics to distinguish membranes coming from different species, different cells, and various subcellular structures. For example, the membrane of the nucleus of a cell is very distinguishable from the ER's membranes (endoplasmic reticulum) [4]. In

this introduction, we focus mainly on the eukaryotic mammalian cellular membrane: the plasma membrane.

The mammalian cellular membrane is mainly composed of a double layer of phospholipids in which proteins are embedded in or attached to it (***Figure I-2)***. The lipid bilayer membrane is made of two monolayers of amphiphilic molecules: they are molecules made of a hydrophilic polar head and hydrophobic acyl chains, affine to apolar substances. Due to the amphiphilic characteristic of these molecules, they spontaneously form a lipid bilayer, where the polar parts are headed to the aqueous environment outside and inside the cell. The function of the cellular membrane depends on the main substances present in it. The lipid bilayer is heterogeneous, made of different types of lipids, which will be listed in detail in the next paragraph. It includes mainly phospholipids and cholesterol responsible for the structural functions and affects the membrane's permeability. Other lipids, such as glycolipids (lipids containing sugars) and sphingolipids, protect the membrane from harsh conditions such as low pH and degradative enzymes. The mammalian cellular membrane is made of 30% of proteins (~7000 proteins), which are either bounded only to the membrane surface or buried within the membrane on one or both sides of [5]. They are divided into two major groups: Integral proteins (intrinsic) and Peripheral (extrinsic) proteins which only interact with the hydrophobic core of the lipid bilayer.

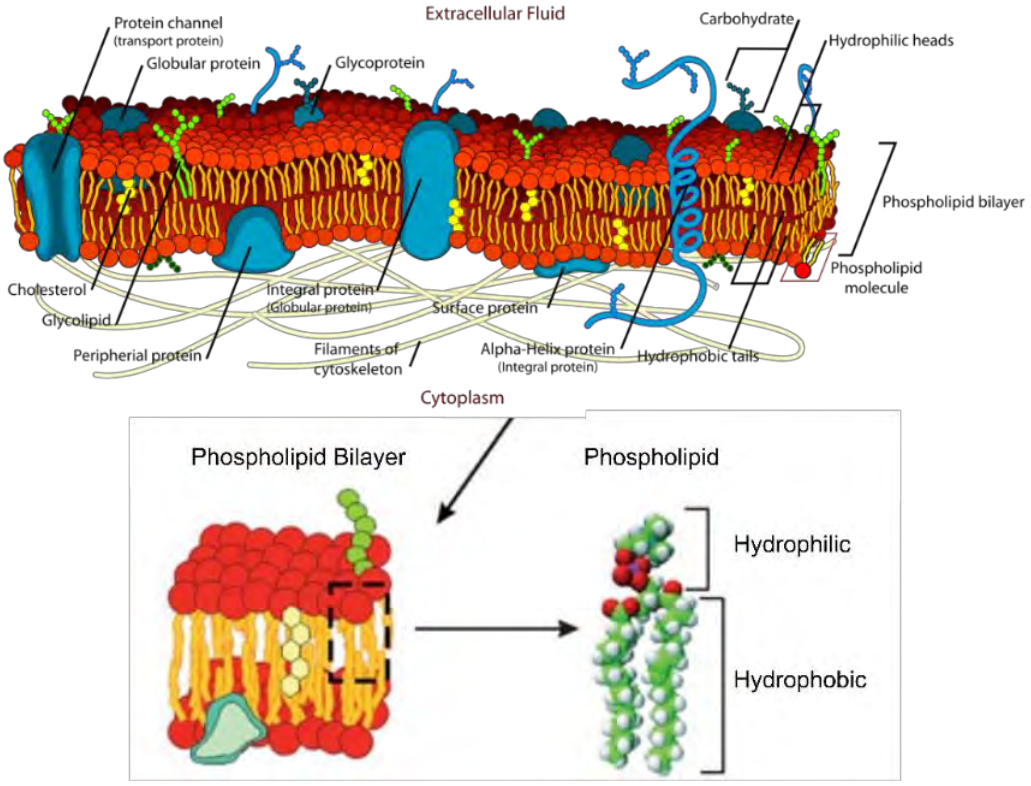

Figure I-2 : Mosaic of a cellular membrane. The main components of the cellular membrane are the phospholipid bilayer (in red the hydrophilic head, linked to the yellow hydrophobic acyl chains) and the different classes of proteins anchored into or attached to the membrane [4].

Proteins' main functions include energy conversion, triggering intracellular signaling pathways, neurotransmission, and cell-cell interactions. Together with the lipid bilayer, they selectively control and transport molecules and ions across the membrane. Therefore, 60% of drugs today target a membrane protein [6]

1.1.2 Lipid composition of cellular membrane

1.1.2.1 Lipids are divided into three distinct classes

Typical lipid membrane contains more than 100 species of lipids, divided into three major classes:

- **Phosphoglycerides**
- **Sphingolipids**
- **Sterols**

The composition of these lipid classes is detailed in ***(Figure I-3)*** [7]**. Phosphoglycerides (PGL)** and **Sphingolipids** can be combined under one category, called phospholipids. They are composed of a (i) *hydrophobic Acyl chains*, (ii) *hydrophilic head group,* and (iii) an *acid backbone* linking the head and the tails together. The chemical diversity in these lipids comes from the various combinations of the three different block which compose them:

(i) The fatty acid chains vary in length as they are typically between 14 and 24 carbon atoms. They also vary in the number and position of saturation and unsaturation. In fact, sn-1 fatty acid present in the chains tends to be saturated (without double bond) or monounsaturated, whereas the sn-2 tends to be monounsaturated or polyunsaturated. However, the N-acyl chains of sphingolipids tend to be more saturated and can be longer than the acyl chains of PGL.

The length of the carbon chains affects how the lipids can tightly pack to each other and, therefore, affect the properties of the membrane [8]. The head and the tails are linked to each other by a backbone (iii) made of either Glycerol (Phosphoglycerides) or Sphingoid base, which is simultaneously the backbone and a hydrophobic tail for Sphingolipids.

(ii) The polar head of the Phosphoglycerides is made of a phosphate group, linked to one of these 6 groups: Choline - phosphatidylcholine (PC) zwitterionic lipid, Ethanolamine - phosphatidylethanolamine (PE) zwitterionic lipid, Serine - phosphatidylserine (PS), and Inositol - phosphatidylinositol (PI) anionic lipids, phosphatidic acid (PA) and phosphatidylglycerol (PG) ***(Figure I-4)***. The polar heads of Sphingolipid are also diverse and define the sphingolipid name. An example is the Phosphocholine head group, which gives the Sphingomyelin name of the lipid: Brain Sphingomyelin (SM) is found at exceptionally high concentrations in the membranes of nerve cells and red blood cells.

Sterols are smaller than phospholipids. They are made of one single polar head group, attached to a rigid steroid ring structure and a short hydrophobic tail. The heads and tails of sterols are respectively

embedded in the membrane with the heads and tails of the phospholipids. Therefore, the sterols' tails affect the membrane's mechanical properties. Cholesterol is the principal sterol component of the mammalian cell membrane.

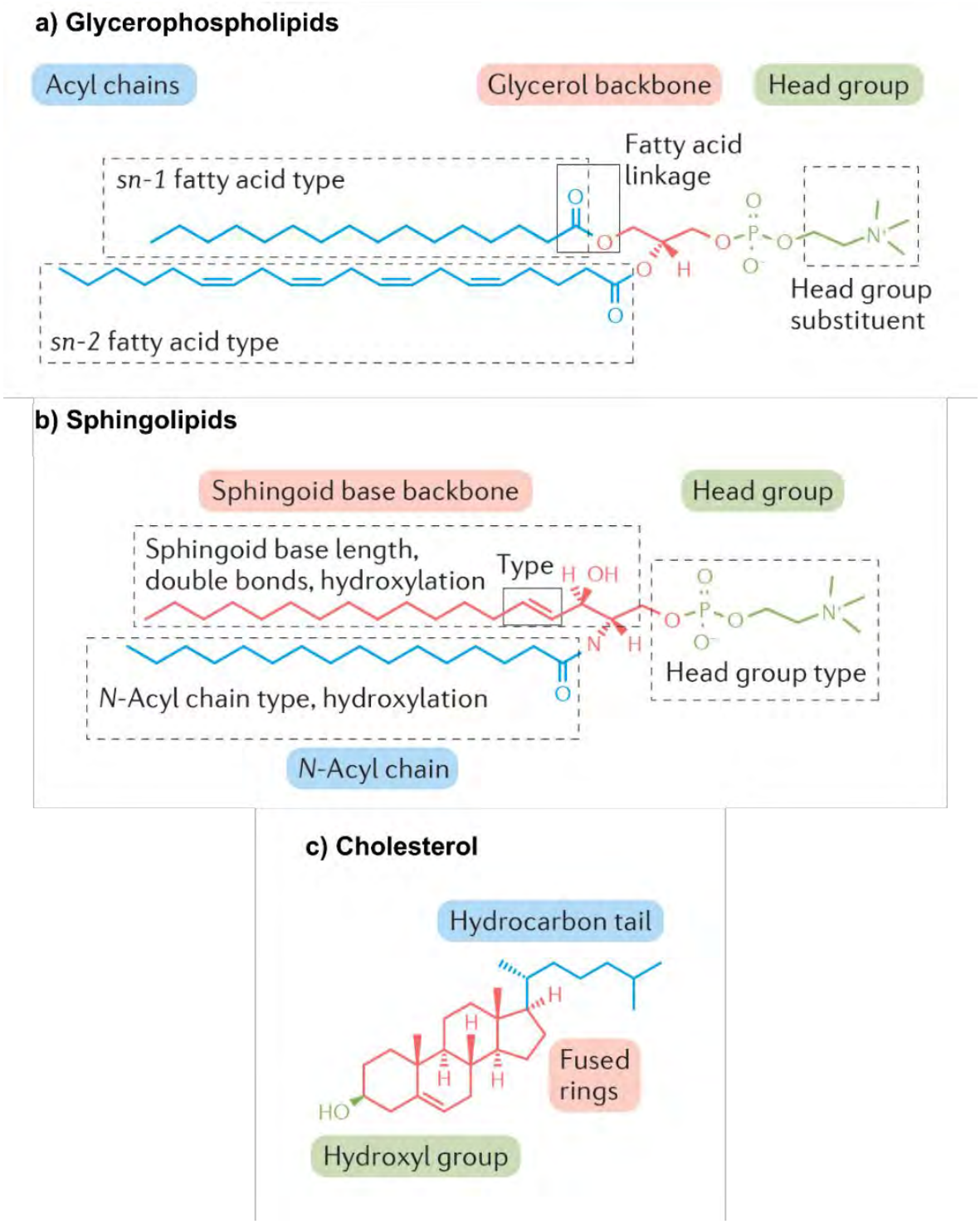

Figure I-3 : Chemical diversity of mammalian lipid membrane. (a) Glycerophospholipids composed of head group, fatty acid chains at the sn-1 and sn-2 positions, linked together by a Glycerol backbone. (b) Sphingolipids consisting of a head group, an N-Acyl chain, and a Sphingoid base backbone, which connects the head and the tail and is also a hydrophobic tail. (c) Cholesterol, which is the made sterol component of the mammalian cell membrane [7].

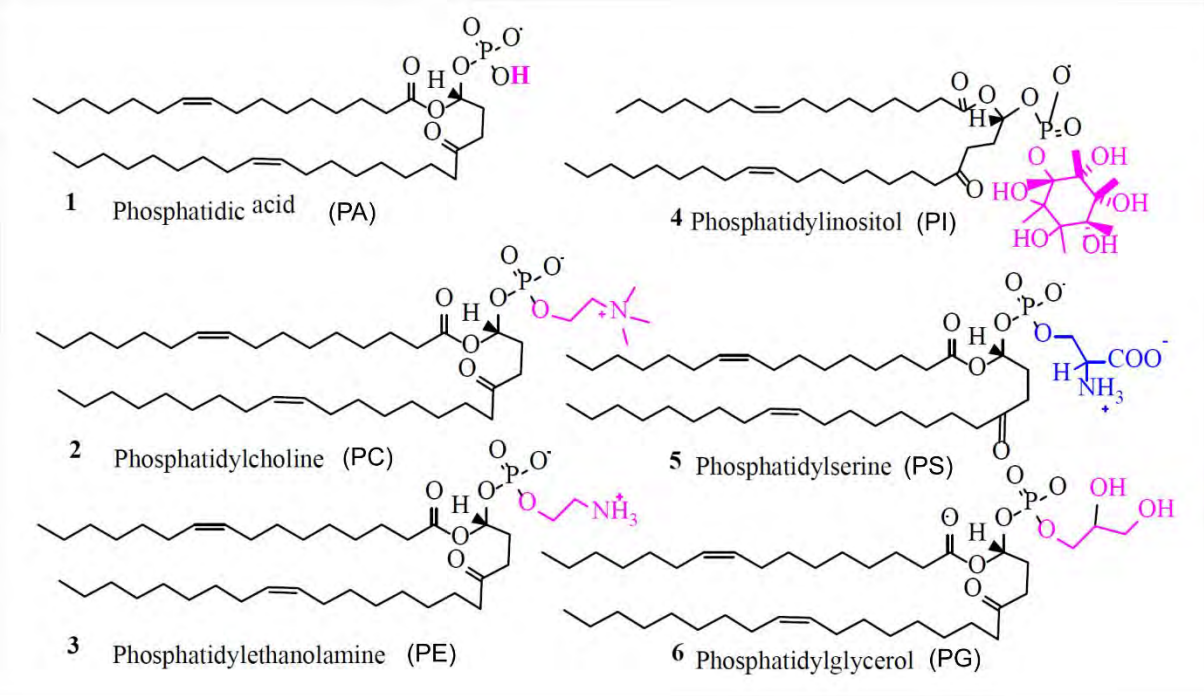

Figure I-4: Functional groups and the name of phospholipids along with the corresponding structures. Phospholipids are divided into 6 groups: Phosphatidyl acid (PA), Phosphatidylcholine (PC), Phosphatidylethanolamine(PE), Phosphatidylinositol(PI), Phosphatidylserine(PS) and Phosphatidylglycerol (PG) [9]. *PC, PS, and PE are the dominant ones in the cellular membrane. PI and PA are present in the cellular membrane in a small amount. And Finally, PG does not exist in the plasma membrane, but they are important in the bacterial membranes.*

1.1.2.2 Lipid shape and organization in the cellular membrane

Because of the amphipathic nature of the lipids (polar head and hydrophobic tail), they can form bilayers or micelles in aqueous solutions. Moreover, the relative size of their head group and hydrophobic tails affects the shape of the lipids, and therefore the spontaneous curvature of the membrane [7]. Two major interactions (hydrophobic tails-water and hydrophilic-water) act as "opposing forces" and imposes the shape of the lipids: the hydrophobic tails force tends to decrease the contact with water, and the polar head tends to increase its interfacial area per molecule when in contact with water [10]. To determine the shape, three parameters are to be considered: the volume "*v*" of their hydrocarbon chain (assumed fluid), the area "*a*" of their polar head, and the maximum length "*l*" that the chains assume. Once these parameters are measured or estimated, it is possible to determine the lipids' structure that they can take. The "packing parameter" is given by : $\frac{v}{al}$. Three different cases can be presented: if $\frac{v}{al} < \frac{1}{3}$ the lipids will form spherical micelles or non-lamellar hexagonal shape, if $\frac{1}{3} < \frac{v}{al} < \frac{1}{2}$ the lipids form non-spherical micelles or non-lamellar inverted shape and finally if $\frac{1}{2} < \frac{v}{al} < 1$ the lipids form bilayers [10]. ***Table I-1*** shows some examples of phospholipids with different head groups and acyl chains and the different shapes each can take, and the geometry of the structures in which they participate [11]. PC or SM presents a cylindrical shape based on head

and tail proportion. Others, such as LPC (lysophosphatidylcholine) have a higher head-to-tail proportion which gives an inverted conic shape which causes a positive membrane curvature. And finally, PA, PE, PS, and DAG present small head-to-tail proportions, which provides coned-shape lipids and causes a negative membrane curvature.

Table I-1 : shape and structure of different lipids and the extended geometry of the structures in which they participate: PC lipids take a cylindrical shape and form a lamellar bilayer structure. PE lipid takes a conic shape and forms inverted micelles, and finally, LPC (with one hydrophobic tail) takes an inverted conic shape and creates a micelle shape [11].

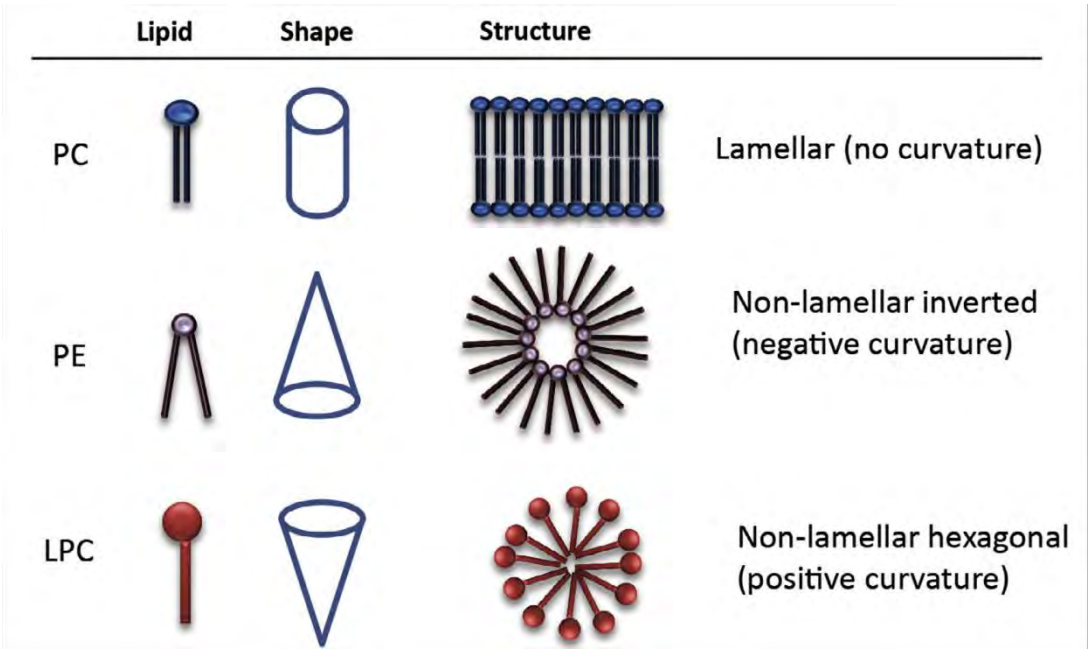

1.1.2.3 Lipid diversity and asymmetry in mammalian biological membrane

The lipid composition of mammalian biological membranes is heterogeneous and contains hundreds of different lipids. In fact, the Plasma membrane is composed of a high ratio of sphingolipids and sterol [12], mainly cholesterol (44%) [13] (whereas only 8% are present In Golgi, 6% in Endoplasmic reticulum (ER), and 3% in mitochondria). As sterols are rigid lipids, they allow the plasma membrane to resist mechanical stress. Phosphatidylcholine (PC) is the second most abundant phospholipid (Glycerophospholipids with Choline as a polar head group) in a healthy plasma membrane with 34%. The rest is divided between PE (4%), DAG (4%), PS (2%), Pi (1%)… Some of these lipids have some clear and unique functional roles; for example, phosphoinositide (PI) is responsible for binding and regulating protein effectors [14]. However, most of the functions or roles of most of the other lipids remain unknown.

To understand the complexity of plasma membrane, simulations have been done to give a fundamental view on the lateral organization of lipids in a plasma membrane. They showed 63 different lipids species and combined 14 types of head group, and 11 types of tails and that are asymmetrically distributed across the inner and outer leaflet of the membrane. One of the deduction

is that phosphoinositide (PI) shows preferential clustering in the inner leaflet [15], and the consequence of the transfer of it to the surface serves as a pathophysiological signal in processes such as apoptosis and blood coagulation [11] .

Diversity in the PC lipid species is also an essential factor to consider ***(Figure I-5)***. The PC species are also classified into saturated acyl chains, unsaturated acyl chains, and hybrid chains with the highest ratio [13].

The lipid membrane's complexity comes from its heterogeneity in the lateral displacement of the lipids and the possibility of having asymmetric leaflets within the bilayer. Two different types of lipid can be present concurrently in the outer and inner parts of the bilayer. For example, Phosphatidylethanolamines (PE) and phosphatidylserines (PS) are mainly found in the inner leaflet of the plasma membrane. At the same time, phosphatidylcholine (PC) and sphingomyelins (SM) are essentially based in the outer leaflet [16].

The distribution of cholesterol between the two leaflets is still debated [17]: because cholesterol has a small head group, it can dissolve in the phospholipid stratum and move in between the two leaflets. This fast transbilayer movement makes it difficult to determine either the distribution of cholesterol in the membrane either the exact rate value of this movement, but it appears to be less than a second [18]. The asymmetry of the lipids in biological membranes is responsible for membrane curvature, which is important for biological processes, such as membrane fusion and vesicle budding. However, changes in lipid composition are found in several diseases such as cancer or type 2 diabetes, but it is not clear if they are the cause or a symptom of such conditions [7]. Nonetheless, in genetic diseases, a mutation in lipid-related enzymes can cause an abnormal lipid composition which causes a biological dysfunction.

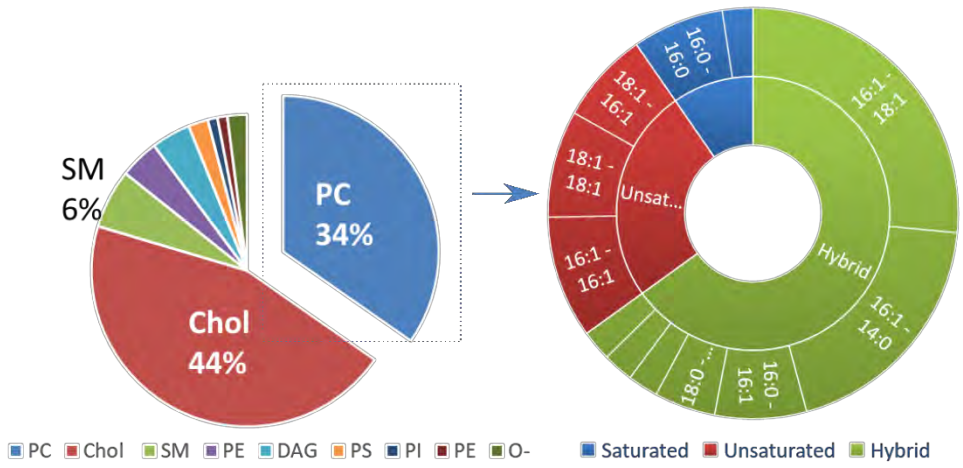

Figure I-5: Lipid diversity in plasma membrane and distribution of phosphatidylcholine (PC) lipids. Cholesterol is the highest composition of the plasma membrane, followed by PC and SM species. PC lipids are grouped by hybrids fatty acyl chains, with the highest ratio, followed by unsaturated acyl chains and saturated chains [13].

1.1.2.4 Lipid movement and charges in the cellular membrane

Movements of lipids

The fluid characteristic of the plasma membrane comes from the ability of the bilayer components (lipids and proteins) to move freely. As for the lipids, we distinguish three types of movement: rotational, lateral, and transverse or also called "flip flop" ***(Figure I-6).***

Lateral movement is characterized as "Hop diffusion" rather than Brownian movement: lipids stay in one region for a short time before hopping to another location. C_D is the diffusion coefficient that characterizes the lateral movement of the lipids: $C_D = 10^{-7}$ to 10^{-10} $cm^2.s^{-1}$ This movement takes less than a minute to occur [19]. The lateral movement is faster in the inner leaflet than the outer one as the latter one is made of PC and SM lipids which are more saturated than the PS and PE lipids present in the inner leaflet.

Rotational movement is the movement of the lipid around its perpendicular axis, characterized by its rotational diffusion coefficient, which defines the angular rotation of a lipid molecule around its axis perpendicular to the plane bilayer. This movement is in the timescale of nanoseconds [20].

Spontaneous ***"Flip flops" movement*** is relatively slow (in the order of the hours, possibly days) [21] due to the high resistance of polar heads to cross the hydrophobic environment of tails; therefore, to maintain the asymmetry of the membrane, transverse movement is usually assisted by membrane proteins and catalyzed movement: Flippases and Floppases [22]. Flippases move phospholipids from the outer leaflet to the inner leaflet (such as PS lipids which are mainly present in the inner leaflet), while Floppases move them in the opposite direction. These movements are promoted by short chains and double bonds in acyl chains of phospholipids, creating spaces in the bilayer membrane.

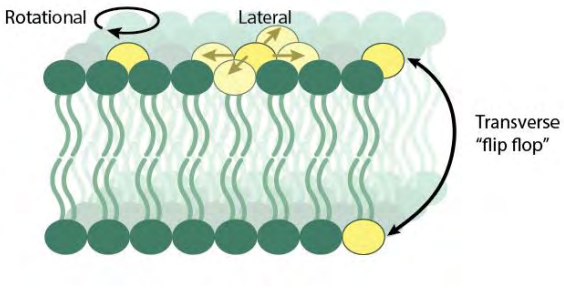

Figure I-6 : Movement of phospholipids in the plasma membrane. 3 types of movement are distinguished: rotational, lateral, and transverse [mechanobio.info]

All the movements mentioned above have a significant role on the properties of the membrane. An example of mixed lipid movement in a liver plasma membrane was caused due to interaction with ethanol. In fact, after exposure of hepatoma cells to ethanol for 3 weeks, the movement of lipids led to an increase in the ratio of phosphatidylcholine/sphingomyelin (PC/SM), which increased membrane fluidity [23].

Charges of lipids

Due to the asymmetry of the cellular membrane and the transversal movement that the lipids undergo to maintain it, the charges of the lipids are also asymmetrically distributed between the two leaflets of the plasma membrane: the inner leaflet is negatively charged, and the outer leaflet is mainly neutral. In fact, the outer leaflet is mainly made of zwitterionic PC and neutral sphingomyelin, while the inner leaflet is mostly made of anionic phospholipids such as PA, PE, PS. The low acid dissociation constant (pKa) values of the phosphate groups of the lipid head group are responsible for the negative charge of these lipids [24].

1.1.2.5 Membrane liquid-ordered and liquid-disordered phases

Lipid phases in the cellular membrane

As the polar head of lipids is responsible for the charges of the lipids, the acyl chains are, however, responsible for the lipid phases. In fact, lipids of biological membranes in physiological conditions can exist in multiple possible phases, liquid-disordered phase (L_d) or (L_α), solid gel phase (S_o) or (L_β), and liquid-ordered (L_o) [12]. Sphingomyelin (SM) lipids chains are long and saturated, so they tend to adopt a solid-like phase and have a high melting temperature. Glycerophospholipids (GPL) are rich in unsaturated and shorter hydrocarbon chains; therefore, they tend to be enriched in liquid phases and have a much lower melting temperature than the SM. And finally, sterols by themselves do not form bilayer phases, though they have a high melting temperature. However, if combined with a bilayer-forming lipid, they tend to adopt a liquid-ordered phase [25] ***(Figure I-7)***. T_m is the temperature needed to generate the lipid melting from a gel phase to a liquid-disordered phase (liquid phase). T_m is a particularity of each lipid type, as it depends on the nature of the hydrophobic chains. In fact, if the length of acyl chains increases, T_m increases. However, if the degree of unsaturation in the chains increases, T_m is decreased. For example, DOPC melting temperature is -20°C, whereas DPPC is 41°C (DOPC contains 18 carbons in its chain with 1 unsaturation on each, while DPPC contains 16 atom carbons in its chain with no unsaturation on any of it).

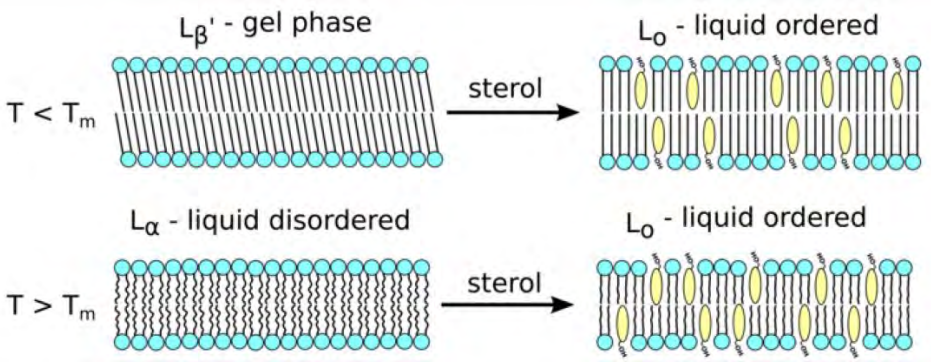

Figure I-7 : Cross-sectional view of the liquid-ordered phase obtained by insertion of cholesterol in the gel phase and the liquid-disordered phase. The liquid-ordered represent a hybrid of the liquid-disordered and the gel phases. The yellow molecules are the cholesterol [26]

Membrane's phase separation

Since plasma membrane contains a mixture of lipids of different lengths and degrees of unsaturation, it results in different T_m's. At physiological temperature, lipids that have a high melting temperature undergo the transition to the gel phase before the rest of the lipids with low melting temperature [26]. This results in the formation of small, heterogeneous, and highly dynamic microdomains that are enriched in cholesterol and sphingolipids, which contain long saturated acyl chains ***(Figure I-8)***. This evolved model in the lipid model was brought by *Simons et al*. [27] and *Browns et al.* [28]*, in 1997.* These microdomains arise from the interaction of cholesterol with saturated acyl chains and produce packed and tight lipids compared to phospholipids, which contain unsaturated chains [28]. The size of these microdomains is between 10-200 nm, which is lower than the resolution of conventional optical microscopy [27]. The co-existence of phospholipids and sphingolipids leads to phase separation in a cell's membrane. These two phases would be separated into a liquid-ordered phase (L_o) and a liquid disordered phase (L_d). However, it is interesting to mention that macroscopic phase separations are seen in model membranes but not in living cells. Therefore, the *in vivo* existence of these domains is still debated [29].

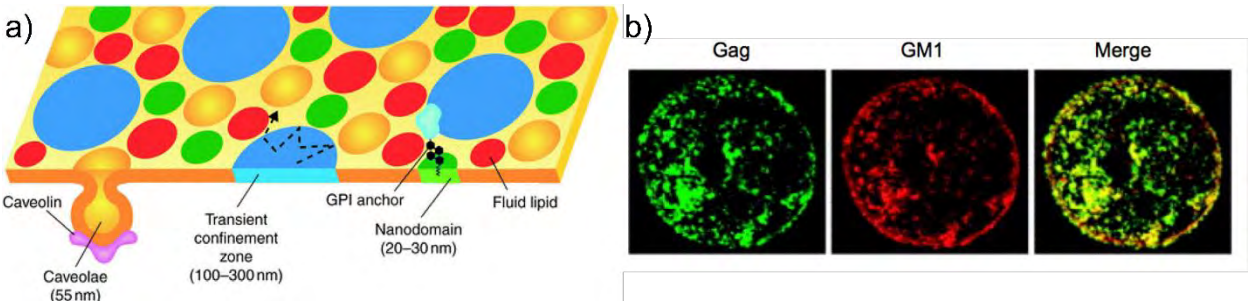

Figure I-8: a) Mosaic domain model of the plasma membrane, modeling the different lipid domains: caveolae, nanodomains, TCZ and zones of fluid enriched lipids [30] *b) Microdomains in Jurkat membrane cells, marked with the GM1 raft marker (in red)* [31].

1.1.2.6 Lipid influence on membrane properties

Membrane's different properties

Several of the membrane properties have been discussed already in the previous paragraphs, such as (i) the diffusion of lipids inside the membranes and the flip-flop transversal movement, which are essential to maintain asymmetry. Also discussed is (ii) the fluid or non-fluid phase, which is a characteristic of the membrane which can affect the rotation and diffusion of proteins and other molecules within the membrane. Another property is the (iii) shape of the membrane that is imposed by the lipids form, which gives the spontaneous positive or negative curvature of the membrane. Another property also linked to the curvature of the membrane is (iv) the bending modulus which will be detailed in chapter II. Finally, the cellular membrane is semi-permeable and is generally repellent

to large molecules and to ions. Characterizing membrane permeability (v) for molecules is important for drug delivery tests.

Effect of lipids on membranes properties

Membrane properties are influenced by lipid composition. Given the structural diversity and quantitative variability of lipids in cellular membranes, their actual properties will be the results of different combinations of several parameters [32]. The fluidity of the membrane is characterized by the number of unsaturation and length of the acyl chains: unsaturated and short fatty acid leads to higher membrane fluidity. The degree of unsaturation in the acyl chain also influences the surface area covered by them. Therefore, it imposes the shape of the lipid, and together with the shape of the polar head, affect the spontaneous membrane curvature. The surface charge of the membrane is determined by the chemical properties of the lipid head groups. And finally, the interaction between specific lipids (SM and cholesterol) leads to domain formation in the membrane. In the coming chapters, I will be discussing more deeply the effect of these characteristics on the membrane.

Furthermore, the localization of proteins in the membrane can be influenced by their thickness. For example, TMDs (transmembrane domains proteins), present in the plasma membrane, are longer than the TMDs present in the Golgi or ER membrane. And that is explained by the fact that the plasma membrane is thicker than the one of Golgi or ER [33]. And any changes in the thickness of the membrane can lead to a dislocation of the proteins.

Biological cellular membranes have fascinating structures and mechanisms. However, no one can deny the degree of complexity and sophistication that scientists and biologists face in order to fully understand this system. In vitro studies of cells have surely pushed our knowledge, whether using 2D or 3D cell cultures [22] [23], or studying a population of cells as a whole (such as tumor cells, neurons cells …), or even turning it down to a single cell. Nonetheless, a lot of mechanisms can be co-dependent, making it hard to understand and decipher solo performances of cell membranes' species. And more, cellular interactions with any nutrients, reagent, or drug inside our body are initiated first through the membrane, as it is the barrier between the inside and outside environment of the cell. For these reasons and more, and for the last few decades, scientists and biophysicists worked on developing biomimetic membranes, aiming at modeling cellular membranes [27], [36].

1.2 Artificial biomimetic membrane

Model membranes have been developed to study different membrane properties such as lipid structures and function, processes happening in the membrane, curvature effect [37], ion channels, and interaction of lipids with drugs or nanoparticles [38], as well as investigating membranes activity of diverse natural or synthetic compounds such as peptides [39]. Model membranes' fabrication and manipulation can be delicate and require know-how. However, it is possible to simplify and control the composition contrary to the biological membranes, which are complex, difficult to extract and maintain under physiological conditions. This simplified model membrane can facilitate the identification of the different mechanisms of the membrane.

1.2.1 Model membranes: their purpose and their characterization techniques

Figure I-9 shows the different models of lipid membranes used to study the different properties of cellular membranes: lipid vesicles or liposomes come in different size (going from 10 nm to 100 µm). Micelles are also spherical but they are made of a single lipid layer with the hydrophobic core pointed to the inside. Lipid monolayers and supported lipid bilayers: both are planar model membrane. There are other lipid models that are not shown in ***Figure I-9***, but are still used as model membranes such as: tethered bilayers which are bilayer membranes that are pushed away from the solid substrate, using a hydrophobic polymer anchored in the membrane and bound to the substrate, or lipid bilayer formed on top of a polymer which was coated on a substrate [41]. The main model membrane used and which I will detail in the paragraphs below are: Lipid monolayer, supported lipid bilayers and the vesicles [42], [43], [44], [45].

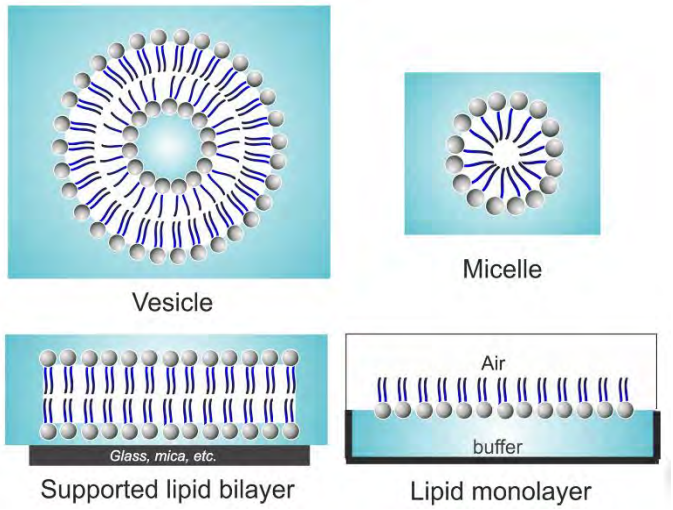

Figure I-9: Different model membrane systems. Lipid vesicles or liposomes are spherical objects consisting of aqueous solution enclosed by a lipid bilayer. Micelles are also spherical, but they are made of one monolayer, with the hydrophobic core on the inside and no water. Supported lipid bilayer is a planar model made of a flat lipid bilayer supported on a solid surface such as glass, silicon or mica. Lipid monolayer are obtained by spreading a lipid on a buffer, and the lipid molecule have an orientation where the polar head is towards the buffer and the hydrophobic core is pointed towards the air [40].

1.2.1.1 Lipid monolayers

Lipid monolayer, also called Langmuir monolayer, is half a bilayer membrane that is formed by spreading amphiphilic molecules on the surface of a liquid. Lipid monolayers are homogeneous, stable and plane and therefore are useful for certain studies such as: to evaluate membrane insertion of compounds (drugs, peptide, etc.), and to study interactions of the lipids as a function of different parameters, such as the nature of spread molecules, temperature, pH, etc. These parameters are characterized by isotherms compression, obtained by measuring the surface pressure of the interfacial film as a function of the mean molecular area of the molecules spread at the air-water interface. In order to visualize the interfacial organization of the lipids in the monolayer, fluorescent and Brewster angle microscopy is used by offering a lateral resolution in the micrometer range. However, these methods are not suited to visualize phase properties in the lipid monolayer at high resolution.

1.2.1.2 Supported lipid bilayers

Supported lipid bilayers (SLBs) are stable flat lipid bilayers that are supported on a solid substrate such as mica, glass, or silicon. In this model, the polar heads are facing the substrate while the hydrophobic acyl chains are headed towards the other chains from the second layer. Contrary to other model membranes, SLB models, due to their fabrication techniques, are able to keep the asymmetric aspect of the biological membrane. Since their development three decades ago by *Tamm et al.* [45], SLB is used to predict phase behavior and the organization of the molecules in a biological membrane. SLB is also used to investigate molecular interactions of drugs with cell membranes. Visualization and characterization of SLB membranes are easy as they are compatible with surface-sensing techniques such as AFM, secondary ion mass spectroscopy (SIMS), fluorescent microscopy, X-ray, and neutron reflectivity [40], [45]. One of the disadvantages of using SLBs model membranes is the proximity of the lipid bilayer to the substrate, which could affect membrane mobility or incorporation of proteins. Therefore, tethered lipid bilayers have been developed and are suitable models for studying membrane-protein interactions [46]. By characterizing the diffusion coefficient of lipids, FRAP technique (fluorescence recovery after photo-bleaching) measurement has demonstrated high lateral mobility of the lipids in such a system. Tethered lipid bilayers can be used for a variety of medical applications [47].

1.2.1.3 Lipid vesicles

Lipid vesicles or liposomes are the simplest model system of a closed cellular membrane. It consists of a closed compartment of a bilayer lipid membrane, with an aqueous solution from inside and outside, usually sucrose solutions. Multi lamellar vesicles (MLVs) are composed of several spherical lipid bilayers and are formed upon hydration of a dried lipid film above lipid phase transition temperature. MLVs can be used for cosedimentation and coflotation assays, as well as for solid-state

nuclear magnetic resonance. Unilamellar vesicles are composed of a single spherical lipid bilayer. Small unilamellar vesicles are formed by sonicating the MLV solution is a classical ultra-sound sonicator. Large unilamellar vesicles (LUVs) are formed by extruding the MLVs solution through a porous membrane, with determined pores size, or by several freeze-thaw cycles. However, the extrusion of the MLVs should be performed at a temperature above the highest melting temperature of the lipid mixtures, or else the extrusion will be unsuccessful because of the rigid phase state of the membrane. Small and Large unilamellar vesicles are suitable for spectroscopy and sedimentation-based assays. However, their size does not allow light microscopy imaging to characterize membrane dynamics, for example.

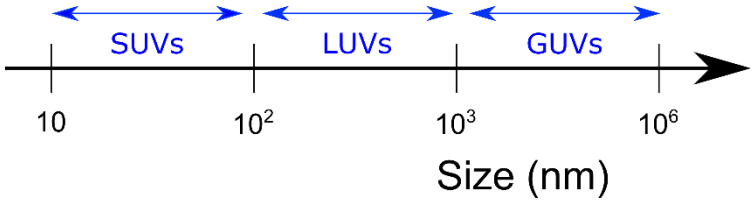

Figure I-10: Lipid vesicles distribution by their size [49]. Small unilamellar vesicles (SUVs), size between 1 and 100 nm. Large unilamellar vesicles (LUVs), size between 100 nm and 1µm. And finally, Giant unilamellar vesicles (GUVs), size going from 1µm to 1 mm.

Giant unilamellar vesicles (GUVs) fabrication techniques will be detailed in the following paragraphs, but in general, GUVs are formed by hydrating a dried lipid film for a long time (36 hours) or with the help of an external electrical field. Lipid vesicles have different sizes, depending on the method of fabrication for each [48]. It varies between 10 nm (SUVs) to 100 µm (GUVs) **(*Figure I-10*).** GUVs are the closest in size to actual cells and can be visualized and characterized using optical microscopy (fluorescent and confocal), atomic force microscopy (AFM), which requires the adherence of the lipid vesicle onto solid support [49]. GUVs can also be individually micromanipulated. Lipid vesicles are a good model to characterize membrane mechanical properties, permeability and they are suitable to investigate membrane processes such as membrane fusion, molecular recognition, cell adhesion and membrane trafficking. The application of such systems is enormous, especially in pharmacology and dermato-cosmetology as these vesicles are used as biomimetic membrane systems for drug delivery systems [50] and also allow the prediction of pharmacokinetic properties of drugs, such as their transport, their distribution, their accumulation, and therefore their efficacy [45].

GUVs present an excellent model membrane system for microscopic studies. In order to investigate mechanical properties of the membrane such as: bending rigidity, stretching elasticity, and phase separation, we chose to work with Giant unilamellar vesicles as model membranes.

1.2.2 Fabrication techniques of Giant unilamellar vesicles

A GUV is described to be a compartment made out of a lipid bilayer of 4-5 nm thickness and an aqueous solution inside the compartment. Depending on the method of fabrication, the outer environment of the vesicle can be the same or different from the inside solution. The methods of fabrication can be grouped into two major categories [51]: methods based on vesicle swelling on substrates and methods based on the assembly from fluid interfaces. In general, both methods have several steps and considerations in common. For example, the lipids ought to be in the fluid phase in order to form GUVs; therefore, the temperature at which the GUVs are forming has to be above the main transition temperature T_m of each lipid. If using a mixture of different lipids with different transition temperatures, the temperature has to above the highest transition of the mixture.

1.2.2.1 Swelling based method

These typical methods are based on spreading a lipid solution in a volatile solvent on a substrate, and leaving it to completely dry, and forming a film. The volatile solvent generally used is Chloroform ($CHCl_3$). The film is then hydrated with an aqueous solution, which first hydrates de polar head and then continuously swells the bilayer. Upon mechanical disturbing, the hydrated bilayer fragment detaches from the surface into the bulk aqueous solution, where they self-close and form heterogeneous GUVs. Self-closing occurs in order to eliminate the energetically unfavorable interaction between the lipophilic interior of an open bilayer and excess water [51]. The swelling can be spontaneous or assisted with the presence of a gel or an electrical field.

Spontaneous Swelling

Gently hydrating the lipid film [52] starts with a pre-swelling step in a water-saturated atmosphere followed by an overnight step of swelling in an aqueous solution. Many modifications were made to this method based on the deposit of lipid mixtures, localized heating, sugars, etc. For example, the use of 10-20 mol% of charged lipids such as phosphatidylserine (PS) or phosphatidylglycerol (PG) provides electrostatic repulsion between membranes and facilitates GUVs formation. However, a higher fraction of charged lipids can form low GUVs quality [53]. Divalent ions such as (Ca^{2+} or Mg^{2+}) also promote vesicle formation because the membrane is separated and stabilized when net charges on the membranes produce large enough electrostatic repulsion [54].

Gel-assisted swelling

Gel-assisted swelling, is based on the spontaneous swelling explained before, except that the substrate is a polymer-based gel. It was first introduced by (Horger et al., 2009) [55], by spreading a lipid solution (usually the solvent is Chloroform) on agarose, partially drying it, and then hydrating them in an aqueous solution. This trick provided a high yield formation of GUVs in a matter of minutes

compared to the gentle method, which takes a way longer time. However, residual agarose can stay in the solution of GUVs, contaminating the solution. And secondly, agarose is autofluorescent, which can be problematic for fluorescent microscopy studies. More polymer-based swelling tests were conducted, using cross-linked polyvinyl alcohol (PVA) [54], cross-linked dextran-poly (ethylene glycol) [56]. These methods show promising high yield and rapid formation of GUVs.

Electroformation

Electroformation method **(*Figure I-11*)**, firstly introduced by Angelova and Dimitrov (1986) [57] is probably the most used technique to generate GUVs. It is also based on controlled hydration of a completely dried lipid film which was a deposit on a substrate. However, the swelling process is assisted by an external alternative electrical field. Thus the substrate on which the film is deposit has to be electrically conductive such as Indium tin oxide (ITO) coated glass slide. During the past decades, various optimizations of the electroformation technique were made by changing the voltage, and the frequency applied to obtain the best combination possible to have clean GUVs [58]. Optimal alternative current and frequency values are between 1 and 3V and 10Hz, respectively, for a duration of 2 to 3 hours. However, these parameters have to be tuned when creating more complex GUVs with lipid mixtures (DOPC/DPPC/cholesterol), or under physiologically relevant conditions (presence of electrolyte buffer) [59]. In fact, if the electroformation is to be made in a high salinity solution (250 mM NaCl), the voltage applied is almost doubled than the DI water solution or with a lower salinity solution (1300 V/m compared to 700 V/m), and the frequency is 50 times more (500 Hz compared to 10 Hz) [60]. However, the duration is still the same, around 3 hours. Another group showed the possibility of reconstituting proteins in the GUVs during the electroformation [61]. And finally, *Pereno et al.* demonstrated the possibility of electroformation on stainless steel electrodes, which is faster and cheaper than ITO glass substrate, and the GUVs showed no sign of oxidation [62]. A commercialized setup is available for electroformation; however, most labs are able to fabricate a homemade setup [13]. In our lab, and for this project, we built a homemade setup at the beginning, then we used the commercial version.

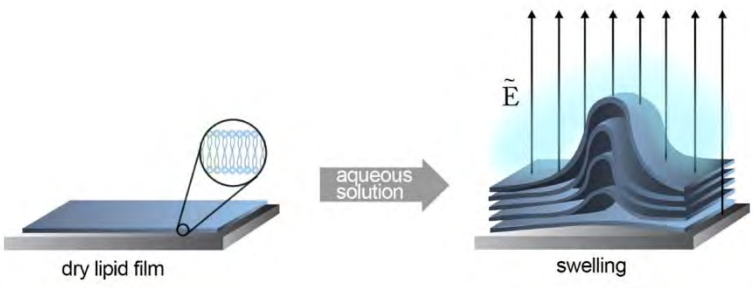

Figure I-11: Schematic of vesicle electroformation from a dry lipid bilayer deposited on a substrate. Swelling is fastened upon hydration and the application of an alternating electric field [59].

Vesicle swelling methods are direct and easy methods to fabricate GUVs. Nonetheless, it is important to take into consideration some of the drawbacks of these methods. First, and most importantly, these methods do not allow fabricating asymmetric GUVs (outer and inner leaflet are different), which is an important criterion of a cellular membrane. Second, these methods do not generate homogeneously sized GUVs as the swelling is poorly controlled. Depending on the application, this could be problematic to some. Moreover, the gel-assisted method can leave residual polymers in the solution and therefore affects the fluidity of the membrane. Furthermore, it was demonstrated that electroformation could induce oxidation in the unsaturated lipid membranes. In fact, mass spectroscopy analyses showed that the oxidation level of the phospholipids increases with the level of unsaturation as well as the amplitude and the duration of the electric field [58]. This can have an effect on the mechanical properties of GUVs membrane. Finally, as the GUVs formation in swelling methods is uncontrollable, it is highly possible that during the swelling, several bilayers detach and form multi-objects one inside another, such as Multi lamellar vesicles or Giant Multi lamellar vesicles, which can sometimes be noticeable from the higher intensity of fluorescent in the membrane. A way to fix this is to homogenize the spreading of the lipid film before the hydration step, which is not always easy.

1.2.2.2 Methods based on assembly from fluid interfaces: The droplet-transfer method

The droplet-transfer method is usually made in three steps: first, water droplets are suspended in a nonpolar solvent containing lipids. A monolayer of lipids enwraps the droplet of water in oil, forming the inner leaflet of the GUVs. Secondly, the water-in-oil (w/o) emulsion crosses to an intermediate phase of oil containing the same or another type of lipid. Finally, at the interface of the intermediate oil phase and water, the lipids enwrap the droplets forming, therefore, the outer leaflet of the vesicles. Note that if the lipid used in the first emulsion and in the intermediate phase is the same, the GUVs have a symmetric bilayer membrane. However, to obtain asymmetric bilayer membranes, the lipids used in both oil phases are to be different. The transfer of the droplet-in-oil emulsion droplets can be spontaneous (by gravity) or assisted using capillary or microfluidics.

Emulsion-based method

The emulsion-based method is made of two steps: first, obtaining a good water-in-oil emulsion (w/o), and secondly, the transfer of the w/o emulsion droplets to the external aqueous phase **(*Figure I-12*)**. The water in oil emulsion is prepared by spreading a small amount of water in an oil containing lipid solutions. The lipids present in the oil, and which are amphiphilic molecules, form a monolayer which enwraps the droplets, where the polar head is headed towards droplet of water (the inner solution), and the hydrophobic chains are headed outside. The transfer of the droplets to the external aqueous solutions is made by pouring the w/o solution gently into another oil containing the same or other

kinds of lipids [64], [65]. Because water density is higher than oil, the droplets of water cross the interface oil/water due to gravity and therefore forming the second lipid layer of the GUVs membranes. This final step can be accelerated and more efficient by applying a centrifugal force.

The emulsion based method was one of the droplet-transfer technique, but other methods were developed based on capillary - generated droplets and microfluidic - assisted approaches. These techniques, based on droplet transfer techniques will be detailed in chapter III, "Microfluidics: a tool to manipulate biomimetic membranes".

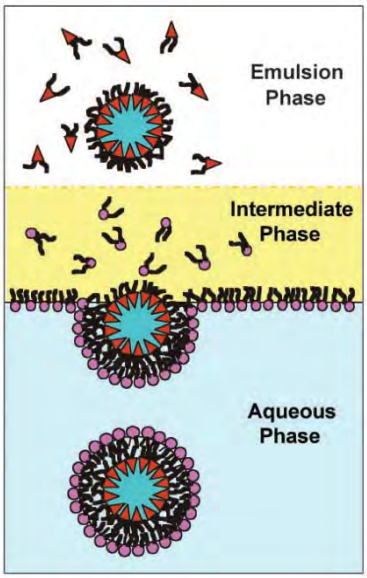

Figure I-12 : Schematic illustration of the droplet in oil emulsion technique used to fabricate GUVs. This technique is made of three steps: an initial solution of water droplets in lipid-saturated oil is stabilized by lipid molecules that form the inner leaflet. The droplets cross an intermediate phase of lipid-saturated oil, which is heavier than the first emulsion phase and where the lipids form a monolayer at the oil/water interface. Finally, the droplets across the interface due to the higher density and the lipids in the intermediate phase form the outer leaflet of the GUVs bilayer. If the lipids used in the intermediate phase are the same as the first emulsion, we obtain symmetric GUVs if not, we form GUVs with asymmetric lipid bilayer [63].

Whichever technique used, the important criteria to obtain are:

- ✓ mainly unilamellar vesicle
- ✓ Formed of the exact composition that is needed (no residual solvent or oil)
- ✓ Enough stability for the application needed
- ✓ Monodispersed GUVs (if needed)

As this project consists of using the microfluidic tool to characterize the mechanical properties of GUVs, we needed to fabricate GUVs in quantities to have enough during the microfluidics experiments. Secondly, to investigate the mechanical properties of GUVs, the membranes ought to be clean with no residual polymers or oil, and the electroformation technique turned out to be very useful to study the physics of the phospholipid bilayers [66], [67]. As the micropipette experiments (details explained later) are critical and long, the GUVs had to be also stable. Therefore, our choice landed on

the electroformation technique to generate GUVs during all this project, as it is also simple to implement and a homemade setup is easy to build.

However, we were also interested in fabricating asymmetric GUVs to characterize their mechanical properties. We developed a setup and tested the continuous droplet interface crossing encapsulation (cDICE) method. Preliminary results showed homogenously fabricated DOPC membranes. Nonetheless, due to the lack of time, this part of the project was set aside.

References

[1] K. Points and K. Terms, “5 . 1A : Components of Plasma Membranes,” pp. 1–2.

[2] M. Zagnoni, “Miniaturised technologies for the development of artificial lipid bilayer systems,” *Lab Chip*, vol. 12, no. 6, p. 1026, 2012, doi: 10.1039/c2lc20991h.

[3] B. Janson Cohen, *The Human Body in Health and Disease*, 12th ed. 2000.

[4] Y. Xu, T. S. Tillman, and P. Tang, *Membranes and Drug Action*, 1st ed. Elsevier Inc., 2009.

[5] E. Wallin and G. Von Heijne, “Genome-wide analysis of integral membrane proteins from eubacterial, archaean, and eukaryotic organisms,” *Protein Sci.*, vol. 7, no. 4, pp. 1029–1038, 1998, doi: 10.1002/pro.5560070420.

[6] M. A. Yildirim, K. Il Goh, M. E. Cusick, A. L. Barabási, and M. Vidal, “Drug-target network,” *Nat. Biotechnol.*, vol. 25, no. 10, pp. 1119–1126, 2007, doi: 10.1038/nbt1338.

[7] T. Harayama and H. Riezman, “Understanding the diversity of membrane lipid composition,” *Nat. Rev. Mol. Cell Biol.*, vol. 19, no. 5, pp. 281–296, 2018, doi: 10.1038/nrm.2017.138.

[8] W. Rawicz, K. C. Olbrich, T. McIntosh, D. Needham, and E. A. Evans, “Effect of chain length and unsaturation on elasticity of lipid bilayers,” *Biophys. J.*, vol. 79, no. 1, pp. 328–339, 2000, doi: 10.1016/S0006-3495(00)76295-3.

[9] M. Alagumuthu, D. Dahiya, and P. Singh Nigam, “Phospholipid—the dynamic structure between living and non-living world; a much obligatory supramolecule for present and future,” *AIMS Mol. Sci.*, vol. 6, no. 1, pp. 1–19, 2019, doi: 10.3934/molsci.2019.1.1.

[10] J. N. Israelachvili, S. Marcelja, R. G. Horn, and J. N. Israelachvili, “Physical principles of membrane organization,” *Q. Rev. Biophys.*, vol. 13, no. 2, pp. 121–200, 1980, doi: 10.1017/S0033583500001645.

[11] E. M. Bevers and P. L. Williamson, “Getting to the outer leaflet: Physiology of phosphatidylserine exposure at the plasma membrane,” *Physiol. Rev.*, vol. 96, no. 2, pp. 605–645, 2016, doi: 10.1152/physrev.00020.2015.

[12] G. Van Meer, D. R. Voelker, and G. W. Feigenson, “Membrane lipids: where they are,” *Nat. Rev. Mol. Cell Biol.*, vol. 101, no. 1, pp. 1–4, 2009, doi: 10.1038/nrm2330.Membrane.

[13] R. Dimova, *The Giant Vesicle Book*. 2019.

[14] P. A. Janmey and U. Lindberg, “Cytoskeletal regulation: Rich in lipids,” *Nat. Rev. Mol. Cell Biol.*, vol. 5, no. 8, pp. 658–666, 2004, doi: 10.1038/nrm1434.

[15] H. I. Ingólfsson *et al.*, “Lipid organization of the plasma membrane,” *J. Am. Chem. Soc.*, vol. 136, no. 41, pp. 14554–14559, 2014, doi: 10.1021/ja507832e.

[16] J. E. Rothman and J. Lenard, “Membrane asymmetry; the nature of membrane asymmetry provides clues to the puzzle of how membranes are assembled,” *Science (80-.).*, vol. 195, no. 2, pp. 743–753, 1977, [Online]. Available: http://www.ncbi.nlm.nih.gov/entrez/query.fcgi?cmd=Retrieve&db=PubMed&dopt=Citation&

list_uids=402030.

[17] T. L. Steck and Y. Lange, “Transverse distribution of plasma membrane bilayer cholesterol: Picking sides,” *Traffic*, vol. 19, no. 10, pp. 750–760, 2018, doi: 10.1111/tra.12586.

[18] W. F. D. Bennett, J. L. MacCallum, M. J. Hinner, S. J. Marrink, and D. P. Tieleman, “Molecular view of cholesterol flip-flop and chemical potential in different membrane environments,” *J. Am. Chem. Soc.*, vol. 131, no. 35, pp. 12714–12720, 2009, doi: 10.1021/ja903529f.

[19] R. Billow, P. Overath, and J. Davoust, “Rapid Lateral Diffusion of the Variant Surface Glycoprotein in the Coat of Trypanosoma brucei,” *Biochemistry*, vol. 27, no. 7, pp. 2384–2388, 1988, doi: 10.1021/bi00407a020.

[20] T. C. Squier and D. D. Thomas, “Selective detection of the rotational dynamics of the protein-associated lipid hydrocarbon chains in sarcoplasmic reticulum membranes,” *Biophys. J.*, vol. 56, no. 4, pp. 735–748, 1989, doi: 10.1016/S0006-3495(89)82721-3.

[21] M. Nakano *et al.*, “Flip-flop of phospholipids in vesicles: kinetic analysis with time-resolved small-angle neutron scattering,” *J. Phys. Chem. B*, vol. 113, no. 19, pp. 6745–6748, 2009, doi: 10.1021/jp900913w.

[22] F. X. Contreras, L. Sánchez-Magraner, A. Alonso, and F. M. Goñi, “Transbilayer (flip-flop) lipid motion and lipid scrambling in membranes,” *FEBS Lett.*, vol. 584, no. 9, pp. 1779–1786, 2010, doi: 10.1016/j.febslet.2009.12.049.

[23] F. . Polokoff, M.A.; Simon, T.J.; Harris A.; Simon, “Chronic ehtanol increases liver plasma membrane fluidity,” *Biochemistry*, vol. 24, no. 13, 1985.

[24] Y. Ma, K. Poole, J. Goyette, and K. Gaus, “Introducing membrane charge and membrane potential to T cell signaling,” *Front. Immunol.*, vol. 8, no. NOV, pp. 1–11, 2017, doi: 10.3389/fimmu.2017.01513.

[25] F. A. Heberle and G. W. Feigenson, “Phase separation in lipid membranes,” *Cold Spring Harb. Perspect. Biol.*, vol. 3, no. 4, pp. 1–13, 2011, doi: 10.1101/cshperspect.a004630.

[26] “3.1: Membrane Phase Transitions,” pp. 1–4, 2015, [Online]. Available: https://bit.ly/2XM5lPe.

[27] K. Simons and E. Ikonen, “Functional rafts in cell membranes,” *Nature*, vol. 387, no. 6633, pp. 569–572, 1997, doi: 10.1038/42408.

[28] D. A. Brown and E. London, “Structure and function of sphingolipid- and cholesterol-rich membrane rafts,” *J. Biol. Chem.*, vol. 275, no. 23, pp. 17221–17224, 2000, doi: 10.1074/jbc.R000005200.

[29] T. Harayama and H. Riezman, “Understanding the diversity of membrane lipid composition,” *Nat. Rev. Mol. Cell Biol.*, vol. 19, no. 5, pp. 281–296, 2018, doi: 10.1038/nrm.2017.138.

[30] J. Cuevas, *Structure and Function of Membranes ☆*, no. October 2014. Elsevier Inc., 2015.

[31] A. A. Waheed and E. O. Freed, “The role of lipids in retrovirus replication,” *Viruses*, vol. 2, no. 5, pp. 1146–1180, 2010, doi: 10.3390/v2051146.

[32] C. Klose, M. A. Surma, and K. Simons, "Organellar lipidomics-background and perspectives," *Curr. Opin. Cell Biol.*, vol. 25, no. 4, pp. 406–413, 2013, doi: 10.1016/j.ceb.2013.03.005.

[33] H. J. Sharpe, T. J. Stevens, and S. Munro, "A Comprehensive Comparison of Transmembrane Domains Reveals Organelle-Specific Properties," *Cell*, vol. 142, no. 1, pp. 158–169, 2010, doi: 10.1016/j.cell.2010.05.037.

[34] B. M. Baker and C. S. Chen, "Deconstructing the third dimension-how 3D culture microenvironments alter cellular cues," *J. Cell Sci.*, vol. 125, no. 13, pp. 3015–3024, 2012, doi: 10.1242/jcs.079509.

[35] K. Duval *et al.*, "Modeling physiological events in 2D vs. 3D cell culture," *Physiology*, vol. 32, no. 4, pp. 266–277, 2017, doi: 10.1152/physiol.00036.2016.

[36] D. A. Brown and E. London, "Structure of detergent-resistant membrane domains: Does phase separation occur in biological membranes?," *Biochem. Biophys. Res. Commun.*, vol. 240, no. 1, pp. 1–7, 1997, doi: 10.1006/bbrc.1997.7575.

[37] E. Evans and D. Needham, "Physical properties of surfactant bilayer membranes: Thermal transitions, elasticity, rigidity, cohesion, and colloidal interactions," *J. Phys. Chem.*, vol. 91, no. 16, pp. 4219–4228, 1987, doi: 10.1021/j100300a003.

[38] C. Montis, D. Maiolo, I. Alessandri, P. Bergese, and D. Berti, "Interaction of nanoparticles with lipid membranes: a multiscale perspective," *Nanoscale*, vol. 6, no. 12, pp. 6452–6457, 2014, doi: 10.1039/C4NR00838C.

[39] P. Gehan *et al.*, "Penetratin translocation mechanism through asymmetric droplet interface bilayers," *Biochim. Biophys. Acta - Biomembr.*, vol. 1862, no. 11, p. 183415, 2020, doi: 10.1016/j.bbamem.2020.183415.

[40] H. Zhao and P. Lappalainen, "A simple guide to biochemical approaches for analyzing protein-lipid interactions," *Mol. Biol. Cell*, vol. 23, no. 15, pp. 2823–2830, 2012, doi: 10.1091/mbc.E11-07-0645.

[41] P. Bassereau, B. Sorre, and A. Lévy, "Bending lipid membranes: Experiments after W. Helfrich's model," *Adv. Colloid Interface Sci.*, vol. 208, pp. 47–57, 2014, doi: 10.1016/j.cis.2014.02.002.

[42] Y. H. M. Chan and S. G. Boxer, "Model membrane systems and their applications," *Curr. Opin. Chem. Biol.*, vol. 11, no. 6, pp. 581–587, 2007, doi: 10.1016/j.cbpa.2007.09.020.

[43] B. Membranes, "5 . 1 : Model Membranes vs . Biological Membranes Biological Membranes : Composition and Functions," pp. 1–6, 2020.

[44] M. Eeman and M. Deleu, "From biological membranes to biomimetic model membranes," *Biotechnol. Agron. Société Environ.*, vol. 14, no. 4, pp. 719–736, 2010.

[45] C. Peetla, A. Stine, and V. Labhasetwar, "Biophysical interactions with model lipid membranes: Applications in drug discovery and drug delivery," *Mol. Pharm.*, vol. 6, no. 5, pp. 1264–1276, 2009, doi: 10.1021/mp9000662.

[46] W. Knoll, I. Köper, R. Naumann, and E. K. Sinner, "Tethered bimolecular lipid membranes-A novel model membrane platform," *Electrochim. Acta*, vol. 53, no. 23, pp. 6680–6689, 2008,

doi: 10.1016/j.electacta.2008.02.121.

[47] J. A. Jackman, W. Knoll, and N. J. Cho, "Biotechnology applications of tethered lipid bilayer membranes," *Materials (Basel).*, vol. 5, no. 12, pp. 2637–2657, 2012, doi: 10.3390/ma5122637.

[48] R. Articles, "Current trends in the production and biomedical applications of liposomes : a review," *J. Biomed. Sci.*, vol. 4, no. 1, pp. 9–21, 2005.

[49] E. Schäfer, M. Vache, T. T. Kliesch, and A. Janshoff, "Mechanical response of adherent giant liposomes to indentation with a conical AFM-tip," *Soft Matter*, vol. 11, no. 22, pp. 4487–4495, 2015, doi: 10.1039/c5sm00191a.

[50] A. Lorin, C. Flore, A. Thomas, and R. Brasseur, "Les liposomes: Description, fabrication et applications," *Biotechnol. Agron. Soc. Environ.*, vol. 8, no. 3, pp. 163–176, 2004.

[51] P. Walde, K. Cosentino, H. Engel, and P. Stano, "Giant Vesicles: Preparations and Applications," *ChemBioChem*, vol. 11, no. 7, pp. 848–865, 2010, doi: 10.1002/cbic.201000010.

[52] B. Kubsch, T. Robinson, J. Steinkühler, and R. Dimova, "Phase behavior of charged vesicles under symmetric and asymmetric solution conditions monitored with fluorescence microscopy," *J. Vis. Exp.*, vol. 2017, no. 128, pp. 1–17, 2017, doi: 10.3791/56034.

[53] N. Rodriguez, F. Pincet, and S. Cribier, "Giant vesicles formed by gentle hydration and electroformation: A comparison by fluorescence microscopy," *Colloids Surfaces B Biointerfaces*, vol. 42, no. 2, pp. 125–130, 2005, doi: 10.1016/j.colsurfb.2005.01.010.

[54] K. Akashi, H. Miyata, H. Itoh, and K. Kinosita, "Formation of Giant Liposomes Promoted by Divalent Cations : Critical," *Biophys. J.*, vol. 74, no. June, pp. 2973–2982, 1998.

[55] K. S. Horger, D. J. Estes, R. Capone, and M. Mayer, "Films of agarose enable rapid formation of giant liposomes in solutions of physiologic ionic strength," *J. Am. Chem. Soc.*, vol. 131, no. 5, pp. 1810–1819, 2009, doi: 10.1021/ja805625u.

[56] N. L. Mora *et al.*, "Preparation of size tunable giant vesicles from cross-linked dextran(ethylene glycol) hydrogels," *Chem. Commun.*, vol. 50, no. 16, pp. 1953–1955, 2014, doi: 10.1039/c3cc49144g.

[57] M. I. Angelova and D. S. Dimitrov, "Liposome Electro formation," *Faraday Discuss. Chem. SOC*, vol. 81, pp. 303–311, 1986, doi: 10.1039/dc9868100303.

[58] M. Breton, M. Amirkavei, and L. M. Mir, "Optimization of the Electroformation of Giant unilamellar vesicles (GUVs) with Unsaturated Phospholipids," *J. Membr. Biol.*, vol. 248, no. 5, pp. 827–835, 2015, doi: 10.1007/s00232-015-9828-3.

[59] P. Méléard, L. A. Bagatolli, and T. Pott, "Giant unilamellar vesicle Electroformation. From Lipid Mixtures to Native Membranes Under Physiological Conditions," *Methods Enzymol.*, vol. 465, no. C, pp. 161–176, 2009, doi: 10.1016/S0076-6879(09)65009-6.

[60] T. Pott, H. Bouvrais, and P. Méléard, "Giant unilamellar vesicle formation under physiologically relevant conditions," *Chem. Phys. Lipids*, vol. 154, no. 2, pp. 115–119, 2008, doi: 10.1016/j.chemphyslip.2008.03.008.

[61] E. M. Schmid, D. L. Richmond, D. A. Fletcher, B. Program, and L. Berkeley, "Reconstitution of proteins on electroformed giant unilamellar vesciles," pp. 319–338, 2017, doi: 10.1016/bs.mcb.2015.02.004.Reconstitution.

[62] V. Pereno *et al.*, "Electroformation of Giant unilamellar vesicles on Stainless Steel Electrodes," *ACS Omega*, vol. 2, no. 3, pp. 994–1002, 2017, doi: 10.1021/acsomega.6b00395.

[63] S. Pautot, B. J. Frisken, and D. A. Weitz, "Engineering asymmetric vesicles," *Proc. Natl. Acad. Sci. U. S. A.*, vol. 100, no. 19, pp. 10718–10721, 2003, doi: 10.1073/pnas.1931005100.

[64] C. Claudet, M. In, and G. Massiera, "Method to disperse lipids as aggregates in oil for bilayers production," *Eur. Phys. J. E*, vol. 39, no. 1, pp. 1–6, 2016, doi: 10.1140/epje/i2016-16009-6.

[65] T. Hamada, Y. Miura, Y. Komatsu, Y. Kishimoto, M. Vestergaard, and M. Takagi, "Construction of asymmetric cell-sized lipid vesicles from lipid-coated water-in-oil microdroplets," *J. Phys. Chem. B*, vol. 112, no. 47, pp. 14678–14681, 2008, doi: 10.1021/jp807784j.

[66] R. Dimova, S. Aranda, N. Bezlyepkina, V. Nikolov, K. A. Riske, and R. Lipowsky, "A practical guide to giant vesicles. Probing the membrane nanoregime via optical microscopy," *J. Phys. Condens. Matter*, vol. 18, no. 28, 2006, doi: 10.1088/0953-8984/18/28/S04.

[67] R. Dimova, "Giant Vesicles and Their Use in Assays for Assessing Membrane Phase State, Curvature, Mechanics, and Electrical Properties," *Annu. Rev. Biophys.*, vol. 48, pp. 93–119, 2019, doi: 10.1146/annurev-biophys-052118-115342.

Chapter II

2 Mechanical properties of model membranes

The complex structure of plasma membrane has pushed scientists over the year to develop different model membranes in order to facilitate the studies and better understand biological processes which happen in the membrane. Because of the different techniques of fabrication, the different models we can obtain as well as the mixture and combination of lipids which is an important characteristic of heterogeneity of the membrane, it is crucial that any new lipid membrane obtained be characterized. Moreover, the cellular membrane undergoes a lot of changes in its shape and structure, especially as a response to external exposure such as drugs or nanoparticles. Those changes are mainly possible because of the capability of the membrane to bend and curve due to its fluidity. And characterizing those properties of the membrane is also crucial for experimentation, such as drug-membrane interactions.

Helfrich was one of the first scientists to energetically describe the membrane, with three main elastic properties, characteristic of a fluid membrane. Since then, many new techniques have been developed to characterize the physicochemical properties of the membranes. Some of them are based on microscopic observations only, and others induce deformation in the membranes, and by characterizing the response of the membranes, it is possible to extract elastic moduli such as the bending and the stretching. Nevertheless, all the techniques have one thing in common: the physical and mathematical description of the model made by Helfrich.

Micropipette aspiration is one of the most useful techniques, which allows the characterization of not only the elastic properties of the membrane but also properties such as the permeability, the thermal transition and thermomechanical behavior, and finally, molecular exchange and interactions between two pairs of vesicles. Micropipette aspiration technique was first applied on cells such as red blood cells and then was largely used to characterize the Giant unilamellar vesicles. Micropipette aspiration, along with the other techniques, has characterized many parameters that affect the elasticity of the membrane, such as the temperature, the lipids chain length, and degree of unsaturation, besides many other parameters which will be developed in this chapter.

Finally, as the cellular membrane is the main barrier and protection of the cell, it is the first place of contact of molecules and particles coming from outside the cell. Model membranes have been used

as platforms in order to investigate the interaction of nanoparticles with the membranes and the possible effects on the properties of the membranes.

In this chapter, I will first introduce the main elastic moduli of the fluid membranes, which were introduced by Helfrich. Then I will discuss the main techniques developed to characterize the elastic properties of the membrane; most of which are used on Giant unilamellar vesicles because of their size and the possibility to both manipulate and observe them under microscopy. Then I will go into the details of the experimental set-up and protocol of the micropipette aspiration as it is the most common technique used and because it will be the main body of my Ph.D. project, which is to develop a micropipette aspiration platform using microfluidics. Next, I will discuss the possible reasons for the different values of the bending and stretching moduli obtained from the different techniques, which could come from environmental effects such as the temperature and the sugars and salt used to fabricate the membranes. Then I will move to discuss other parameters that could affect the elasticity of the membrane. Finally, I will discuss the interaction of cellular membranes and model membranes with the different nanoparticles and the possible effects of the different characteristics of the nanoparticles on the properties of the membrane.

2.1 Characterization techniques of elastic properties of model membranes

2.1.1 Membranes main elastic properties

W. Helfrich is one of the first scientists who proposed to describe the lipids membrane elastic properties by considering that the membrane is a two-dimensional fluid with an unrestricted internal fluidity [1]. When a membrane is exposed to in-plane or normal stresses, it undergoes different changes, which lead to different independent deformations. These elastic deformations are characterized by: an isothermal change in the membrane caused by isotropic stress and characterized by an area dilation, an in-plane extension under a constant membrane area which is caused by surface shear stress and is characterized by shear strain and finally a change in the membrane's curvature, which is characterized by its bending modulus [2]. Lipid membranes are infinitely thin 2D membranes, and their mechanics can be compared to the mechanics of a thin-surface material, as seen in ***Figure II-1.***

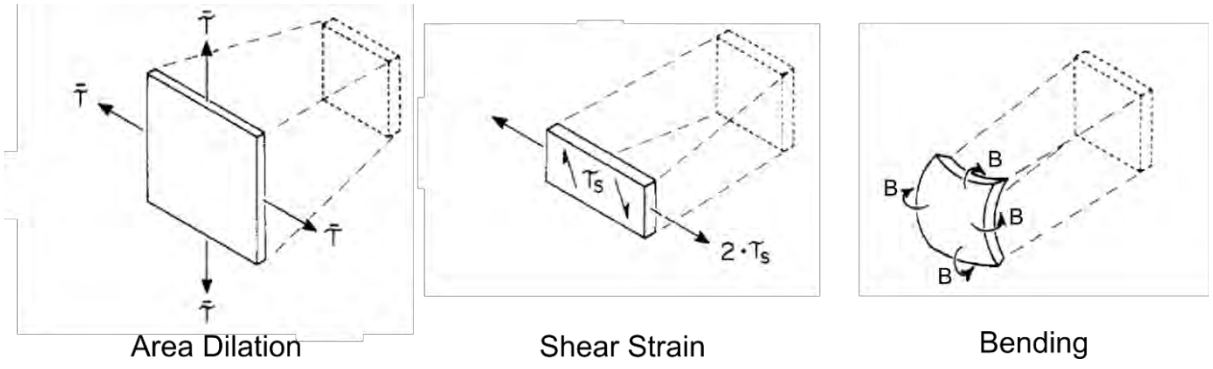

Figure II-1: Independent modes of deformation for thin membranes: Area dilation is caused by isotropic stress, bending is caused by curvature changes, and the shear strain is caused by shear stress under a constant membrane area [2].

The bending energy of a membrane depends on two material parameters: the spontaneous curvature *m* and the bending rigidity. When a membrane is not exposed to any external force, it takes a spontaneous curvature *m,* due to the asymmetry of the lipids forming it. However, if exposed to any external constraints, the membrane is forced to assume a mean curvature M, and a spontaneous tension will be present in the membrane [3]. Membrane bending is characterized by the bending rigidity K_b, given by the ratio of the change in membrane bending moment ΔB, to changes in total membranes curvature ΔC:

$$\Delta B = K_b \Delta C \qquad 2\text{-}1$$

Bending modulus is also defined as the amount of energy required to deform a membrane. Knowing that a membrane is composed of two monolayer leaflets, for one leaflet to bend, the other one has

to be stretched. Following this logic, researchers observed that the bending modulus increases with the membrane thickness [4]. Bending modulus is also an intrinsic property of the membrane, and it depends on the lipid composition in the membrane. For fluid membranes, bending modulus is in the same order of magnitude of thermal energy and ranges from 10 k_BT to less than 100 k_BT [5], where k_BT is the thermal energy, and k_B is the Boltzmann constant

The curvature's change of a locally deformed membrane is characterized by the change of the principal curvatures ($C_1 = 1/R_1$ and $C_2 = 1/R_2$):

$$\Delta C = \Delta(\frac{1}{R_1} + \frac{1}{R_2}) \qquad 2\text{-}2$$

The area dilation is characterized by the isothermal area expansion modulus K_A given by the ratio between the fractional change in the membrane area or area expansion α and the isotropic membrane stress or also called the membrane tension τ:

$$\Delta\tau = K_A\alpha \qquad 2\text{-}3$$

In fact, in the absence of external forces or constraints, a membrane is defined by its optimal area or its initial area A_0, which corresponds to the optimal packing of its molecules. However, when the membrane experiences a mechanical tension, its area changes from the optimal one in order to adapt to the deformation [3]. This deformation is the area expansion α and is expressed by:

$$\alpha = (A - A_0)/A_0. \qquad 2\text{-}4$$

In general, for a membrane that is in its liquid phase, the two relevant elastic deformations are the area dilation and the bending, as membranes above their phase transition temperature cannot support elastic shear. However, membranes that are in their solid or gel phase do support elastic shear and shear viscosity [2]. Therefore, the total elastic energy of a membrane is the combination of both bending and stretching regime.

In this chapter, I will focus mostly on the bending and area dilation modulus and will discuss more the shear effect on model membranes in the next chapter, where microfluidics is used as a tool to characterize model membranes.

2.1.2 The different techniques to characterize model membranes

Over the last decades, many techniques were developed to characterize the elastic moduli of lipid model membranes. As the bending modulus is characterized by the thermal fluctuations of the membrane, some characterizations can be done without the need to induce a deformation in the membrane. However, in these cases, the stretching modulus is harder to be characterized, as the deformation is not sufficient to extract it. Other techniques would be to induce a low or high

deformation in the membrane from external constraints, and by measuring the response deformation, the elastic properties of the membrane can be extracted. All these methods have one thing in common: the data analysis is always based on Helfrich's model [5]. The techniques that do not induce any deformation in the membrane are vesicle fluctuation analysis, X-ray and neutron scattering, whereas the techniques that induce a deformation in the membrane are the micropipette aspiration, pulling a membrane nanotube, and electro-deformation ***(Figure II-2)***. Micropipette aspiration became the most common and used technique and the main objective of our studies is to adapt it by using microfluidics techniques. Therefore, I will briefly go through the other techniques mentioned before I go into the details of the micropipette aspiration technique.

2.1.2.1 Vesicle Fluctuation Analysis (VFA) technique

This technique is specifically used to characterize the bending modulus of the lipid membrane. Lipid membranes display fluctuations that correspond to thermal undulations, which are mainly controlled by the bending elasticity of the membrane. The purpose of vesicle fluctuation analysis is to first lively record the contour fluctuations of the membrane using optical microscopy ***(Figure II-2A)*** and then construct spatial and temporal correlations to characterize the shape of the fluctuations from the recording [6]. As the interval of time between two pictures of the recording is short and around 20ms (to prevent blurring the configurational details due to the membrane motion), the choice of camera and microscope should be very well taken into considerations as well as the experimental set-up to provide an accurate contour detection [7]. The bending modulus is extracted by fitting the curve of the fluctuation spectrum of the membrane as a function of the wave vector corresponding to the projection of the position of a point of the membrane, as seen in ***(Figure II-2A). Table II- 1*** represents some of the values of the bending modulus from the literature obtained from the vesicle fluctuations analysis, at temperatures above their phase transition one. The lipids showed in this table are DLPC (12:0), DMPC (14:0), and DPPC (16:0). They belong to the phosphatidylcholine family of lipids, with, respectively, 12, 14, and 16 carbon atoms and saturated acyl chains. The table shows that the bending modulus values are dependent on the number of carbons in the acyl chains, which also characterize the membrane thickness. The bending modulus of thicker membranes is bigger than thinner membranes. A complete table of the bending moduli extracted from the VFA method, under different temperatures, and from different groups is shown in [8]. In that table, the bending moduli obtained using the same method were highly different from each others.

This method does not require heavy equipment other than a good microscope with phase contrast optics and a good camera. However, this method does not work well for complex membranes such as membranes that exhibit phase separation or heterogeneities at optically resolvable length scale or membranes that are crowded with proteins, for example.

Table II- 1: Elastic bending modulus K_b deduced from thermally excited shape fluctuations of Giant unilamellar vesicles [8].

Lipid	Temperature (°C)	K_b (x 10^{-19} J)
DLPC (12:0)	18, 24	0.92 ± 0.05 [9]
DMPC (14:0)	30	1.3 ± 0.08 [9]
DPPC (16:0)	47.4	1.5 ± 0.09 [9]

2.1.2.2 X-rays and Neutron scattering techniques

X-rays and Neutrons scattering are very efficient techniques to characterize lipid membrane organization in stack of bilayers as they present a very good spatial resolution non-accessible to optical microscopy. The fundamental differences between the techniques lie in the source of information; X-rays are scattered by electronic clouds, while neutrons are fundamental particles that interact directly with the nuclei of the atoms in the structures ***(Figure II-2B)***. From these data, scientists are able to explore the symmetries within the membranes and understand their structures, and its analysis allows extracting the bending modulus [10]. ***Table II- 2*** presents some values of bending modulus of DMPC lipid membranes using different X-rays and neutrons scattering techniques at 30°C.

The main limitation of these techniques is the complicated physics behind it as it is a non-direct way of characterization. Another constraint is the limited access to very controlled large facilities with such big equipment and the large time consuming to perform these experiments. Not to mention the budget or grants that are necessary to use these techniques.

Table II- 2: Bending modulus values of DMPC lipid membranes obtained from different X-rays and neutrons scattering techniques under 30°C.

	Diffuse X-ray scattering from aligned bilayers	X-ray scattering from vesicles	Inelastic neutron scattering from aligned bilayers
DMPC K_b (x 10^{-19} J)	0.69 [11]	0.8 [12]	0.61 [13]

The techniques mentioned above represent characterization techniques that do not require any induced external constraints on the membranes, and therefore they remain in their normal state without deforming. Moreover, the X-rays and neutrons scattering techniques are mostly done on stacks of bilayer membranes and not GUVs. Because of the relatively large size of the GUVs and the possibility to micro manipulate them, their deformation upon induced constraints can be directly visualized with optical microscopy. This is the case of the following techniques developed to characterize the elastic moduli of lipid vesicles.

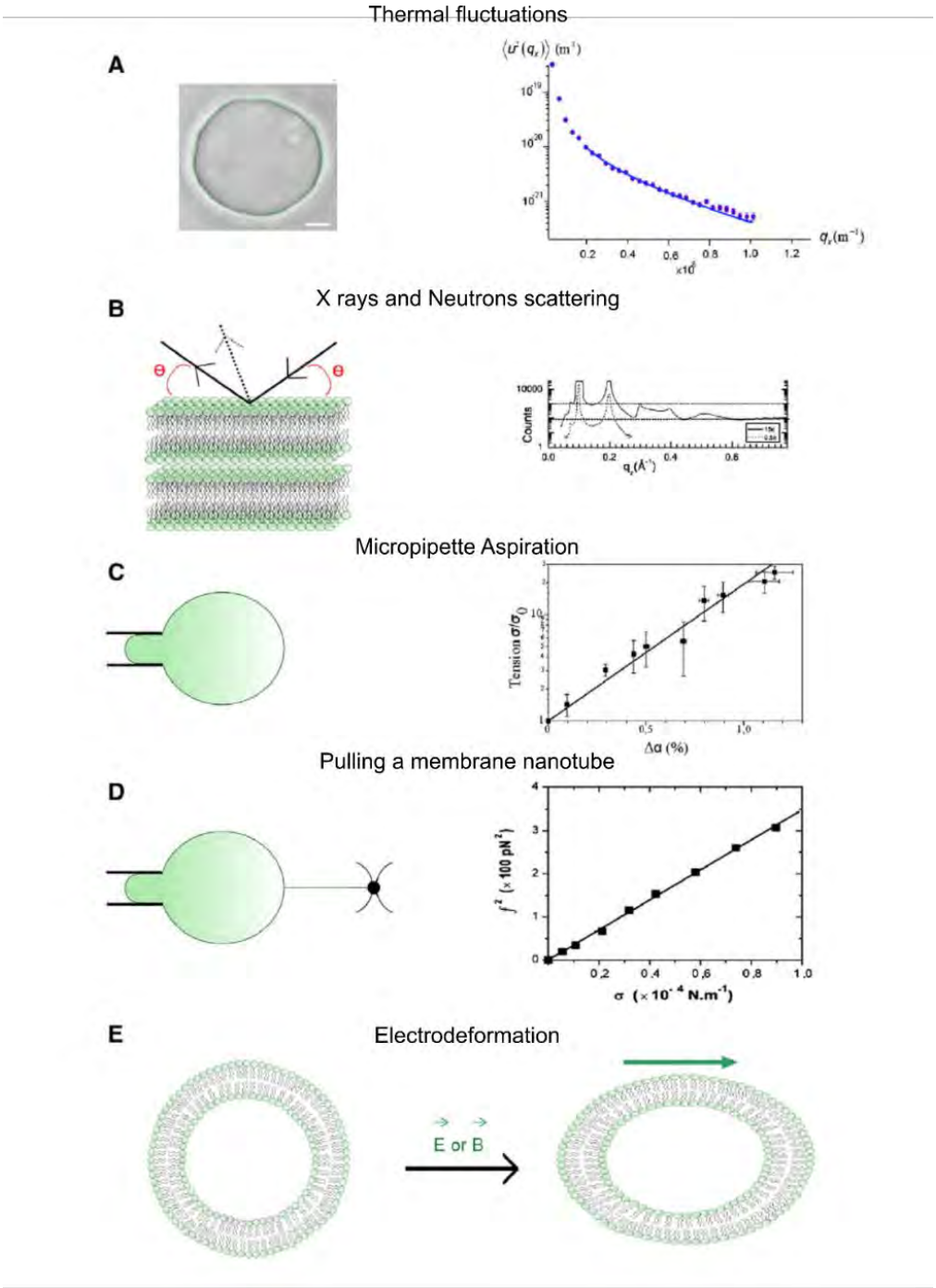

Figure II-2: Different methods to characterize membrane mechanics [5] *. A) corresponds to the vesicle fluctuations analysis based on the thermal fluctuations. The method consists of analyzing the contour of the GUVs. The bending modulus is extracted from the Fourier analysis of the fluctuation spectrum. B) corresponds to X-rays and neutron scattering methods. The elastic moduli can be deduced from the analysis of the intensity around the Bragg peaks and from the intensity at large wave vectors. C) corresponds to the micropipette aspiration method. GUV is aspirated inside a pipette, and the bending modulus can be extracted by fitting the curve of the tension of the vesicles as a function of the deformation. D) corresponds to pulling a nanotube from a membrane aspirated in a micropipette. Bending rigidity is extracted from the curve of the force f applied on the tube vs. the membrane tension. E) corresponds to the electro deformation or deformation induced by a magnetic field. Bending modulus is obtained from the elongation dependence with the field.*

2.1.2.3 Pulling a nanotube from the vesicle – Force measurement

This method consists in pulling a nanotube from the surface of the vesicle using external forces of different origins. The most common technique is to use optical tweezers to pull the nanotube from a vesicle that is aspirated by a micropipette [14]. The pulling is done by sticking a microbead to the membrane and using it as a handle to pull on the membrane. When aspirated inside the micropipette, the vesicle exhibits a surface tension that depends on the pressure applied on the object, the diameter of the micropipette, and the vesicle's radius. This is deduced from Laplace law which will be fully elaborated in the paragraph about the micropipette aspiration technique. The increase of the pressure on the vesicle increases its surface tension. In parallel, the force applied to pull a nanotube is proportional to the relative displacement of the bead from its previous position [6]. The bending modulus is extracted from the fitting of the curve of the force vs. the surface tension ***(Figure II-2D)***. Building and calibrating an optical tweezer set-up is complicated; therefore, it can be replaced by another micropipette where the bead is placed at the exit of the second micropipette.

Pulling a nanotube from a vesicle to characterize membrane's mechanics has several advantages, such as the simplicity and the well-controlled shape of the tubes, which, combined with confocal microscopy, can perform a highly quantitative measurement. Nevertheless, this technique suffers from low throughput and complicated set-up. Microfluidics can bring solutions: combined with optical traps, vesicles can be immobilized in multiple traps to perform parallel experiments. More about this topic will be detailed in the following chapter.

2.1.2.4 Deforming a Giant unilamellar vesicle with an external electrical or magnetic field

The electro deformation technique consists in applying an electrical field on the membrane, which induces deformation in the membrane ***(Figure II-2E)*** . In fact, when applying an alternating electrical field, a transmembrane potential develops across the membrane and induces an effective electrical tension which transforms the shape of the membrane from spherical to ellipsoid [5]. The tension is therefore related to the electrical field force applied, which frequency range between 25 and 300 kHz. In parallel, the deformation of the GUV is recorded. The bending modulus is then extracted from the curve of the deformation of the vesicle vs. the tension. ***Table II- 3*** shows some of the bending modulus values obtained from the electro deformation technique [15]. Deforming a GUV using a magnetic field was also done by filling the GUVs with Ferro fluids [16]. Following the same approach of analysis as the electro-deformation, the bending modulus of lipid membranes could also be extracted. The values of the bending modulus obtained by this technique are very low compared to the other techniques. A comparison between the methods and the reasons behind the different values of elastic moduli will

be discussed after the detailed paragraph about micropipette manipulation [8], [5], as it will also elaborate on some of the purposes of this project.

Table II- 3: Bending modulus values for SOPC and DOPC lipid membranes using the electro-deformation technique under 21°C.

Lipid	Temperature (°C)	K_b (x 10^{-19} J)
SOPC	21	0.32 ± 0.05
DOPC	21	0.17 ± 0.03

On the other hand, simulations have also been made in order to characterize the mechanical properties of model membranes. In the following review [17], both experimental techniques and simulations were discussed and compared, where different methods of simulation also provided different results. I will not go into any detail considering the simulation as it is far from the field of study conducted during my Ph.D. However, in ***Figure II-3,*** I represent the bending modulus values of DMPC (14:0), DOPC (18:1) and DPPC (16:0) lipid membranes obtained by different experimental techniques and different simulations methods. The difference in the experimental methods will be detailed in the following paragraphs, however the simulations gave values that are close to the Shape Fluctuations Analysis technique. This means that simulations are a good tool that can be used to extract the bending modulus of lipid membranes in case there is no access to experimental set-ups.

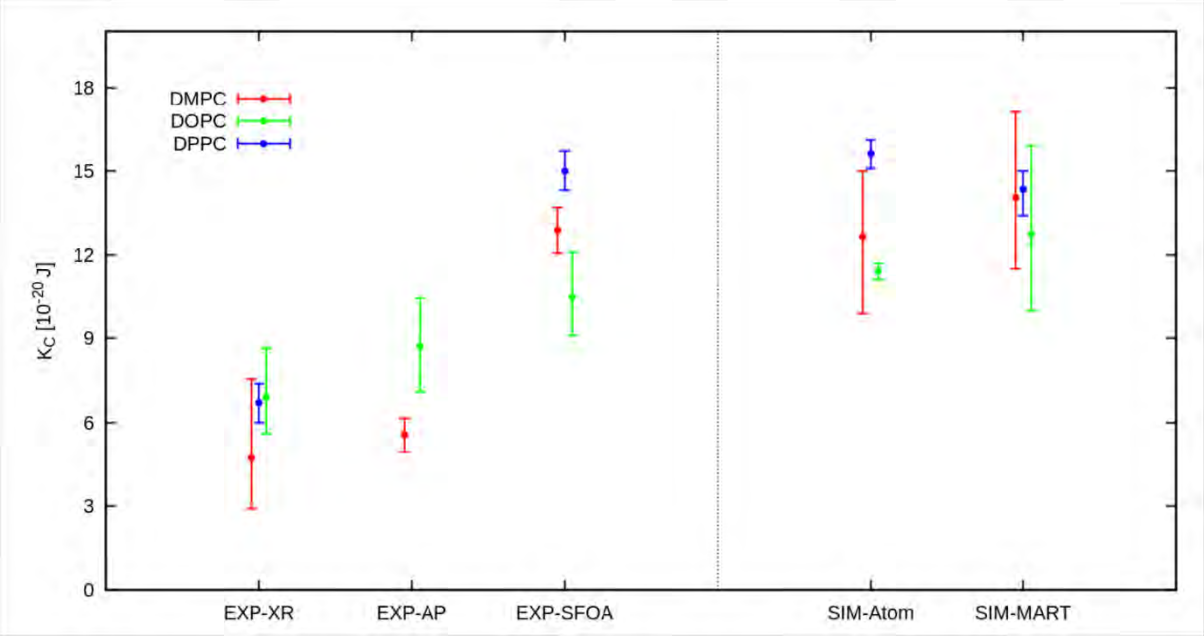

Figure II-3:Bending moduli obtained from experiments and simulations for DMPC, DOPC and DPPC [17]. *XR, AP and SFOA corresponds respectively to X-Ray, Aspiration Pipette and Shape Fluctuations Optical Analysis experimental techniques. Atom and MART corresponds to atomistic and MARTINI simulations methods.*

2.2 Micropipette Aspiration technique

During 5 decades, micropipette aspiration became the gold standard technique to characterize mechanical properties of a variety of biological samples such as cells or even cells within tissues [18]. For example, it was used to measure cell surface tension of white blood cells, as well as the elasticity of embryonic tissues, as it is a non-destructive method. Micropipette aspiration has been also widely used to characterize Giant unilamellar vesicles' elastic properties as the bending and stretching modulus, the latter one being difficult to extract or reach with the other methods listed before, as well as the tensile strength (for fluid phase membranes), the yield shear and shear viscosity (for the solid phase membranes). It is a versatile tool that is used to characterize membrane permeability, the molecular exchange between a pair of vesicles as well as the adhesion and fusion between two vesicles.

In general, micropipette aspiration method consists in using a micropipette in glass to apply a suction pressure on a GUV. The pressure applied on the object, deforms it and allows the GUV to slide inside the micropipette. The deformation of the object increases as the pressure is increased progressively. The pressure is then linked to the surface tension of the object, and by plotting the curve of the surface tension values as function of the deformation, the elastic moduli are extracted.

In order to understand well all the experimental details of the micropipette aspiration technique, we visited in March 2020 for three days the team of Patricia Bassereau in the Curie Institute, where they have a complete set-up of the micropipette aspiration as it is one of their main line of research. With the help of Stephanie Mangenot, we learnt several tips and details that are usually not completed in the literature and which helped us understand better some behavior when conducting our micropipette aspiration on-chip.

2.2.1 Experimental Set-Up

The micropipette set-up is very sophisticated and consists of three major subsystems which allow to carry out successfully the experiment: a) the micropipette forging and the preparation of the chamber of the GUVs solution, b) the pressure application and the measurement of the deformation of the GUVs and finally c) the recording and image acquisition of the experiment. ***Figure II-4 A-D*** presents pictures of the steps of the set-up of the Institute Curie during our stay. The main ideas of this paragraph are taken from [6] and from my notes taken during the experiments. A complete detailed protocol of the micropipette aspiration can be found in [19].

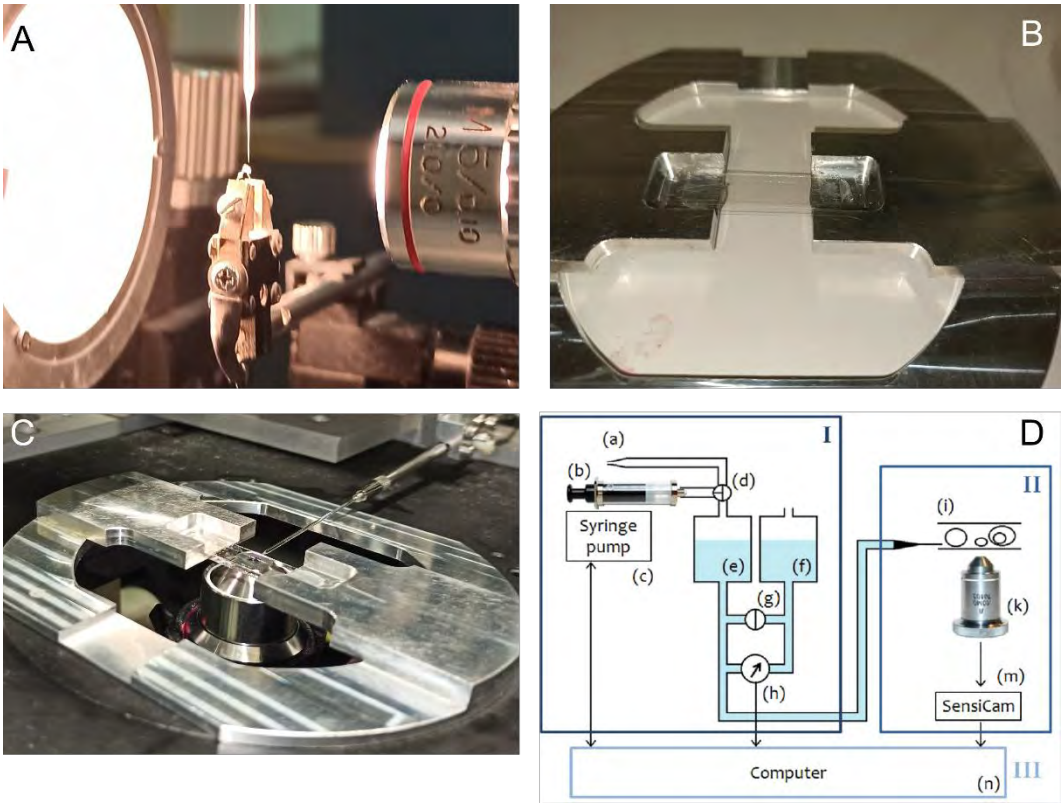

Figure II-4: Micropipette aspiration set-up of an experiment made during our stay in Curie Institute in Paris in March 2020. A) Forging process of the glass micropipette: the tip of the pipette is held by a micromanipulator and is inserted into a low-melting-point glass bead formed at the platinum wire. B) Aluminum support for the microscope and of the glass chamber for the GUVs solutions. C) the Aluminum support is positioned on the microscope, the glass chamber is filled with the GUVs solution, and the glass micropipette is calibrated inside the chamber. The chamber is then sealed using an oil solution to avoid evaporation of the water from the chamber. D) Schematic of the water-filled pressurizing system for the micropipette aspiration [20].

2.2.1.1 Micropipette and chamber preparation

The micropipettes are made of borosilicate glass capillaries that are forged to obtain the necessary diameter for the experiment. In fact, the choice of the diameter for the micropipette aspiration of the GUVs is very important: if the vesicle is too small compared to the pipette diameter, the GUV would slightly expand and be completely aspirated, whereas if it's too big, the GUV will tend to neck in and pinch off. An optimal choice of the pipette would be around one-third the size of the GUV. In any case, the glass capillary is first pulled to give two pulled glass needles. Then, a two-step forging process is needed to create an open tip pipette with the specific diameter. Using a commercial micro forge, a small amount of low-melting-point glass is used to first insert the pipette inside it, and secondly, once the glass is solidified, the tip is broken and left inside it ***(Figure II-4A).*** The pipette is then filled with the same solution where the GUVs will be suspended. This step is very critical, as a bubble could get trapped inside the pipette during the filling, causing the total change of the pipette.

The chamber of the GUVs is made of two thin slides of glass that are deposit on an aluminum holder for the microscope stage ***(Figure II-4B).*** The two glasses are separated by polytetrafluoroethylene (PTFE) to allow the introduction of the solutions to the chamber. Before that, the chamber and the pipette are treated for 5-10 minutes with solutions such as the Bovine serum albumin (BSA) or Casein 0.1% to avoid adhesion of the GUVs on the glass walls of the pipette or the chamber. They both are completely rinsed before introducing the GUVs.

Once the chamber is ready, the GUVs solution is then introduced with the final solution in which the GUVs would be suspended. It is necessary for the GUVs to sediment in the chamber in order to easily find them and better control them than if they are floating. Therefore, a solution with a close osmotic pressure to the one inside the GUVs but with lower density is to be introduced with the GUVs solution. The micropipette is then carefully introduced inside the chamber and well-calibrated in the z-plane of the objectives in order to have good imaging resolutions ***(Figure II-4C)***. Finally, once the set-up is completed, the chamber is sealed using oil to avoid the evaporation of the water that would cause changes in the osmotic pressure.

2.2.1.2 Pressure application on the GUV

Micropipette aspiration experiments require very accurate control of the aspiration pressure. In fact, the most reliable way to do so is by controlling the hydrostatic pressure by adjusting and controlling the vertical position of two water reservoirs using an automated controller managed by a computer, as seen in ***Figure II-4D.*** For a precise measurement, the syringe and the tubing should be filled with deionized (DI) water and degassed water to avoid any air bubbles trapped in the pressure circuit. Before any starting of measurement, the determination of the equilibrium of the hydrostatic pressure is required. To do so, it is best to find a small dust particle or vesicle in the chamber and bring the pipette closely to it and control the flux until the dust is neither floating inside the pipette neither pushed far of the pipette because of the flux. This determines the P_0, reference pressure of the experiment. Later, and in order to induce a pressure on the object, one of the reservoir is moved vertically down, inducing a difference in the height of both water level, which increases the pressure applied on the object.

2.2.1.3 Deformation of the GUV while increasing the pressure and image acquisition

An inverted microscope with phase contrast optics is needed to visualize the GUVs if no fluorophore dye is inserted in the membrane. However, a low amount of fluorescent dye (0.1% typically) is included in the membrane and the deformation of the membrane is visualized under confocal or epifluorescence microscopy. Once a GUV is spotted with a good dimension compared to the pipette diameter, a first step of pre-stressing the GUV is made to eliminate any possible defects in the

membrane, which could alter the results. To do so, several increasing steps of pressure are applied on the GUV and held up to 0.5mN/m surface tension for around 1 minute before completely releasing the GUV outside the pipette. Following this step, the pipette is brought close to the GUV, and increasing steps of pressure (lower than the one applied to pre-stress) are applied on the GUV. The GUV starts to deform inside the pipette, and a projection of a length L_p (seen in ***Figure II-5***) is formed inside the pipette. The pressure is to be held steady for several seconds to ensure that the GUV is at an equilibrium state. Images are taken for each pressure-deformation to measure the following parameters: the vesicle's diameter outside the pipette D_v, the projected length L_p inside the pipette, and the pipette's diameter D_p ***(Figure II-5).***

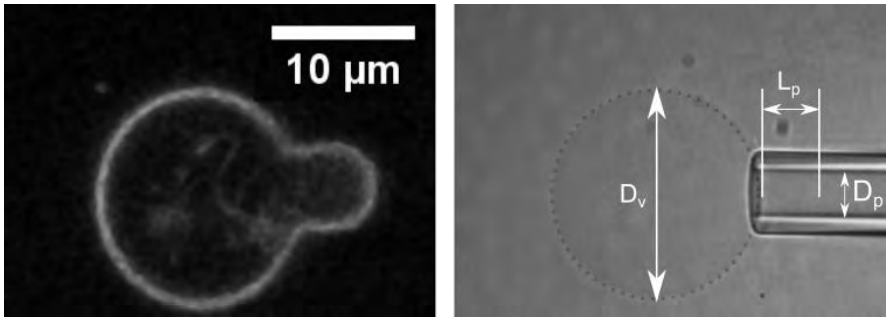

Figure II-5: Confocal and phase-contrast microscopy of a DOPC GUV aspirated in a micropipette of 5 µm diameter. The GUV is stained with Liss Rhodamine. L_p is the elongation of the membrane inside the pipette, which increases with the increase of pressure. D_v is the diameter of the spherical GUV outside the pipette, and D_p is the diameter of the pipette.

2.2.2 Equations to extract the elastic moduli of lipid membranes

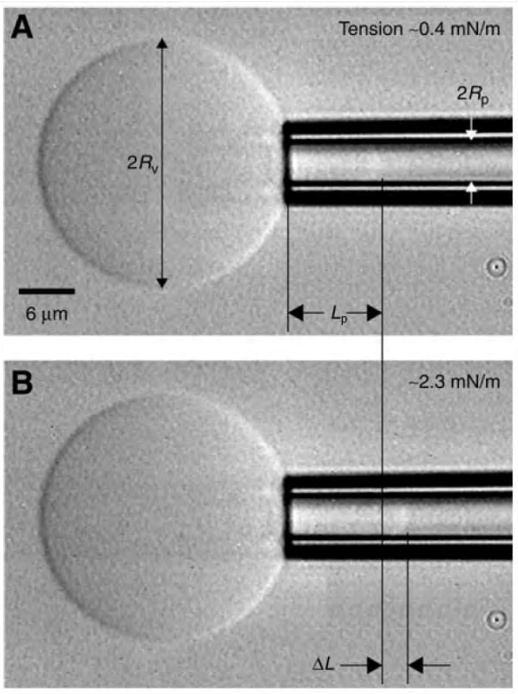

Figure II-6:Micropipette aspiration of a GUV aspirated at A) a low and B) high tension. The change in the projection length (ΔL) is proportional to the change in apparent surface area (ΔA) [21].

2.2.2.1 Extracting surface tension and area increase of the GUV

The physical model for the micropipette aspiration equations has been very well established since 1980 [22] ***(Figure II-6)***. The pressure applied on the membrane produces a constant uniform tension τ over the entire surface of the GUV and would be called surface tension. Due to the Young-Laplace law of capillary pressure in a tube, the pressure jump across the GUV's surface is related to the radius of the surface and the tension by the following equations:

$$P_v - P_p = \frac{2\tau}{R_p} \text{ and } P_v - P_0 = \frac{2\tau}{R_v} \qquad 2\text{-}5$$

Where R_p and R_v are the radii of curvature of the vesicle respectively inside and outside the pipette, P_v is the pressure inside the vesicle, P_p inside the pipette, and P_0 is the pressure in the chamber. Because the pressure in the GUV is homogeneous and the surface tension is uniform, the micropipette suction pressure is given by $\Delta P = P_p - P_0$, by subtracting the two equations of ***2-5***, membrane tension would be given by:

$$\tau = \frac{\Delta P R_p}{2(1 - \frac{R_p}{R_v})} \qquad 2\text{-}6$$

Laplace's law is only applicable when the elongation inside the pipette $L_p \geq R_p$, otherwise the radius of the spherical cap inside the pipette will not be equal to R_p.

On the other hand, the pressure applied to the GUV deforms it and generates an increase in the area of the vesicle, with the increase of the pressure. In order to extract the equations of the area increase, the total volume of the vesicle during the experiment is considered to be conserved. In fact, if the osmolarity outside and inside the GUV is conserved, and because the applied pressure is small compared to osmotic driving forces (~ 10^5 Pa), the volume of the GUV is conserved during the time scale of the experiment. The area increase for an elongation L_0 corresponding to the initial elongation inside the pipette, and an elongation L_p under a pressure ΔP, of the GUV is given by $\Delta A = A - A_0$:

$$\Delta A = 4\Pi R_v^2 \left(-1 + \left(1 - \frac{3}{4} \frac{(R_p)^2}{(R_v)^3} \Delta L \right)^{\frac{2}{3}} \right) + 2\pi (R_p \Delta L) \qquad 2\text{-}7$$

For bigger vesicles of a size two and a half times bigger than the size of the micropipette, a first order Taylor expansion is applied and the formula is reduced to the following:

$$\Delta A = 2\Pi R_p \Delta L (1 - \frac{R_p}{R_v}) \qquad 2\text{-}8$$

The area increase is linearly dependent on the length of the membrane projection aspirated by the pipette ΔL. Then, the fraction of area increase is given by the ratio of the Area increase over the initial state area A_0:

$$\alpha = \Delta A / A_0 \qquad 2\text{-}9$$

The different parameters in both equations ***2-6*** and ***2-8*** are directly analyzed from the images. The relation between the equations above will give access to the elastic moduli of the GUVs, such as the bending and the stretching modulus, introduced in the first paragraph.

2.2.2.2 Extracting the Bending modulus

At small pressure suction, the thermal undulations, characteristic of the bending modulus, are transformed into a small but noticeable area expansion. This high deformation compared to the low pressure applied is linked to the bending modulus, and the experiment to measure it is very delicate and requires a lot of precision. In fact, these tension values are between 0.001 and 0.5 mN/m which corresponds to an applied pressure of 0.1 Pa to 2-3 x 10^2 Pa for $D_p = 10\ \mu m$, . Therefore, at the beginning of the micropipette aspiration experiment, small increments of ΔP are to be applied in order to study the tension at a very low range. The accurate way to characterize the bending modulus is to follow the analysis made by Evans and Rawicz [23] and Evans [24] which are based on the physical model of the membranes and is giving the following equation :

$$\alpha = \frac{k_B T}{8\pi K_b} \ln\left(1 + \frac{c\tau A}{K_b}\right) + \frac{\tau}{K_A} \qquad 2\text{-}10$$

Equation ***2-10*** describes the total deformation of the vesicle, which is an effect of the bending and stretching regime combined together. In fact, this equation came as a correction of several previous works where bending and stretching regimes were considered as totally independent modes of deformation of the GUV. α represents the area expansion of the GUV, k_BT is the thermal energy, K_b and K_A are respectively the bending and stretching modulus, and c is a constant that depends on the type of modes of surface undulation, c ~ 0.1.

At the low - tension regime the area expansion is linked to the surface tension by the following expression:

$$\ln\left(\frac{\tau}{\tau_0}\right) \approx \frac{8\pi K_b}{k_B T}\alpha \qquad 2\text{-}11$$

Therefore, the bending modulus K_b is extracted from the fitting of the curve of $\ln\left(\frac{\tau}{\tau_0}\right)$ vs. α ***(Figure II-7C)***, τ_0 being the tension at which the bending regime stops and the stretching regime starts. τ_0 Depends on the lipid membranes, but it is usually around 0.5 mN/m.

Figure II-7 represents the bending and stretching regime state of the GUV under micropipette aspiration and the graphs that correspond to the deformations under both regimes ***(Figure II-7B – C)***

representing the curves of the membrane tension as a function of the apparent area expansion. In fact, the first high deformations at low tension τ (0 – 0.5 mN/m) correspond to the bending regime, and the linear part of the curves (1-8 mN/m) corresponds to the stretching regime.

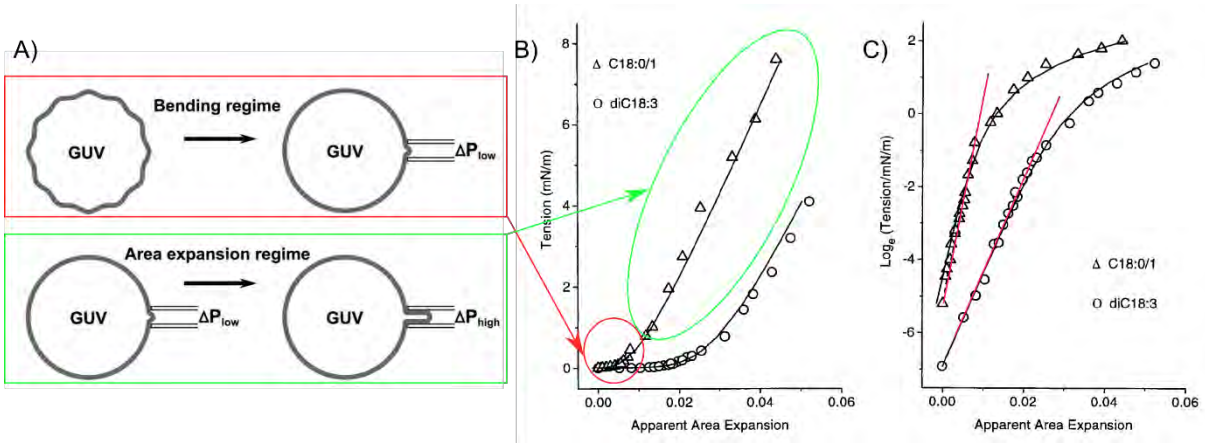

Figure II-7: Bending and stretching regime extracted from micropipette aspiration experiments: A) Scheme of the floppy GUV due to its thermal undulations and the state of the GUV after aspiration under low and high pressure suction, corresponding respectively to the bending and stretching regime [25] *B)- C) Graphs of membrane tension and ln(membrane tension) as a function of apparent area expansion for different lipid membranes obtained by micropipette aspiration experiments* [24].

2.2.2.3 Extracting the Stretching modulus

In order to reach the stretching regime of the membrane, much larger pressure suctions have to be applied. In fact, after reaching a membrane tension ~ 0.5mN/m, which corresponds to ~ 200 Pa for $D_p = 10\ \mu m$, the deformation of the GUV becomes more resistant. Therefore, the ΔP increments are larger than the one used to characterize the bending modulus until reaching a final pressure between 1 and 3 x 10^3 Pa, which corresponds to a membrane tension of around 3 to 8 mN/M. Membrane's area increases around 3% under these tensions. However, if this tension is exceeded, the membrane risks rupture. By plotting the tension vs. the area expansion from equation ***(2-3),*** an apparent stretching modulus K_{app} is extracted by fitting the linear part of the curve ***(Figure II-7B).***

However, as mentioned before, the new model of the elastic moduli of the membranes in the micropipette aspiration technique consists of combining both bending and stretching regimes to characterize its deformation (equation ***2-10*****).** Therefore, the apparent stretching modulus is derived from a superposition of smoothing of thermal bending undulations and reduction in lipid surface density. A correction is made to the equations in order to extract the direct stretching modulus, which does not take into account the smoothing of the thermal undulations:

$$\alpha_{dir} = \alpha - \frac{k_B T}{8\pi K_{bavr}} \ln\left(\frac{\tau}{\tau_0}\right) \qquad 2\text{-}12$$

Equation 2-12 removes the contribution of the bending modulus to the apparent area expansion by taking into account the average of all the bending modulus obtained for a lipid (K_{bavr}). The direct

stretching modulus K_A is then extracted from the linear fitting of the curve of the tension vs. α_{dir}. In general, K_A is significantly higher than the apparent stretching moduli, as the effect of the smoothing of the membrane is removed ***(Table II- 4)***.

Table II- 4: Bending, apparent, and direct stretching modulus extracted from micropipette aspiration experiments for different lipids and under different temperatures [24], [26].

Lipid	K_b (x 10^{-19} J)	K_{app} (mN/m)	K_A (mN/m)
DMPC	0.56 ± 0.06 (29°C)	150 ± 14 (29°C)	234 ± 23 (29°C) 290 ± 6 (15°C)
SOPC	0.90 ± 0.06 (18°C)	208 ± 10 (18°C)	235 ± 14 (18°C) 290 ± 17 (32-35°C)
DOPC	0.85 ± 0.10 (18°C)	237 ± 16 (18°C)	310 ± 20 (15°C) 265 ± 18 (18°C)

Micropipette aspiration has been a powerful tool to characterize the different elastic properties of lipid membranes, such as the bending and the stretching modulus, but also the shear rigidity for the membrane that is in the gel phase [2]. Moreover, it has been used to characterize thermal transition in GUVs membrane, the effect of cholesterol on the rigidity of the membrane, and the characterization of elastic properties of binary and ternary mixing membranes [26] as well as hybrid vesicles made of lipids and copolymers [27]. Furthermore, the effect of sugars on the elastic modulus [28], the effect of the lipids structures on the elasticity of lipid membrane [24], water permeability of lipid membranes [29] were also characterized using micropipette aspiration experiments. Micropipette aspiration has also been used to characterize asymmetric GUVs made of DMPC/DOPC in the inner/outer leaflet and vice versa [25], as well as to characterize the effect of polymers (such as PEG) on membranes mechanical properties [30].

Nonetheless, when looking at all the tables of the elastic modulus values obtained from different methods of characterization ***(Tables II-1, II-2, II-3, and II-4)***, we realize that there are big differences in the values obtained, especially for the bending modulus. It is important to understand the reasons behind the differences as some of them made the objective of my Ph.D project.

2.3 The reasons behind the difference in the elastic moduli

As seen in the previous paragraphs, characterizing the same system (same type of lipid membrane) using different techniques, resulted in different bending modulus values. If the same conditions were to be applied to a system (same GUV model studied under the same temperature in the same aqueous solution), the difference comes from the techniques of measurements. However, not all the conditions were the same when characterizing a system, which normally also resulted in different bending and

stretching moduli values. There have been a lot of speculations for the reasons behind the differences in the values of the elastic moduli obtained from different methods of characterization and sometimes even from the same methods of characterization but made by different groups of research [31].

2.3.1 Differences coming from different methods of characterization

Bochicchio *et al.,* and Nagle *et al.,* discussed this in their reviews [17],[31]. One important difference, which I already mentioned above, is the combination of both bending and stretching regime effect in the study of the deformation by micropipette aspiration, which is not the case for the rest of the methods. This tends to slightly lower the values of the bending modulus for the micropipette aspiration method. Moreover, in a relatively recent study, researchers investigated the difference between two methods, electro-deformation and the fluctuation analysis on vesicles prepared in the same batch. And by applying the same logic made in the micropipette aspiration for the electro-deformation method, a correction was also made on the bending modulus, which resulted in a lower value compared to the fluctuation analysis method [20]. Another reason for the difference between these two methods could come from the magnitude of the applied field, which could be non - homogeneously applied on the vesicles.

In general, the shape fluctuation measurements' values are significantly larger than the rest of the methods, including the micropipette aspiration. The reason for that could be the difference in the length scale of the experiments as detailed in the following reference [31]. The difference of the values of K_b obtained from the X-ray method and fluctuation analysis could come from the fact that the first measurements are made on stacks of bilayers that have an inter-bilayer constraining the range of wavelength to less than 0.5 µm. However, those values are close to the values obtained by micropipette aspiration.

Finally, the GUVs prepared in different laboratories, and different conditions (such as temperature and the sugars or salt used in the solutions) can have an effect on the mechanical properties of the membrane, giving, therefore, the difference in the values of the elastic moduli of the GUVs. Even though it is biophysically important to obtain accurate values of K_b, having different values of elastic modulus when characterizing different models of membranes (same lipid mixture) using different methods is commonly observed, as was mentioned by Nagle et *al.,* in their review [32].

2.3.2 Differences coming from environmental effects

2.3.2.1 Effect of temperature on the mechanical properties of lipid membranes

As seen in chapter one, each lipid has a temperature of phase transition which determines the phase state of the vesicle: if $T < T_m$ (T_m = temperature of phase transition), the lipids are in the gel phase,

whereas if T > T_m, the lipids are in the liquid phase. This clearly has an impact on the rigidity of the membrane, therefore on the mechanical properties of the membrane. In fact, the effect of the temperature on elastic moduli of lipid membranes has been studied a lot in the 90s, and clear effects were established. Many methods of characterization were used to do so, such as: Fluctuation analysis [9], [33], electro-deformation [15] and micropipette aspiration [2]. Some of the results for DPPC membrane were grouped in one graph ***(Figure II-8)***, which was discussed by R.Dimova in [34]. In fact, there is a clear dependence of the bending modulus on temperatures which are very close from both sides to the temperature of transition. The bending modulus decreases significantly close to the temperature of transitioning from a gel to a liquid phase and then reaches constant values when the temperature is increased and is far from T_m. These results are simply explained by the fact that close to the phase transition temperature, membranes become more flexible in order to rearrange from a gel phase to a liquid phase. On the other hand, even if temperature has a clear effect on the bending modulus, there was no clear effect in the literature of temperature on the stretching modulus of the membrane.

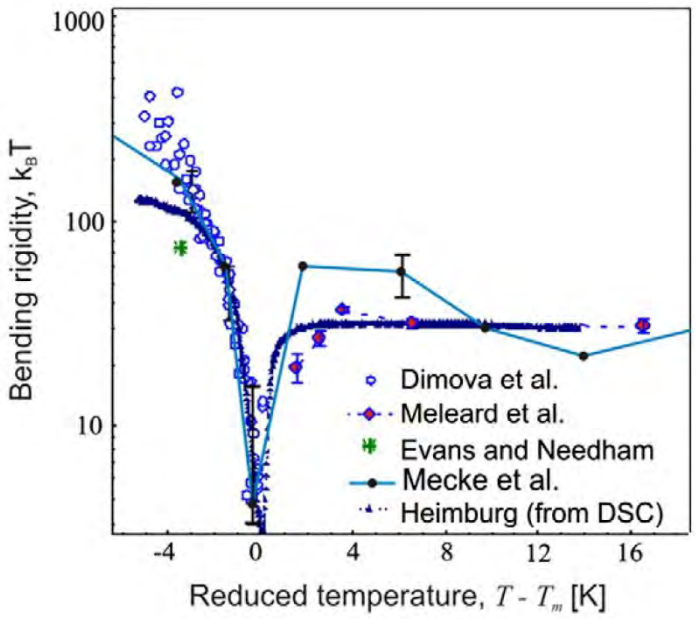

Figure II-8: Temperature dependence of DPPC bending rigidity close to the main phase transition temperature Tm [34] *. The open circles represent data using the approach of optical dynamometry. The red diamonds show data adapted obtained with fluctuation spectroscopy. The green asterisk is a single-point data collected from micropipette aspiration. The black dots and solid lines represent data from neutron reflectivity on floating bilayers in the vicinity of solid support. The solid blue triangles are data calculated from the heat capacity curve of dipalmitoylphosphatidylcholine (DPPC) liposomes.*

For membranes that have a melting temperature which is close to the temperate of the study, or for example, the room temperature, such as (DMPC (24°C) and DPPC (41°C)), it is better to perform the mechanical characterizations studies in a heated cell.

2.3.2.2 Effect of Sugars and Salts on the mechanical properties of lipid membranes

As mentioned before, one of the reasons for the differences between the bending moduli obtained is the way the GUVs are fabricated, and more specifically, the aqueous solution that is inside and outside them. In fact, most of the GUVs are prepared with a sugar solution because it increases the optical contrast when using phase-contrast microscopy, and it osmotically stabilizes the vesicles, especially when they have to settle at the bottom of the chamber for easier microscopic observation. While going through the literature, a wide range of sucrose concentrations is used during the preparation of the GUVs, going from 3 to 250 mMol/L. A study showed that at low concentrations, small sugars are strongly bonded to the lipid membrane causing the membrane to laterally expand and reduce its thickness. Whereas at a higher concentration ~200 mMol/L, the sugars are gradually expelled from the membrane [35]. One can then argue if the concentration of sugars affects the thickness of membranes and the bending modulus is a characteristic of membrane thickness; therefore, the bending modulus must be affected by the sucrose concentrations. This subject is still very debated in the literature, even if some data show that there might be a correlation. In fact, the two first studies of the sugar's effect on lipid membranes showed a significant decrease in the bending modulus of the SOPC membrane when the concentration of sucrose inside the GUVs was increased up to 300 mMol/L, using micropipette aspiration and vesicle fluctuation analysis methods to characterize it [36],[28] ***(Figure II-9).*** However, to investigate more this point, Nagle *et al.* characterized the effect of glucose and sucrose on DOPC membrane using X-ray scattering techniques [32]. The results showed no effect of these sugars on the DOPC lipid membrane.

The two contradictory results, as well as the absence of characterization of sugars effect on the stretching modulus, show the need to investigate more this effect, as we did as part of the Ph.D. project.

Salts and ions can also be part of the aqueous solutions when preparing the GUVs, and they are important factors to consider as they are physiologically relevant solutions. Fluctuations spectroscopy analysis is made on POPC lipid membranes with different concentration of NaCl, going from 0 – 0.1 M [37]. On the other hand, other studies made on the effect of KCl and KBr on different PC membranes showed no change in the bending rigidity [38]. Therefore, same as the sugar's effect, this topic is still debated because of the lack of data to confirm any effect on the elastic properties of the lipid membranes.

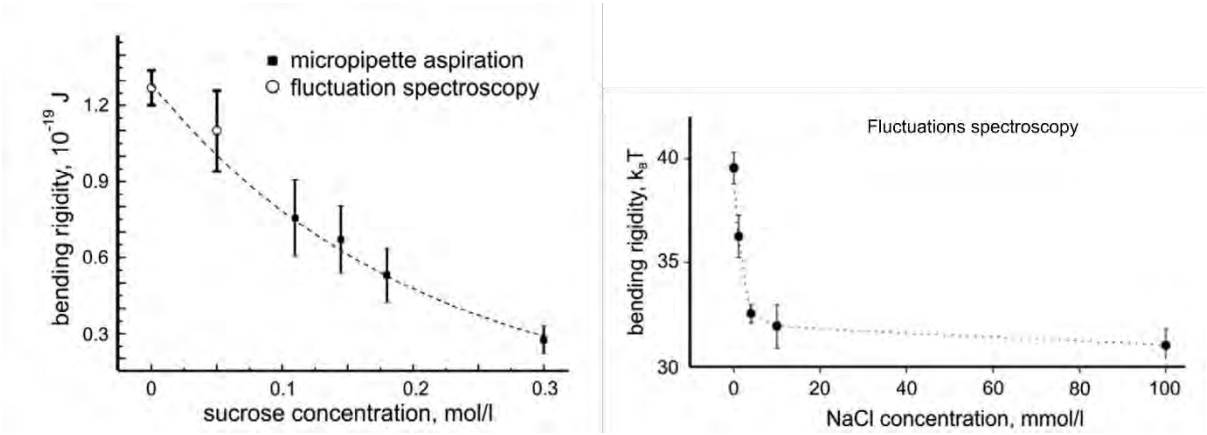

Figure II-9: Effect of sucrose and NaCl concentration on the bending modulus of SOPC and POPC lipid membrane respectively [28]*,* [37]*. The characterization of the bending modulus of SOPC was made by vesicle fluctuation analysis for low sucrose concentration (0 - 0.05 mol/l) and by micropipette aspiration technique for a higher concentration of sucrose (0.11 – 0.30 mol/l). The characterization of the bending modulus of POPC was made by vesicle fluctuation analysis.*

2.3.3 How does membrane's composition affect the mechanical properties of lipid membranes?

2.3.3.1 Effect of length and unsaturation of lipids on the mechanical properties of lipid membranes

As seen in chapter 1, the cellular membranes are mainly composed of cholesterol and phospholipids, which have a different chemical composition that differs (especially for the phospholipids) by the length and the degree of unsaturation in the acyl chain. In order to characterize the effect of the properties of the lipid on the membrane's elastic properties, Rawicz *et al*., performed micropipette aspiration on different PC (phosphatidylcholine) lipids [24]. Those results became the basics of elastic properties of lipids membrane and the basis to which every scientist comes back to, in order to compare new results. In fact, the phosphatidylcholine lipids chosen were: saturated lipids with short acyl chains (13 and 14 carbon atoms), medium chains (18 carbon atoms) but with different degree of unsaturation (going from 1 to 6 double bonds per lipid) and finally long unsaturated chains (20 and 22 carbon atoms). Three main results are discussed in this article. First, the stretching modulus values were slightly different between the different lipids but there is no correlation to the lipids acyl chain length neither to its degree of unsaturation was noticed. Secondly, bending modulus of saturated and mono-unsaturated acyl chains increased with the increase of the length of the acyl chain from 13 to 22 carbon atoms. However, bending modulus dropped significantly and proportionally when the lipid had two or more double bonds. Finally, the bending values obtained were correlated to the thickness of the membrane as it was demonstrated before. X-ray diffraction measurements proved that the

bilayer thickness of saturated and mono-unsaturated lipids increases with the increase of the acyl chain length, whereas the bilayer membranes with two or more unsaturation in their acyl chains are thinner, which explains the low values of bending modulus.

Correlation between Stretching modulus K_A and bending modulus K_b

The bending and stretching modulus were then related to each other by a model called "*polymer brush model*" [24]. In this model, each monolayer is viewed as a collection of extended polymer chains held together by hydrophobic interactions at the interface (because of the hydrophobic nature of the acyl chains). The brush model predicts the following:

$$(\frac{K_b}{K_A})^{1/2} = (h_{pp} - h_0)/24 \qquad \textit{2-13}$$

Where K_b and K_A are respectively the bending and the stretching modulus, h_{pp} is the peak-to-peak headgroup distance (thickness of the bilayer lipids from head to head), and h_0 is the distance from the headgroup to the compact hydrocarbon region. In fact, the stress distribution across the bilayer is mainly in the hydrophobic chains, and the elastic properties of the lipid membrane are governed by the mechanical thickness $h = h_{pp} - h_0$. This theoretical model shows that the ratio $(\frac{K_b}{K_A})^{1/2}$ is linearly dependent of the thickness of the lipid bilayer. However, it was demonstrated that this model is applicable to membranes made of saturated and mono-unsaturated lipids but not to membranes made of lipids that are poly-unsaturated. This model is very interesting as it can predict certain mechanical behavior of the membrane, especially when external stress is applied on the membrane, for example in the case of membrane-molecule or membrane-particle interactions.

More micropipette aspiration experiments were also performed on binary and ternary lipid mixtures [26] as these compositions are closer to the real cellular membranes. In fact, as discussed in the previous chapter, the presence of a different mixture of lipids in the membrane creates micro-domains that are observable in the model membranes and which alters the membrane's elastic properties ***(Figure II-10)***. The results showed an increase of the stretching modulus of binary mixtures (PC + Chol or SM + Chol) and ternary mixtures (SM + DOPC + Chol) compared to the single PC or SM membrane. However, no results were given on the bending modulus of these membranes.

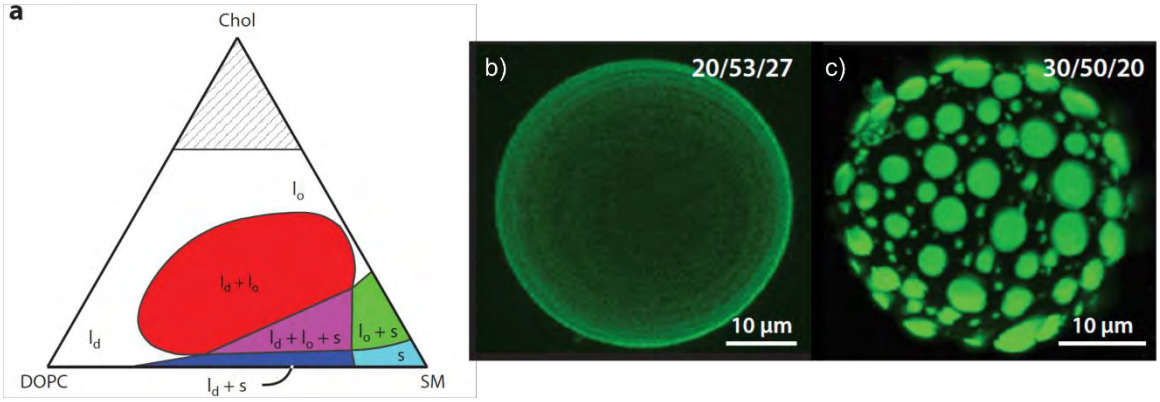

Figure II-10: Phase diagram deduced from fluorescent microscopy of giant vesicles [39]. *a) Example of a phase diagram of a ternary lipid mixture of DOPC, cholesterol and SM lipids at 23°C, showing the coexistence of liquid-ordered (l_o), liquid disordered(l_d), and gel phases (s). b) and c) are 3-D projections of confocal microscopy of GUVs with b) homogeneous membrane or c) liquid-ordered and liquid-disordered phases. The molar ratios are respectively for DOPC/SM/chol.*

2.3.3.2 Effect of Cholesterol on lipid membranes

Cholesterol forms around 44 % of the lipids in the eukaryotic plasma membrane. It is a key player in stabilizing membrane domains which are believed to be responsible for the correct functioning of membrane proteins [34]. It also plays an important role in regulating lipid chain order and the lateral organization and diffusion of lipid membranes which affects their mechanical properties. For example, the permeability of the membrane is affected by the presence of cholesterol. In fact, the presence of 40 mol % of the cholesterol in a DPPC membrane led to the thickening of the lipid membrane, therefore increasing the permeability barrier [40].

The first studies of cholesterol's effect suggested a universal effect of rigidifying the lipid membranes expressed by an increase of both of their bending and stretching modulus. In fact, vesicle fluctuations analysis showed an increase of 4 times of the bending modulus of DMPC (14:0) lipid membranes with the increase of cholesterol up to 30 mol% [41],[33]. Micropipette aspiration also showed an increase of 60% of the stretching modulus, and an increase of 125 % of the bending modulus of POPC (16:0/18:1) lipid membrane with the increase of cholesterol up to 30 mol% [42]. And Finally, tethered GUVs and micropipette aspiration showed respectively an increase of 3 times of the bending in SOPC (18:0/18:1) lipid membranes with the increase of cholesterol up to 50 mol% [43], and an increase of 6 times for stretching modulus with SOPC and cholesterol up to 89 mol% [44].

Nonetheless, the effect of cholesterol on lipid membranes appeared as less universal when more lipid membranes were studied. In fact, a study was made to characterize the effect of cholesterol on DOPC (18:1) and SM membranes by comparing two methods of characterization: electro-deformation and vesicle fluctuation analysis [20]. Both methods showed that the bending modulus of DOPC membranes is not affected by cholesterol even for a high percentage (50 mol%). However, Vesicle

Fluctuation Analysis showed a 50% decrease of the bending modulus of SM/Chol membrane with the increase of cholesterol up to 50 mol %, and the same for electro-deformation methods ***(Figure II-11)***. The effect of cholesterol on the bending modulus of DOPC and SM membrane seems to be incoherent with the effect of cholesterol on the stretching modulus of these membranes characterized by micropipette aspiration where the stretching modulus increases significantly with the percentage of cholesterol [26]. This could be explained as follows: as seen in chapter I, when cholesterol is mixed with a membrane in its gel phase, the membrane shifts from gel to liquid-ordered phase. Whereas, when cholesterol is mixed with a liquid disordered phase, it shifts to a liquid-ordered phase. The shifting from gel to liquid-ordered phase (case of SM/Chol) can decrease the thickness of the membrane, which could be the reason of the decrease of the bending modulus.

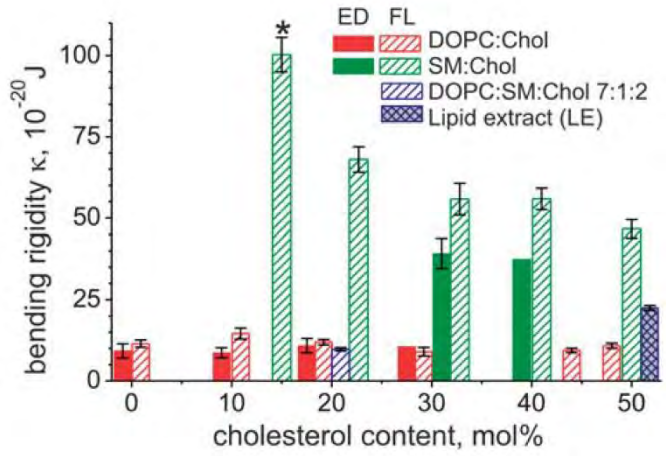

Figure II-11: Cholesterol effect on bending rigidity modulus of different lipids measured by electro-deformation methods (full colored bars) and fluctuation spectroscopy method (hatched bars) [20].

Nagle *et al.,* suggested then that the effect of cholesterol on the mechanical properties of lipid membranes is not universal but depends on the specific architecture of the lipid building of the membrane. More studies using X-ray scattering to characterize the DOPC-cholesterol membranes showed that DOPC bending modulus is not altered by the presence of cholesterol [45], [46]. Same for diC22:1 membrane, which contains 22 carbon atoms and 2 total unsaturation in its acyl chain. The same study showed again the increase of both bending and stretching modulus of SOPC (18:0:1) lipid membranes. The general deduction of cholesterol effects on bending modulus is the following:

- Cholesterol does not affect the bending modulus of the membranes made out of phosphatidylcholine (PC) lipids which have two or more total unsaturation in their acyl chains.
- Cholesterol increases both stretching and bending modulus of membranes made of phosphatidylcholine (PC) lipids which have two completely saturated acyl chains but less dramatically for one unsaturated acyl chain lipids.
- The stretching modulus of all lipids increases with the presence of cholesterol.

The reasons behind these results are still not very clear. However, those results are biologically in favor of the cellular membrane mechanisms. In fact, the presence of cholesterol in cellular membranes is inevitable. Nonetheless, if the cellular membrane only contained saturated and monounsaturated lipids, the membrane would become less flexible to adapt to changes that the membrane is required to do all the time [45].

Due to their fluidity, cellular membranes are highly dynamic and undergo changes in their shapes to react to environmental changes or external stimuli. Characterizing the elastic moduli of the cellular membrane is crucial, especially the bending modulus, as it shows the capability of the membrane to bend and adapt to the different possible interactions. The changes in their shape and physical state affect their mechanical properties, as seen in this chapter until now. Because of the relatively easy way to access them and their different possible way of characterization, model membranes have been widely used for different applications. One important axis of research focuses on using the model membranes, especially the GUVs, as platforms to investigate the effect of diverse molecules, drugs or nanoparticles on them. In fact, in order for a nanoparticle to cross the cellular membranes, it can induce stress and changes on the membranes and therefore maybe changing their mechanical properties. The next paragraph will explain how the membrane reacts to adapt when nanoparticles or nano drugs come in contact with the cellular membrane.

2.4 Application of model membranes: Membrane – Particle interactions

Engineered nanoparticles have been increasingly used in many fields, especially for nanovaccines[47], nanodrugs [48] and as diagnostic imaging tools [49]. But also, industrial processes are basing some of their products on nanoparticles, such as food, paints, and cosmetics. Evidently, the excessive use of nanoparticles calls attention to investigate nanotoxicity effect on cells and organisms, taking into consideration particles' different sizes, shapes, and surface chemistry.

In fact, for the nanoparticle to enter the cell and deliver its specific function into the organism, the particle has to first cross the cellular membrane, which is the main barrier between the inner and outer cell environment. Due to its fluidity, the cellular membrane undergoes several mechanical and physical changes to allow such passage to happen. Characterizing this fluidity is necessary to understand the possible changes happening to the membrane. Thanks to the different characterization techniques discussed before, model membranes offer a great tool to reproduce cellular membranes and to be used as a platform to investigate the effect of the nanoparticles on membranes.

2.4.1 What are the different processes induced in particle-membrane interaction?

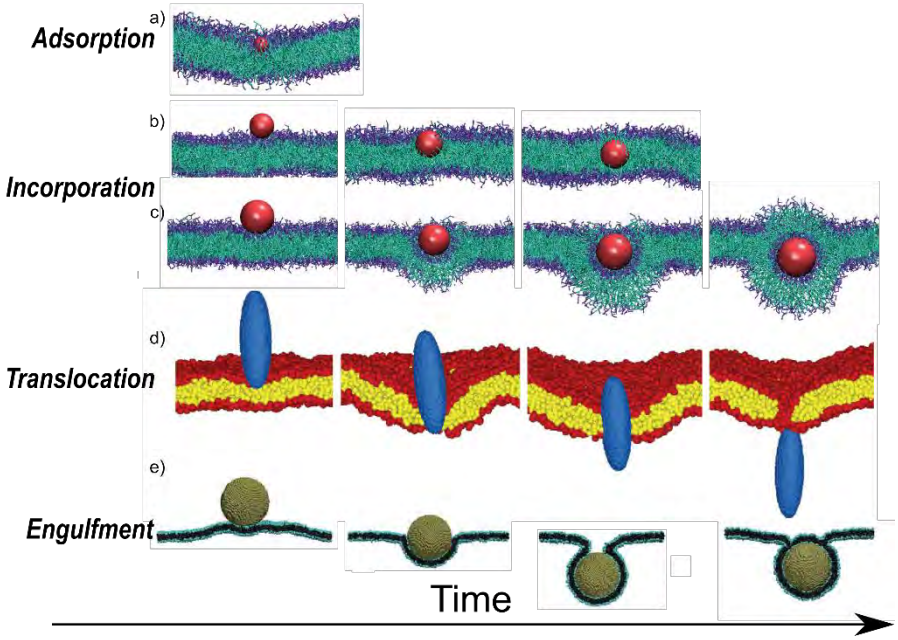

Figure II-12: Time–series snapshot pictures of simulation of different processes induced by particle-membrane interaction. a) adsorption, (b-c) incorporation, d) translocation and e) engulfment. The hydrophilic heads of the lipids are represented in blue (a-c), red (d), and turquoise (e). At the same time, the hydrophobic parts of the membrane are represented in green (a-c), yellow (d), and black (e). The overall picture is taken from the Giant Vesicle book [6] *but a-c) is from* [50]*, d)* [51] *and e)* [52].

2.4.1.1 Nanoparticles basic properties

When a nanoparticle interacts with a membrane, it induces changes in the membrane's architecture and shape, which allows one of the following processes to happen, such as the adsorption of the particle in the surface of the membrane or its incorporation inside the bilayer membrane, the translocation towards inside the cell or the engulfment of the particle [6] ***(Figure II-12)***. However, these processes will depend not only on the membrane's elastic and chemical properties but also on the particle's characteristics, such as the size, shape, and surface chemistry [53].

First, nanoparticles can have sizes going from less than 1 nanometer up to hundreds of nanometers. Taking into consideration that the membrane's thickness is around 5nm, particles that are smaller than that will interact differently than particles that have a comparable or larger size than the membrane's thickness.

Secondly, nanoparticles used are generally spherical; however, different shapes can also be fabricated, such as elongated shapes (carbon nanotubes) or gold nanorods. And the shapes combined with their size will also have different interactions with the membrane.

Finally, the surface chemistry of the particles also influences the way the particle interacts with the membrane. Remembering that the bilayer has hydrophilic heads on the surface, linked by hydrophobic tails between the two layers. If the particle is hydrophilic or hydrophobic, it might be integrated within the polar heads or inside the hydrophobic core of the bilayer. Another type of functionalization can also affect the interaction, such as the surface charge of the particle, taking into account that the membrane is negatively charged.

All these characteristics will influence the way the particle interacts with the membrane.

Characterizing the synthesized NP is crucial to measure their size and shape and be sure of their exact composition. An interesting review has enumerated the common experimental techniques to characterize NPs size and discussed both their advantages and limitations [54]. Some of the techniques are TEM (Transmission Electron Microscopy), DLS (Dynamic Light Scattering), FCS (Fluorescence Correlation Spectroscopy), AFM (Atomic Force Microscopy), etc.

2.4.1.2 Nanoparticle – Membrane induced processes

As seen in ***Figure II-12,*** there are different processes in which the nanoparticle interacts with the membrane. These processes have been demonstrated by simulation, and some of them are not yet experimentally demonstrated. The different combinations that will determine the processes are the following:

(i) If the particle is smaller than the membranes thickness or comparable size (~ 5nm) and is hydrophilic (which means the particle cannot go inside the hydrophobic tails of the membrane), the particle is most likely to be adsorbed on the surface of the membrane ***(Figure II-12a)***. The asymmetric adsorption process of particles (proteins, polymers, and ions or small molecules) onto the bilayer membranes generates a spontaneous curvature. It was demonstrated that the spontaneous curvature also generates a spontaneous tension in the membrane, which varies from 2 x 10^{-8} mN/m (for sugar solutions) up to 1 mN/m (for Bar domains proteins) [55].

(ii) If the particle is also small but hydrophobic, the particle will incorporate inside the bilayer onto the hydrophobic core of the membrane ***(*Figure II-12*b).*** This was the case of poly (N-isopropyl acrylamide) microgels of sizes $2.7 \pm 0.1\, nm$ interaction with DOPC lipid membrane [56]. Some simulations showed the possibility of a hydrophilic nanoparticle to be incorporated inside the hydrophobic core of the membrane ***(Figure II-12c)***. For this to happen, the NP has to be completely wrapped by the hydrophilic part of the membrane, and this requires a lot of energy for the membrane to change its topology. This behavior has not yet been seen experimentally.

(iii) If the particle is small but presents both hydrophilic and hydrophobic properties (such as hydrophobic nanoparticles that are covered with lipids), the particle can translocate and cross the membrane without inducing any damage to it. An interesting study investigated the interaction of DMPC lipid membrane, with gold NP covered with DMPC lipids [57]. It was demonstrated that particles that are smaller than 5nm are adsorbed into the surface, whereas particles that are larger than 5 nm (bilayer thickness), the gold NPs coated with lipids insert the bilayers, open pores, and translocate outside the membrane. Other particles can be forced to go through the membrane by external forces, using, for example, atomic force microscopy ***(Figure II-12d).***

(iv) Finally, if the particles are larger than few times the thickness of the membrane (particles few nanometers to several micrometers), the processes described above become energetically unfavorable. In this case, and if the interaction of the hydrophilic surface of the membrane and the particle is attractive, the membrane spreads onto the particle and engulfs it ***(Figure II-12e)***. In this process, the particle is completely enwrapped by the membrane but still attached to the mother membrane by a small neck. This process is one of the most important ones because if the neck breaks, the vesicle-particle would have been effectively transported inside the membrane. This is one of the cases of the *endocytosis* phenomena, which is a cellular process and the main pathway in which substances are brought into the cell.

A study on gold nanoparticle uptake was investigated in Hela cells where they demonstrated that the 50 nm size particle has the highest percentage of membrane crossing compared to particles of 14 and

74 nm [58]. This shows the importance of the size of the nanoparticles in order to achieve the highest drug delivery efficacy.

One of the most recent examples of Nanomedicine is one of the Covid19 vaccines, which was developed by Pfizer company during the on-going pandemic: in fact, the vaccine uses a messenger RNA which is a genetic material that our cells read to make proteins. However, this molecule is very fragile and would be chopped to pieces by our natural enzymes if it were injected directly into our body. Therefore, in order to protect it, the molecule is wrapped by a lipid nanoparticle mainly made of DSPC (1,2-distearoyl-sn-glycero-3-phosphocholine) and cholesterol [59]. Once injected, the vaccine particles come in contact with cells, and the lipid membrane of the vaccine fuse with the plasma membranes of the cells releasing then the molecule inside the cells to do its job. This is an example of translocation of nanoparticles inside the membranes. These type of nanoparticles are great tools for drug deliveries purposes.

2.4.2 Effect of nanoparticles on the physicochemical properties of cellular membranes

The plasma membrane is a selectively permeable membrane which is a favorable characteristic in order to protect the cell. Small molecules can naturally diffuse across the membrane through proteins that allow membrane transport. However, large nanomaterials are incapable of crossing the plasma membrane on their own, which is why phenomena such as endocytosis help internalizing the particles inside the cells. For endocytosis or exocytosis (the transport of a molecule from inside the cell to outside) phenomena to happen, the membrane has to bend and change shape, and this is a characteristic of the bending modulus which influence the transport of the molecules through the membranes. On the hand, upon interaction with NPs the mechanical properties of the membrane could be altered. Over the years, scientists have synthesized many biological nanomaterials which purpose is to cross the plasma membrane and penetrate inside the cell, which is usually the case of drug delivery goals. However, not all nanomaterials are able to penetrate cellular membranes: aside from very small molecules or needle-shaped materials, only cationic nanoparticles can pass through the cell membranes [60].

2.4.2.1 Gold Nanoparticles

Gold nanoparticles AuNP are inorganic chemically stable structures and relatively inert in biological systems, and due to their optical and electronic properties, they have been used increasingly in several biomedical applications. For example, they have been used in cancer therapy, drug delivery, or as vaccine carriers [61] and in biosensing systems such as SPR (surface plasmon resonance) and in electrochemical biosensors [62]. Gold nanoparticles are also easily functionalized and can be

synthesized in many sizes (1-200nm) in order to achieve the desired efficacy and limit the toxicity towards the cells when injected or in contact with any organ in our body. The effect of Gold nanoparticles on the physical properties of lipid membranes has been investigated. For example, hydrophobic spherical gold nanoparticles, of sizes around 3 – 4 nm, incorporated in the hydrophobic core of the membrane and increased the fluidity of DPPC lipid bilayer [63]. The same behavior was seen when characterizing the effect of gold nanoparticles on the elastic properties of lipid membranes. In fact, in the following study [64], gold nanoparticles of an average size of 3 and 3.8 nm were functionalized with dodecanethiol, which makes the nanoparticles hydrophobic. Upon their incubation with DPPC/DPPG lipid membrane, the hydrophobic NPs are incorporated into the hydrophobic bulk of the membrane. Vesicle fluctuations analysis was performed to characterize the bending modulus. The results showed a decrease of 15 % of the bending modulus after interaction with gold NP of 3.8 nm diameters. The overall softening of the membrane is caused by local fluidization due to the NPs' incorporation in the membrane. Small-angle neutrons scattering (SANS) measurement was done to characterize the thickness of the membrane. The results showed a relatively small increase in the membrane thickness upon interaction with the lipid membranes. The two contradictory results showing at the same time the decrease of the bending modulus and the increase of membranes thickness proves the drastic reduction of the stretching modulus. This is supported by brush model, in equation ***2-13***.

Moreover, a study was made by the CSGI laboratory and the University of Florence to characterize the effect of gold nanoparticles which have two different coatings, on POPC lipid membranes [65]. The spherical gold nanoparticles were 15 nm diameter and they were either capped by citrate (NPs@Ct) and which represents the "naked" NPs or coated by corona proteins (NPs@PC) which represents "biological fluid passivated" NPs. Confocal laser scanning microscopy and FCS (Fluorescence Correlation Spectroscopy) were used to characterize respectively the permeability of the lipid membranes to small molecules and the lipid diffusion coefficient by tracking the lipid mobility. These characterization techniques represent a multiscale nature of the interaction of the NPs with the GUVs lipid membranes, which are affected at the molecular scale and the colloidal scale, as seen in ***Figure II-13.*** In fact, it was demonstrated that the NPs@Ct increased the permeability of the POPC lipid membrane seen by the increase of the trafficking across the bilayer, it even caused the complete loss of the barrier function and aggregation of NPs@Ct were seen inside the GUV. On the opposite, the NPs@PC only slightly enhanced the permeability of the membrane. Moreover, scaling down to the molecular range, the diffusion coefficient value of lipids in the membrane decreased 4 times in the presence of either of the NPs, which meant the possible formation of rigidified lipid domains as seen in chapter I. These results could imply that the mechanical properties of lipid membranes would be

altered in the presence of such gold nanoparticles, especially the NPs coated with Citrate. More studies were performed where PC lipid membranes were in contact with gold nanoparticles coated by Citrates in order to characterize the membranes phase reaction [66]. It was shown that membranes that have higher fluidity induce faster aggregation of AuNPs, which causes local gelation in fluid membranes such as the DOPC lipid membranes. This effect was not seen on gel phase membranes as the aggregations of Gold NPs on gel phase membranes are unfavorable.

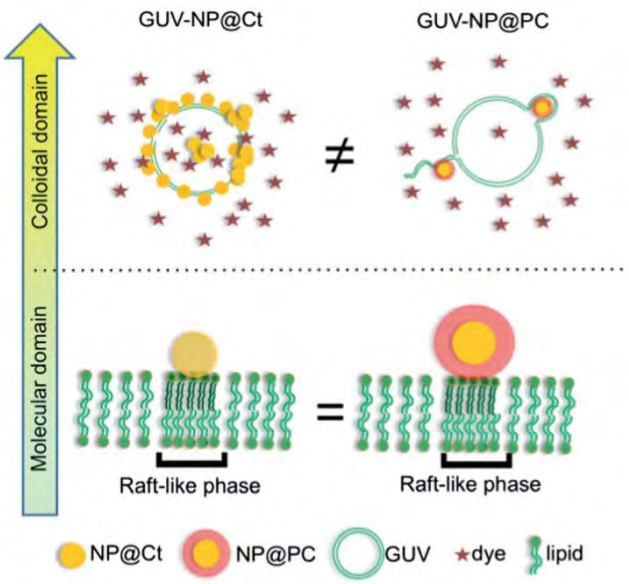

Figure II-13: Schema representation of the interaction of NPs@Ct and NPs@PC on the GUV lipid membranes. The interaction is a multiscale nature: the molecular domain and the colloidal domain. At the molecular domain, both NPs seem to create a raft-like phase in the lipid bilayer. On the Colloidal domain, the NPs@Ct enhance the permeability of the GUV, allowing the crossing of big molecules inside the membranes, unlike the NPs@PC [65].

2.4.2.2 Polymer nanoparticles

Polymer nanoparticles' effect on lipid membranes phase was also investigated: a destruction of the liquid phase of DMPC lipid membrane was seen when challenged with 8 nm size cationic dendrimers polymers, whereas the gel phase was not affected [67]. In fact, a DMPC membrane whose phase transition temperature is around 24°C was heated up to a temperature where both liquid and gel phases occur and investigated with atomic force microscopy (AFM) ***(Figure II-14a)***. Dendrimers are spherical, highly ordered polycationic macromolecules, which destroyed the liquid phase of the membrane by creating holes, as clear in ***(Figure II-14b-d).*** This study suggests that the membrane phase should be explicitly considered when employing low temperature or chemical species that can influence the membrane structural phase, especially when studying the cellular uptake of nanoparticles.

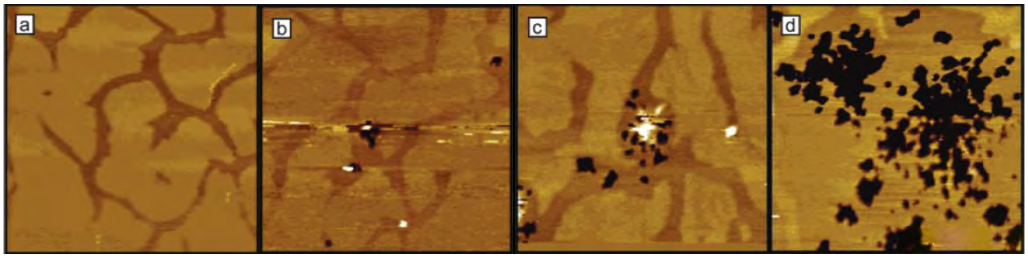

Figure II-14: AFM images of supported DMPC bilayer during phase transition from gel to liquid, before and after adding the PAMAM dendrimers NP. The light shades represent the gel phase, and the darker shades are the liquid phase of the membrane. b) c) and d) are images of respectively 3, 8, and 17 min after adding the NPs, where total destruction of the liquid phase is seen (dark spots). Scan size 1 µm, color height scale 0-5 nm [67].

Other interesting NPs are based on self-assembled block copolymer micelles which are used as nanocarriers of photosensitizer for photodynamic therapies [68], such as poly(ethylene oxide)-block-poly(ε-caprolactone) PEO-PCL and poly(ethylene oxide)-block-poly styrene PEO-PS. These NPs were used on DOPC LUVs (large unilamellar vesicles ≈ 100 nm) lipid membranes and human cancer cells [69], by our collaborator in IMRCP lab (chap V). The ability of the micelles and the photosensitizer to translocate inside the membranes was studied by characterizing the concentration of photosensitizer found inside the membranes and the cells. However, the colocalization of photosensitizer was found in higher concentrations using the PEO-PCL copolymers micelles to deliver it. Moreover, the effect of the NPs on the permeability of the membranes was characterized by performing a leakage experiment which showed an increase in the permeability of the lipid membranes after interaction with the PEO-PCL copolymers ***(Figure II-15)***.

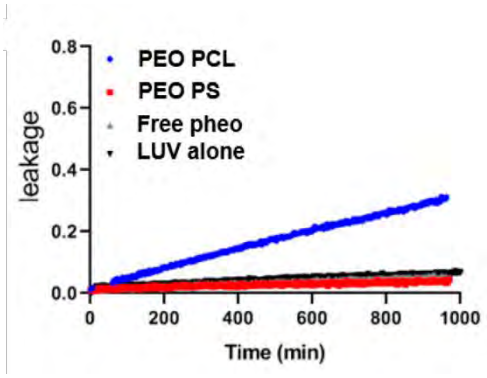

Figure II-15: Carboxyfluoresceine leakage from DOPC LUVs alone and DOPC LUVs challenged with free Pheo (photosensitizer) and with the PEO-PCL and PEO- PS micelles [69].

2.4.2.3 Charged nanoparticles

Charged nanoparticles (carboxyl-modified and amidine-modifies PS) were tested on lipid membranes to investigate their effect on membrane fluidity and their ability to induce surface reconstruction [70]. The PC membranes used are zwitterionic (not charged) as seen in chapter I, and the nanoparticles size ranges between 4 and 20 nm. Positively charged (cationic) and negatively charged (anionic)

nanoparticles were challenged with lipid membranes as follows: negatively charged NPs were added to DOPC and DLPC lipid membranes which phase transition temperatures are below room temperature, and local gelation appeared in the fluid bilayer membranes. Positively charged NP were added to DPPC membrane, which phase transition temperature is + 40°C, which means the membrane was in its gel phase at room temperature. The cationic NP induced local fluidization on the gelled bilayer. In fact, as seen in the previous chapter, PC membranes contain phosphate (P^-) and choline (N^+). The positively and negatively charged particles interact respectively with the phosphate and the choline and change the tilt angles of the polar heads, which affects membrane fluidity. The gelation and the fluidization of the lipid membrane are direct proofs of the alteration of the mechanical properties of the membranes upon interaction with NPs.

2.4.2.4 Nanoparticles and cytotoxicity effects

On the other hand, some aspects of the NPs used can have a toxic effect on the cells, which is also crucial to determine and characterize. In fact, NPs can invade the human body through inhalation, ingestion, or through the skin. Once inside the body, the NPs come into contact with a wide variety of biomolecules which immediately coat the NP surfaces and form the 'protein corona'. In order to evaluate the toxicity effects of NPs, some approaches have been established and discussed in the review [71], such as the functional assays to determine the effects of NPs on cellular processes and the viability assays to probe whether the NPs cause death in a cell or a system of cells. However, these methods suffer from many limitations, and work is still yet to be done to advance this field.
Some of the studies of NPs effect on cells showed that small NPs are more toxic than large ones. For example, AuNPs (1.4 nm) caused rapid death by necrosis within 12h, whereas larger AuNPs (15nm) showed low toxicity [72].

Nanoparticles effect on lipid membranes is not universal. It depends on both the characteristic of the particle (such as the size, the coating and the type of material) and the phase of the lipid membrane. However, all interactions of NP with cellular membranes induce changes in the membrane, which affects their biochemical properties, which dictate many biologically relevant processes. Important properties that are not very well established in the literature are the effect of the NPs on the mechanical properties of the membranes. In our project, we focused on using different types of NPs such as gold NPs and copolymers micelles to investigate their effects on the mechanical properties of lipid bilayer membranes.

2.5 Conclusion

The elastic properties of the membrane are responsible of the membrane's capability to bend and change shape and structure to adapt to many biological processes that are happening in the membrane. Characterizing the model lipid membranes is a crucial step after fabricating them as it gives access to many properties of the membrane. Even though there are different techniques to characterize the GUV, micropipette aspiration is the most commonly used. However, it still involves long experimentation, especially to prepare all the set-up and calibrate the micropipette inside the chamber, as well as the manual hydrostatic pressure control over the pressure. Moreover, parallelizing experiments is not possible, as well as changing the solution around the GUVs to investigate other membrane properties at the same time.

Many parameters affect the membrane mechanical properties, such as the temperature, the lipids structure, the chains length and the degree of unsaturation. Some parameters' effects are well established and agreed on between scientists especially that many methods were used to prove these effects. However, some parameters' effects seem to be still very debatable as different experiments are giving contradictory results. For example, the cholesterol effect on the properties of the membrane seems to be non-universal but depends mostly on the structure of the lipids in the membrane. Another example is the effect of sugars and salts on the membrane's properties, where some experiments showed a potential effect and others showed no correlation between the concentration of sugars and salt on the elasticity of the membrane. Some of my Ph.D objectives is to include thorough studies to characterize the effect of cholesterol and sucrose concentration on the bending and stretching modulus of the membranes, and hoping that my results would help clarify these effects.

Finally, model membranes are used to investigate the interaction of nanoparticles and cellular membranes. Even though numerous experiments have been made to determine the possible effects of different nanoparticles on the physicochemical properties of the membranes, many informations are still missing, which includes the effect of NPs on the elasticity of the membrane.

During the last years, scientists have tried to combine microfluidics with model membranes in order to characterize more properties of the Giant unilamellar vesicles, such as the permeability, the mechanical properties and more interactions of NPs with lipid membranes. Micropipette aspiration allows a full study of the elasticity of the membrane, however, it still presents some limitations. Using microfluidics could be an efficient way to easily manipulate GUVs and conduct experiments, as it also allows a fast-changing of the solutions around the GUVs. Therefore, in the next chapter, I will be introducing the use of microfluidics to study GUVs.

References

[1] W. Helfrich, “Elastic Properties of Lipid Bilayers: Theory and Possible Experiments,” *Zeitschrift fur Naturforsch. - Sect. C J. Biosci.*, vol. 28, no. 11–12, pp. 693–703, 1973, doi: 10.1515/znc-1973-11-1209.

[2] E. Evans and D. Needham, “Physical properties of surfactant bilayer membranes: Thermal transitions, elasticity, rigidity, cohesion, and colloidal interactions,” *J. Phys. Chem.*, vol. 91, no. 16, pp. 4219–4228, 1987, doi: 10.1021/j100300a003.

[3] R. Lipowsky, “Coupling of bending and stretching deformations in vesicle membranes,” *Adv. Colloid Interface Sci.*, vol. 208, pp. 14–24, 2014, doi: 10.1016/j.cis.2014.02.008.

[4] D. Boal, “Mechanics of the cell, second edition,” *Mech. Cell, Second Ed.*, pp. 1–608, 2012, doi: 10.1017/CBO9781139022217.

[5] P. Bassereau, B. Sorre, and A. Lévy, “Bending lipid membranes: Experiments after W. Helfrich’s model,” *Adv. Colloid Interface Sci.*, vol. 208, pp. 47–57, 2014, doi: 10.1016/j.cis.2014.02.002.

[6] R. Dimova, *The Giant Vesicle Book*. 2019.

[7] J. Pécréaux, H. G. Döbereiner, J. Prost, J. F. Joanny, and P. Bassereau, “Refined contour analysis of giant unilamellar vesicles,” *Eur. Phys. J. E*, vol. 13, no. 3, pp. 277–290, 2004, doi: 10.1140/epje/i2004-10001-9.

[8] D. Marsh, “Elastic curvature constants of lipid monolayers and bilayers,” *Chem. Phys. Lipids*, vol. 144, no. 2, pp. 146–159, 2006, doi: 10.1016/j.chemphyslip.2006.08.004.

[9] L. Fernandez-Puente, I. Bivas, M. D. Mitov, and P. Méléard, “Temperature and chain length effects on bending elasticity of phosphatidylcholine bilayers,” *Epl*, vol. 28, no. 3, pp. 181–186, 1994, doi: 10.1209/0295-5075/28/3/005.

[10] G. Pabst, N. Kučerka, M. P. Nieh, M. C. Rheinstädter, and J. Katsaras, “Applications of neutron and X-ray scattering to the study of biologically relevant model membranes,” *Chem. Phys. Lipids*, vol. 163, no. 6, pp. 460–479, 2010, doi: 10.1016/j.chemphyslip.2010.03.010.

[11] N. Chu, N. Kučerka, Y. Liu, S. Tristram-Nagle, and J. F. Nagle, “Anomalous swelling of lipid bilayer stacks is caused by softening of the bending modulus,” *Phys. Rev. E - Stat. Nonlinear, Soft Matter Phys.*, vol. 71, no. 4, pp. 1–8, 2005, doi: 10.1103/PhysRevE.71.041904.

[12] H. I. Petrache, N. Gouliaev, S. Tristram-Nagle, R. Zhang, R. M. Suter, and J. F. Nagle, “Interbilayer Interactions: High Resolution X-ray Study,” *Phys. Rev. E*, vol. 57, no. 6, pp. 7014–7024, 1998.

[13] M. C. Rheinstädter, W. Häußler, and T. Salditt, “Dispersion relation of lipid membrane shape fluctuations by neutron spin-echo spectrometry,” *Phys. Rev. Lett.*, vol. 97, no. 4, pp. 1–4, 2006, doi: 10.1103/PhysRevLett.97.048103.

[14] D. Cuvelier, I. Derényi, P. Bassereau, and P. Nassoy, “Coalescence of membrane tethers: Experiments, theory, and applications,” *Biophys. J.*, vol. 88, no. 4, pp. 2714–2726, 2005, doi: 10.1529/biophysj.104.056473.

[15] G. Niggemann, M. Kummrow, and W. Helfrich, “The Bending Rigidity of Phosphatidylcholine

Bilayers: Dependences on Experimental Method, Sample Cell Sealing and Temperature," *J. Phys. II*, vol. 5, no. 3, pp. 413–425, 1995, doi: 10.1051/jp2:1995141.

[16] O. Sandre, C. Ménager, J. Prost, V. Cabuil, J. C. Bacri, and A. Cebers, "Shape transitions of giant liposomes induced by an anisotropic spontaneous curvature," *Phys. Rev. E - Stat. Physics, Plasmas, Fluids, Relat. Interdiscip. Top.*, vol. 62, no. 3 B, pp. 3865–3870, 2000, doi: 10.1103/PhysRevE.62.3865.

[17] D. Bochicchio and L. Monticelli, "The membrane bending modulus in experiments and simulations: A puzzling picture," *Adv. Biomembr. Lipid Self-Assembly*, vol. 23, no. April, pp. 117–143, 2016, doi: 10.1016/bs.abl.2016.01.003.

[18] B. González-Bermúdez, G. V. Guinea, and G. R. Plaza, "Advances in Micropipette Aspiration: Applications in Cell Biomechanics, Models, and Extended Studies," *Biophys. J.*, vol. 116, no. 4, pp. 587–594, 2019, doi: 10.1016/j.bpj.2019.01.004.

[19] K. Guevorkian and J. L. Maître, "Micropipette aspiration: A unique tool for exploring cell and tissue mechanics in vivo," *Methods Cell Biol.*, vol. 139, pp. 187–201, 2017, doi: 10.1016/bs.mcb.2016.11.012.

[20] R. S. Gracià, N. Bezlyepkina, R. L. Knorr, R. Lipowsky, and R. Dimova, "Effect of cholesterol on the rigidity of saturated and unsaturated membranes: Fluctuation and electrodeformation analysis of giant vesicles," *Soft Matter*, vol. 6, no. 7, pp. 1472–1482, 2010, doi: 10.1039/b920629a.

[21] M. L. Longo and H. V. Ly, "Micropipet aspiration for measuring elastic properties of lipid bilayers," *Methods Mol. Biol.*, vol. 400, no. 6, pp. 421–437, 2007, doi: 10.1385/1-59745-519-9:421.

[22] R. Kwok and E. Evans, "Thermoelasticity of large lecithin bilayer vesicles," *Biophys. J.*, vol. 35, no. 3, pp. 637–652, 1981, doi: 10.1016/S0006-3495(81)84817-5.

[23] W. Plesiewicz, "Entropy-Driven tension and bending," *Phys. Rev. Lett.*, vol. 56, no. January, pp. 2419–2422, 1986, doi: 10.1103/PhysRevLett.3.32.

[24] W. Rawicz, K. C. Olbrich, T. McIntosh, D. Needham, and E. A. Evans, "Effect of chain length and unsaturation on elasticity of lipid bilayers," *Biophys. J.*, vol. 79, no. 1, pp. 328–339, 2000, doi: 10.1016/S0006-3495(00)76295-3.

[25] L. Lu, W. J. Doak, J. W. Schertzer, and P. R. Chiarot, "Membrane mechanical properties of synthetic asymmetric phospholipid vesicles," *Soft Matter*, vol. 12, no. 36, pp. 7521–7528, 2016, doi: 10.1039/c6sm01349j.

[26] W. Rawicz, B. A. Smith, T. J. McIntosh, S. A. Simon, and E. Evans, "Elasticity, strength, and water permeability of bilayers that contain raft microdomain-forming lipids," *Biophys. J.*, vol. 94, no. 12, pp. 4725–4736, 2008, doi: 10.1529/biophysj.107.121731.

[27] D. Chen and M. M. Santore, "Hybrid copolymer-phospholipid vesicles: Phase separation resembling mixed phospholipid lamellae, but with mechanical stability and control," *Soft Matter*, vol. 11, no. 13, pp. 2617–2626, 2015, doi: 10.1039/c4sm02502d.

[28] V. Vitkova, J. Genova, M. D. Mitov, and I. Bivas, “Sugars in the aqueous phase change the mechanical properties of lipid mono- and bilayers,” *Mol. Cryst. Liq. Cryst.*, vol. 449, no. 1, pp. 95–106, 2006, doi: 10.1080/15421400600582515.

[29] K. Olbrich, W. Rawicz, D. Needham, and E. Evans, “Water permeability and mechanical strength of polyunsaturated lipid bilayers,” *Biophys. J.*, vol. 79, no. 1, pp. 321–327, 2000, doi: 10.1016/S0006-3495(00)76294-1.

[30] A. Mahendra, H. P. James, and S. Jadhav, “PEG-grafted phospholipids in vesicles: Effect of PEG chain length and concentration on mechanical properties,” *Chem. Phys. Lipids*, vol. 218, no. July 2018, pp. 47–56, 2019, doi: 10.1016/j.chemphyslip.2018.12.001.

[31] J. F. Nagle, “Introductory lecture: Basic quantities in model biomembranes,” *Faraday Discuss.*, vol. 161, pp. 11–29, 2012, doi: 10.1039/c2fd20121f.

[32] J. F. Nagle , "NIH Public Access,” *Bone*, vol. 185, pp. 3–10, 2015, doi:10.1016/j.chemphyslip.2014.04.003.

[33] P. Méléard *et al.*, “Bending elasticities of model membranes: Influences of temperature and sterol content,” *Biophys. J.*, vol. 72, no. 6, pp. 2616–2629, 1997, doi: 10.1016/S0006-3495(97)78905-7.

[34] R. Dimova, “Recent developments in the field of bending rigidity measurements on membranes,” *Adv. Colloid Interface Sci.*, vol. 208, pp. 225–234, 2014, doi: 10.1016/j.cis.2014.03.003.

[35] H. D. Andersen, C. Wang, L. Arleth, G. H. Peters, and P. Westh, “Reconciliation of opposing views on membrane-sugar interactions,” *Proc. Natl. Acad. Sci. U. S. A.*, vol. 108, no. 5, pp. 1874–1878, 2011, doi: 10.1073/pnas.1012516108.

[36] J. Genova, A. Zheliaskova, and M. D. Mitov, “The influence of sucrose on the elasticity of SOPC lipid membrane studied by the analysis of thermally induced shape fluctuations,” *Colloids Surfaces A Physicochem. Eng. Asp.*, vol. 282–283, pp. 420–422, 2006, doi: 10.1016/j.colsurfa.2005.11.065.

[37] H. Bouvrais, “Bending Rigidities of lipid bilayers : Their determination and main inputs un biophysical studies,” *Adv. Planar Lipid Bilayers Liposomes*, vol. 15, pp. 1–75, 2012.

[38] H. I. Petrache, S. Tristram-Nagle, D. Harries, N. Kuĉerka, J. F. Nagle, and V. A. Parsegian, “Swelling of phospholipids by monovalent salt,” *J. Lipid Res.*, vol. 47, no. 2, pp. 302–309, 2006, doi: 10.1194/jlr.M500401-JLR200.

[39] R. Dimova, “Giant Vesicles and Their Use in Assays for Assessing Membrane Phase State, Curvature, Mechanics, and Electrical Properties,” *Annu. Rev. Biophys.*, vol. 48, pp. 93–119, 2019, doi: 10.1146/annurev-biophys-052118-115342.

[40] O. G. Mouritsen and M. J. Zuckermann, “Mouritsen_Zuckermann_2004,” vol. 39, no. 11, pp. 1101–1113, 2004.

[41] B. Group, “Lipid Bilayers : Modulation,” vol. 51, pp. 945–961, 1990.

[42] J. Henriksen *et al.*, “Universal behavior of membranes with sterols,” *Biophys. J.*, vol. 90, no. 5,

pp. 1639–1649, 2006, doi: 10.1529/biophysj.105.067652.

[43] J. Song and R. E. Waugh, "Bending rigidity of SOPC membranes containing cholesterol," *Biophys. J.*, vol. 64, no. 6, pp. 1967–1970, 1993, doi: 10.1016/S0006-3495(93)81566-2.

[44] D. Needham and R. S. Nunn, "Elastic deformation and failure of lipid bilayer membranes containing cholesterol," *Biophys. J.*, vol. 58, no. 4, pp. 997–1009, 1990, doi: 10.1016/S0006-3495(90)82444-9.

[45] J. Pan, S. Tristram-Nagle, and J. F. Nagle, "Effect of cholesterol on structural and mechanical properties of membranes depends on lipid chain saturation," *Phys. Rev. E - Stat. Nonlinear, Soft Matter Phys.*, vol. 80, no. 2, pp. 1–12, 2009, doi: 10.1103/PhysRevE.80.021931.

[46] and K. C. M. Mhatre V. Ho, Ji-Ann Lee, "NIH Public Access," *Bone*, vol. 23, no. 1, pp. 1–7, 2012, doi: 10.1038/jid.2014.371.

[47] P. Lakshmi, S. Bhaskaran, and C. Saroja, "Recent trends in vaccine delivery systems: A review," *Int. J. Pharm. Investig.*, vol. 1, no. 2, p. 64, 2011, doi: 10.4103/2230-973x.82384.

[48] F. Meng, R. Cheng, C. Deng, and Z. Zhong, "Intracellular drug release nanosystems," *Mater. Today*, vol. 15, no. 10, pp. 436–442, 2012, doi: 10.1016/S1369-7021(12)70195-5.

[49] J. W. Yoo, D. J. Irvine, D. E. Discher, and S. Mitragotri, "Bio-inspired, bioengineered and biomimetic drug delivery carriers," *Nat. Rev. Drug Discov.*, vol. 10, no. 7, pp. 521–535, 2011, doi: 10.1038/nrd3499.

[50] E. M. Curtis, A. H. Bahrami, T. R. Weikl, and C. K. Hall, "Modeling nanoparticle wrapping or translocation in bilayer membranes," *Nanoscale*, vol. 7, no. 34, pp. 14505–14514, 2015, doi: 10.1039/c5nr02255j.

[51] K. Yang and Y. Q. Ma, "Computer simulation of the translocation of nanoparticles with different shapes across a lipid bilayer," *Nat. Nanotechnol.*, vol. 5, no. 8, pp. 579–583, 2010, doi: 10.1038/nnano.2010.141.

[52] K. A. Smith, D. Jasnow, and A. C. Balazs, "Designing synthetic vesicles that engulf nanoscopic particles," *J. Chem. Phys.*, vol. 127, no. 8, pp. 0–10, 2007, doi: 10.1063/1.2766953.

[53] A. Albanese, P. S. Tang, and W. C. W. Chan, "The effect of nanoparticle size, shape, and surface chemistry on biological systems," *Annu. Rev. Biomed. Eng.*, vol. 14, no. April 2012, pp. 1–16, 2012, doi: 10.1146/annurev-bioeng-071811-150124.

[54] L. Shang, K. Nienhaus, and G. U. Nienhaus, "Engineered nanoparticles interacting with cells: Size matters," *J. Nanobiotechnology*, vol. 12, no. 1, pp. 1–11, 2014, doi: 10.1186/1477-3155-12-5.

[55] R. Lipowsky, "Spontaneous tubulation of membranes and vesicles reveals membrane tension generated by spontaneous curvature," *Faraday Discuss.*, vol. 161, no. October, pp. 305–331, 2012, doi: 10.1039/c2fd20105d.

[56] J. Liu *et al.*, "Influence of surface chemistry on particle internalization into giant unilamellar vesicles," *Langmuir*, vol. 29, no. 25, pp. 8039–8045, 2013, doi: 10.1021/la4015652.

[57] Y. Guo, E. Terazzi, R. Seemann, J. B. Fleury, and V. A. Baulin, "Direct proof of spontaneous translocation of lipid-covered Hydrophobic nanoparticles through a phospholipid bilayer," *Sci. Adv.*, vol. 2, no. 11, pp. 38–40, 2016, doi: 10.1126/sciadv.1600261.

[58] B. D. Chithrani, A. A. Ghazani, and W. C. W. Chan, "Determining the size and shape dependence of gold nanoparticle uptake into mammalian cells," *Nano Lett.*, vol. 6, no. 4, pp. 662–668, 2006, doi: 10.1021/nl052396o.

[59] The European Medicines Agency - EMA, "Caelyx Anexo I: Ficha tecnica o resumen de las caracteristicas del producto 1," *Agencia Eur. Medicam.*, pp. 1–33, 2006, [Online]. Available: https://www.ema.europa.eu/en/documents/product-information/zerbaxa-epar-product-information_es.pdf.

[60] A. Verma and F. Stellacci, "Effect of surface properties on nanoparticle-cell interactions," *Small*, vol. 6, no. 1, pp. 12–21, 2010, doi: 10.1002/smll.200901158.

[61] Y. S. Chen, Y. C. Hung, W. H. Lin, and G. S. Huang, "Assessment of gold nanoparticles as a size-dependent vaccine carrier for enhancing the antibody response against synthetic foot-and-mouth disease virus peptide," *Nanotechnology*, vol. 21, no. 19, 2010, doi: 10.1088/0957-4484/21/19/195101.

[62] A. F. Versiani *et al.*, "Gold nanoparticles and their applications in biomedicine," *Future Virol.*, vol. 11, no. 4, pp. 293–309, 2016, doi: 10.2217/fvl-2015-0010.

[63] S. H. Park, S. G. Oh, J. Y. Mun, and S. S. Han, "Loading of gold nanoparticles inside the DPPC bilayers of liposome and their effects on membrane fluidities," *Colloids Surfaces B Biointerfaces*, vol. 48, no. 2, pp. 112–118, 2006, doi: 10.1016/j.colsurfb.2006.01.006.

[64] S. Chakraborty, A. Abbasi, G. D. Bothun, M. Nagao, and C. L. Kitchens, "Phospholipid Bilayer Softening Due to Hydrophobic Gold Nanoparticle Inclusions," *Langmuir*, vol. 34, no. 44, pp. 13416–13425, 2018, doi: 10.1021/acs.langmuir.8b02553.

[65] C. Montis, D. Maiolo, I. Alessandri, P. Bergese, and D. Berti, "Interaction of nanoparticles with lipid membranes: a multiscale perspective," *Nanoscale*, vol. 6, no. 12, pp. 6452–6457, 2014, doi: 10.1039/C4NR00838C.

[66] F. Wang, D. E. Curry, and J. Liu, "Driving Adsorbed Gold Nanoparticle Assembly by Merging Lipid Gel/Fluid Interfaces," *Langmuir*, vol. 31, no. 49, pp. 13271–13274, 2015, doi: 10.1021/acs.langmuir.5b03606.

[67] A. Mecke, D. K. Lee, A. Ramamoorthy, B. G. Orr, and M. M. B. Holl, "Synthetic and natural polycationic polymer nanoparticles interact selectively with fluid-phase domains of DMPC lipid bilayers," *Langmuir*, vol. 21, no. 19, pp. 8588–8590, 2005, doi: 10.1021/la051800w.

[68] M. Demazeau, L. Gibot, A. F. Mingotaud, P. Vicendo, C. Roux, and B. Lonetti, "Rational design of block copolymer self-assemblies in photodynamic therapy," *Beilstein J. Nanotechnol.*, vol. 11, pp. 180–212, 2020, doi: 10.3762/bjnano.11.15.

[69] L. Gibot *et al.*, "Role of polymer micelles in the delivery of photodynamic therapy agent to liposomes and cells," *Cancers (Basel).*, vol. 12, no. 2, pp. 1–22, 2020, doi: 10.3390/cancers12020384.

[70] B. Wang, L. Zhang, C. B. Sung, and S. Granick, “Nanoparticle-induced surface reconstruction of phospholipid membranes,” *Proc. Natl. Acad. Sci. U. S. A.*, vol. 105, no. 47, pp. 18171–18175, 2008, doi: 10.1073/pnas.0807296105.

[71] S. A. Love, M. A. Maurer-Jones, J. W. Thompson, Y. S. Lin, and C. L. Haynes, “Assessing nanoparticle toxicity,” *Annu. Rev. Anal. Chem.*, vol. 5, no. March, pp. 181–205, 2012, doi: 10.1146/annurev-anchem-062011-143134.

[72] Y. Pan *et al.*, “Size-dependent cytotoxicity of gold nanoparticles,” *Small*, vol. 3, no. 11, pp. 1941–1949, 2007, doi: 10.1002/smll.200700378.

Chapter III

3 Microfluidics: a tool to manipulate biomimetic membranes

By definition, microfluidics is the science of manipulating and controlling fluids in the range of picoliters (10^{-12}L) to microliters (10^{-6} L) in networks of channels with dimensions ranging from tens to hundreds of micrometers. Microfluidics first started in 1990s, as application for molecular analysis and has grown exponentially ever since, to be involved in more applications. Cosmetics (emulsions and formulations), pharmaceuticals (drug discovery), health (personalized medicine and diagnosis), chemistry (flow synthesis and screening assays), biology (cell culture and 3D printing) and finally energy (for example micromodels made to represent a micro version of saturated rock with crude oil, for enhanced oil recovery or EOR) benefit from the wide range of applications of microfluidics. The reasons for the use of microfluidics for all these applications are countless but most importantly: the ability to handle small volumes and low reagent consumptions, for example when working with DNA present in a small quantity of volume. Secondly, the analyses go faster and with high resolution and sensitivity due to the shorter reactions/separations time. Finally, these techniques are low cost, not only in their fabrication, but thanks to the reduction of heavy and expensive instruments which can be replaced by microfluidics chips. The scientific and technological interest in the field of microfluidics has led to new concepts called lab-on-chip systems, which involve developing entire bio/chemical laboratories on the surface of silicon or polymers surfaces in miniaturized devices.

In this chapter, I will introduce some of the basic concepts in microfluidic flows, such as the Reynolds number and the laminar flow and how to calculate the hydraulic resistance by tuning the dimensions of microfluidic channels to impose a flow repartition. Secondly, I will give an overview on the different fabrication processes and materials, enabling to obtain a functional microfluidic chip. Moreover, I will discuss how microfluidics has been used as a tool to fabricate Giant unilamellar vesicles and to characterize membranes properties such as the permeability and the shear effect. Finally, I will present how microfluidic chips have been successful platforms to trap single or multiple vesicles to perform particle - lipid and protein - lipid interaction and combined with model membranes they present a promising tool for drug screening assays.

3.1 Basic concepts in microfluidics

Navier – Stokes equation describes how a fluid flows through its environment. It describes how the spatio-temporal evolution of the velocity field $\mathbf{v}$ (bold notation for vectors) is related to forces. In the absence of external forces apart from pressure gradients, it reads for a Newtonian fluid:

$$\rho \frac{\partial \boldsymbol{v}}{\partial t} = -\rho(\boldsymbol{v}.\boldsymbol{\nabla})\boldsymbol{v} - \boldsymbol{\nabla}P + \eta\Delta\boldsymbol{v} \qquad 3\text{-}1$$

With ρ the mass density, η the dynamic viscosity, P the pressure.

In general, Navier – Stokes equations are used by biomedical researches to model for example how the blood flows through the body but also by petroleum engineers to reveal how oil is expected to flow through a pipeline. Even at the micron scale, a fluid can be seen as a continuum and Navier-Stokes equation is still applicable. Since inertia can be neglected with respect to viscous effects, analytical solutions of these equations for an incompressible Newtonian fluid can be computed, which leads to the useful concept of hydraulic resistance.

3.1.1 Reynolds number and laminar flow

Microfluidics concerns the manipulation of small volumes of microfluidics within networks of channels that have dimensions of tens to hundreds of micrometers. When scaling down to these dimensions, the inertial forces (linked to the velocity) become negligible compared to the friction forces (linked to the viscosity of the liquid). As the inertial forces are the cause for creating turbulences, at small dimensions (microfluidics) the flow regime is laminar [1]. The ratio of inertial forces and viscous forces, computed from equation ***3-1,*** defines Reynolds number *Re*. Reynolds number characterizes the type of flow regime and depends of the geometry of the channel ***(Figure III-1)*** [2]: if *Re* > 2300 , the inertial forces are dominant, and the flow is turbulent. If *Re* < 2000, the flow is laminar [3].

In the case of microfluidics, *Re* <<1, so that viscous forces are dominant. Reynolds number is a dimensionless number and is given by the following formula:

$$Re = \frac{\rho V L}{\eta} \qquad 3\text{-}2$$

Where ρ is the liquid density, V is the characteristic speed of the fluid, L is the typical length of the flow and η is the dynamic viscosity of the fluid. In microfluidics and if we take the example of water, the parameters are the following: $\eta = 10^{-3}$*Pa.s,* $\rho = 1000$*Kg* m^{-3}*,* $1 < L < 500$ *µm and* $0.1 < V < 1$*mm* s^{-1}*.* It gives an order of magnitude of Reynolds number in a laminar flow: $0.0001 < Re < 0.5$. In microfluidics, the flow velocities are much smaller than the velocity of pressure waves (sound) in the liquid, therefore the fluid can be treated as being incompressible [4]. The volume of an incompressible fluid does not change (or the change is very tiny) and its density is treated as a constant.

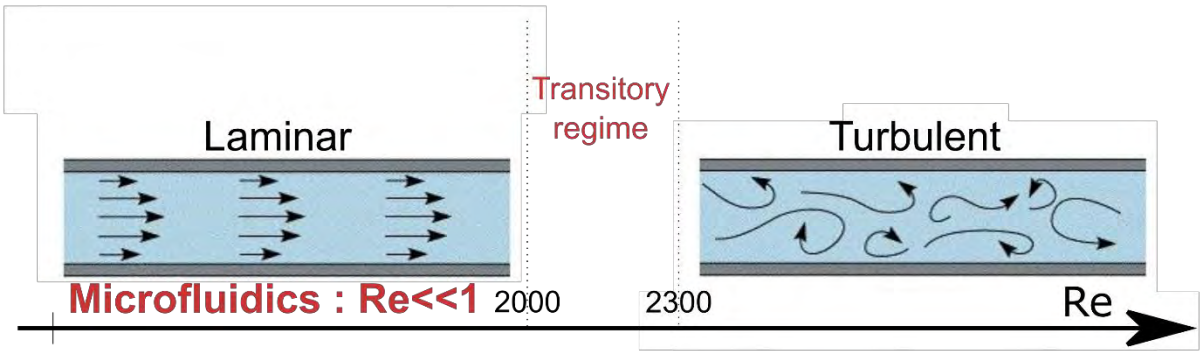

Figure III-1: Comparison of turbulent flow (dominated by inertial forces) and the laminar flow where the surface forces are dominant. Reynolds number is lower than 2000 for laminar flow and higher than 2300 for turbulent flow. In between these values, there is a transitory regime. [2]

3.1.2 Hydraulic Resistance in microfluidic channels

As a liquid flows through a microchannel, energy is lost because of friction between the surface of the channel and liquid, and because of interactions between the liquid molecules [3]. The frictional lost energy is referred to as pressure drops.

The analytical solution for Navier - Stokes equations of a laminar viscous flow corresponds to the Poiseuille flow, where the flow inside an infinitely long invariant channel is pressure-driven with a steady state flow.

For low Reynolds number, and in such a steady state, the equation reduces to the linear stokes equation:

$$\boldsymbol{\nabla} p = \eta \Delta \boldsymbol{v} \qquad 3\text{-}3$$

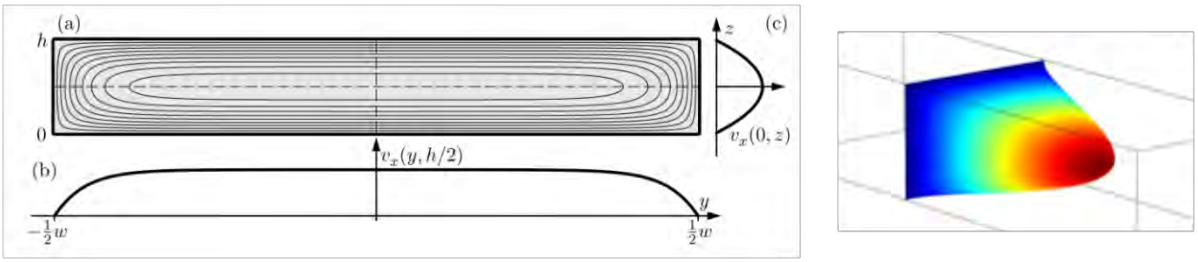

Figure III-2: Scheme of the Poiseuille flow in a rectangular shape cross section channel. a) Contour lines for the velocity field $v_x(y,z)$. b) Plot of $v_x(y, h/2)$ along the center line parallel to e_y. c) plot of $v_x(0,z)$ along the short center-line parallel to e_z.[5] *On the left is a Comsol simulation of the flow profile in a Poiseuille flow .The profile of the flow is parabolic along the smallest dimension: the speed is the highest in the center of the channel and the lowest (almost negligible) at the borders, close the walls of the channel.*

Micro channels can have different shape of cross sections depending on the different methods of fabrication. The analytical solution of the linear Stokes equations can be solved for a rectangular cross section shape of the Poiseuille flow, corresponding to very common microfluidic platforms (chapter IV) ***(Figure III-2).***

In such a rectangular channel, the pressure decreases linearly along the channel, and the resulting velocity field is defined by the following : $-\frac{1}{2}w < y < -\frac{1}{2}w$ and $0 < \mathrm{z} < \mathrm{h}$

$$v_x(y,z) = \frac{4h^2\Delta P}{\pi^3 \eta L}\sum_n^{\infty}\frac{1}{n^3}\left[1 - \frac{cosh\,(n\pi\frac{y}{h})}{cosh\left(n\pi\frac{w}{2h}\right)}\right] sin\,(n\pi\frac{z}{h}) \qquad 3\text{-}4$$

The volumetric flow rate (Q) is defined as the fluid volume discharged by the channel per unit time. By determining the velocity for a rectangular cross section*:*

$$Q = \int dydz v_x(y,z) \qquad 3\text{-}5$$

$$Q = \frac{4h^2\Delta P}{\pi^3 \eta L}\sum_n^{\infty}\frac{1}{n^3}\frac{2h}{n\pi}\left[w - \frac{2h}{n\pi}tanh\,(n\pi\frac{w}{2h})\right] \qquad 3\text{-}6$$

for a flat and very wide channel, approximation results can be obtained in the limit $\frac{h}{w} \to 0$, where $\frac{h}{w}\tan(\mathrm{n}\pi\frac{w}{2h}) \to \frac{h}{w}\tan h(\infty) = \frac{h}{w}$ and Q becomes:

$$Q \approx [1 - 0.630\frac{h}{w}]\frac{h^3 w}{12\eta L}\Delta P \qquad 3\text{-}7$$

Equation ***3-7*** relates the pressure drops in the channel and the steady state flow rate in a rectangular cross section microfluidic channel.

Since Stokes equation is linear, the pressure driven, steady-state flow of an incompressible Newtonian fluid, links the pressure drops in a microfluidic channel to the flow rate by the following general equation:

$$\Delta P = R_{hyd}Q = \frac{1}{G_{hyd}}Q \qquad 3\text{-}8$$

Where R_{hyd} is the hydraulic resistance, the inverse of G_{hyd}, the hydraulic conductance in a microfluidic channel. Hydraulic resistance is defined as the resistance of a fluid to flow through channels of specific dimensions. Therefore, it depends on the dimensions of the channels and specially the cross-section shape and the viscosity of the fluid. Hydraulic resistance is very important when characterizing and designing microfluidic channels in any lab-on-chip system. However, depending on the fabrication techniques, not all the shapes are feasible or accessible. ***Table III-1*** presents some of the different hydraulic resistance expression and values for different cross-sections shapes, and typical microchannel's length *L*, using the viscosity of water.

Table III-1 : List of the hydraulic resistance for straight channels with different cross section shapes. The numerical values corresponds to η = 1mPas (viscosity of water), L = 1mm, a = 100µm, b = 33µm, h = 100µm and w = 300µm [4].

Shape		R_{hyd} expression	$R_{hyd}\ 10^{11}\ [\frac{Pas}{m^3}]$
Circle		$\frac{8}{\pi}\eta L\frac{1}{a^4}$	0.25
Ellipse		$\frac{4}{\pi}\eta L\frac{1+\left(\frac{b}{a}\right)^2}{\left(\frac{b}{a}\right)^3}\frac{1}{a^4}$	3.93
Triangle		$\frac{320}{\sqrt{3}}\eta L\frac{1}{a^4}$	18.5
Two plates		$12\eta L\frac{1}{h^3 w}$	0.4
Rectangle		$\frac{12\eta L}{1-0.63(\frac{h}{w})}\frac{1}{h^3 w}$	0.51
Square	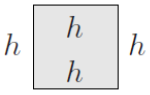	$28.4\eta L\frac{1}{h^4}$	2.84
Parabola		$\frac{105}{4}\eta L\frac{1}{h^3 w}$	0.88
Arbitrary		$\approx 2\eta L\frac{\mathcal{P}^2}{\mathcal{A}^3}$	-

3.1.3 Analogy between electrical resistance and hydraulic resistance

Microfluidic chips can contain several micro channels, which are connected in parallel or in series or even a mix of both, depending on the application needed. Therefore, it can be complicated to keep track of the exact values of pressure or flow in the channels, especially if it is needed to be controlled at all time. Hence, an analogy between the electrical resistance and the hydraulic one is made, to facilitate the calculations. In fact, Ohm's law relates the electrical potential drop ΔV to the electrical current I in a wire, by its electrical resistance R: $\Delta \boldsymbol{V} = \boldsymbol{RI}$. Same as in Poiseuille law, the pressure drop ΔP is related to the flow rate Q, by its hydraulic resistance R : $\Delta \boldsymbol{P} = \boldsymbol{RQ}$ [5]. In fact, the flow is similar to the flux of electrons in an electrical circuit and the pressure drop is similar to the electrical potential drop.

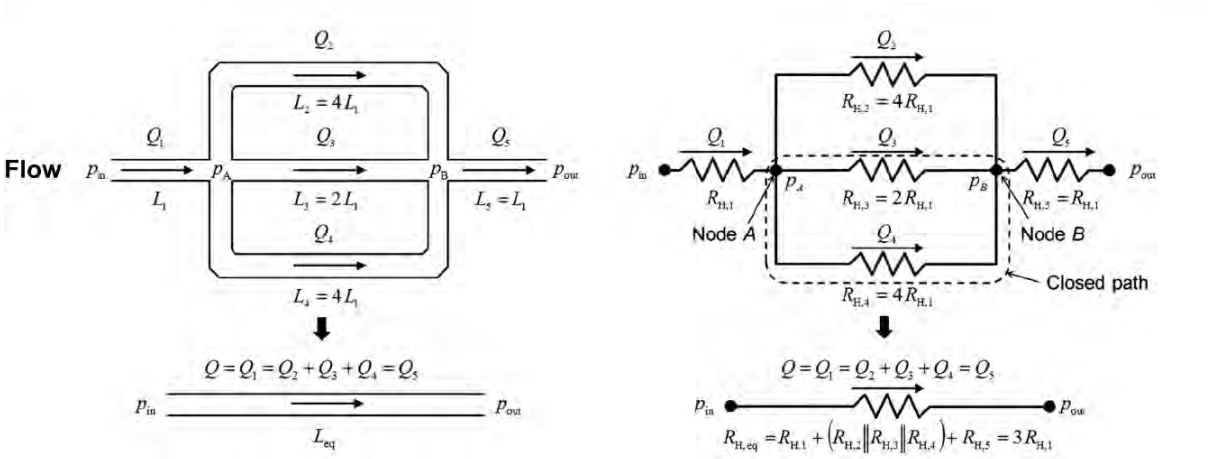

Figure III-3 : A simple microfluidic network connected with different channel lengths, but with the same cross-sectional area and shape and its equivalent electrical circuit with fluidic resistors and an equivalent single fluidic resistor [6]

For a more generic microfluidic network, Kirchhoff's laws apply ***(Figure III-3)*** [6]:

- The sum of the flows into a node should be equal to the sum of the flows leaving the node. Therefore, the mass conservation at a node is:

$$\sum_{n=1}^{N} Q_n = 0 \qquad 3\text{-}9$$

- The energy required to move a charge from X to Y in a circuit is independent from the path chosen. The pressure drop relation for energy conservation in a closed path is:

$$\sum_{n=1}^{N} \Delta P_n = 0 \qquad 3\text{-}10$$

Following this analogy, hydraulic resistances in a network of micro channels obey the same rules for series and parallel coupling as the electrical resistances in linear circuit theory [7]. Therefore, for two hydraulic resistance R_1 and R_2 we have:

$$R_{hyd}^{series} = R_1 + R_2 \qquad 3\text{-}11$$

$$R_{Hyd}^{parallel} = \left(\frac{1}{R_1} + \frac{1}{R_2}\right)^{-1} \qquad 3\text{-}12$$

For a pressure division across a channel network of N series fluidic channels[6]:

$$\Delta P_n = \frac{R_{H,n}}{R_{H,1} + R_{H,2} + \cdots + R_{H,n}} \Delta P_s = \frac{R_{H,n}}{R_{H,equ}} \Delta P_s \qquad 3\text{-}13$$

Equation ***3-13*** allows us to compute the pressure drop that appears across an arbitrary n^{th} fluidic channel of the series. With this computation, we can identify the pathways of the flow as it is driven

through the least fluidic resistance. Fluidics cannot go through dead-end channels due to their infinite hydraulic resistance. The use of pressure and flow division method provides intuitive and practical ideas for configuring segments of channel networks in the design of complex microfluidic systems.
These equations facilitate the design and the optimizations of channels within a microfluidic chip. In fact, as seen in the previous chapter (mechanics of membranes), in order to extract the membranes tension of a GUV, it is necessary to know the pressure applied on the object as they are related by Laplace law. Therefore, by following the analogy made in this paragraph, we can compute the pressure applied on the object directly from the initial pressure applied in the chip. This will be detailed in chapter IV.

3.2 Microfluidic chips: from a concept to the realization

3.2.1 An overview of microfluidic devices: materials, fabrication techniques

The development of microfluidic devices has emerged historically from four different main subjects: molecular analysis, biodefense, molecular biology and microelectronics [8]. Microelectronic fabrication techniques, such as the lithography and associated technologies that had been successful in silicon microelectronics and MEMS, were to be directly applicable to microfluidics. Indeed, the first fluidic platforms were done in silicon and glass chips [9]. Over the years, more materials were to be used such as thermoplastic materials using hot embossing technique such as: Polystyrene (PS), polyvinyl chloride (PVC), polymethylmethacrylate (PMMA), cyclic olefin copolymer (COC) and polycarbonate (PC). Thermoplastics are cross-linked polymers that can be remolded many times after being cured by reaching glass transition temperature and that can retain their shape after cooling. Hot embossing of plastic parts uses a mold of micro channels, usually made in metal, glass, silicon or even PDMS [10]. The mold and the thermoplastic material are then sandwiched together with a pressure applied on the sandwich and put under high temperature to ensure the replication of the structures onto the material.
Depending on the application needed, it is sometimes required to have physiological environment conserved in the microfluidic device. For example, when working with cells, exchange of gases and control of temperature is indispensable. Moreover, in micro analytical applications, the presence of pumps and valves are necessary. Hence, silicon/glass, plastic or in general rigid materials are less likely to be used. Polydimethylsiloxane (PDMS), is a silicon based organic polymer that was introduced in 1996 for the fabrication of optical devices [11]. Since then, PDMS has been widely used especially in microfluidic devices [12], [13]. It is a powerful material offering several advantages; it's cheap compared to glass and silicon wafers, it is optically transparent contrary to silicon which is opaque, and finally, it is cell-culture compatible, which means it offers a good environment for cellular

manipulation in microfluidics. Nonetheless, some applications are more complicated than others and PDMS couldn't answer all needs. New techniques were developed that allows the fabrication of multilayer chips using Dry Films technologies [14]. And finally, 3D printing technologies allowed fast and functional three dimensional microfluidic devices [15] although high resolutions are hard or very long to achieve .

All microfluidic chips undergo somewhat the same path of fabrication, from the idea to its realization: in order to target any biological or chemical question, a microfluidic chip purpose is to bring a solution. Then, a mask is designed containing all the necessary micro patterns to obtain the full chips. Depending on the device and the fabrication techniques, several masks may be needed to obtain different parts of the chip. The conception of the masks could be done in 2D for lithography techniques of fabrication, or directly in 3D, if stereolithography techniques are used to fabricate the chip. The next step would be the printing of the mask (for lithography techniques), on glass support or transparent plastic sheet. Then with the lithography technique, the design is transferred on a substrate (silicon, glass…). From this step forward, many other steps might be needed in order to reach a complete function microfluidic chip.
Lithography is the process of transferring a pattern from a master into a substrate (glass, silicon…) containing a transfer layer: the resist [16]. Lithography techniques are divided depending on the kind of energy beam used to illuminate the resist : photolithography, electron beam lithography, X-ray lithography, ion beam lithography, I-line lithography, and deep UV lithography [1]. The most common technique is the photolithography.

After explaining the photolithography process, I will go through the basics of the most used materials and fabrication techniques to generate microfluidic chips.

3.2.2 Photolithography: main process of fabrication

Photolithography is the common process between all the fabrication techniques. It involves the transfer of a pattern into a pattern transfer layer which is the resist [16]. The resist layer is sensitive to UV light and it is deposited on the substrate needed, by different methods: spin coating or spray coating (if the resist is in a viscous liquid form), or lamination if the resist is in a film form. In the case of a liquid resist, the thickness of the resist is defined by the viscosity of the resist and the speed, acceleration and time of deposition of the resist on the wafer. If it is a film resist, the thickness is pre-defined by the thickness of the film. More often, photolithography is used to create a mold of micro patterns, which will be duplicated later with PDMS. Therefore, most of the cases, the wafer mold is in silicon. However, if the substrate were to be the final chip, glass is a better option for optical reasons

(this process will be explained in the coming chapters). As seen in the paragraph before, a mask with the patterns is needed.

3.2.2.1 Mask Fabrication

The mask fabrication consists in transferring the 2D design of the micro-channels on a transparent substrate, usually quartz or glass. The final material used to cover the glass or quartz substrate is Chrome, though the fabrication of the mask undergoes several steps. A thin layer (~ hundred nanometers) of Chrome is deposited on the substrate followed by another deposition of 500 nanometers of a protective photoresist. The resist is then exposed to a laser, which will define the patterns of the design. After developing the resist and removing the non-exposed part, the chrome part under the removed resist is now accessible. Chrome is then etched and removed, leaving a transparent part of the substrate to let the UV light pass through, during the photolithography process. This process is called the lift off process. Finally, the rest of the resist is removed leaving only the chrome as a non-transparent layer on the substrate. The lateral resolution of the laser lithography depends on the laser beam spot, and is around 0.5 µm.

3.2.2.2 Photolithography process

The process of creating a mold with a photoresist on a silicon wafer is shown in ***Figure III-4.*** Briefly, the resist deposited on the wafer goes through several steps [16]. First, a prebake step is required to remove all solvent present in the resist. Combining the UV light and the necessary tooling for holding and moving the mask in a precisely defined way against the substrate, first layer is patterned. Using the advanced optics of photolithography machines, it is possible to have a precise alignment of the mask and the wafer down to 1 µm, especially when multilayer with different thicknesses is needed during the fabrication. The photoresist contains a small amount of photoinitiators. When exposed to a UV light, the photoinitiator either cross-link (negative tone resist) and causes the hardening of the resist or undergo scission (positive tone resist). Another step of post bake is added to enhance the cross-linking between the molecules. Finally, the resist is developed to remove the unwanted part and leave the necessary patterns. Following this step, and depending on the final chip wanted, other steps can be added: to fabricate a PDMS chip, additional step of soft lithography is to be made. However, if the silicon or glass substrate are to be integrated within the chip, the wafers can undergo etching process, using the resist layer as a protective layer for the parts that are not to be etched. Detail of this process will come in the following chapters.

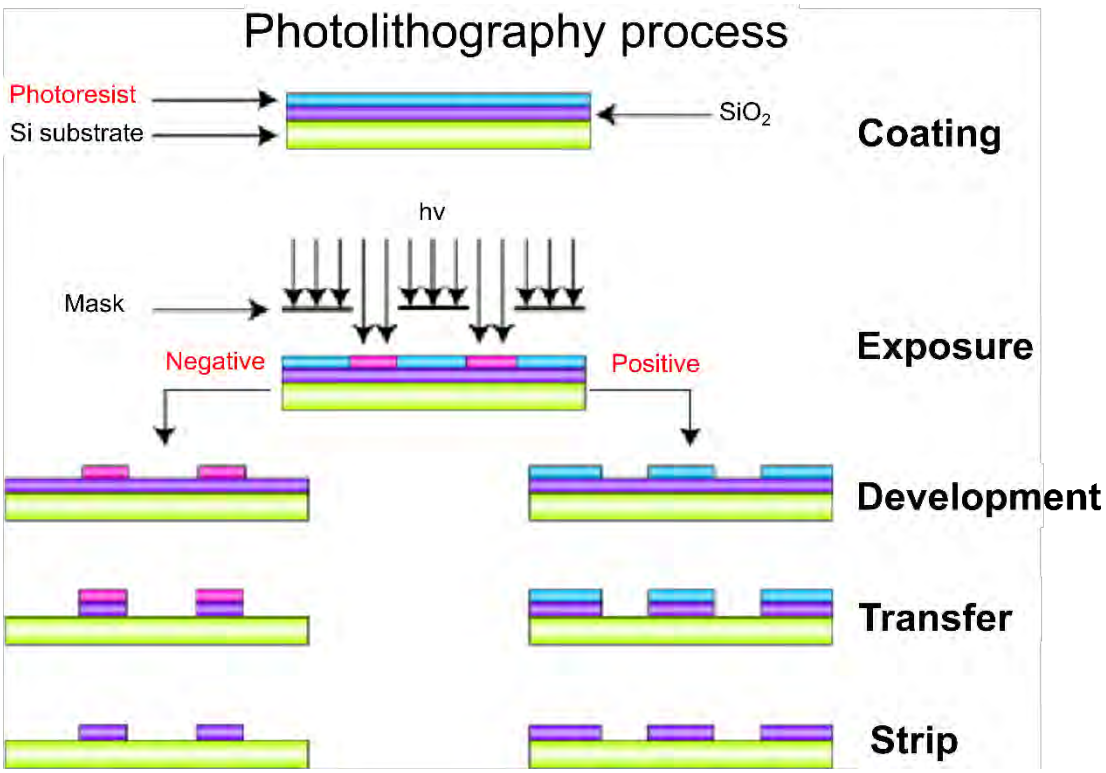

Figure III-4 :Cross view of the photolithography process : process of creating a mold on a silicon wafer with a positive and negative photoresist

3.2.3 Materials and fabrication techniques

3.2.3.1 Silicon – based method

Silicon based material was the first material used in microfluidics as it was the primary material used in electronics and MEMS (Micro Electro Mechanical Systems) also. Typical processes allow to selectively remove silicon material from the substrate and leave the needed part [1]. To do so, a protective layer of resist is deposited by the photolithography process, which conserves the parts that are not to be eliminated. This layer is to be removed by the end of the etching process. There are two ways to etch a silicon substrate: the wet and the dry etching. The wet etching relies on the use of chemicals to remove silicon parts by following its crystalline structure, therefore it is characterized as anisotropic process [17]. Dry etching relies on the use of gases, and does not depend on the crystalline structure of the silicon, and is characterized as isotropic process. More details about silicon etching are shown in chapter IV, with SEM pictures showing the results of etched micro channels. After etching and cleaning the silicon wafer, the wafer is bonded with a glass wafer (for optical reasons) to close the micro-channels.

3.2.3.2 Glass – based method

Glass is used in microfluidic chips because it is optically transparent, stable at high temperature, chemically and electrically resistive and biocompatible for medical and biological applications. The fabrication of the micro channels in glass substrate is very similar to the wet etching process of silicon wafers [18]. A protective photoresist layer is deposited by lithography process to cover the parts that are not to be removed. The channels are than chemically etched using a buffered oxide etch (BEO, made of ammonium fluoride and hydrofluoric acid). The protective layer of resist is then removed. Holes can be drilled in another glass wafer to allow the fluidic connections to the channels, and both glass wafers are aligned and bonded together. A downside of glass etching is that it creates rough surface rather than smooth which could be problematic in a lot of cases. In the clean room of LAAS, we developed a process of dry etching of glass substrate, followed by a wet etching process to smooth the rough surface. Details of this protocol is elaborated in chapter IV.

3.2.3.3 Polymer – based method: Soft Lithography

Polymer based microfluidic materials became widely used as they are cheaper than silicon and glass processes, and their process of fabrication can be easily adapted for mass production of microfluidic chips with no need of high level clean room environment. However, common steps between the methods mentioned before, such as the photolithography, are still required: a mold of micro channels made of photoresist is still needed, and made by photolithography. Soft lithography is one of the most common example of polymer-based methods and uses PDMS as an elastomeric polymer [19]. ***Figure III-5*** shows the process of fabricating PDMS chips, using a silicon mold made by photolithography. Briefly, liquid PDMS is poured on the mold of patterns, and cured in the oven. In this step, the patterns of resist produce open channels in the PDMS. The mold of PDMS is then peeled off the silicon mold and cut into small chips. To allow fluidic entrance and exit, the PDMS is then pierced with a puncher. And finally, PDMS pieces are bonded and sealed together with a glass substrate, using plasma bonding. In fact, after cleaning the PDMS and the glass substrate, they are both treated with oxygen or air plasma. Plasma treatment of PDMS and glass increases the expose to Silanol groups (-OH) at their surfaces so that they form strong covalent bonds (Si-O-Si) at the PDMS – Glass interface when they are brought together. This sealing is irreversible, and the two substrate are practically inseparable.

Many are the applications of PDMS microfluidic chips, however there is a big challenge when it comes to multilayering channels with hanging structures. *Cottet et al.,* were able to align and bond a PDMS chip with a glass electrode with an alignment of 50µm, using the optical mask aligner of the photolithography machines [20]. Nonetheless, this becomes more difficult if one of the substrate is not as rigid as glass, such as a thin layer of PDMS required for optical reasons. Or if the alignment

required is less than 50 µm. We also worked on developing new techniques to align and bond two PDMS chips, with a precision lower than 10 µm which will be elaborated in chapter IV.

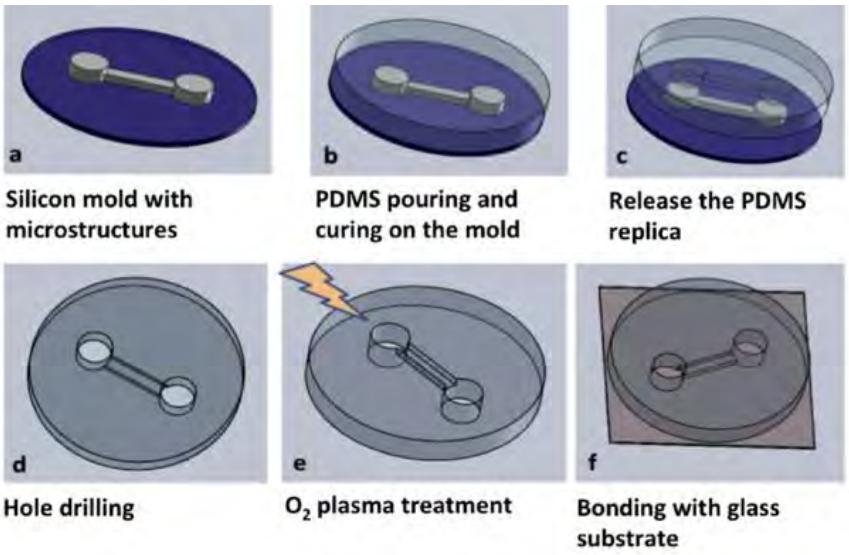

Figure III-5 : Process of PDMS microfluidic chip fabrication. a) A silicon mold made by photolithography is needed. b) PDMS is degassed and poured on the mold of the micro-channels. c) and d) PDMS is then cut and removed and holes of inlets and outlets are punched. e) and f) PDMS and glass substrate are treated with plasma O_2 and bonded together [21].

Microfluidic devices are widely used for Lab-on-a-Chip technologies [22] and micro total analysis systems (µTAS) [23]. Because of its ability to handle small volume and small objects, and the ability to control several parameters such as the pressure applied in a channel as seen in the previous paragraphs, microfluidics offered a great tool to fabricate and manipulate model membranes especially giant unilamellar vesicles.

3.3 Role of microfluidics in the manipulation of Giant unilamellar vesicles

Traditional methods of fabricating and handling Giant unilamellar vesicles (GUVs) can be complicated especially if targeting single membrane studies. Therefore, and due to the many advantages of microfluidics, manipulating such objects using micro channels can advance the studies of model membranes. Indeed, when using microfluidic chips, it is possible to easily change the environment around the GUVs and expose it to chemical stimulus (drugs, nanoparticles, proteins,…) to characterize their effect on the membrane. Due to microfluidics, it is also possible to either trap a single vesicle and study it, or even trap hundreds of them in different chambers and make parallel different experiment at the same time. Another important aspect is the control over pressure and flow and their effect on model membranes, which is something not easily achieved without microfluidic channels. And finally, it is even possible to create GUVs using microfluidic channels. The coming paragraphs will detail first the use of microfluidics to generate giant unilamellar vesicles, and then to characterize different properties of giant unilamellar vesicles.

3.3.1 Microfluidics to fabricate lipid membranes

In chapter I, I introduced some of the fabrication techniques to generate Giant unilamellar vesicles such as the swelling based method, and the method based on assembly from fluid interfaces. Each method presented different characteristics. Generating GUVs using microfluidics and capillarity are also other techniques which are based on droplet-transfer method through microchannels or microcapillary tubes and which can assure many aspects such as monodispersion of the size of the vesicles, and possibility to create asymmetric GUVs.

3.3.1.1 On chip fabrication of lipid bilayer

Ota et al., created a microfluidic technique to form multiple lipid membranes on micro chamber arrays to analyze the transport in membranes [24]. Using a PDMS chip with micro chamber arrays, the main chambers are first filled with a buffer solution to push the bubbles out of the porous PDMS. Then, the buffer solution is replaced with an organic solvent containing the lipids, which is not miscible with the buffer solution; the latter solution is trapped in the micro chamber, and a first monolayer is formed on the interface buffer/oil. A final buffer solution is used to flush the oil away, pushing the residual oil-containing lipids to self-assemble with the first monolayer, forming a bilayer lipid membrane ***(Figure III-6)***. Imaging of the membranes is done in Z axis, unlike previous works. This system relates to the water in oil droplets system seen in chapter I, without having an actual droplet form. The advantage of such method combines both bilayer membranes and microfluidics. The fabrication of lipid bilayer is directly integrated within the microfluidic chip, which allows at the same time to

perform study on it. However, this method only allows the formation of a symmetric bilayer membrane and it is a limited model of the cell membrane.

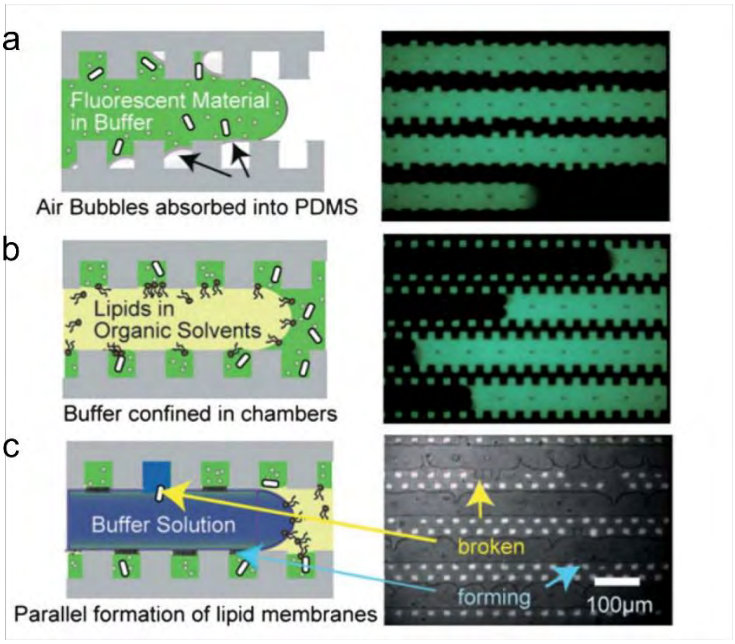

Figure III-6: Schematic procedure (left) and fluorescent imaging (right) to form lipid membranes on micro chambers. a) the device is filled with an aqueous solution containing membrane protein and dyes while pushing air out through the PDMS. b) oil containing dissolved lipids is then sent confining the aqueous solution in the chamber array. c) flushing the channels with buffer solution. Membranes are then formed on the interface oil/buffer in the micro arrays [24].

3.3.1.2 On chip electroformation to generate GUVs

The standard electroformation technique (explained in chapter I) can be adapted using microfluidic chips. In fact, in the following example [25], the on-chip electroformation generates lower amount of GUVs which have better quality than the off-chip standard electroformation technique. The ability to generate GUVs and conduct high throughput analysis in one single chip, provides the potential to widen the accessibility of GUVs as membrane models to study lipid-lipid and lipid-proteins interaction. The outline of the microfluidic chip is shown in ***(Figure III-7):*** To generate the GUVs, the lipid mixture is spin coated on an ITO glass, and then the PDMS chip is bonded on the ITO glass. The PDMS/ITO device is then clamped to form a glass-PDMS-glass sandwich. GUVs are then fabricated by generating a sinusoidal tension in the electroformation chamber. The GUVs are then transferred to the microtrap chamber, by flushing a iso-osmotic solution in channel 2. When the GUVs are trapped, they are exposed to antimicrobial peptide (AMP) from channel 3 to characterize the permeability of the membrane, by performing a dye-leakage experiment. The quality of the GUVs fabricated here is better than the off-chip ones, as the reduced flow velocity does not allow the detachment of unwanted non-vesicular lipid debris. The size of the generated GUV is between 5 and 40 µm.

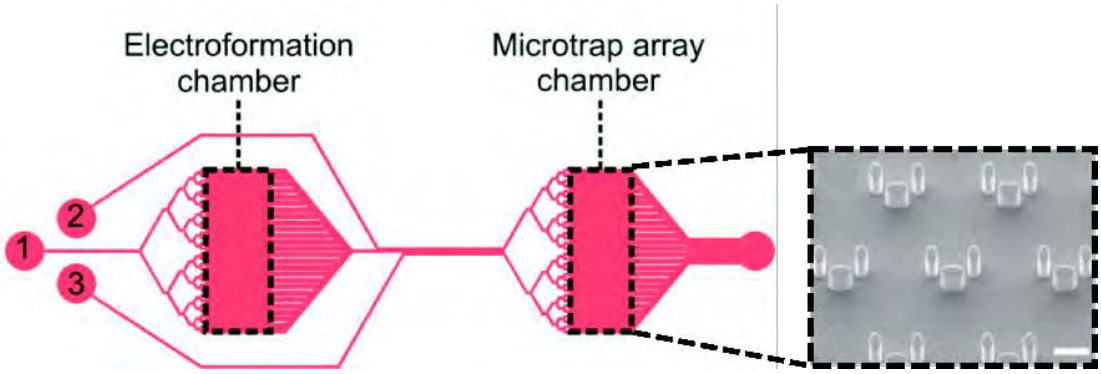

Figure III-7: Plan view of the microfluidic chip design, showing the electroformation and microtrap analysis chamber, connected by microfluidic channels (1). (2) and (3) are respectively the washing channels and the peptide channels. The Dashed lines on the electroformation chamber were excised from the PDMS device, in order to carry out the electroformation procedure [25].

3.3.1.3 On Chip Droplet interface crossing and double emulsion techniques to generate Giant unilamellar vesicles

Droplet Interface Crossing

The concept of the droplet interface crossing to generate GUVs is very similar to the one explained in chapter I, when introducing the different techniques of fabrication of GUVs. The main idea is to generate droplets of water in oil containing lipids, or water-in-oil emulsion where at the first interface water/oil, a monolayer of lipids enwraps the water droplets due to the amphiphilic characteristics of the lipids. Secondly, when crossing another interface of oil/water, another lipids monolayer enwraps the droplets forming the bilayer GUV membrane. The same concept was applied using capillary generated droplets and microfluidic chips.

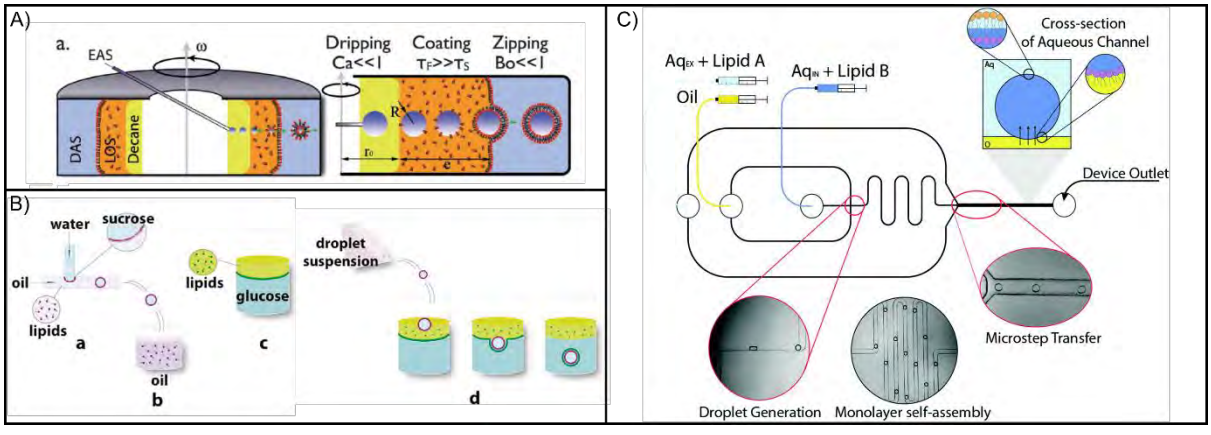

Figure III-8: Droplet interface crossing to generate GUVs: A) Schematic view of the continuous droplet interface crossing encapsulation (cDICE) method. The capillary is fixed and the chamber is rotating at a ω speed [26]. *B) Asymmetric fabrication of Giant unilamellar vesicles using a microfluidic chip. Aqueous droplets are fabricated due to an interface of water and oil (containing dissolved lipids) flowing in two perpendicular channels. The droplets with a monolayer lipid are then transferred to a vessel containing another oil/water interface, forming therefore the bilayer GUVs* [27]. *C) 2D schematic and images of the microfluidic set-up to fabricate GUVs. The lipids are dissolved in both aqueous solutions unlike the rest of the methods: the bilayer GUVs are formed by crossing water-oil-water interface* [28].

A continuous droplet interface crossing encapsulation (cDICE) method was first developed by *Abkarian et al* [26]. It consists in using a fixed capillary tube to generate continuous water droplets into a rotating chamber at a ω speed. The chamber contains the oil where the first lipid is, another oil containing the same (or different) lipid, and finally the outer aqueous solution ***(Figure III-8 A)***. This method was also used to generate GUVs made out of charged lipids, and in solutions that have high ionic strengths [29]. The size of the GUVs is controlled by the rotation speed and the capillary tube diameter.

The use of capillary tubes was then substituted using microfluidic chips. In fact, in the following example, the fabrication of the GUVs is made in two steps [27] as shown in ***Figure III-8 B***: a PDMS chip is made of two perpendicular channels, where oil (containing dissolved lipids) and water circulate in each of them. At the interface of oil/water, a droplet of water is formed, with one monolayer of lipids (the inner leaflet of the GUVs membrane). In the second step, the solution of droplets of water obtained in the microfluidic chip is transported to an outside vessel containing another oil/water interface, with another lipid dissolved in the oil phase. Centrifugation was used to force the vesicles through the interface, forming therefore the outer leaflet of the bilayer. The size of droplets obtained in this method was dispersed and varied between 10µm and 120µm.

Droplet interface crossing technique was also directly integrated in microfluidic chips where the generation of GUVs is completely done in the devices with no additional step or transfer is necessary, as seen before. In the following example [30], the PDMS chip was made of micro channels connected by junctions to create water in oil droplets. The first junction forms the interface of the oil flowing channel (containing the dissolved lipids) and the water flowing channels. At this interface, the first droplets of water with a monolayer of lipid are formed and are flowing in the oil phase (water in oil emulsion W/O). The droplets (water in oil) arrive to a second junction of water channels. By crossing the interface oil/water, another layer of lipids is formed, creating therefore the bilayer giant unilamellar vesicles. The GUVs formed in this microfluidic chip are symmetric as the oil solution containing the dissolved lipids is the same one at both interfaces. This microfluidic platform was than adapted to generate asymmetric GUVs [28], by dissolving two different lipids in the aqueous solutions instead of the oil solution as shown in ***Figure III-8 C.*** By adjusting the flow rates, they were able to control the diameter of the W/O emulsions, thus the assembled GUVs. The vesicles diameter ranges between 40 and 80 µm. This method, as well as all the water in oil emulsions techniques, does suffer from residual oil in the bilayer.

Water in oil double emulsions

The concept of water in oil double emulsions is based generally on the fabrication of a water in oil single emulsion droplet, and then forcing this emulsion to cross another interface of water, which creates a double emulsion of water-in-oil-in water. A common and important step between all the microfluidic techniques that generates GUVs based on w/o/w emulsions, is to finally be able to evaporate the oil inside the double emulsion in order to obtain a bilayer lipid membrane which encapsulate only an aqueous solution from inside. Some techniques, as will be discussed later, use extremely volatile organic solvent such as octanol instead of oil for it to evaporate faster.

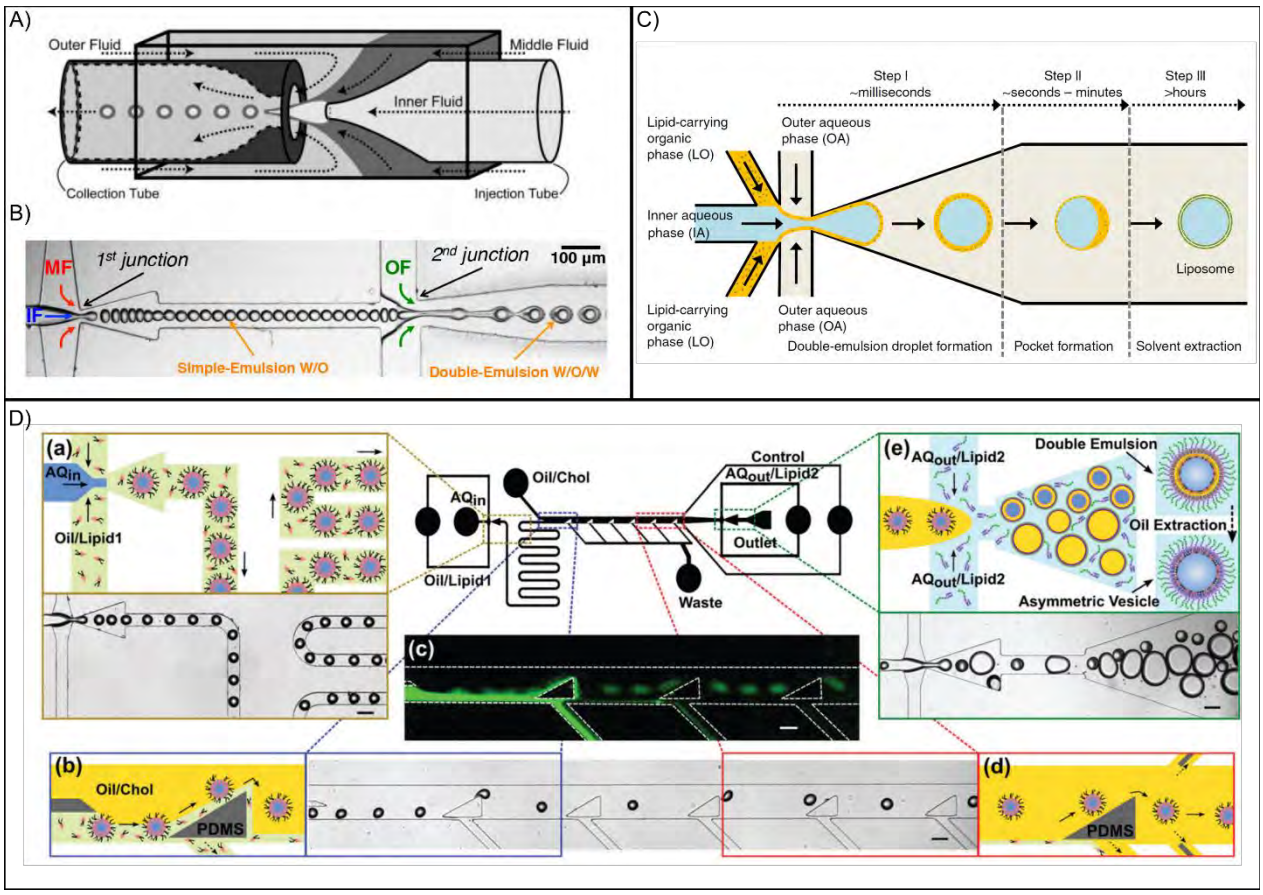

Figure III-9:Microfluidic capillarity and chips to generated GUVs based on double emulsion method A) Schematic microcapillary geometry for generating double emulsion from coaxial jets [31]. *The middle and outer fluid have to be immiscible, same for the middle and inner fluid. The collection tube is a cylindrical tube with a constriction. The glass square tube is typically around 1 mm, and the inner diameter of the glass tube of the inner fluid is between 10 and 50 µm, which will determine the size of the droplets. B) PDMS microfluidic device to produce a water-in-oil-in-water (W/O/W) double emulsion. The chip feature two consecutives junctions, one to create the first simple emulsion, and when crosses the second junction the double emulsion if formed* [32]. *C) Microfluidic device scheme representing the production of liposomes using a double-emulsion solvent extraction mechanism* [33]. *D) Schematics of the operation of the microfluidic chip based on water-in-oil-in-water double emulsion: a PDMS barrier built to force the water-in-oil droplets to shift in another oil solution, and leaving the first oil solution to migrate to a waste outlet. Fluorescence imaging shows the complete change of the first oil solution to the other oil solution, where only the droplet of water-in-oil emulsion still flows. This process generates a double emulsion of water-in-oil-in-water double emulsion GUVS with asymmetric membrane* [34].

One of the first capillary devices to generate water in oil double emulsion is introduced by *Utada* et al [31], where a fluidic device generates double emulsion in a single step with a precise control over the outer and inner drop's size and the number of droplets encapsulated in each larger drop. ***Figure III-9A*** shows the concept of the glass capillary device where three different fluids are simultaneously pumped into the system at controlled flow rates. An inner fluid is confined inside an injection tube with an inner diameter of 10 to 50 µm which generate droplets at the interface with the middle fluid which is not miscible with the first fluid. The droplets are then flown inside a collection tube, containing the outer fluid which is also immiscible with the middle fluid. This technique was then adapted and used to generate polymer vesicles (polymersomes) [35], where the copolymers are dispersed in an organic solvent which is highly volatile and immiscible with the other aqueous solutions (Tetrahydrofuran and toluene 50-50 wt%). The organic solvent is then slowly evaporated until the polymers organizes into a vesicle. The complexity of such device is to be able to have a perfect alignment of the three tubes to allow a coaxial flow, necessary to generate the droplets.

Water in oil double emulsions was then also directly integrated in microfluidic chips, which solves the difficult alignment in the previous example. *Petit* et al., fabricated a PDMS microfluidics based on a double-emulsion template formed in flow-focusing configuration [32]. The chip is presented in ***Figure III-9B:*** the PDMS chip features 2 cross-junctions at which the emulsions of water-in-oil then oil-in-water are fabricated. The liposomes fabricated have a diameter between 20 and 60 µm. In order to extract the residual oil in the lipids membrane, ethanol was added to the outer aqueous solution (OF) which aided to extract the oil. The solvent extraction method was demonstrated before in this reference [36].

A more direct PDMS chip is made based on octanol-assisted liposome assemble (OLA) to remove the residual oil present in the GUVs upon its fabrication in the microfluidic chip [33]. In fact, the microfluidic chip consisted in a six-way PDMS junction where: lipid dissolved in an organic phase (LO) arrives from two channels to meet from one side the inner aqueous solution, forming an interface oil/water, and also an outer aqueous solution (AO) forming another oil/water interface as seen in ***Figure III-9C.*** To remove the residual oil in the GUVs, 1-octanol solution was mixed with the inner aqueous solution which then helped with the evaporation of the oil from the GUVs. However, this final step takes around 10 hours to fully remove the oil from the GUVs. Therefore, the oil where the lipids are dissolved was then replaced directly with octanol solution as it is also a good solvent for the lipids. The same process of fabrication of GUVs is then carried out and residual octanol budding was present in the GUVs. However, the last step of evaporation of the octanol from the GUVs takes between 1 and 5 minutes, therefore 1000 times faster than evaporating the oil residual. This chip is

able to generate GUVs between 5 and 20 µm by tuning the different flow velocities. However, both method described above dot not allow to fabricate asymmetric GUVs.

Finally, the team of Paul R. Chiarot developed a PDMS microfluidic chip to fabricate GUVs, based on water-in-oil-in-water double emulsion (w/o/w) [34], [37], which is able to fabricate asymmetric Giant unilamellar vesicles. ***Figure III-9D*** explains the details of the chips operation : (a) a water-in-oil emulsion is first formed where a monolayer of lipid around the water droplet is formed (the inlet leaflet). The solution then crosses a PDMS barrier which separates the first oil solution from another one, forcing the droplets to join the second oil solution (b). Fluorescent imaging shows the complete change of the first oil solution to the other one (c). Finally, the water in oil droplets cross another aqueous junction containing another type of lipid, and generating therefore an oil-in-water droplet with a bilayer of lipids (e). The extraction of oil from the droplets is made following the examples mentioned before, by adding ethanol solutions to the final double emulsions. The second type of lipids, different from the first one, allows the formation of asymmetric GUVs, with diameter between 50 and 150 µm. The GUVs obtained were stable up to 6 weeks and the asymmetry was maintained up to 30 hours.

Due to microfluidics, there are now several ways to create GUVs mostly based on the droplet interface crossing and the double emulsions method, and some of them allow the fabrication of asymmetric membranes. The size of the GUVs can be controlled by tuning the dimensions of the microfluidic channels when designing and fabricating the microfluidic chip and by regulating the different flow rate in the different micro channels. The advantage of integrating the fabrication of GUVs inside microfluidic chip is the additional studies that can be perform on the fabricated GUVs directly in the chip, which eliminate additional steps of transferring the GUVs inside the chip. That was the example of Al Nahas *et al.,* who developed an integrated lab-on-chip multilayer microfluidic chip that is able to first create GUVs based on the octanol-assisted liposomes double emulsion method explained before, and secondly on the same chip, to conduct screening assays [38].

3.3.2 Microfluidics as a tool to characterize Giant unilamellar vesicles

The advances of microfabrication techniques in clean room facilities allows the development of different shapes, levels and constrictions of micro channels. This leads to widen the applications for model membranes. For example, it is now possible to trap single or multiple GUVs in micro traps and characterize their physico-chemical properties such as membranes permeability. Moreover, microfluidics presents a promising tool to characterize the shear effects on model membranes, as it is possible to tune the flow rates inside the microfluidic channels. And finally, microfluidic presents a promising engine to investigate drug effects on model membranes. The following examples will show

how to investigate transport through membranes by trapping GUVs, and how shear stress can affect the membranes. Moreover, we will discuss how microfluidics has been successfully used as platforms to investigate drugs interaction with membranes.

3.3.2.1 Study of permeability and transport through membranes

The intrinsic permeability of a membrane to a solute is defined by the ratio of the volume flux of water through the membrane, per unit area per unit time over the concentration gradient. Permeability is essential to characterize, as it shows the ability of a membrane to allow or not, the permeation of molecules inside the cells. This phenomenon can be the case of active processes such endocytosis and exocytosis (seen in chapter II) which are biological processes that occurs normally in the cells but also for drug testing applications. In the case of drug testing applications, characterizing the ability of a particle or a molecule to permeate inside the cell is essential to determine a drug's efficacy.

To gain information on this process, Bhatia *et al.,* present a PDMS microfluidic chip to characterize membrane's permeability using GUVs as model membranes [39]. The PDMS chip uses 6 integrated ring-valves surrounding large number of GUV traps allowing 6 independent experiments per chip and large experimental throughput ***(Figure III-10A)***. When pressurized, the ring-valve isolates the vesicles trapped from the rest of the solution. When depressurizing, the ring-valves allow the immediate exposure of the GUVs to an exchanged external solution. The external solution introduced to the trapped GUVs contained higher or lower concentration of sugars than the solution inside the GUVs. This leads to an increase or decrease of the osmotic pressure on the GUVs. Permeation then takes place across the surface area of the GUV, which deforms to create inward tubes (cylindrical or necklace-like) or buds in the vesicles. Using confocal fluorescence microscopy, the area and volume of both mother GUVs and GUVs after deflation or inflation were measured ***(Figure III-10A (a-e))*** and the permeability coefficient was plotted as function of the time, which gave an average value of : $p = 15.7 \pm 5.5\ \mu\mathrm{m\ s^{-1}}$ for POPC:Chol (9:1) membrane.

A comparable microfluidic chip concept was also used to study Calcein transport through a membrane pore [40]: GUVs containing fluorescent Calcein were trapped in the micro-traps. Later, the microfluidic device allowed rapid and total change of solution with DI water without bothering the trapped GUVs. And finally the valves were opened and closed for 2s to rapidly expose the GUV to a solution of αHL (α-hemolysin). αHL is a protein that forms a heptameric pore once inserted in the lipid membrane [41]. Using confocal microscopy, the authors investigated the intensity of fluorescence of Calcein inside the GUVs as function of time after exposing the GUVs to the αHL protein solution ***(Figure III-10B a - b)***. It was demonstrated that indeed, the fluorescence of the Calcein decreased rapidly the first 5 minutes, even faster when exposing it to a higher concentration of αHL, and reached finally a steady

fluorescence intensity ***(Figure III-10B c)***. This was due to two processes: (i) the diffusion to and incorporation of αHL into the membrane and (ii) diffusion of Calcein across the membrane due to a concentration gradient of αHL.

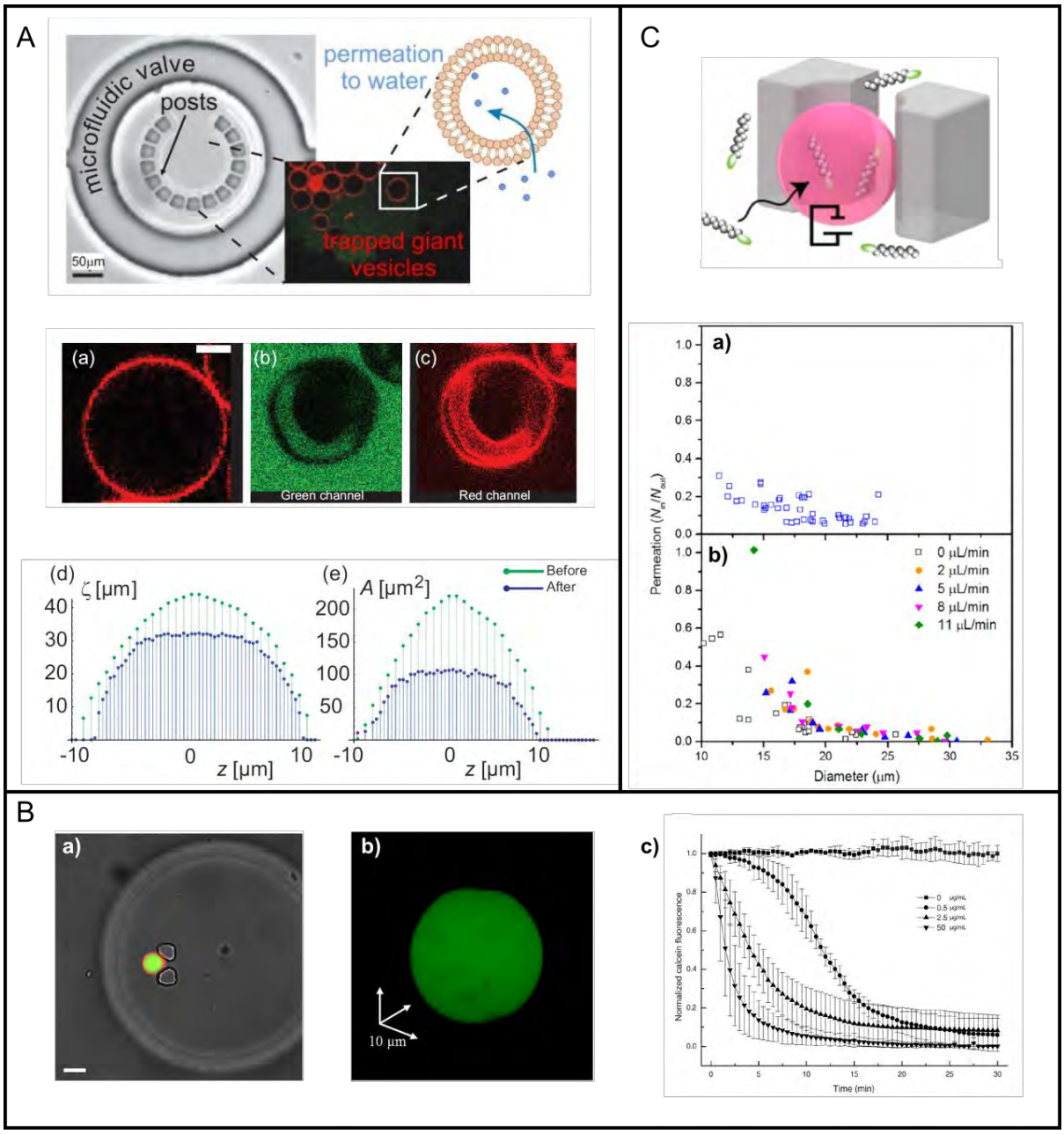

Figure III-10:PDMS Microfluidic methods to measure membrane permeability by trapping giant vesicles and performing quick solution exchange together with confocal microscopy A)(a)and (b-c) confocal microscopy of GUVs before and after deflation respectively: red color is the membranes staining, and green is the Calcein solution. (d) and (e) 2D cross sectional circumference and Area of the same GUV as function of the vertical z-height before (green) and after (Blue) deflation [39]. *B a) Bright field image of the trap, overlaid with a fluorescent microscopy of the trapped GUV stained in red. b) 3-D rendering of the Calcein fluorescent showing a minimum deformation of the trapped GUV. c) Kinetics of Calcein release for different αHL concentrations* [40]. *C) PDMS walls in microfluidic chip to trap GUVs and keep the flow around it. (a-b) correlation between the permeation of Calcein into individual GUVs and their sizes. a) permeation into a negative membrane potential under static conditions. b) permeation into a neutral membrane under static conditions as well as different flow rates.*

A less complicated example of traps are PDMS walls made to trap GUVs but still keep a flow around it ***(Figure III-10C)***. Chao-Chen *et al.* used these traps to investigate the influence of membrane's potential on the permeation of cationic peptides [42]. Combined with FCS measurement (fluorescence correlation spectroscopy), it was first demonstrated that the permeation of Calcein inside the GUVs is inversely proportional to the size of the GUVs, and this could be caused by the different amount of residual oil between the bilayers (from the water-in-oil method of fabrication). Then, it was shown that the permeation of Calcein is independent of the flow applied on the trapped GUV. In fact, while increasing the flow from 2 µL/min to 11 µL/min, the permeation of POPC/POPS membranes remained constant ***(Figure III-10C a-b)***. And finally, a negative membrane potential is necessary for cationic peptides to translocate inside the GUV.

The clear advantage of using microfluidics for monitoring membrane transport kinetics is the speed at which the surrounding solutions can be completely exchanged and the possibility to control the dynamics around the GUVs, to characterize GUVs response to chemical/physical stress. Moreover, due to the precise positioning of the immobilized giant vesicles, automated imaging could be easily implemented. These microfluidic platforms can be suitable platform for modeling permeability of pharmaceutics candidates.

3.3.2.2 Study of shear effect on GUVs

Red blood cells, endothelial cells ECs (layer of cells that line all blood vessels) and many other type of cells in our bodies are frequently exposed to hydrodynamic fluid flow, therefore to a shear stress. Red blood cells have complex structures consisting of a lipid bilayer with incorporated proteins coupled to the spectrin network and their morphological changes under shear flow were investigated [43], [44]. Shear flow effect was also investigated on human pulmonary artery ECs and on Giant unilamellar vesicles using two-photon imaging and Fluorescence Recovery After Photobleaching (FRAP) measurements [45]. Both ECs and GUVs showed an increase in the lipid fluidity as the shear increased from 0.5 to 2 Pa, due the decrease of their lipid-order phase and increase of their lipid disordered phase.

High blood flow associated shear stress causes physiological and pathophysiological biochemical processes in ECs. These processes are initiated by modifications in plasma membrane lipid domains which are characterized as liquid-ordered (L_o) or liquid disordered (L_d) (chapter I). By characterizing the diffusion of probes in ECs under a flow up to 10 dynes/cm^2 using single-molecules fluorescence microscopy, the shear effect on the membrane's microdomains was characterized [46]. In fact, *DiI-C_{12}* and *DiI-C_{18}* are dyes that probe respectively L_d and L_o phases. This was determined by measuring the dyes' lifetime using a reverse single photon imaging system [47], and which gives an information on

the intensity of the dyes response as function of time: the average fluorescence lifetime is longer in the gel phase state than in the fluid state. Back to the first reference [46], the authors demonstrated that the shear stress induced an early and transient decrease in *DiI-C_{12}* lifetime, whereas it induced a later and sustained decrease in *DiI-C_{18}* lifetime. This result suggests that the shear-induced decreases L_o and L_d micro viscosity. Moreover, it was shown that shear stress induced a later and transient increase in lateral diffusion of *DiI-C_{18}* but not *DiI-C_{12}* which remained constant. This means that the *DiI-C_{18}* – labeled domains (L_o) become smaller and more mobile as a results of shear stress. These results confirm the shear stress effect on membrane's viscosity which affected by the liquid ordered and liquid disordered states.

However, despite these efforts, the organization and properties of the membrane under shear stress remain unclear. For example, due to experimental constraints, the visualization of phase-dependent behavior remains difficult, and requires high speed and resolution imaging. Microfluidics technology offers a great tool to trap GUVs and impose controlled flows. Combined with confocal microscopy, investigation of shear flow effects on GUVs was done in several microfluidic chips.

On-chip studies to investigate shear effect on GUVs membranes

A basic approach to trap GUVs in microfluidic chip while keeping the flow around it, is in micro channels with 2 different heights. In this following study [48], two effects of the flow were observed : first, the transmission of the shear flow towards inside the membrane and second the effect of the flow on the deformation of the GUV, due to its elastic energy. To do so, a PDMS chip made of wells of 30 µm heights is fabricated in order to trap GUVs, while it is still partially exposed to a shear flow ***(Figure III-11A)***. The velocity of the fluid around the GUV was related to the pressure drop in the channels, and by modeling each section of the channel as a linear resistor. By tracking fluorescent lipids in the membrane and inside the GUV, the flow on the edge and in the GUV center was also characterized. The authors demonstrated that the outer flow is higher than the flow on the edge which is also higher than the flow transmitted inside the GUV ***Figure III-11A (a-c)***. Moreover, the effect of the shear flow on the shape of the trapped GUVs was also investigated; in fact, if trapped and the flow is Off, the GUV is in its initial spherical shape. However once the flow in imposed, the GUV deforms to go inside the channel, which increases the membrane elastic energy. The GUV is then released from the trap upon a critical velocity U_c. A mechanical model is developed from the geometry of the deformation of the GUVs inside the channels. The model links the viscous effect from the outer flow to the elastic effects based on the variation of the membrane stretching energy.

The effect of mechanotransmission of shear stress across lipid bilayer membranes of GUVs was also investigated using defocusing microscopy for a 3D visualization at high precision [49]. In fact, GUVs

enclosing fluorescent tracer particles were immobilized in a microfluidic chip and were exposed to a shear flow. The shear forces around the GUV are transmitted to the membrane and further into the lumen (the liquid inside the GUV), and induce therefore the bead movement and the vesicle deformation. Two types of flow with multiple different rate were applied on the GUV: a symmetric and asymmetric one. The symmetric flow showed no significant difference in the luminal dynamics between the two vortexes of the GUV, unlike the asymmetry flow: the liquid exchange between hemispheres is generally faster in GUVs exposed to asymmetric flow profile.
Moreover, the effect of cholesterol in the membrane on the mechanotransmission efficacy under flow was also investigated. Mechanotransmission efficacy ε is characterized by the ratio of luminal flow to external flow. They showed that without cholesterol in the membrane, $\varepsilon = 0.094$ whereas for 16 mol % of cholesterol in the membrane, $\varepsilon = 0.043$. Therefore, the mechanotransmission efficacy is 50% higher in membranes that lack cholesterol, and this is due to the decrease of the fluidity of membrane in the presence of cholesterol.

As mentioned before, the shear flow alters the membrane's liquid order and liquid disordered phases which affects directly membrane's fluidity. A way to visually characterize this is to fabricate GUVs which exhibit both phase behavior, and expose them to a shear flow [50]. In this study, a PDMS microfluidic chip is designed to allow the capture of the GUVs without an actual physical trap like the case of the first example mentioned before. In fact, the GUV is tethered to the glass support of the PDMS chip by a coating of cholesterol on the glass which capture the GUV, but still allows the rotation of the GUV under a flow without deforming it and without leaving the field of view ***(Figure III-11B)***. The concept of the chip was introduced in the paragraph before, as it was also used to study transport through a membrane's pore [40]. In this application, GUVs are fabricated with ternary lipid mixtures which exhibit lipid microdomains that can be visualized by different fluorescent staining ***(Figure III-11B a)***. Due to the application of flow (40µL min^{-1}), the microdomains which were circular at equilibrium change to non-deterministic shapes. Once the flow was stopped, the domains begin to return to their circular shapes to minimize the energy by maximizing area-to-perimeter ratio. The fusion of the domains is characterized over the time by measuring the total number of edge point (TEP) which corresponds to the number of domains ***(Figure III-11B b)*** . In the same studies, same ternary mixture but different molar ratio is used. However, even if the micro domains move during and after the exposure to the flow, they do not mix into larger domains but even seem to repel each other. This is assumed to be a consequence of the increased area fraction of the l_d phase and the presence of domain budding previously studied by Yanagisawa *et al.,* [51].

To summarize, shear flow has a strong effect on the lipid membranes by altering their phase distribution: depending on the lipid composition, the microdomains fuse into larger ones until they reach equilibrium, and this phenomenon can be faster under high temperatures. The plasma membrane and associated transmembrane proteins are candidate for mechanoreceptors which convert the extracellular stimulus into intracellular biochemical signals. Therefore, the effect of flow on membranes fluidity can strongly affects processes of mechano-transduction in living cells [52].

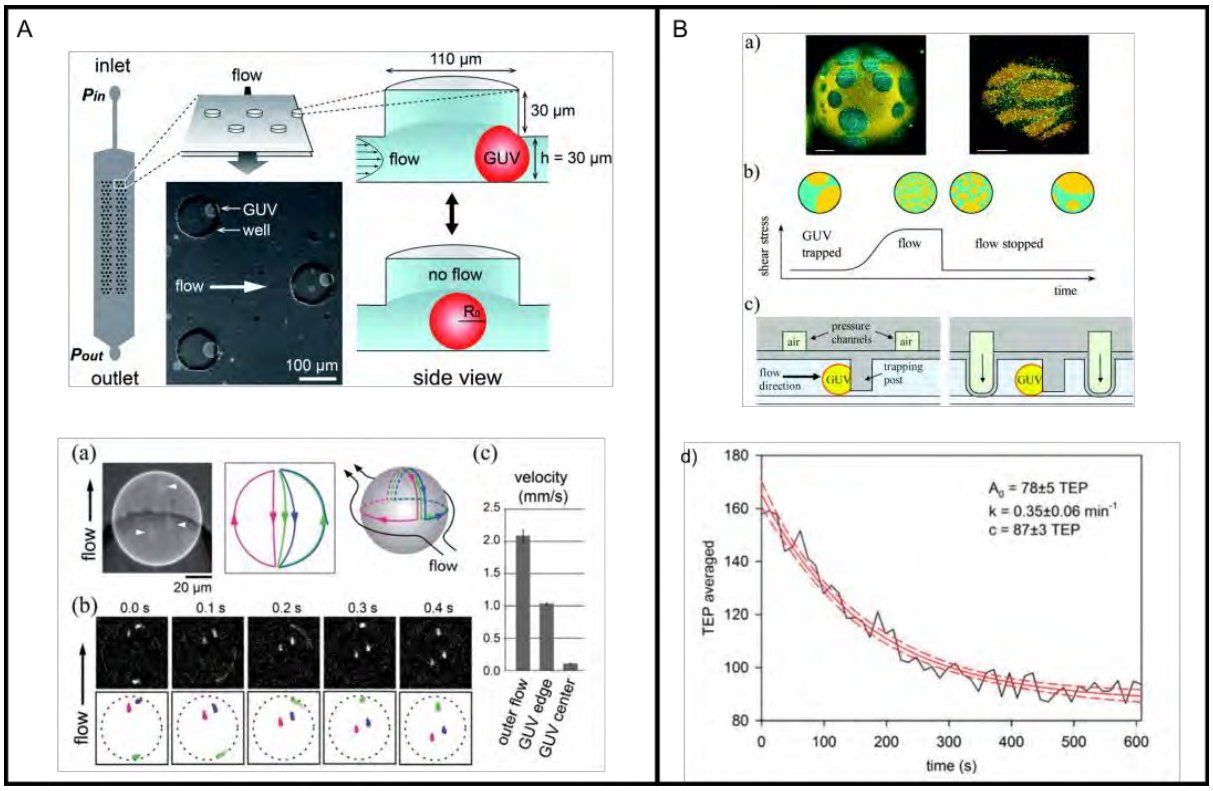

Figure III-11: Microfluidic chips to characterize the effect of the flow on GUVs membranes. A) PDMS microfluidic chip for trapping GUVs. (Left) is a top view of the whole channels, (upper middle) is close-up view of the wells etched into the ceiling of the channel (right). Fluorescence microscopy image of trapped GUVs containing a fluorescent lipid and phase contrast image of wells etched on the top surface of the microfluidic channel taken from the bottom of the channel (lower middle) [48].*(a-c) flow characterization in the lipid bilayer membrane of the trapped GUV. a) Fluorescent image of the GUV trapped and the illustration of the 3D view. b) Fluorescent imaging of signals appearing on the membrane and their representation over time. c) velocities of the flow on the edge and in the center of the GUV. B) a) GUV with microdomains at equilibrium (left) and under a flow (right). Scale bar :5µm. b) experimental scheme: after the GUV is trapped, a flow is applied. Study of the relaxation of the domains is done after the flow is stopped. c) and d) are respectively a cross and top view of the trapped GUV. The GUV is exposed to a flow as long as the valves are opened. To stop the flow on the GUV, the valves are closed by actuating the pressure channels with air. d) Total number of edge point (TEP) over time representing the number of domains in the membrane* [50].

3.3.2.3 Microfluidics for drug testing on GUVs

Giant unilamellar vesicles are simplified models of cellular membranes. As the interactions between the outer environment of the cell and inside the cell happen first on the cellular membrane, GUVs have been widely used as model membranes in several field such as synthetic biology and drug discovery. It is a simplified way to understand the membrane's reaction upon interaction with an

external stimulus such as drugs and nanoparticles. As microfluidics provides access to trap GUVs while imposing a certain flow around it, it can also be possible to expose to chemical stimulus and investigate the membranes reaction while being trapped and easily visualized, such as the previous examples with the αHL.

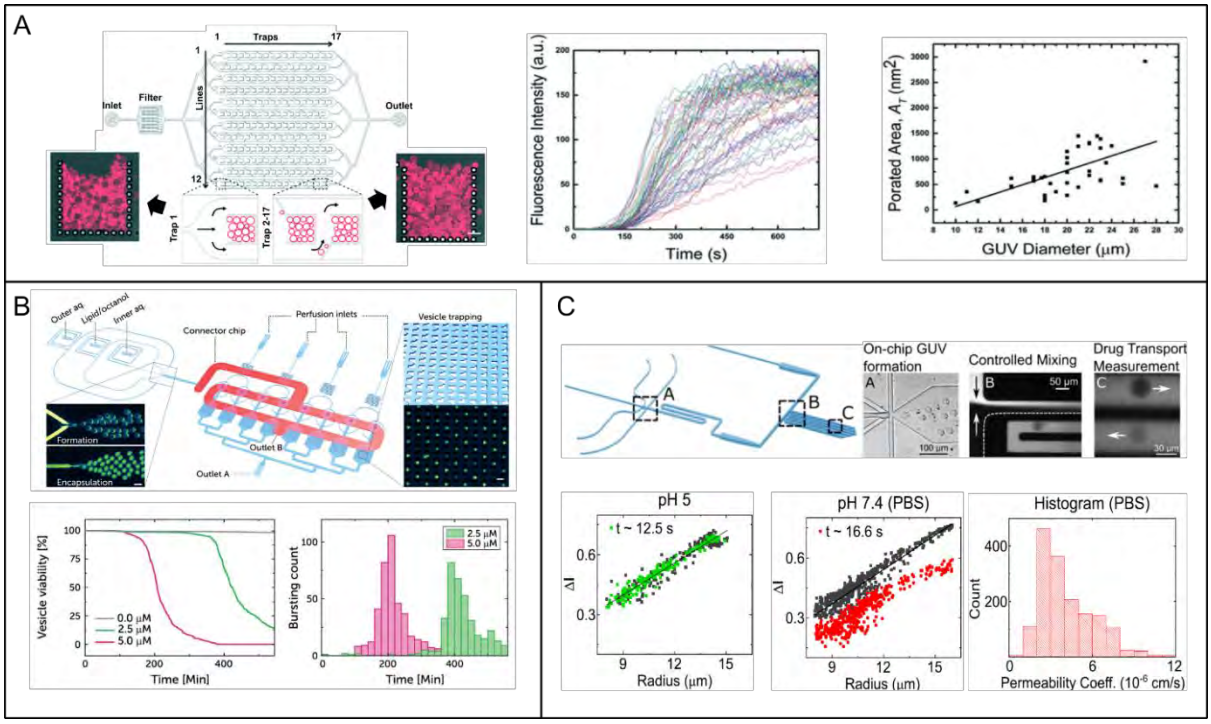

Figure III-12: A) Microfluidic chip design for high capacity trapping GUVs. On the right, confocal microscopy images of the trapped GUVs (labeled with $DiIC_{18}$ probe in red) inside the PDMS traps. The graphs represent high throughput measurement using a single device for the intensity of Calcein fluorescence inside the GUVs as function of time and the porated area plot as function of the GUV diameter[53]. *B) Microfluidic chips to generate GUVs, trap them and conduct analyses on them. The graphs represent respectively the vesicles viability as function of time for 3 different concentration of antibiotics and the number of bursted GUVs in time for two different concentrations of antibiotics* [38]. *C)* An integrated microfluidic chip to a) generate GUVs based on the octanol-assisted liposome assembly (OLA) b) vesicles are exposed to a drug solute at a T junction, where the two flows mix in a controlled manner in the serpentine channel. c) vesicles surrounded by the autofluorescent drug (λex = 350 nm), can be monitored at different parts of the channel, corresponding to different times that the liposome has been exposed to the drug. The graphs represent the intensity of the fluorescence of the drug inside the GUVs as function of their diameter and for different pH values, and the permeability coefficient [54] .

In the following study [53], a PDMS chip was designed and fabricated to confine a very large number of GUVs in one single chamber, in the idea of creating a futuristic prototissue of GUVs. The device is made of 12 separated lines with 17 traps each, filling about 114 GUVs each, making an average total amount of 23 000 GUVs per chip ***(Figure III-12A)***. The characteristic time to fill one single trap is around 20 minutes, when using a flow rate of 10μL min^{-1}. By changing the heights of the channels, only GUVs with diameter lower than the channel can be trapped. Due to the small opening on the side of the channel (~ 10μm), they demonstrated that in less than a minute the solution around the GUVs can be totally changed, while the GUVs do not escape. Moreover, only 2μL of solution is required to replace the solution around the GUVs, which is important for precious samples such as nanoparticles, drugs

or proteins. As a proof of concept, end-point pH detection measurements were conducted. It was shown that the fluorescent intensity of the molecules inside the GUVs was decreasing with the decrease of the pH value, and it's because the hydrogen ions present in the pH solution are able to permeate across the lipid membranes and protonate the fluophore. Another proof of concept is the introduction of α-HL protein to the surrounding solution of the GUVs, which is known to create pores in the membrane and allows passive transport of small molecules. After replacing the proteins solution with a fluorescent solution of Calcein, the fluorescence intensity inside the GUV increased in time ***(Figure III-12A).***

The example above shows the possibility to conduct analysis on an ensemble of GUVs, which gives access to statistics and overview of the responses of all the GUVs. However, it is more difficult to access the response of a single GUV, without it being affected by its neighboring GUVs. Hence, Al Nahas *et al.,* developed an integrated lab-on-a-chip multilayer microfluidic chip that is able to perform three main tasks ***(Figure III-12B)*** [38]: first as mentioned in the previous paragraphs, the chip is able to fabricate GUVs in physiologically relevant buffer (physiological salt concentrations) . The second part of the chip is made of 372 individual traps, which allows the immobilization of the vesicle for a long time, in order to perform studies on them. And finally, those traps are connected to separate perfusion inlets, to make vesicle-based screening assay. In this specific study, the efficacy of antimicrobial peptides antibiotic (AMPs) on GUVs mimicking a bacterial membrane was performed. Upon interaction with the antibiotic, the fluorescence inside the GUVs decreased over time proving the pore formation in the membrane. To determine its efficacy, different concentration of antibiotic was tested and the viability of the GUVs was characterized over time until complete bursting of the GUVs ***(Figure III-12B)***.

Finally, it is possible to conduct drug testing on single GUVs without the need to immobilize them. In the following example [54], a microfluidic chip is fabricated to generate GUVs based on the octanol-assisted liposomes double emulsion to investigate the drug permeation inside the membranes ***(Figure III-12C)***. The GUVs fabricated have a negatively charged membrane and physiological pH and salt concentration to mimic the bacterial membranes. A T-junction connects the drug channel to the GUVs channel and leads to a serpentine channel shape which allows the mixing of both solutions, and the interaction of the GUVs with the drug. By controlling the leakage of fluorescent dye present in the drug solution towards the inside of the GUVs, the permeability coefficient of norfloxacin and ciprofloxacin drugs was characterized ***(Figure III-12C).***

3.3.2.4 Microfluidics to assess mechanical properties of Giant unilamellar vesicles

When in contact with a particle or a drug, cellular membranes undergo deformation and changes to allow or not absorption, and which are strongly influenced by mechanical properties. Therefore, any artificial cell constructed from a new model system has to have its mechanical properties fully characterized [55]. The ability to trap GUVs in microfluidic chip and have a good control over the pressure and the flow can surely be used as a tool to investigate the mechanical properties of GUVs. One of the most common way is to combine optical traps with microfluidics to both trap the GUV and deform it through the lasers beam applied on it. The main advantage of these techniques is that is doesn't require any contact with the GUV. Generally, the GUVs are flowed to a microfluidic chip using a pump. When the GUV are close to an optical trap, the flow is decreases gradually until stopped. The power of laser is then increased gradually, and the deformation of the GUV is measured. Thanks to physical models, it is possible to relate the strain (deformation) to the tension (stress applied from the laser) in order to extract the elastic modulus of the GUVs. The physical model is very close to the ones seen in chapter II, where the tension is translated from the stress applied on the object and the strain from the deformation of the GUV after determining the initial area and the increased area.

One of the examples is the use of dual-beam optical trap (DBOT) based on optical fibers integrated with a capillary flow channel to stretch the GUV [56]. In fact, the radiation pressure pulls the GUV into the center of the two beams and creates a stable trap. The light coming from the beams creates a surface stress and therefore deforms the GUV. With the increase of the power of the beams, the deformation is increased. And by plotting the strain vs the tension, the bending modulus of POPC membrane was extracted ***(Figure III-13A)***. However, due to the low laser power used, stretching regime couldn't be achieved and therefore the stretching modulus could not be extracted.

In fact, the use of high power laser beams in dual-beam optical trap can induce heating in the membranes, affecting therefore the mechanical properties concerning the deformation and the phase transition in the membrane. That's why in the following study of combining microfluidic chips and optical traps, they investigated the dependence of vesicle deformation on temperature coming from the heating present in the traps [57]. The advantage of this study is the possibility to induce separately optical mechanical stresses and temperature increase by using lasers with different wavelengths ***(Figure III-13B)***. The deformation of the GUV was analyzed under three different laser wavelength (808, 1064 and 1480 nm). In fact, using higher laser wavelength to deform GUVs induced a non-steady and hysteretic decreased deformation compared to the lower laser wavelength. Bending modulus and an initial tension value were extracted from the fitting of the tension vs strain curves ***(Figure III-13B).***

Finally, the difficult microfluidic set-up in the examples showed above did not allow high-throughput mode to generate statistics concerning bending modulus values, which is very tedious usually to characterize and which differs from a method to another. Therefore, the next study shows a combination of microfluidics and DBOT system that rapidly process large number of samples, to yield population statistics for the bending modulus of GUVs that have different phases (gel and liquid) [58] ***(Figure III-13C)***. In this study, the effect of cholesterol on bending modulus was investigated by characterizing pure POPC membrane, POPC membrane with 20 mol% of cholesterol and DPPC membrane with 20 mol% of cholesterol. It was demonstrated with this technique that cholesterol does not affect the bending modulus of mono-unsaturated membrane.

As seen in the previous examples, characterizing the mechanical properties in microfluidics is possible when combined with optical traps to both trap the GUVs and deform it due to the increasing laser power. However, all methods did not allow the complete characterization of the elastic modulus of GUVs which combine also the stretching modulus. This proves that until now, microfluidics has not yet fulfilled its purpose to fully characterize the mechanical properties of the GUVs. More developments are still needed to combine microfluidics and model membranes to characterize different mechanical properties of GUVs.

In chapter II, I introduced most of the techniques used to characterize the mechanical properties of model membranes, especially the micropipette aspiration technique which became the gold standard technique applied of cells, aggregates and model membranes. A lot of efforts have been put to develop on chip micropipette aspiration which were used to characterize the mechanical properties of breast cancer cells, but no direct applications were made on model membranes. In the two following examples [59], [60], PDMS microfluidic chip with hanging trap in the middle of two deeper channels, were developed and are able to trap and apply pressure to single cells in designated aspiration arrays. The autonomous cell trapping eliminates the manual search of cells and is able to perform several measurements in parallel. As this micropipette on chip technique was successfully applied on cells, we based our first design on this micropipette on chip in order to characterize the mechanical properties of model membranes. This will be the main objective of chapter IV.

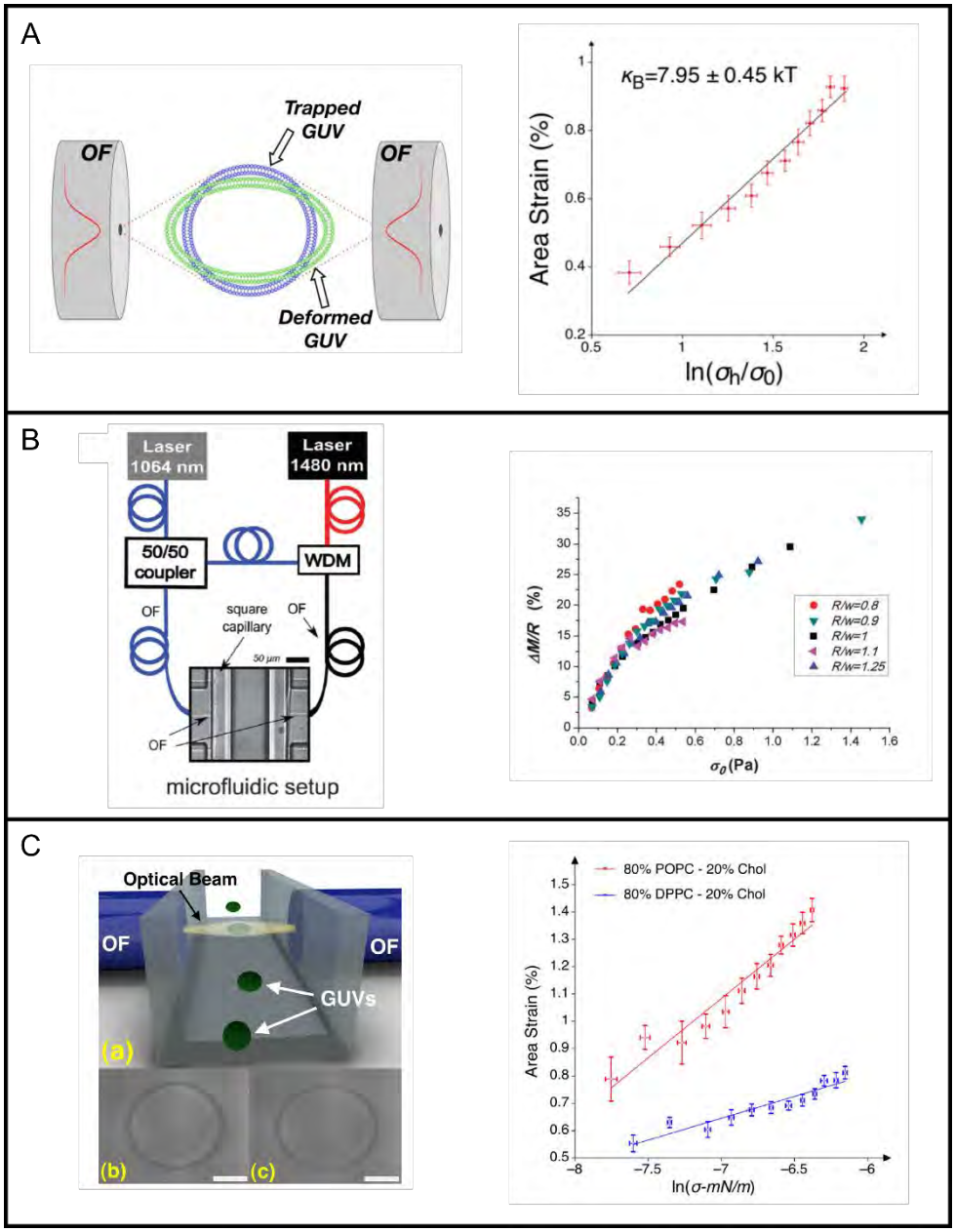

Figure III-13: Optical traps in microfluidic chips to characterize mechanical properties of GUVs. A) Schematic of the stretching of a GUV using dual Gaussian beams launched by optical fibers. The graph represents the average percentage area strain for each laser power plotted versus the scaled lateral tension, and the fitting of the curves represent the bending modulus value [56]. *B) Sketch of the combination of lasers and microfluidic set-up. The optical fibers are aligned perpendicular to a square micro-capillary. The graph represents the deformation of the vesicles by the maximum of the major axis strain versus maximum optical stress* [57]. *C) Schematic of dual-beam optical fibers sources integrated with a microfluidic channel. b-c) are optical images of trapped GUVs with respectively minimal power and maximum power. The graphs represent the deformation of the vesicle by the apparent area strain versus the ln(tension) for two different mixture of lipids. The bending modulus is extracted from the fitting of the curves* [58].

3.4 Conclusion

Microfluidics is considered as a powerful tool, and many fields such as pharmaceutical, medical and analytical applications utilize it to conduct part of their research. The possibility to use low amount of reagent and the speed of experiments are some of the many advantages that microfluidic offers. Moreover, by tuning the hydraulic resistance in the microfluidic channels, it is possible to control the flow repartition in the microfluidic chip which is needed in many applications. Microfluidic chips are fabricated in different processes depending on the material used, but the most common one are glass, silicon and PDMS. Though all processes have one important step in common which is the Photolithography. Following this step, soft lithography can be done if the final chip is PDMS, or etching process if the final chips are glass or silicon.

Microfluidic chip application on giant unilamellar vesicles has been widely used. First of all, the droplet interface crossing and the double emulsion concepts to generate GUVs were adapted to fully take place in microfluidic chips and by controlling the channels dimensions and the flow rates, the size of the generated GUVs can be tuned. Moreover, the composition of the lipids in the GUVs membrane can also be controlled to fabricate symmetric or asymmetric membranes, an important characteristic in cellular membranes.

Secondly, it is possible to trap large ensemble of GUVs to conduct an overall experiment of permeations of the membranes. It is also possible to trap single GUV, with a control flow around it to investigate the effect of the shear stress on lipid mobility, fluidity and mechanotransduction. Optical traps inside microfluidic chips are also possible to characterize some mechanical properties of GUVs such as the bending modulus.

Finally, GUVs can be used as model membranes to conduct drug and antibiotics tests, by trapping them and using fluorescence microscopy to characterize leakage experiments when in contact with molecules.

However, a full characterization of the mechanical properties of model membranes (the bending and the stretching modulus) have not yet been done using microfluidic techniques. As micropipette aspiration is a powerful tool which combines the characterization of both bending and stretching moduli of model membranes (seen in chapter II), micropipette on chip has not yet been successfully applied on model membranes. On another hand, when in contact with a particle or a drug, GUVs membrane undergoes deformations and changes characterized as mechanical properties, which are defined by each lipid type. In general, the characterization of such properties is quite critical and more difficult than other properties. Off-chip methods have been largely developed to characterize them,

but the combination with microfluidics has not yet been done. In the next chapter, I will introduce the first micropipette on chip which we fabricated in order to characterize mechanical properties of model membranes.

References

[1] C. Kumar, *Microfluidic Devices in Nanotechnology*. New Jersey, 2010.

[2] O. Français and H. Horsin Molinaro, “La microfluidique : principes physiques et mise en œuvre d ’ écoulements continus,” no. figure 2, pp. 1–10, 2016.

[3] E. Shashi Menon, *Fluid Flow in Pipes*. 2015.

[4] H. Bruus “Theorethical Microfluids,” vol. 1, pp. 1689–1699, 2015, doi: 10.1017/CBO9781107415324.004.

[5] H. Bruus, “Lecture Notes Theoretical microfluidics,” *Physics (College. Park. Md).*, vol. 18, no. 33235, p. 363, 2008.

[6] K. W. Oh, K. Lee, B. Ahn, and E. P. Furlani, “Design of pressure-driven microfluidic networks using electric circuit analogy,” *Lab Chip*, vol. 12, no. 3, pp. 515–545, 2012, doi: 10.1039/c2lc20799k.

[7] H. Bruus, “Governing Equations in Microfluidics,” pp. 1–28, 2015.

[8] G. M. Whitesides, “The origins and the future of microfluidics,” *Nature*, vol. 442, no. 7101, pp. 368–373, 2006, doi: 10.1038/nature05058.

[9] Z. B. Qi *et al.*, “Disposable silicon-glass microfluidic devices: Precise, robust and cheap,” *Lab Chip*, vol. 18, no. 24, pp. 3872–3880, 2018, doi: 10.1039/c8lc01109e.

[10] V. N. Goral, Y. C. Hsieh, O. N. Petzold, R. A. Faris, and P. K. Yuen, “Hot embossing of plastic microfluidic devices using poly(dimethylsiloxane) molds,” *J. Micromechanics Microengineering*, vol. 21, no. 1, 2011, doi: 10.1088/0960-1317/21/1/017002.

[11] Y. Xia, E. Kim, X. Zhao, J. A. Rogers, M. Prentiss, and G. M. Whitesides, “°° L,” pp. 6–8.

[12] E. Delamarche, A. Bernard, H. Schmid, B. Michel, and H. Biebuyck, “Patterned delivery of immunoglobulins to surfaces using microfluidic networks,” *Science (80-.).*, vol. 276, no. 5313, pp. 779–781, 1997, doi: 10.1126/science.276.5313.779.

[13] D. C. Duffy, J. C. McDonald, O. J. A. Schueller, and G. M. Whitesides, “Rapid prototyping of microfluidic systems in poly(dimethylsiloxane),” *Anal. Chem.*, vol. 70, no. 23, pp. 4974–4984, 1998, doi: 10.1021/ac980656z.

[14] R. Courson *et al.*, “Low-cost multilevel microchannel lab on chip: DF-1000 series dry film photoresist as a promising enabler,” *RSC Adv.*, vol. 4, no. 97, pp. 54847–54853, 2014, doi: 10.1039/c4ra09097g.

[15] G. Weisgrab, A. Ovsianikov, and P. F. Costa, “Functional 3D Printing for Microfluidic Chips,” *Adv. Mater. Technol.*, vol. 4, no. 10, 2019, doi: 10.1002/admt.201900275.

[16] R. Luttge, *Basic technologies for microsystems*. 2016.

[17] G. T. A. Kovacs, N. I. Maluf, and K. E. Petersen, "Bulk micromachining of silicon," *Proc. IEEE*, vol. 86, no. 8, pp. 1536–1551, 1998, doi: 10.1109/5.704259.

[18] C. H. Lin, G. Bin Lee, Y. H. Lin, and G. L. Chang, "A fast prototyping process for fabrication of microfluidic systems on soda-lime glass," *J. Micromechanics Microengineering*, vol. 11, no. 6, pp. 726–732, 2001, doi: 10.1088/0960-1317/11/6/316.

[19] Y. Xia and G. M. Whitesides, "Soft lithography," *Angew. Chemie - Int. Ed.*, vol. 37, no. 5, pp. 550–575, 1998, doi: 10.1002/(sici)1521-3773(19980316)37:5<550::aid-anie550>3.3.co;2-7.

[20] J. Cottet, C. Vaillier, F. Buret, M. Frénéa-Robin, and P. Renaud, "A reproducible method for µ m precision alignment of PDMS microchannels with on-chip electrodes using a mask aligner," *Biomicrofluidics*, vol. 11, no. 6, 2017, doi: 10.1063/1.5001145.

[21] P. Spuul, P. Y. Chi, C. Billottet, C. F. Chou, and E. Génot, "Microfluidic devices for the study of actin cytoskeleton in constricted environments: Evidence for podosome formation in endothelial cells exposed to a confined slit," *Methods*, vol. 94, no. May, pp. 65–74, 2016, doi: 10.1016/j.ymeth.2015.09.001.

[22] S. Haeberle and R. Zengerle, "Microfluidic for Lab-on-a-Chip," *Compr. Microsystems*, vol. 2, pp. 463–516, 2007, doi: 10.1016/B978-044452190-3.00038-0.

[23] W. Snyder, G. Bilbro, Y. S. Han, R. Whitaker, and S. Pizer, "Image Relaxation: Restoration and Feature Extraction," *IEEE Trans. Pattern Anal. Mach. Intell.*, vol. 17, no. 6, pp. 620–624, 1995, doi: 10.1109/34.387509.

[24] S. Ota, H. Suzuki, and S. Takeuchi, "Microfluidic lipid membrane formation on microchamber arrays," *Lab Chip*, vol. 11, no. 15, pp. 2485–2487, 2011, doi: 10.1039/c1lc20334g.

[25] D. J. Paterson, J. Reboud, R. Wilson, M. Tassieri, and J. M. Cooper, "Integrating microfluidic generation, handling and analysis of biomimetic giant unilamellar vesicles," *Lab Chip*, vol. 14, no. 11, pp. 1806–1810, 2014, doi: 10.1039/c4lc00199k.

[26] M. Abkarian, E. Loiseau, and G. Massiera, "Continuous droplet interface crossing encapsulation (cDICE) for high throughput monodisperse vesicle design," *Soft Matter*, vol. 7, no. 10, pp. 4610–4614, 2011, doi: 10.1039/c1sm05239j.

[27] D. van Swaay *et al.*, "Advances in Transport Phenomena 2011," *Lab Chip*, vol. 3, no. 11, pp. 1434–1440, 2012, doi: 10.1039/C2LC41121K.

[28] K. Karamdad, R. V. Law, J. M. Seddon, N. J. Brooks, and O. Ces, "Studying the effects of asymmetry on the bending rigidity of lipid membranes formed by microfluidics," *Chem. Commun.*, vol. 52, no. 30, pp. 5277–5280, 2016, doi: 10.1039/c5cc10307j.

[29] M. C. Blosser, B. G. Horst, and S. L. Keller, "CDICE method produces giant lipid vesicles under physiological conditions of charged lipids and ionic solutions," *Soft Matter*, vol. 12, no. 35, pp.

7364–7371, 2016, doi: 10.1039/c6sm00868b.

[30] K. Karamdad, R. V. Law, J. M. Seddon, N. J. Brooks, and O. Ces, "Preparation and mechanical characterisation of giant unilamellar vesicles by a microfluidic method," *Lab Chip*, vol. 15, no. 2, pp. 557–562, 2015, doi: 10.1039/c4lc01277a.

[31] A. S. Utada, E. Lorenceau, D. R. Link, P. D. Kaplan, H. A. Stone, and D. A. Weitz, "Monodisperse double emulsions generated from a microcapillary device," *Science (80-.).*, vol. 308, no. 5721, pp. 537–541, 2005, doi: 10.1126/science.1109164.

[32] J. Petit, I. Polenz, J. C. Baret, S. Herminghaus, and O. Bäumchen, "Vesicles-on-a-chip: A universal microfluidic platform for the assembly of liposomes and polymersomes," *Eur. Phys. J. E*, vol. 39, no. 6, 2016, doi: 10.1140/epje/i2016-16059-8.

[33] S. Deshpande, Y. Caspi, A. E. C. Meijering, and C. Dekker, "Octanol-assisted liposome assembly on chip," *Nat. Commun.*, vol. 7, pp. 1–9, 2016, doi: 10.1038/ncomms10447.

[34] S. Maktabi, J. W. Schertzer, and P. R. Chiarot, "Soft Matter Dewetting-induced formation and mechanical models (GUVs) with controlled inner-leaflet," pp. 3938–3948, 2019, doi: 10.1039/c9sm00223e.

[35] E. Lorenceau, A. S. Utada, D. R. Link, G. Cristobal, M. Joanicot, and D. A. Weitz, "Generation of polymerosomes from double-emulsions," *Langmuir*, vol. 21, no. 20, pp. 9183–9186, 2005, doi: 10.1021/la050797d.

[36] S. Y. Teh, R. Khnouf, H. Fan, and A. P. Lee, "Stable, biocompatible lipid vesicle generation by solvent extraction-based droplet microfluidics," *Biomicrofluidics*, vol. 5, no. 4, pp. 1–12, 2011, doi: 10.1063/1.3665221.

[37] L. Lu, J. W. Schertzer, and P. R. Chiarot, "Continuous microfluidic fabrication of synthetic asymmetric vesicles," *Lab Chip*, vol. 15, no. 17, pp. 3591–3599, 2015, doi: 10.1039/c5lc00520e.

[38] K. Al Nahas *et al.*, "A microfluidic platform for the characterisation of membrane active antimicrobials," *Lab Chip*, vol. 19, no. 5, pp. 837–844, 2019, doi: 10.1039/c8lc00932e.

[39] T. Bhatia, T. Robinson, and R. Dimova, "Membrane permeability to water measured by microfluidic trapping of giant vesicles," *Soft Matter*, vol. 16, no. 31, pp. 7359–7369, 2020, doi: 10.1039/d0sm00155d.

[40] T. Robinson, P. Kuhn, K. Eyer, and P. S. Dittrich, "Microfluidic trapping of giant unilamellar vesicles to study transport through a membrane pore," *Biomicrofluidics*, vol. 7, no. 4, 2013, doi: 10.1063/1.4816712.

[41] K. A. Dresser *et al.*, "Song1996," vol. 30701, no. December, 1996.

[42] C.-C. Lin, M. Bachmann, S. Bachler, K. Venkatesan, and P. S. Dittrich, "Tunable Membrane Potential Reconstituted in Giant Vesicles Promotes Permeation of Cationic Peptides at

Nanomolar Concentrations," *ACS Appl. Mater. Interfaces*, vol. 10, p. acsami.8b12217, 2018, doi: 10.1021/acsami.8b12217.

[43] M. Abkarian, M. Faivre, and A. Viallat, "Swinging of red blood cells under shear flow," *Phys. Rev. Lett.*, vol. 98, no. 18, pp. 2–5, 2007, doi: 10.1103/PhysRevLett.98.188302.

[44] M. Abkarian and A. Viallat, "Vesicles and red blood cells in shear flow," *Soft Matter*, vol. 4, no. 4, pp. 653–657, 2008, doi: 10.1039/b716612e.

[45] K. Yamamoto and J. Ando, "Endothelial cell and model membranes respond to shear stress by rapidly decreasing the order of their lipid phases," *J. Cell Sci.*, vol. 126, no. 5, pp. 1227–1234, 2013, doi: 10.1242/jcs.119628.

[46] T. Tabouillot, H. S. Muddana, and P. J. Butler, "Endothelial cell membrane sensitivity to shear stress is lipid domain dependent," *Cell. Mol. Bioeng.*, vol. 4, no. 2, pp. 169–181, 2011, doi: 10.1007/s12195-010-0136-9.

[47] B. S. Packardt and D. E. Wolf, "Fluorescence Lifetimes," 1985.

[48] A. Yamada, S. Lee, P. Bassereau, and C. N. Baroud, "Trapping and release of giant unilamellar vesicles in microfluidic wells," *Soft Matter*, vol. 10, no. 32, pp. 5878–5885, 2014, doi: 10.1039/c4sm00065j.

[49] B. Sebastian, T. Favero, and P. S. Dittrich, "The Effects of Shear Force Transmission Across Vesicle Membranes," *J. Phys. Chem. Lett.*, vol. 8, no. 24, pp. 6128–6134, 2017, doi: 10.1021/acs.jpclett.7b02676.

[50] F. Sturzenegger, T. Robinson, D. Hess, and P. S. Dittrich, "Membranes under shear stress: Visualization of non-equilibrium domain patterns and domain fusion in a microfluidic device," *Soft Matter*, vol. 12, no. 23, pp. 5072–5076, 2016, doi: 10.1039/c6sm00049e.

[51] M. Yanagisawa, M. Imai, T. Masui, S. Komura, and T. Ohta, "Growth dynamics of domains in ternary fluid vesicles," *Biophys. J.*, vol. 92, no. 1, pp. 115–125, 2007, doi: 10.1529/biophysj.106.087494.

[52] J. H. Miller, W. E. Wilson, C. E. Swenberg, L. S. Myers Jr, and D. E. Charlton, "Rapid Communication," *Int. J. Radiat. Biol.*, vol. 53, no. 6, pp. 901–907, 1988, doi: 10.1080/09553008814551261.

[53] N. Yandrapalli and T. Robinson, "Ultra-high capacity microfluidic trapping of giant vesicles for high-throughput membrane studies," *Lab Chip*, vol. 19, no. 4, pp. 626–633, 2019, doi: 10.1039/C8LC01275J.

[54] M. Schaich *et al.*, "An Integrated Microfluidic Platform for Quantifying Drug Permeation across Biomimetic Vesicle Membranes," *Mol. Pharm.*, vol. 16, no. 6, pp. 2494–2501, 2019, doi: 10.1021/acs.molpharmaceut.9b00086.

[55] T. Robinson, "Microfluidic Handling and Analysis of Giant Vesicles for Use as Artificial Cells: A Review," *Adv. Biosyst.*, vol. 3, no. 6, pp. 1–9, 2019, doi: 10.1002/adbi.201800318.

[56] M. E. Solmaz *et al.*, "Optical stretching of giant unilamellar vesicles with an integrated dual-beam optical trap," *Biomed. Opt. Express*, vol. 3, no. 10, p. 2419, 2012, doi: 10.1364/boe.3.002419.

[57] U. Delabre *et al.*, "Deformation of phospholipid vesicles in an optical stretcher," *Soft Matter*, vol. 11, no. 30, pp. 6075–6088, 2015, doi: 10.1039/c5sm00562k.

[58] F. Paquin, J. Rivnay, A. Salleo, N. Stingelin, and C. Silva, "Multi-phase semicrystalline microstructures drive exciton dissociation in neat plastic semiconductors," *J. Mater. Chem. C*, vol. 3, no. 207890, pp. 10715–10722, 2015, doi: 10.1039/b000000x.

[59] L. M. Lee and A. P. Liu, "A microfluidic pipette array for mechanophenotyping of cancer cells and mechanical gating of mechanosensitive channels," *Lab Chip*, vol. 15, no. 1, pp. 264–273, 2015, doi: 10.1039/c4lc01218f.

[60] L. M. Lee, J. W. Lee, D. Chase, D. Gebrezgiabhier, and A. P. Liu, "Development of an advanced microfluidic micropipette aspiration device for single cell mechanics studies," *Biomicrofluidics*, vol. 10, no. 5, 2016, doi: 10.1063/1.4962968.

Chapter IV

4 On-Chip Micropipette – Initial approach

In this chapter, I will introduce the first microfluidic platform that we developed to build an on-chip micropipette, in order to characterize mechanical properties of Giant unilamellar vesicles. The purpose of this chip is to first, develop a micropipette where an object is led to a trap and its deformation inside the trap is characterized over the increase of pressure applied on the object. Secondly, to validate the chip's operation, we characterized a known lipid composition, in this case DOPC lipid. The fabrication technique is based on the classical approach of level-by-level microfabrication. However, the fabrication of such device is challenging: we developed 3 different microfabrication processes that enable obtaining the required 3-level channels including a micropipette in the intermediate level, with micrometric alignment, with sufficiently low adhesion and roughness. I will explain in details the optimization and the development of the 3 different techniques, even if the final experiments were all conducted in the silicon-glass final chip. Because of the square form of the micropipette, we extended the theoretical analysis of micropipette, valid for cylindrical geometries that microfabrication does not allow, to the on-chip geometry, by considering the deformation of a vesicle in a square cross-section trap. We confirmed the validity of our approach thanks to experiments performed on GUVs with well-characterized compositions: the obtained values of the membrane stretching modulus are in quantitative agreement with the literature. However, we encountered many difficulties during the fabrication and the microfluidic experiments, due to some limitations that I will be discussing in the end of the chapter. Even if some experiments were conducted on DOPC membranes that were challenged with nano particles of copolymers micelles, not enough data were obtained to show them in this chapter. More data of such experiments will be elaborated in the next chapter, in the second approach of the micropipette on chip.

4.1 Microfluidic design to trap GUVs and characterize their deformation

4.1.1 Design Principle

In order to characterize the mechanical properties of GUVs, a microfluidic chip should (1) steer the GUV to a confinement trap, (2) permit to characterize its deformation inside the microtrap upon pressure increase. Such functionality was achieved by designing a chip in the spirit of the one developed by Lee and Liu in 2014 [1],[2]. It is composed of the following elements ***(Figure IV-1A)***: an inlet/outlet, two long channels coming from the inlet and going to the outlet, a trap and bypass channels in the middle way between the two inlet and outlet channels. The GUVs sizes are of the order 10 to 40 microns. Therefore, the trap width and height were set to be 10 µm to be efficient without leading to a too high hydraulic resistance, and all the other channels widths and heights, where the GUVs circulate, were set to be 40 µm. Generally, traditional glass micropipettes are cylinders and the objects propagate symmetrically as they are aspirated inside the micropipette. Likewise, to maintain the symmetric deformation, the trap was built in the middle height of the channels ***(Figure IV-1B).***

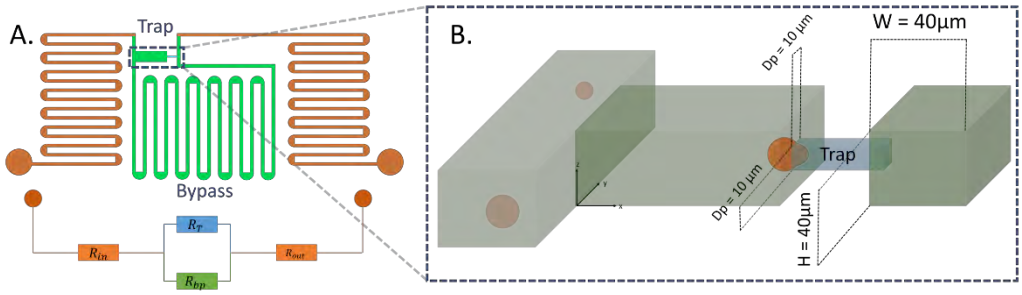

Figure IV-1: A) Overview of fluidic chip design (not to scale). Bottom: scheme of hydraulic resistances. B) Configuration of the micropipette: flow separates into a bypass channel and a 10 x 10 µm² square cross-section trap. Once a GUV is blocked, no more liquid flows into the trap and the vesicle is submitted to a pressure difference fixed by the viscous pressure drop in the bypass channel.

4.1.2 Hydraulic Resistance Choices

An appropriate choice of the hydraulic resistance of each chip segment, fixed by setting their dimension, is crucial for the operation of the chip. For a channel with a square cross-section, the hydraulic resistance is: $R = 28.4\,\eta\,L\frac{1}{h^4}$ as seen in chapter III, with η is the dynamic viscosity of the liquid, L is the length of the microfluidic channel and h is its height. In order to confine the GUV inside the trap, the bypass and trap's hydraulic resistances were chosen equal: $R_{bp} \approx R_T$. It was a practical compromise for two reasons. First, if the bypass resistance was smaller than the trap's, the GUVs would prefer to go in the bypass instead of the traps, thus making the study almost impossible (very

low probability to trap a GUV). On the other hand, if we increase so much the resistance of the bypass, it will highly increase the time of filing of the chip. The flow thus equally separated into the bypass and trap branches: an object arriving at the interception of the trap and the bypass had 50% chance to be trapped. As already mentioned, the lateral dimensions of the trap were fixed at 10 µm in width and height. Its length was set to a minimum of 50 µm in order to properly block GUV and have enough length to measure its deformation, without it being expelled rapidly. With minimum lateral dimensions of the bypass also fixed (40 µm not to block other GUVs), it led to a length of 1.3 cm for the bypass.

Once a GUV was trapped, it stopped the flow in the trap channel (the resistance of the trap became very high) and the other objects coming continued their way to the bypass through the outlet channels, without disturbing the trapped vesicle. In this situation, the pressure difference ΔP applied on the trapped object corresponds to the viscous pressure drop inside the bypass channel. While the trap was blocked the chip operated as a simple pressure divider (analogous to the voltage divider of electronics)[3], so that ΔP was fixed by ΔP_{tot}, the total pressure difference applied to the chip, multiplied by the ratio of the bypass resistance to the total chip resistance: $\Delta P = \Delta P_{tot} R_{bp}/(R_{bp} + R_{in} + R_{out})$. Long inlet/outlet channels, with associated high resistance, permitted to control the required low level of pressure drop applied on the object with increased precision: in our typical experiments, $\Delta P = \Delta P_{tot}/5$.

An increase of pressure led to the deformation of the trapped object, and more specifically to an increase of the length of the GUV entering the trap channel. An analysis of this deformation was used to characterize the mechanics of the trapped GUV, like in micropipette experiments. Details of the computation, and in particular extension of the classical cylindrical micropipette to our geometry, are given in the next paragraphs.

The fabrication of such design is highly challenging as it is made of three levels of channels, where the micropipette is hanging in the middle of two deeper levels. Moreover, the lateral alignment of the micropipette in the middle of the channels is critical. In order to fulfill these requirements, an extensive work and development of different fabrication techniques had to be made.

4.2 Microfabrication approaches for PDMS and Dry Film Chips

As mentioned in the previous section, the chip design required a total channel height of 40 µm and an intermediate 10 µm-high trap level. Suitable imaging resolution required working with a high numerical aperture microscope objective. The associated working distance being small, the transparent substrate had to be thin (typically 170 µm, the thickness of standard microscope coverslip). All the requirements mentioned above generated the necessity to fabricate a 3-layer

microfluidic chip with the second one hanging in the middle of the two above and below with an alignment better than 10 µm, as illustrated in ***Figure IV-2*** for the silicon-glass approach. The first two fabrication techniques that we developed are PDMS-PDMS chips and Dry Film chips techniques. The two techniques are described below, but they were finally discarded because of their respective limitations (difficulty of reproducible alignment, and adhesion issues).

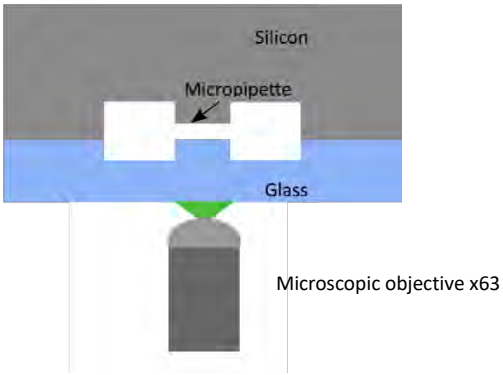

Figure IV-2 : Schematic of the cross-section architecture required to obtain a micropipette integrated in a microfluidic network. This scheme is to be followed and applied for all techniques that were tried, but here we represent the Silicon-Glass approach with the micropipette hanging in the middle. The glass is thinner than the silicon section for optical reasons.

4.2.1 PDMS-PDMS technique

4.2.1.1 Principle of the microfabrication technique

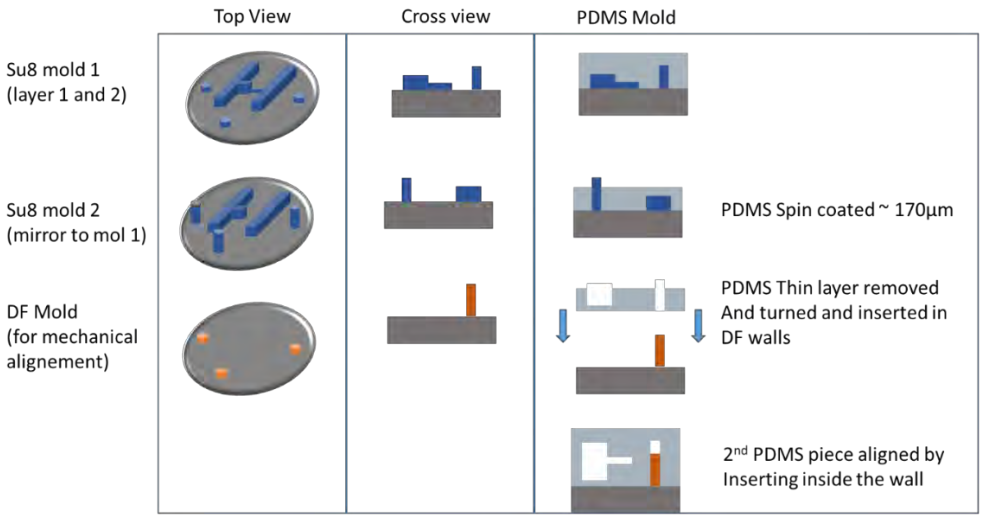

Figure IV-3: Mechanical alignment for PDMS chip fabrication: Top view and cross view of the two SU8 molds fabrication, and the DF mold. Cross view of the PDMS mold fabrication and the mechanical pre-alignment using the walls of the DF mold.

The choice to use PDMS as a first material for the microfluidic chips is because generally it is the easier choice regarding the transparency, the fabrication technique and the possibility to create endless PDMS chips with one silicon wafer (chapter III). However, this was not a classical way of PDMS fabrication. First of all, the chip is a 3 level channels, with the micropipette hanging in the middle of two deeper channels. This required the fabrication of two SU-8 silicon molds: first one containing two

levels (the main deep channel and the micropipette) and the second one contains the second part of the channel, designed as a mirror of the first wafer. The final idea would be to have both PDMS mold of both wafers, channels aligned with a precision of less than 10 microns and bonded together to have the final three levels PDMS chip ***(Figure IV-3)***. Which brings me to the first challenge of this fabrication technique: the alignment of the two PDMS molds with such precision. The second requirement mentioned before is the small working distance of the microscopic objectives and the high resolution needed to well characterize the elongation of the GUVs inside the trap. This meant that one of the PDMS mold needed to be around 170 µm thickness. Therefore, the second challenge would be: manipulating a thin PDMS layer without harming it. Combining the challenges together, we had to come up with the following solutions to align both PDMS molds: a purely optical alignment, and a mechanical-optical alignment.

4.2.1.2 Challenging Alignment techniques

The two layers had to be bonded together with a precise alignment (better than 10 µm), which is known to be very challenging for PDMS chips, in particular since the second block constituting the down part of the chip needed to be unmolded and reversed before being sealed to the bottom one [4]. To that purpose, we worked on three different alignment techniques: the first one relied on a mechanical-optical alignment using a wafer with walls as a way to pre-align the PDMS mold by depositing the PDMS on it. The second technique was an optical alignment using photolithography machines. And finally, an optical-manual alignment technique.

Mechanical - optical Alignment

The aim of the mechanical-optical alignment is shown in ***Figure IV-3 – line 3:*** A third silicon wafer is fabricated out of lamination of DF (dry film) resist layers to build high walls of 700µm. The purpose of this wafer is to be able to pre-align the two PDMS layers by deposing the thin one first inside the walls, and then under the microscope, aligning the second PDMS mold with the first one. To do so, an additive layer of *SU8 500 µm* was added on the second mold, to build 4 poles dispersed on the wafer to be used as pre-alignment marks for the PDMS molds ***(Figure IV-4)***. Therefore, when the PDMS is spin coated on the wafer, then removed, holes would be opened in the PDMS, where the poles were.

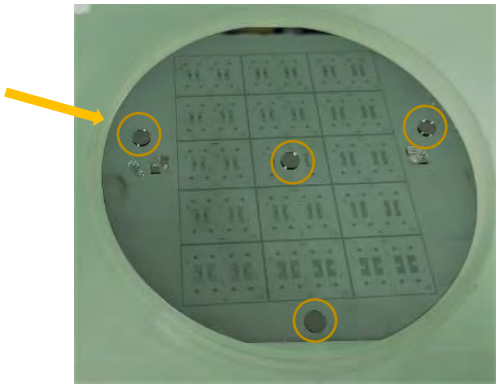

Figure IV-4: Picture of the second SU8 mold with 15 µm thickness of the channels and 500 µm of the Poles. The poles are added so that when the PDMS is spin coated on this wafer, the holes would already have opened.

Optical alignment

For the optical technique, we tried two strategies: photo-aligner machines *(Suss MA6)* where the thick PDMS layer was placed instead of the mask and the thin layer was placed instead of the wafer, and the other strategy is using a machine dedicated to nanoimprint lithography *(Nanonex).* The two layers were aligned by using the optical microscope of the machines. They were then put in hard contact to provoke the bonding between the two layers. Because the thickness of the PDMS mold is important in this case, we chose the amount of the PDMS needed to have 3 mm thickness (usual thickness of a glass mask in the photolithography or *Nanonex* machine).

Manual - optical alignment

For the manual alignment, we had to first, cut the PDMS molds chip by chip. Then, under the binocular microscope, we tried to align the two pieces of PDMS manually. A small tip we tried, to avoid direct bonding after plasma activation of the two surfaces, was to add a drop of isopropanol on one of the surfaces, which allows a possible sliding to adjust the alignment after the two surfaces are in contact. And once the isopropanol is evaporated, the two PDMS pieces would be finally bonded.

All three techniques suffered from the following downsides: the thin PDMS layer was very difficult to manipulate and was deformed laterally (typically by a few hundred microns on a 4 inches' wafer) while it was removed from the wafer, which made the alignment almost impossible. Second, PDMS-PDMS sealing required a plasma activation to be achieved just before the bonding, usually less than one minute. By the time to set the PDMS slabs on the machine and do the alignment, the bonding was not efficient enough to ensure leakage free chips. To overcome these limitations, we tried a second fabrication strategy based on dry films lamination which will be detailed in the following paragraphs.

4.2.1.3 PDMS chips - experimental results

Since we couldn't have successful chips that the design imposes (trap in the middle of two deep channels), we decided to use the thick PDMS to fabricate a 2-level chip instead of 3. Therefore, we cut the mold into small pieces (chip by chip) and bonded them to thin glass slides (170 µm). We used those chips to first, characterize the efficiency of trapping of our design, secondly, try the first experiments of mechanical characterization of the GUVs, by trapping them and increasing the pressure progressively. And finally, to characterize the surface-membrane adhesion. While conducting these experiments in Florence, we came to the following conclusions:

- First, the trapping rates was 100 % successful, which would mean, our resistance calculations were well chosen. However, since we were unable to fabricate the complete three level chip, the height of the bypass channel was almost the half, which increased the resistance of the bypass by 16x the designed value, which caused an overcrowding of GUVs seen in ***Figure IV-5A***.
- Second, and as expected, since the trap is not in the middle anymore, due to the fabrication problems, the GUVs deformation is not symmetric inside the trap. ***(Figure IV-5B)***
- And finally, PDMS surface is usually hydrophobic, which means the GUVs (with hydrophilic heads) do not adhere on the PDMS. Moreover, PDMS is transparent. This meant that PDMS was a good candidate to our microfluidic chips, but unfortunately, the design was not compatible with this fabrication technique.

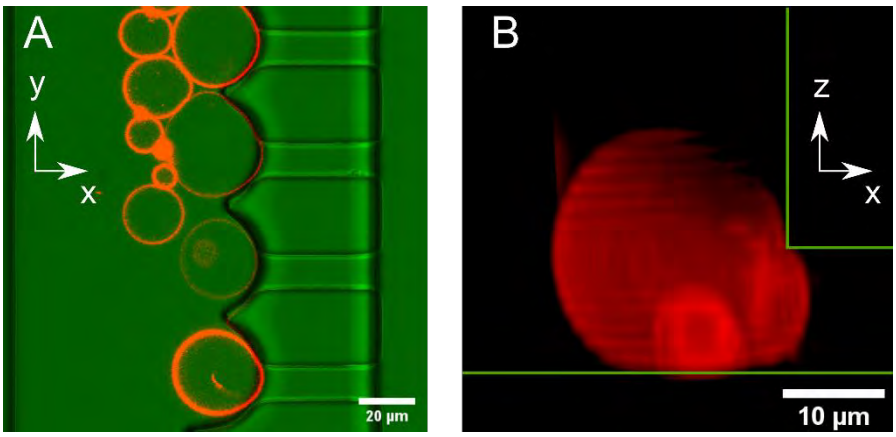

Figure IV-5: A) Overlay Confocal microscopy images of DOPC lipid GUVs trapped in a multiple trap microfluidic PDMS chip. DOPC membranes are stained with Lissamine rhodamine Fluophore. A) Shows the traffic GUVs on the entrance of the traps. B) 3D reconstruction of the DOPC GUVs trapped showing the asymmetric deformation of the GUV inside an asymmetric trap, due to the fabrication.

4.2.2 Dry Film chips

The dry films *(DF 1000 series, EMF)* are thin sheets of an epoxy photoresist, initially developed for microelectronics and packaging, that we demonstrated in our lab to be suited to make multilevel microfluidic chips with free hanging structures [3]. The channels were directly fabricated within DF,

on top of a 170 µm glass wafer for imaging compatibility. This technique inherently permitted alignments with micrometric accuracy; and it was faster and cheaper with respect to the use of SU8 epoxy resist.

4.2.2.1 DF Fabrication process

The chip is made with the lamination of 5 layers of DF on a glass substrate with UV-insolation after each layer as shown in ***Figure IV-6***. The first layer is lamination of 5 µm of DF 1005 (a), to keep all walls of channels of the same chemical surface. The second layer is made by the lamination of 15 µm of DF (3 layers of DF1005) (b-c), to open the bottom part of inlet/outlet and bypass channels. The third layer is made by the lamination of DF 10 µm (2 layers of DF1010) (d-e), which is the trap layer. In order to avoid collapsing of the following layers, the temperature of lamination was reduced to 65 °C instead of 100 °C, the pressure was reduced from 2.5 bars to 2 bars, and the speed of the laminator was increased from 0.5 m/min to 1 m/min. The fourth layer is the lamination of DF 15µm (3 layers of DF1005) (f-g), to continue the opening of the upper part of the inlet/outlet and bypass channels. Finally, the fifth layer is DF 25 µm (1 layer of DF1025) (h-i), it closes all the channels but open the holes of the inlet and the outlet for the microfluidic connectivity. The wafer was then cut into small chips containing each one 4 channels. ***Figure IV-7*** shows the final DF chip and a close up view on the channels.

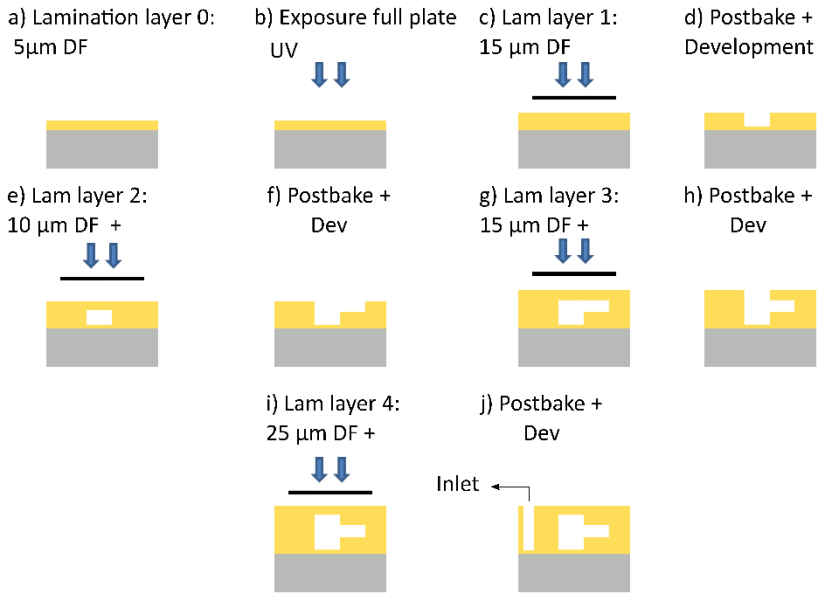

Figure IV-6: Process flow of fabrication of DF mold to fabricate directly the chips on 170µm glass wafer.

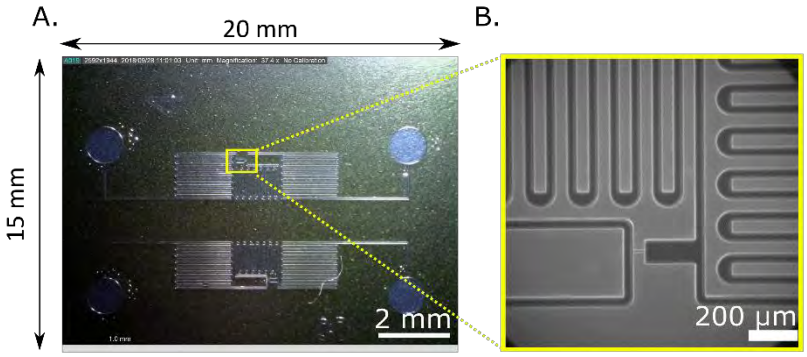

Figure IV-7: Dry Film microfluidic chip. A) Final DF chip after cutting the glass wafer into an assembly of 2 chips each. The chip is 2 x 1.5 cm². The big holes represent the inlet and outlet of the chip, which the serpentine channels in between. B) Microscopic picture of the channels.

4.2.2.2 DF chips - experimental results

Nevertheless, this technique faced downsides and some could affect our deformability measurement. First of all, making several laminations on a thin glass wafer (required for optics) generated a lot of constraints on the wafer and could cause its breaking before the end of the process. Secondly, DF is auto-fluorescent on a large wavelength scale, which added a high level of noise to the fluorescent signal of the dyes inserted in the vesicle membranes. The visualization of the membrane close to the walls in the trap was tricky, and thus complicated the deformation analysis ***(Figure IV-8A).*** Finally, the GUVs adhered on the walls of the chips which led to its contamination, altering the deformation of the object inside the trap ***(Figure IV-8B)***. This was due to the surface chemistry of the DF that we do not fully control, even an anti-adhesion solution (BSA 1% in deionized water at room temperature) did not solve the issue. We thus switched to a third fabrication approach, based on glass and silicon processing.

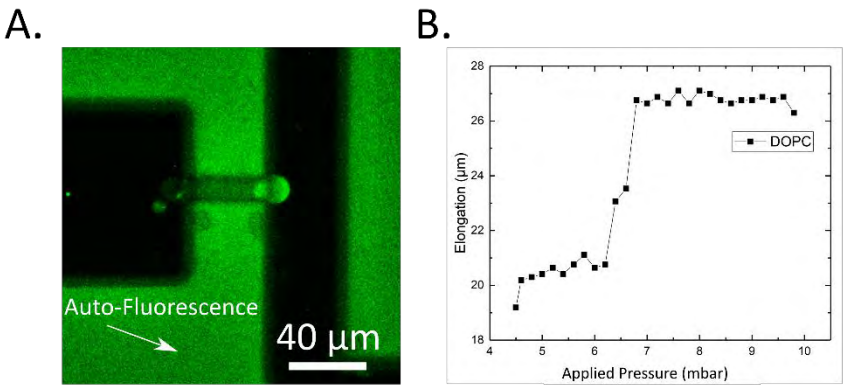

Figure IV-8: Drawback of the DF chips. A) Auto fluorescence of the DF material matching the fluorescence of the GUVs; GUVs stuck on the membrane because of the adhesion of the membrane to the DF. B) Jumps of deformation curve as function of the pressure applied, caused by the adhesion.

4.3 Silicon-Glass Final chip

The technique used was etched Silicon channels bonded on etched glass channels. This technique answered all the disadvantages we faced with PDMS and dry film. First, regarding alignment, glass and silicon are hardly deformable, which means their deformation was very low during the process. We used a glass type with the same thermal expansion coefficient as silicon, which prevented any misalignment upon heating or cooling. Second, the bonding process allowed sealing the two wafers with alignment accuracy better than 10 µm. Moreover, for imaging glass is perfectly transparent and not auto-fluorescent at all. Finally, glass and silicon chemistry (mainly silanol groups) led to low GUV adhesion, and was suited for surface modification to decrease it further. The process is described in the following.

4.3.1 Introducing Plasma Etching Concept

4.3.1.1 Dry plasma etching

I will decompose the title "dry plasma etching concept" into several definitions in order to give a whole view of the concept of this technique. Etching refers to the process of removing parts of a material which surface is not protected by a mask. The etching technique is used a lot in the micro-nano fabrication technologies in order to fabricate very small but defined patterns on a given substrate, such as silicon, glass or even some kind of resists. The etching could be done in different media: could be liquid, and in this case, it's called wet etching. For example, when etching gold deposit layer using a gold etchant (a liquid solution), used in microelectronics for the fabrication of semi-conductor devices. Or, in other cases like here, the media could a plasma, and this case it's called dry etching. Both dry and wet etching techniques have advantages and disadvantages, therefore, depending on the possibility and the application that is used for, it will be better to use one or another.

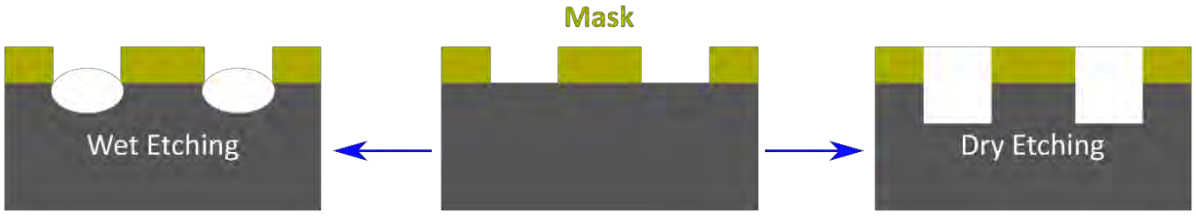

Figure IV-9: Silicon surface shape after wet (isotropic) and dry (anisotropic) etching. Both techniques come from the same mask deposition (Figure in the middle) [5].

Wet etching is based on a chemical liquid interaction with the silicon substrates. In this case, the etching form is isotropic: the etching process follows the crystalline structure of the silicon. This provokes both lateral and vertical etching, giving the rounded form as seen in ***Figure IV-9,*** which does not respect the desired design in microfabrication. On the opposite, dry etching is based on the equilibrium of both ions and chemical compounds (this point will be explained in details later). This

leads to have straight walls with ~ 90° angles, when the process is well optimized. The main advantage and disadvantage of the wet and dry etching techniques are shown in ***Table IV-1***. Note that some expressions (such as selectivity) will be explained in the following sections. Due to the alignment step of the two final wafers, and to respect the design of the chip including the hydraulic resistance, the walls had to be straight. All of that led to use the plasma dry etching to fabricate our microfluidic chips.

Table IV-1: Main advantages and disadvantages of the wet and dry etching techniques.

	Advantages	**Disadvantages**
Wet Etching	✓ High selectivity ✓ Easy process ✓ Scalable (25 wafers at a time)	o Manipulation of dangerous acid o No control of etching profile o Low resolution
Dry Etching	✓ No use of dangerous acid ✓ Profile control of etching ✓ Critical dimensions control ✓ High resolution	o Need of big specific equipment o Use of toxic and corrosive gases o Re-deposition of no volatile particles o 1 wafer at a time

Plasma is one of the 4 states of matter and which consists of gas of ions and electrons (removed from atoms) moving around. In the laboratory, plasma can be artificially made by heating a neutral gas and adding an electromagnetic energy to the point where the ionized gaseous substance becomes highly electrical. The concept of the plasma dry etching and in particular the reactive ion etching (RIE) is the following [6]:

Reactive Ion Etching is based on both physical and chemical dry etching mechanism to achieve high resolution. When generating the plasma in the chamber where the substrate is, the electrons (which are faster than the ions) are accelerated towards the electrodes and therefore do not intervene anymore with the substrates. The ions existing in the plasma are accelerated towards the lower electrode, where the substrate is. When the ions hit the wafer, phenomena called the bombardment, it creates the physical etching and evaporate the species of the etched material. When the reactive species coming from the plasma hit the wafer, they form volatile products which is the chemical etching, and which are led to the pumping and outside the chamber to not intervene anymore with the substrate. That is why it is important to have the good combination of substance in the gas to create volatile products, otherwise, those products will sediment in the surface and create the micro-masking effects [7]. Micro-masking effects happens when the volatile products stay on the substrate and create some sort of masking that prevents from the etching to happen in that specific place, causing therefore and non-homogenous and rough surface. It is mandatory to find the right parameters for both physical and chemical etching to have a good surface plot resolution [8].

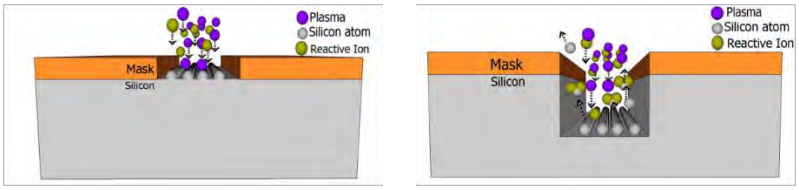

Figure IV-10 The Reactive Ion Etching (RIE) process [5]. *This process combines both physical and chemical dry etching of silicon wafers.*

4.3.1.2 Bosch and continuous process

For our micro channels, we need to etch 15 µm at least inside the silicon and the glass. In micro-nano fabrication, this is considered as deep etching. Therefore, we tried two different techniques of plasma etching: Bosch process and continuous process, both considered as RIE (Reactive Ion Etching) process ***(Figure IV-10)***. However, both had their advantages and their disadvantages. The machine used to etch deepness less than 1 mm was *Alcatel AMS4200*. But first, it is important to know the composition of the plasma gas used, therefore the ions and reactive components present to etch the channels before moving to explain the two different processes.

The gas used for the plasma etching is fluorinated gas: SF_6. Other gases are possible to use such as chlorine gas (Cl_2) or Bromine (Hbr). These other gases have the possibility to create volatile reaction products ($SiCl_4$ and $SiBr_4$) [8], which are mandatory to avoid micro masking effects. However, when going from a Fluorine-to chlorine-and bromine-based chemistry, etch rates decrease and etching mechanism need more ion assistance [7]. In general, for silicon materials, the choice is easy and large since several alternatives exist which allow to tune the etching efficiency. Once ionized, the reactive species (F) accelerate to the substrate, in this case silicon, and create (SiF), which instantly evaporates. The chemical species (the radicals), hit the silicon wafer and creates the volatile components (SiF_4) that are aspirated and pumped outside the chamber [5]. On the other hand, a passivating gas is needed to protect the lateral walls from being bombarded with ions, and therefore blocks lateral etching. In this case, the gas used is C_4F_8 and it does not interact with the substrate.

Continuous process

Continuous process consists of a continuous flow of the etching gas (SF_6) and passivation gas (C_4F_8) at the same time. The first trial of this test on silicon wafers was not very successful (as seen in ***Figure IV-11***), because the edges under the resist were over etched. Since this process is known to be highly selective, our hypothesis comes from the fact that the resist was not well developed. Therefore, we had to optimize the process, by changing the flow of the gases used and improve our photolithography process and the choice of resist that we made.

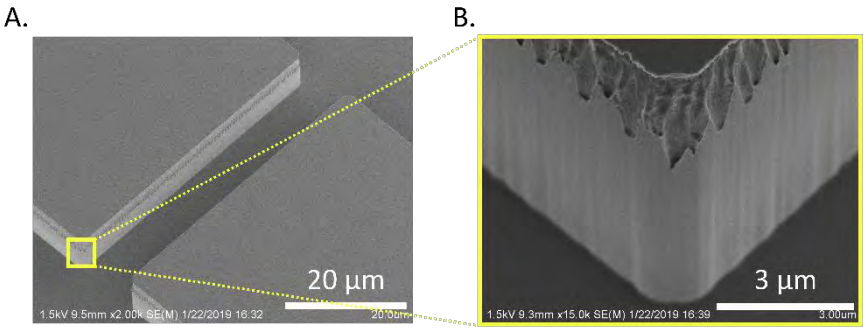

Figure IV-11: SEM pictures of silicon etched channel by the continuous flow process. A) shows the whole micropipette channel (10 x 10 µm²) with borders that are over etched. B) is a close-up image of the border of the channel.

Bosch Process

Bosch process [9] is named after the German chemist Carl Bosch who was the inventor of this etching technique, which became the main industrial process used for etching. It consists in two alternative modes of etching then passivating. In fact, C_4F_8 (passivation layer) is used as a protective layer everywhere on the silicon and the masks but most importantly on the lateral wall side of the substrate. During the Etching step, a part of the sidewall material deposit is removed because of the ions, but still protecting the etching from becoming isotropic (lateral etching) [9]. This works because the etching rate is faster vertically than horizontally. Because of this alternative mode of both gases, a nano meter scalloping structures appears on the vertical wall of the etched substrate (As seen in ***Figure IV-12***).

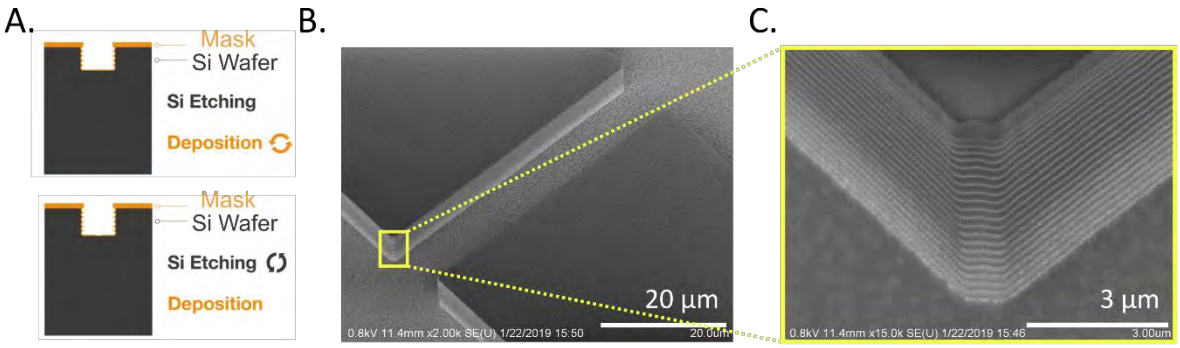

Figure IV-12: Bosh process. A) shows the alternative process between Si etching and the passivation steps, which creates the scalloping structures on the vertical wall of the silicon (in orange). B) and C) are SEM images of microchannel etched using the bosh process. B) shows the whole micropipette channel (10 x 10 µm). C) is a close-up image of the vertical wall after etching, which shows the scalloping structures.

4.3.1.3 Parameters' effect on etched Silicon surface

In order to have a successful result when etching any chosen substrate, optimization of a lot of parameters, before, during and after the etching, is necessary [8]. Luckily, and due to all the development scientist and engineers, especially in the clean room of LAAS, have been doing to

advance this technique, some parameters were already optimized. The parameters that are related to the equipment are:

- Gas choice defines the species in the plasma.
- The Gas flow rate is responsible for the renewal of the species; the pressure is also responsible for the renewal of species, but also for the density of ions and the reactive species.
- The power is responsible for the ionic bombardment and the plasma density; if we increase the power of the plasma, the density of radicals and ions as well as the ion energy increases. However, if the power is really high, there is a risk of overheating the substrate and therefore deteriorate the mask and the surface.
- The temperature of the chuck where the substrate is put during the etching process and which will define the temperature of the substrate by itself is also in an important factor: in fact the temperature influences the etching rate (µm/min), the selectivity, and the surface morphology [7], [8]. Selectivity is the ratio of etching material over mask etching, which is important to consider when choosing the resist which defines the mask.
- Time of etching will determine the depth of etching. The longer we etch, the deeper the channels are.
- And finally, the reactor cleaning to avoid contamination. For example, in the case of the glass: if the glass used is not pure silica, when etching, a lot of metals do not become volatile. As consequence, the metals re-deposit everywhere in the chamber and on the substrate creating contamination.

4.3.2 Optimization of the Silicon etching parameters

4.3.2.1 Silicon etching in continuous process

In the case of the *continuous process,* as seen in the SEM picture in ***Figure IV-11***, over etching of the silicon appeared under the resist layer. This could be problematic for us for two reasons during the microfluidic experiments. When sending the GUVs inside the channels, the roughness created on the edge could lead to first, GUVs adhering on the walls, and in the case of the micropipette, faulting our results. And second, it could also lead to blowing up the GUVs in case they touch it and therefore, contaminating the chip.

We tried three different positive resists to determine which one was the best, in terms of etching result: *ECI3012* (3 µm), *AZ4562* (5 µm) and *AZ40XT* (13 µm). The selectivity of the continuous process is 4/1, which means for every 4 µm of silicon etching, we lose 1 µm of the mask (resist). Since we were etching only 10 µm, we needed a minimum resist thickness of 2.5 µm which was achieved with the tree different resist. After characterizing the channels in SEM, we saw that the over etching problem was still existing. Since it was a well-studied process, our theory went back to check the state of the

resist after the photolithography step. Generally, characterizing the wafers after each fabrication step is important as we keep track in case of problems.

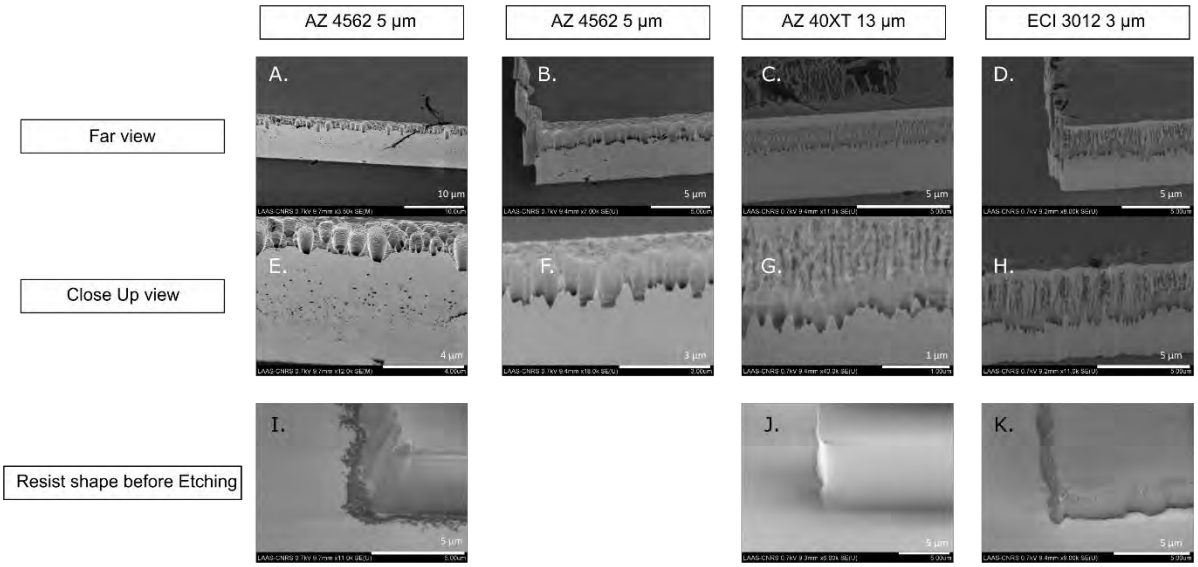

Figure IV-13: SEM images of silicon etched channels and walls of resist after photolithography process. A-D) are the far view of channels showing the over etching on the borders, right under the resist. E-H) are close up view of the over etching borders. I-K) are the close up view of the vertical walls of the resist.

When characterizing the resist after the photolithography steps, two things pop up directly in ***Figure IV-13 (I)*** *(AZ4562)* and ***(K)*** *(ECI3012)*: first one is the dark residue on the silicon wafer right down the base of the resist, and second, the walls of the resist are not 90 ° angle but around 112 ° angle. These two characterizations could be the reason of the over etching results. In fact, because of the residues and the angle formed by the resist, there are part of the silicon which are supposed to be on the same level are etched after others because the residue and the resist are covering these parts. That's why the over etching is just on the top part of the silicon channel. Another interesting comparison, is between ***Figure IV-13 (E)*** and ***(F)***: in these two etching processes, we used the same resist. After the first etching test ***(E)***, some dark points appear in the middle of the wall of the etched channel. This is due to the ions that are hitting the walls during etching, which means the ratio of the flow between passivating gas and the etching gas is not enough. That's why in ***(F)***, we increased the flow of the passivating gas (C_4F_8) from 37 to 39 sccm and reduced the flow of the etching gas (SF_6) from 38 to 36 sccm. By doing so, we protected better the lateral walls of our channels, and avoided to black dots related to the lateral etching.

4.3.2.2 Silicon etching in Bosch process

In parallel, we were also working on the **Bosch process,** as it showed more promising results in the first etching level ***(Figure IV-12).*** The process of both photolithography and etching is shown in ***Figure IV-14.***

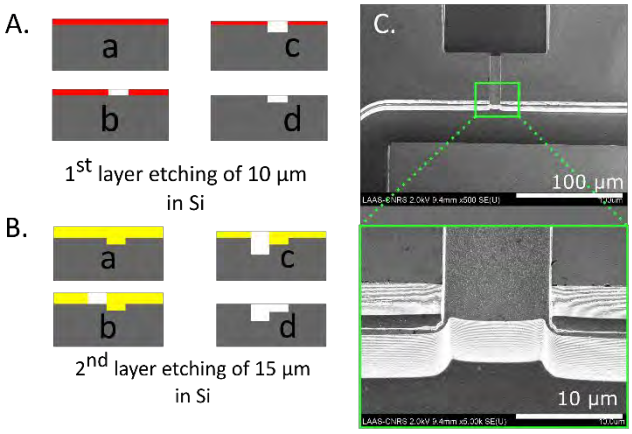

Figure IV-14: Work flow and characterization of Silicon etching process. A) and B) are the work flow of consecutively the first silicon etching level of 10 µm and the second etching level of 15 µm. C) is the SEM picture of the total silicon etching, with a close-up image to better visualize the alignment and the scalloping patterns due to the Bosch process.

The full details of this process are in the material and methods chapter. But briefly, in order to etch the first level of the chip, containing the micropipette and a part of the channels, *ECI* photoresist is deposit on a silicon wafer ***(Figure IV-14A(a-c))***. The first level of 10 µm is then etched ***(Figure IV-14A(d))***. The remaining resist was removed, though it was hard removing it as the resist was partially burnt from all the process of the etching. The wafer then was well cleaned and functionalized for the second etching part. This process has low selectivity and therefore a thin layer of resist should be sufficient as a mask for the second etching. However, the first 10µm etched level ought to be completely covered and protected to avoid any etching in it ***(Figure IV-14B(a-c))***. Evidently, we changed the ECI resist used in the first etching level which can be 3 µm thick maximum, to *AZ40XT* of 20 µm thickness to assure to total cover of the etched channel. Another important step to consider during lithography, is the alignment of the resist with the etched channel in order to avoid any misalignment of the channels during the etching process. Finally, the second level containing only the main channels was etched for 15 µm depth giving a total channel depth of 25 µm ***(Figure IV-14B(d))***.

In order to characterize the depth of the etched channels, we had to characterize first the selectivity of this process (the selectivity was defined from other etching processes but we had to be sure it is still applicable to our process). Selectivity is defined by the etching rate of the silicon over the etching rate of the mask. Therefore, using a mechanical profilometer, we first measure the deepness of the channels with the rest of the resist, and then once the resist is removed, we re-measure the channels, and with that we will have characterized the selectivity of this process: 10/1.

In order to characterize the surface of the channels, SEM images were taken from far and close to the walls ***(Figure IV-14(C))***. First thing we realize is that the alignment is as good as 0.5 µm. This small misalignment is due to the photolithography step, where we have to align the second level to the first one. Nevertheless, 500 nm of misalignment could be a small problematic for our microfluidic

experiment of the deformation of the GUVs. Second thing, is that the bottom surface of the etched channels is very smooth, which shows that the parameters used from the flow gases, to the power and pressure, were very well optimized to avoid any kind of over etching or of micro-masking. And finally, looking closely to the walls of the channels, we notice the scalloping structures of 200 nm. Even so, these scalloping, in nm scale, were too small to cause any problem during the microfluidics experiments. Hence, we decided to go with the Bosch process.

4.3.3 Development of glass etching process

4.3.3.1 Plasma etching of Borofloat glass type

Glass etching was way more critical and way more difficult than silicon etching. In fact, there wasn't a well-defined process for glass etching, and with Aurélie Lecestre, engineer in the cleanroom of LAAS, we had to develop this process. Because the sealing of the silicon and glass parts of the chip was performed with anodic bonding, it required to work with non-purely silica glass type: Borofloat B33, rich in B_2O_3 (12.5%), Na_2O/K_2O (4.5%) and Al_2O_3 (2.5%). A total of impurities of 20%. Therefore, a specific process had to be developed for glass etching.

The different parameters we had to optimize for the glass etching are:

- The resists: in fact, some resists are more unstable than others regarding all the chemical reactions inside the chambers, and some can handle lower or higher temperatures than others without burning or cracking.
- The temperature: as it's already demonstrated, temperature of support of the wafer has strong effect on the surface of the etched substrate. Moreover, lower temperatures improve selectivity [10].
- The etching time, which also depends on the etching rate, because it would determine the depth of the etching, in this case we wanted 15 µm.
- And finally, the decontamination of the chamber. In fact, the etch rate in this case is really slow, so we will have to etch for longer time. Therefore, we had to divide the total time of etching to several small interval and to decontaminate the chamber in between.

Considering the mask, the first resist we used to make the mask was *AZ 125 NXT* negative resist, on a 170 µm thickness glass wafer, at -15 °C**.** As seen in ***Figure IV-15A***, the channel at the end is enlarged and rugosity is important. Not to mention that due to the etching process, the glass wafer of 170 µm was broken after removing it from the chamber, by the end of the process. *AZ 125 NXT* resist and the wafer of 170 µm thickness were both discarded.

We tried another resist, *AZ 15 NXT* negative resist, under -15 °C. SEM pictures in ***Figure IV-15B*** showed no enlargement of the channels, however the resist cracked and created crackers in the wafers also.

Not to mention the rugosity which is still important. This high rugosity is due to the presence of metal in the Borofloat glass type. In fact, the reactive species created from the plasma are not volatile, therefore, instead of being pumped outside the chamber, they redeposit on the glass substrate, which enhance the micro-masking effects, which explains the rugosity we are seeing. By over developing the resist during the photolithography step, we were able to reduce a little bit this rugosity ***(Figure IV-15C and D).***

Finally, the choice of resist landed on *AZ 15 NXT* with an over developing step after the photolithography process. We increased the temperature to try to avoid cracking the resist which cannot handle temperature shock (-15 °C). The microscopic image shows very high rugosity when etching under 20 °C **(F),** however the resist did not crack at all. Nonetheless, under 0°C **(E),** the resist burnt into powders and contaminated the channels and the chambers.

The final process of glass etching is described in Materials and Methods.

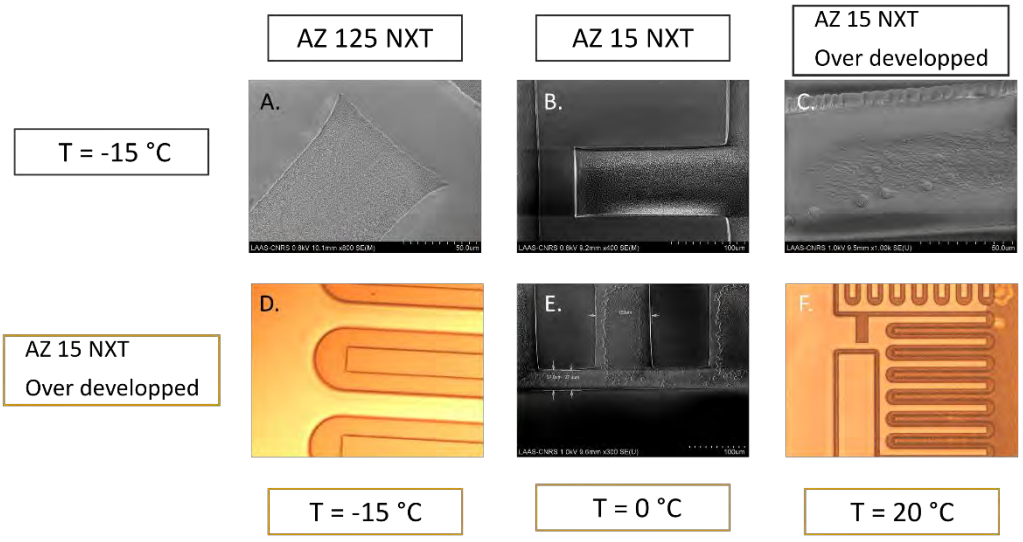

Figure IV-15: Characterization of the different processes of glass etching. A – C) are SEM images of glass etched channels under the same temperature (-15 °C) but changing the mask by changing the resist and resist conditions. D – F) are SEM and microscopic images of etched channels using the same resist for the mask (AZ 15 NXT), and changing the temperature from -15 °C to 20 °C.

4.3.3.2 Complementary wet etching to reduce surface rugosity

The plasma etching of a non-pure silica glass, containing in particular metallic compounds, caused non-homogeneous etching. The associated self-masking led to roughness of order 2 µm, observed by a mechanical profilometer and with SEM imaging ***(Figure IV-16 A – C).*** It might have led to GUV adhesion, and could degrade the optical quality of microscopy imaging.

Therefore, a complementary wet etching was necessary to reduce the important rugosity: we tried two different tests: HF 5% diluted in water, and a mixture of (5% of HF 5%, 10% of HCl 37% and 85 %

of DI water). We characterized the etching rate of both solutions to see which one is more efficient; the first one gave 0.025 µm/min and the mixing solution was 0.075 µm/min.

SEM characterization showed that the mixed solution is more efficient to reduce the rugosity. This etching was almost isotropic even for a material made of silica mixed with metallic impurities, which made the surface more polished. It typically reduced the roughness to less than around 100 nm peak-peak on a 100 µm zone ***(Figure IV-16 D – F)***.

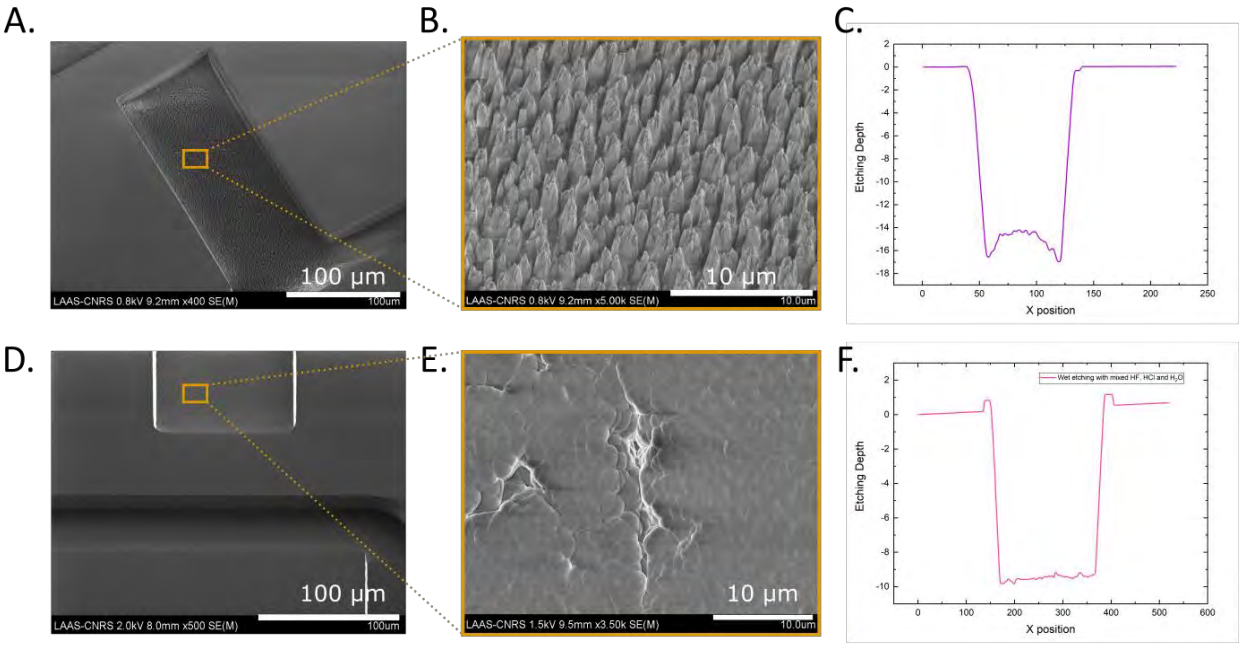

Figure IV-16: Characterization of the glass etched channels after dry etching and after wet etching. A) and B) are SEM images of the channel after plasma etching. B) shows spikes heterogeneous corresponding to the rugosity formed because of the non-pure glass. C) is a graph of the profilometer data which shows the big non-homogenous depth of the trap. D) and E) are SEM images of the channels after a complementary step of wet etching. E) shows a smoother surface of the channel which is also proven by the profilometer data F), where the trap shows more homogenous surface depth.

4.3.4 Glass-Silicon anodic bonding and glass wafer thinning

4.3.4.1 Anodic bonding

Anodic bonding is the mechanism of sealing two wafers together (metal-glass or glass-silicon), with no intermediate layer. Specially in our case, to avoid any adhesion of the vesicles on the walls of the chip, it was necessary to keep both wafers sealed with nothing between them. Anodic bonding has the advantage of offering a strong sealing (high bonding strength), and high chemical resistance [11] in case chemical solutions were to be injected during the experiments. In addition, the glass we chose (B33) and silicon have close thermal expansion coefficient, which means under high temperature, both glass and silicon deformed at the same ratio [12].

The two etched wafers were then cleaned, aligned and sealed together by anodic bonding. The bonding machines we used permitted a precise enough optical alignment, that was made either

before (for *Suss wafer bonder*) or after (for *AML WB4* wafer bonder) heating. Standard bonding parameters were used: 370 °C, 4 mA current, 200 N force, 10 minutes.

4.3.4.2 Glass wafer thinning and smoothing

Finally, high numerical microscope objectives used for high-resolution optics have a short working distance and are typically corrected for 170 µm-thick glass coverslips, but the whole fabrication process had to be carried out on at least 500 µm-thick glass wafers for mechanical manipulation. Consequently, an additional step of thinning and smoothing was made to reduce glass thickness from 500 µm to 170 µm. It consisted in Chemical Mechanical Polishing *(Logitech PM5 machine)*. Several slurry liquids were sequentially used, consisting in aqueous suspensions of alumina particles with decreasing sizes 20 µm, 6 µm, 1 µm at the different steps. The first two steps aimed at efficiently removing materials, to decrease the wafer thickness. The third step (1 µm diameter for the alumina particles), followed by a final polishing step with a softer plate and 0.3 µm diameter Cerium oxide particles, enabled to obtain a low roughness surface (rms roughness r_q<100 nm), with optical quality suited for microscopy. The processed wafer was finally cut into small chips containing each one four channels ready to be used ***(Figure IV-17).***

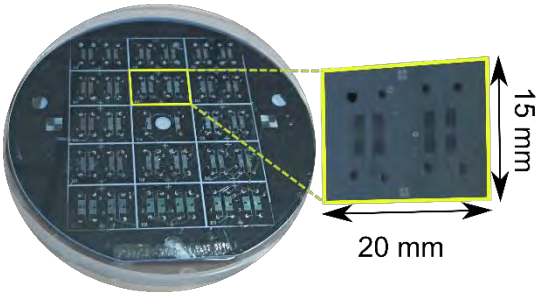

Figure IV-17: Silicon-glass wafer cut into an assembly of 4 chips each, with a dimension of 20 x 15 mm each.

4.4 Microfluidic experiments to trap and characterize the deformation of GUVs in Si-Glass microfluidic chips

The experimental set-up used in this section is the same one used for all the microfluidic experiments that have been done in the sections before (in the PDMS and DF chip) and what will be used in the following sections. GUVs were fabricated using electroformation method (detail of the protocol is in materials and methods).

4.4.1 Microfluidic experiment

A pressure controller (*Fluigent MFSC* – EZ, 0-69 mbar) was used to control the flow in the chip. The chip was pre-treated with an aqueous 0.5 mg/mL *β-casein* solution for 20 minutes, or equivalently with an aqueous 1% *Bovine Serum Albumin* (BSA) solution for 20 minutes, to reduce the adhesion of the GUVs on the walls of the channels. The GUVs solution was then sent in the chip, replacing all the casein (or BSA) solution. In order to avoid any presence of bubbles inside the chip, we made sure that the chip is completely filled with the solutions and the same for the tubes connected to it. To do so, we usually send the solution of functionalization from the outlet of the chip, and then the GUVs from the inlet, insuring a continuous flow inside the chip.

Once a GUV was trapped, the pressure was fairly increased in order to pre-stress the object to eliminate possible defects. Then we decreased the pressure down to the one releasing the GUV from the trap: it defined experimentally the equilibrium pressure P_0, where the object started to get trapped and where the hydrostatic pressure is zero and the flow is completely stopped. We started the deformation study by increasing the applied pressure difference by $\Delta P_{tot} = 0.2$ mbar every 3 seconds, in order to leave enough time for the GUV to equilibrate at each pressure value. Upon each pressure increasing, the GUV was elongated inside the trap. Due to the pressure division imposed by the resistance $\Delta P = \Delta P_{tot} R_{bp} / (R_{bp} + R_{in} + R_{out})$, giving $\Delta P = \Delta P_{tot}/5$, the corresponding increase of ΔP on the object was 0.04 mbar. It corresponded to steps in membrane tension of order $\Delta\tau$ ~ 0.02 mN/m for a 20 µm vesicle. The applied pressure was increased until the GUVs left the trap upon a certain pressure.

The images were acquired using a spinning disk microscope (Leica Microsystems), controlled with micromanager software. The wavelength used for excitation and emission for the GUVs membrane were λ_{exc} = 560 nm and λ_{em} = 580 nm**.** Image analysis was carried out using Image J software.

The chips are reusable upon and efficient cleaning with ethanol to dissolve the lipids that might have attached to the walls or inside the trap. However, due to the long serpentine channels, the cleaning is not always efficient, and therefore for critical measurement such as the micropipette-aspiration, it is better to change the chip after each experiment.

4.4.2 Image analysis and treatment of the deformation of the GUVs inside the trap

When the GUV is trapped a picture of the initial state is taken and the vesicle diameter at rest is measured to calculate the initial area A_0. A picture is later taken upon every increase of the pressure, which shows the vesicle diameter outside the pipette and the elongation inside the trap. Images were then treated using *ImageJ* program. In fact, after the first deformation of GUV inside the micropipette upon a given pressure, a line was drawn on the tip of the cap of the GUV. This line indicates the beginning of the increase of the elongation of the GUV inside the trap. In the same picture, the diameter of the vesicle outside the micropipette was also measured and referred to as D_v. For the rest of the pictures and for each deformation, the new elongation is measured, from the line drawn in the first picture until the new tip of the cap. This measurement will be referred to as ΔL, as it is the difference of elongation between two different state. Again, D_v is measured in each picture (for each pressure). As a summary, the parameters that are measured in each picture, which corresponds to a new increasing pressure are the diameter of the vesicle D_v and the elongation starting from the line drawn on the first GUV cap. To keep track of all the data, the parameters were all handled in excel sheets.

4.5 Results and discussion

Before advancing to the results, a correction of the analytical formulas leading to the area expansion and membrane tension had to be done, to represent the real shape of the GUVs inside the trap. A comparison between the traditional circular and the square micropipette results is made.

4.5.1 Computational formulas for rounded-square GUV shape

Traditional micropipette aspiration experiments are made with circular glass micropipette as shown in ***Figure IV-18A***. However, for our chips, but also for the one used in the work of Liu and Lee [1], [2], the pipette did not have a cylindrical geometry, but rather a square cross-section. Consequently, the deformation of a GUV entering the trap is likely not to follow the previous relationship detailed in chapter III. Let us point out that most fabrication approaches, inherently layer-by-layer, lead to this type of shape, so that extending the cylindrical case to this one can be of significant interest.

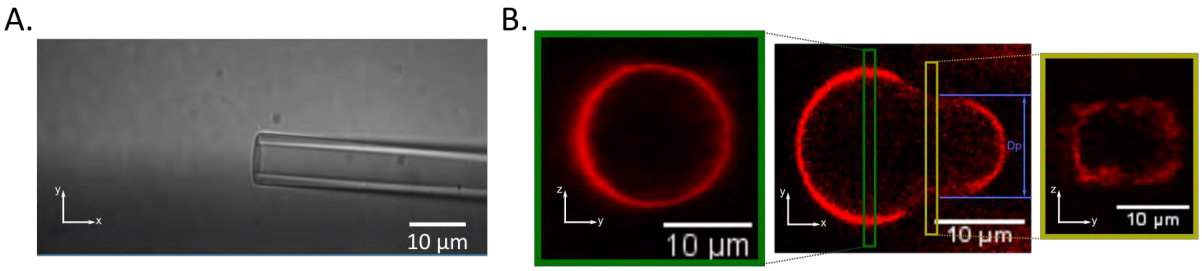

Figure IV-18: Phase contrast (A) and Confocal microscopy images (B) of different configurations of micropipette aspiration experiments. A) Contrast phase image of glass microscopy with a circular shape. B) Experimental cross section of the vesicle perpendicular to the axis X of the pipette (left and right pictures, in the YZ plane), and along the axis X of the pipette (middle picture, in the XY plane).

Before going through the equations, we assumed that because the trap is square, the shape of the GUVs deformation had to be different than the circular one. Contrary to the cylindrical case, the part of the vesicle extending along the walls of the traps cannot totally be in contact with the walls because of sharp corners. It results in the presence of liquid surrounding it, connected to the downstream trap channel. We assumed that the GUVs had "rounded-square" shape at the entrance of the pipette. To prove our theory, we made a z-stack movie for the trapped GUV. In image J, we used the orthogonal views option to cut our z-stack in the *(yz)* axis, in order to see the real shape of the GUV outside the trap and right at the entrance. ***Figure IV-18B,*** even if it is a bit blurry, shows that outside the trap the GUV had a perfect circular shape, whilst right at the entrance of the trap, the GUV seems to have a rounded square shape. The rounded square shape is noticeable by: a square shape of the GUV when touching the walls of the chip, and rather a circular shape of the corners of the square where the membrane does not touch the walls. Therefore, we call the new shape a "*rounded-square"* shape deformation.

In this work, we analyze the geometry of the vesicle and obtain an analytical formula to deduce quantitatively tension and area increase from experiments, for the on-chip micropipette. We focus on the actual vesicle geometry when entering a pipette with square cross-section (trap channel). We consider that the extremity of the vesicle in the trap adopts a half-sphere shape, which is the simplest constant curvature shape, with a diameter equal to the width of the pipette D_p, also equal to its height.

$$\tau = \frac{\Delta P D_p}{4(1 - D_p/D_v)} \qquad 4\text{-}1$$

Equation *4-1* has been obtained for the cylindrical case by equating the Laplace pressure jump on the upstream and downstream sides, that have similar curvatures for the rounded-square shape and for the cylindrical cases. This relation still holds for the rounded-square geometry, where the cylinder diameter just needs being replaced by the pipette width (or height). The rounded square shape consists in flat portions in the middle of each channel face, connected by quarters of cylinders in the

corners. ***Figure IV-19*** shows the details of the shapes of the GUVs in longitudinal cross section (left) in order to well determine the parameters such as the curvature's diameter. The right images show the perpendicular cross section shape inside a square trap and a cylindrical one. Details of computations, as well as the exact formula (before the Taylor expansion) are given below:

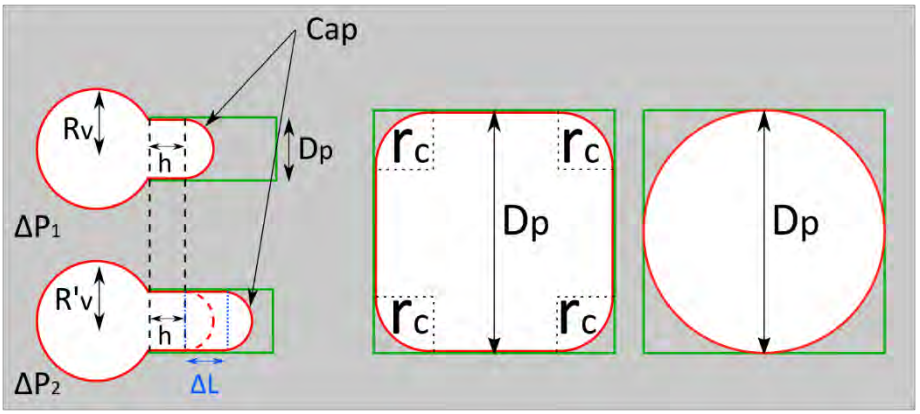

Figure IV-19 Micropipette configuration inside a square cross-section tube. Left: longitudinal cross-sections for two different applied pressure drops. Right: cross-section perpendicular to the pipette, showing the GUV shape.

When the pressure applied on the GUV is changed, the vesicle enters the pipette by an additional length ΔL, which changes its area. As in the traditional cylindrical micropipette, we relate the amount of area increase to ΔL ***(Figure IV-19).***

4.5.1.1 Volume conservation

First, we express the conservation of the GUV volume between two states, due to negligible membrane permeability to water on the experimental time scale. We compute the volume according to the following:

The total volume of the GUV when it is deformed inside the trap is the sum of the volume of the sphere outside the trap (with a radius R_v), the volume of the elongation side the trap (the elongation is h) and finally the volume of the spherical ending of the GUV inside the trap (cap) ***(Figure IV-19)***. Since the trap has a square cross section, the GUV adopts a "rounded square" shape inside the pipette, and illustrated in ***Figure IV-19.*** Therefore, the volume of the elongation inside the trap ($V_{elongation}$) is equal to its length of extension multiplied by the cross–section area of this shape, namely:

$$V_{elongation} = (D_p^2 + \pi r_c^2 - 4r_c^2)\,(h + \Delta L) \qquad 4\text{-}2$$

With the notation h for the elongation of the GUV inside the trap in a reference state (main vesicle radius R_v), and $(h + \Delta L)$ the elongation of the GUV inside the trap for a second state (main vesicle radius R'_v), volume conservation reads:

$$\frac{4}{3}\pi R_v^3 + \left[D_p^2 + \pi r_c^2 - 4r_c^2\right]h + V_{cap} = \frac{4}{3}\pi R_v^{3\prime} + \left[D_p^2 + \pi r_c^2 - 4r_c^2\right](h + \Delta L) + V_{cap} \qquad 4\text{-}3$$

Since V_{cap} is constant during the increase of pressure, this equation simplifies according to:

$$\frac{4}{3}\pi R_v^{3\prime} = \frac{4}{3}\pi R_v^3 - \Delta L\left[D_p^2 + \pi r_c^2 - 4r_c^2\right] \qquad 4\text{-}4$$

Finally:

$$R_v' = R_v\left[1 - \frac{3}{4\pi}\frac{\Delta L\left[D_p^2 + (\pi - 4)r_c^2\right]}{R_v^3}\right]^{1/3} \qquad 4\text{-}5$$

The mechanical equilibrium of the GUV cap (hemisphere of radius $D_p/2$) with the corners inside the pipette enables to relate r_c to the pipette geometry, by imposing the following curvatures equality, that originates from Laplace law relating pressure drop to tension: $\frac{1}{Dp/2} + \frac{1}{Dp/2} = \frac{1}{r_c}$. It reads:

$$r_c = \frac{D_p}{4} \qquad 4\text{-}6$$

By using this relationship, equation ***(4-5)*** becomes:

$$R_v' = R_v\left[1 - \frac{3}{4\pi}\frac{\Delta L\, D_p^2}{R_v^3}\left(\frac{3}{4} + \frac{\pi}{16}\right)\right]^{1/3} \qquad 4\text{-}7$$

For large vesicles, $\frac{\Delta L\, D_p^2}{R_v^3} \ll 1$, and a first-order Taylor expansion of equation (***4-7)*** leads to:

$$R_v' = R_v\left[\,1 - \frac{\Delta L\, D_p^2}{4\pi R_v^3}\left(\frac{3}{4} + \frac{\pi}{16}\right)\right] \qquad 4\text{-}8$$

4.5.1.2 Area Increase

Similarly to the volume conservation computation, we decompose the GUV into three regions in order to relate its area increase to the changes in its elongation inside the pipette: the total area of the GUV is the sum of the area of the sphere outside the trap, the area of the elongation inside the trap and finally the area of the cap ***(Figure IV-19).*** The area increase thus reads:

$$\begin{aligned}\Delta A = &\left[4\pi R_v'^2 + (4D_p - 8r_c + 2\pi r_c)(h + \Delta L) + A_{cap}\right] \\ &- \left[4\pi R_v^2 + \left(4D_p - 8r_c + 2\pi r_c\right)h + A_{cap}\right]\end{aligned} \qquad 4\text{-}9$$

Which simplifies into:

$$\Delta A = (4\pi R_v'^2 - 4\pi R_v^2) + \left(4D_p - 8r_c + 2\pi r_c\right)\Delta L \qquad 4\text{-}10$$

Inserting equation (***4-6)*** into this result, we obtain:

$$\Delta A = 4\pi R_v^2 \left[\frac{R_v'^2}{R_v^2} - 1\right] + \Delta L.Dp\left(2 + \frac{\pi}{2}\right) \quad 4\text{-}11$$

Replacing R_v' by its relation to R_v expressed in equation ***(4-7)*** it leads to:

$$\Delta A = 4\pi R_v^2 \left[\left[1 - \frac{3}{4\pi}\frac{\Delta L\, D_p^2}{R_v^3}\left(\frac{3}{4} + \frac{\pi}{16}\right)\right]^{2/3} - 1\right] + D_p \Delta L\left(2 + \frac{\pi}{2}\right) \quad 4\text{-}12$$

Replacing the pipette radius by its diameter D_v, it finally reads:

$$\Delta A = 4\pi R_v^2 \left[\left[1 - \frac{3}{4\pi}\frac{\Delta L\, D_p^2}{D_v^3}\left(\frac{3}{4} + \frac{\pi}{16}\right)\right]^{2/3} - 1\right] + D_p \Delta L\left(2 + \frac{\pi}{2}\right) \quad 4\text{-}13$$

For large vesicles, $\frac{\Delta L\, D_p^2}{D_v^3} \ll 1$, and a first-order Taylor expansion of equation ***(4-13)*** leads to:

$$\Delta A = \pi D_v^2 \left[1 - \frac{4}{\pi}\frac{\Delta L\, D_p^2}{D_v^3}\left(\frac{3}{4} + \frac{\pi}{16}\right) - 1\right] + D_p \Delta L\left(2 + \frac{\pi}{2}\right) \quad 4\text{-}14$$

$$= D_p \Delta L\left(2 + \frac{\pi}{2}\right) - \frac{\Delta L\, D_p^2}{D_v}\left(3 + \frac{\pi}{4}\right)$$

Or, equivalently:

$$\Delta A = \left(2 + \frac{\pi}{2}\right) D_p \Delta L\left[1 - 4\frac{D_p}{D_v}.\frac{\frac{3}{4} + \frac{\pi}{16}}{2 + \frac{\pi}{2}}\right] \quad 4\text{-}15$$

We can note that the first term $\left(2 + \frac{\pi}{2}\right) D_p \Delta L$ corresponds to the area of the vesicle inserted within the pipette (rounded square perimeter multiplied by tongue length), whereas the additional one (term proportional to D_p/D_v in the bracket) accounts for the diminution of the upstream vesicle area. Equation ***(4-15)***, even if similar in its form to equation ***(4-16)*** in the way area increase relates to measured length, differs by its numerical factors, and should be used to properly extract mechanical moduli from the experiments.

$$\Delta A = \pi D_p (1 - \frac{D_p}{D_v})\Delta L \quad 4\text{-}16$$

Equation ***(4-16)*** corresponds to the area increase of the GUV in a cylindrical shape micropipette, as seen in chapter II.

4.5.2 Results: characterization of DOPC GUV membranes

In order to validate our microfluidic chip, as well as the geometrical considerations developed in the previous paragraph, we measured the progressive deformation of vesicles with a well-characterized composition. Electroformed DOPC vesicles were captured and their deformation upon pressure increase was characterized, following the experimental procedure described previously. The successive shapes of a vesicle upon pressure increase (ΔL as function of ΔP) were captured by

confocal microscopy, as shown in ***Figure IV-20***. These measurements are the basis of all the analysis we need. However, it's a critical step because it consists in defining an initial area of the vesicle, A_0, from which all following measurements start from. It is not always easy to do, as A_0 corresponds to the very first deformation the vesicle undergoes [13], under low pressure. The advantage of our chip is the pressure divider that we included in the design due to the hydraulic resistance. This allowed us to divide the applied pressure by 5 to correspond to the pressure applied on the vesicle. When analyzing the images, we defined first A_0 which corresponded to the first deformation of the vesicle, and then measured the increasing of elongation inside the trap starting from that point. ***Figure IV-20A*** shows the progressive deformation of DOPC GUV inside the trap, where ΔL corresponds to the elongation inside it. ***Figure IV-20B and C*** is the measurements of respectively the GUVs diameter and the elongation inside the trap when undergoing an increasing pressure. The difference in the curves of the 3 different vesicles is because of their different diameters. The diameters of the vesicles did not change a lot, which is normal when the $D_v >> D_p$: the pressure applied on the vesicle is supposed to stretch it but keeping the diameters more or less the same. However, for the elongation curves, a difference is noticeable between the red and blue curve from one side, and the black one. Let's remember that the trap's size is 10 µm square section. The red and blue vesicles have diameters between 12 and 14 µm, only 1.2 and 1.4 times bigger than the trap. In this case, the GUVs are deformed continuously as we can see in the graph. On the other hand, the black vesicle of ~ 25 µm diameter, seems to have the following behavior: under low pressure, the increase of the elongation of the vesicle is important and then the curve seems to flatten showing a less important increase of the elongation with the increasing pressure. This defines the two characteristics of the bending and stretching regime, which will be better seen in the following area expansion-tension curves.

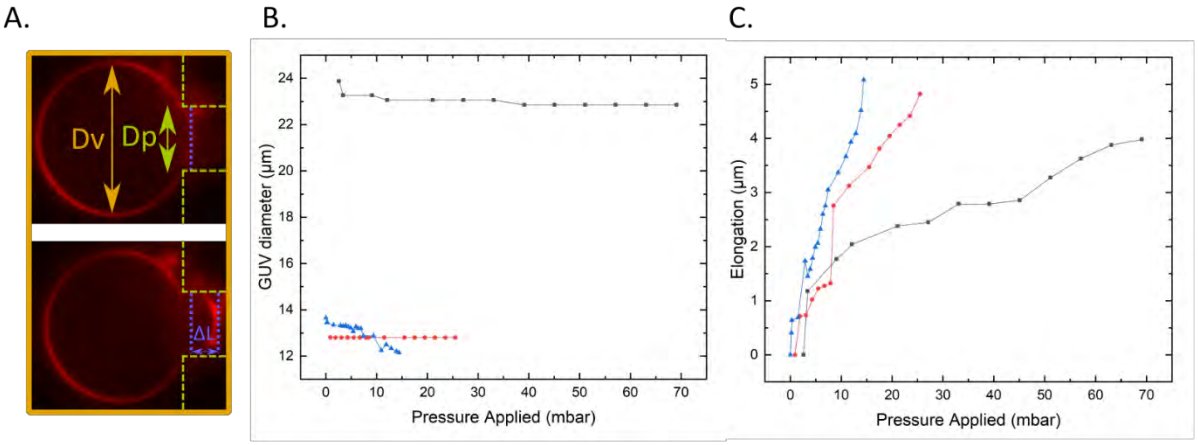

Figure IV-20: Experimental results of the on-chip micropipette experiment. A) are confocal images of a trapped GUV under ΔP_1, where the GUV is trapped but not yet deformed, and ΔP_2 where the GUV is already deformed inside the trap. Graph B) and C) shows respectively the slight decrease and the elongation of 3 different GUVs under pressure.

We first plot the evolution of τ (membrane tension) ***(4-1)*** as function of the apparent area expansion using the formulas demonstrated before for two different cases ***(Figure IV-21)***: the circular case for

the Cylindrical shape of the vesicle (α_{app} C) and the square cross-section case corresponding to the rounded square shape (α_{app} RS). The Apparent area is the area increase (demonstrated in ***(4-15)***), normalized over the initial area A_0.

$$\alpha_{app} = \frac{A - A_0}{A_0} = \frac{\Delta A}{A_0} \qquad 4\text{-}17$$

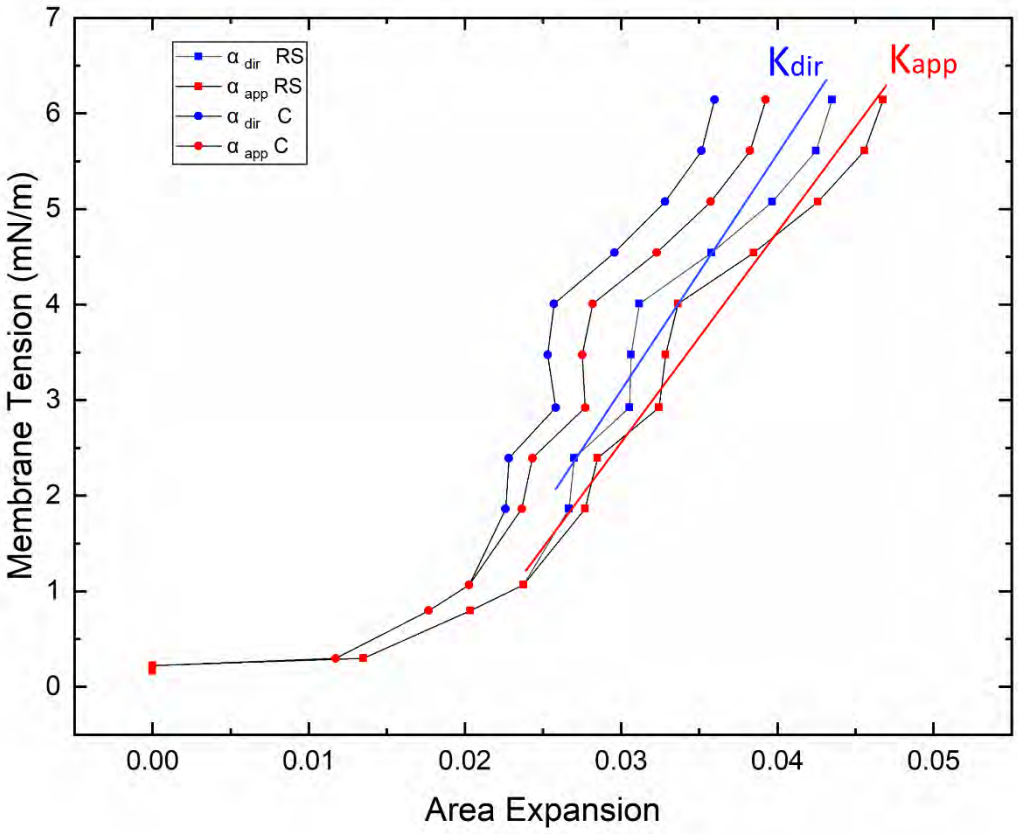

Figure IV-21: Graphs of membrane tension as function of the apparent (α_{app}) in red curves and direct (α_{dir}) blue curves area expansion for both cylindrical(C) and square cross section micropipette (RS).

By comparing the curves of the apparent area for the cylindrical shape and the rounded square shape, we realize that the there is a 15 % shift in the values for the DOPC membrane. In fact, the values of the apparent area are lower for the rounded square shape compared to the cylindrical one.

On another hand, the apparent area increase is a combination of the direct area increase per molecule and the remaining smoothing of undulations (as seen in chapter III). Consequently, for the experimental determination of the direct stretching modulus K_{dir}, the thermal undulations (contribution of the bending modulus to the apparent area increase) need to be subtracted. As detailed in reference [14], K_{dir} is thus deduced by fitting the slope of the direct area increase α_{dir}: $\tau = K_{dir}\alpha_{dir}$, where α_{dir} is deduced for each i-th experimental value from the formula:

$$\alpha_{dir}(i) = \frac{\Delta A(i)}{A_0} - \frac{kT}{8\pi\kappa_c}\ln(\tau(i)/\tau(1)) \qquad 4\text{-}18$$

Even if our design was able to divide the pressure applied on the object by 5, nonetheless, this division was not low enough to extract the bending modulus. In fact, for the pressure controller of 69 mbar, the minimum pressure that could be applied is 0.02 mbar (2 Pa) with a stability of 0.3 mbar (30 Pa). The bending modulus pressure range between 0.2 Pa and 100 Pa, which corresponds due to Laplace law to 0.001 < τ < 0.5 mN/m. This meant that a lot of measurements are missed in the start of the experiments and that corresponds to the bending regime. We thus fixed the bending modulus, required in order to deduce α_{dir}, from the literature: κ_b= 8.5 10^{-20} J [14]. $\tau(1)$ is the initial tension state of the high-tension regime (fixed in our case to 1 mN/m).

Finally, using all the formulas and details explained before, we were able to draw the curves of the direct area expansion as function of the membranes tension ***Figure IV-21*** (blue curves)

4.5.3 Characterization of the stretching modulus

For DOPC membrane, we obtained (average on measurements on two vesicles): $K_{app} = 228 \pm 27$ mN/m and $K_{dir} = 257 \pm 36$ mN/m, the error bar being the standard deviation. The values obtained for pure DOPC vesicles, with the rounded-square hypothesis, is fully compatible with the literature ($K_{app} = 237 \pm 16$ mN/m and $K_{dir} = 265 \pm 18$ mN/m) [13], [14]**.** This is the proof of concept of our chip, and that for the square cross-section shape of channels, the shape of the GUV trapped is to be consider as a rounded-square shape rather than circular.

4.6 Conclusion and limitation

In this chapter, we designed a microfluidic chip that is able to trap GUVs, due to hydraulic resistance in the channels. Fabrication of the chip was critical and challenging because of the hanging structure of the trap in the middle of two deeper channels. The hanging structure is necessary to have symmetric shape during the deformation of these biomimetic objects. To overcome the challenge, we tried 3 different fabrication techniques: PDMS on PDMS chips, Dry film technology chip and finally the silicon-glass etching chips. Each technique required specific development of new protocols and optimizations of others. Finally, the best choice in terms of feasibility, adhesion and transparency was silicon-glass etched chips. Optimization using bosch process and continuous process in silicon etching was also made. The big difficulty of the glass etching was to overcome the high rugosity that is created during the etching process. This required the new development of etching process of Borofloat glass type: by choosing the right resist, tuning the temperature and time of etching and finally by adding a complementary chemical wet etching. Using this chip, we were able to trap DOPC membranes and by applying a pressure, we were able to measure their deformation inside the trap. These measurements, and using the formulas demonstrated before, led to extract the membrane tension of the objects as function of their area expansion. However, because the fabrication of the chip gives a square cross section shape of the trap instead of cylindrical (the traditional shape of a micropipette), we had to extend the formulas of the area expansion valid only to the cylindrical shape. We followed a new shape for the trapped GUV, which we called rounded-square shape, and which was demonstrated by a z-stack orthogonal views in confocal microscopy images. The new formulas corrected the tension vs area expansion curve by shifting the values 15% from the circular shape ones. The apparent stretching modulus was extracted by fitting the curve in the high-tension regime, corresponding to the stretching regime. However, since we couldn't characterize the bending modulus because of the poor control over the small pressure, we used the bending modulus of DOPC membranes extracted from the literature. The bending modulus was necessary to extract again the direct stretching modulus because the thermal undulations needed to be subtracted. DOPC stretching modulus was characterized by the following value: $K_{dir} = 257 \pm 36\ \mathrm{mN/m}$, a value very compatible with the literature.

- **Limitation of the design**

Despite the ability to trap the objects, nonetheless, the time needed from the beginning of the experiments until the GUVs arrived to the trap was too long. In fact, the total hydraulic resistance is the sum of each channels including: the microfluidic tubes, the inlet and outlet channels, and the parallel resistance of trap and the bypass. However, the resistance of the tubes is too small compared to the chip, because their width is big (~ 300 µm diameter), giving a resistance of the order of

$10^{11} Pa.s.m^{-3}$. The total hydraulic resistance in the chip is $R_{total} = 63.8\, x\, \eta\, x\, 10^{16} = 6.38\, x\, 10^{14}\ Pa.s.m^{-3}$. (If we consider the viscosity of water is = $10^{-3} Pa.s$). For a pressure applied of $\Delta P = 69$ mbar, maximum pressure applied to not blow up the GUVs, the average flow in the circuit is:

$$Q = \frac{\Delta P}{R_{total}} = 10.8\, x\, 10^{-11}\ \mathrm{m^3 s^{-1}} = 0.64\ \mu\mathrm{L/min}$$

By calculating the total volume of the chip, we deduce the total time needed to change 1 solution inside the chip. The total time is 90 minutes. Knowing that before sending the GUVs to the chip, the anti-adhesion coating and the rinsing of it needs to be done. Therefore, the total time of the experiment is very long.

Another observation made during the experiment, is the amount the GUVs we would capture by experiment; in fact, because we lowered the trapping efficiency for 50% as explained in the beginning of the chapter, we couldn't trap as much GUVs as we needed to have more data to analyze. Using the same design concept, we added in some of the chips four parallels traps instead of one in order to increase the number of trapped GUVs. As this seemed a given solution, however two aspects were to be considered. First of all, in order to parallelize the deformation study, the four trapped had to be in the field of view of the objectives during the whole experiment. This obviously is important to see the trapped GUVs in all the traps, but also to calculate well the pressure applied on the object. In fact, since the traps were in parallels, the pressure applied on the object depended on the equivalent resistance of these channels which also depended if the traps were empty of blocked by a GUV. This design was therefore discarded.

- **Limitation of the fabrication**

During the fabrication, a lot of steps seem to be straight forward (specially the alignment of two levels of resist during the photolithography process). However, even if the alignment resolution we achieved was 500 nm, sometimes it leaded to an asymmetric deformation of the vesicle at the entrance of the trap ***(Figure IV-22).***

Another problem we encountered also was during the bonding of the two wafers. Even if the thermal expansion coefficient for silicon and the Borofloat glass are close, we tried to make the bonding with two different techniques to compare: first trial is to align both bonding on room temperature first, and later, heating both of them and sealing them together. Second trial was to heat both wafers first and then align them together to then be sealed. This way we are sure they won't expand more if we align then heat after. However, even with both techniques, we encountered problems of misalignments in some of the chips on the wafer, leading to a non-symmetric deformation of the

vesicle. This ever-low misalignment could be due to unintentional movements of the wafers during the process, and still could defaults the experiments of deformation.

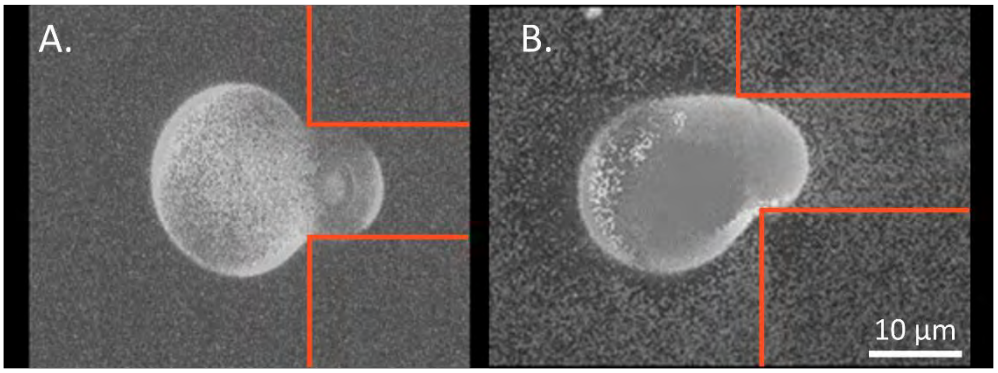

Figure IV-22 Confocal microscopy images of trapped GUVs. A shows a symmetric deformation of vesicle due to the good alignment of the wafers together. B shows a non-symmetric deformation of a vesicle at the entrance of the trap due to the misalignment of the silicon-glass wafers.

And finally, because of the square cross-section shape of the trap, a residual flow is maintained around the trapped GUV which comes from the corners which are not completely blocked by the GUVs. This can induce a shear stress on the GUVs even if for the pressure used, it is still negligible.

Due to the limitation of the design, the fabrication techniques and the amount of data generated, another design of micropipette on chip was designed and were many aspects had to be improved.

- Easier fabrication technique
- Cylindrical shape of the trap.
- Faster time of experiments
- Generating more data by parallelizing traps

The new approach of the micropipette on chip is introduced in the next chapter.

References

[1] L. M. Lee and A. P. Liu, "A microfluidic pipette array for mechanophenotyping of cancer cells and mechanical gating of mechanosensitive channels," *Lab Chip*, vol. 15, no. 1, pp. 264–273, 2015, doi: 10.1039/C4LC01218F.

[2] L. M. Lee, J. W. Lee, D. Chase, D. Gebrezgiabhier, and A. P. Liu, "Development of an advanced microfluidic micropipette aspiration device for single cell mechanics studies," *Biomicrofluidics*, vol. 10, no. 5, 2016, doi: 10.1063/1.4962968.

[3] S. Choi, M. G. Lee, and J. K. Parka, "Microfluidic parallel circuit for measurement of hydraulic resistance," *Biomicrofluidics*, vol. 4, no. 3, pp. 1–9, 2010, doi: 10.1063/1.3486609.

[4] J. Cottet, C. Vaillier, F. Buret, M. Frénéa-Robin, and P. Renaud, "A reproducible method for µ m precision alignment of PDMS microchannels with on-chip electrodes using a mask aligner," *Biomicrofluidics*, vol. 11, no. 6, 2017, doi: 10.1063/1.5001145.

[5] E. Chen, "III . Wet and Dry Etching," *Appl. Phys.*, pp. 1–18, 2004.

[6] A. Misra, J. D. Hogan, and R. Chorush, "Wet and Dry Etching Materials," *Handb. Chem. Gases Semicond. Ind.*, no. 3, pp. 1–5, 2002, doi: 10.1002/0471263850.mis056.

[7] C. Cardinaud, M. C. Peignon, and P. Y. Tessier, "Plasma etching: Principles, mechanisms, application to micro- and nano-technologies," *Appl. Surf. Sci.*, vol. 164, no. 1–4, pp. 72–83, 2000, doi: 10.1016/S0169-4332(00)00328-7.

[8] D. L. Flamm, V. M. Donnelly, and D. E. Ibbotson, *Basic Principles of Plasma Etching for Silicon Devices.*, vol. 8. ACADEMIC PRESS, INC., 1984.

[9] ubodh Prabhu, "Bosch.pdf." pp. 1–4, 2009.

[10] D. L. Flamm, V. M. Donnelly, and D. E. Ibbotson, *Basic Principles of Plasma Etching for Silicon Devices.*, vol. 8. ACADEMIC PRESS, INC., 1984.

[11] P. Knapkiewicz, "Ultra-low temperature anodic bonding of silicon and borosilicate glass," *Semicond. Sci. Technol.*, vol. 34, no. 3, 2019, doi: 10.1088/1361-6641/aafecc.

[12] K. M. Malecki and F. G. Della Corte, "Silicon-glass anodic bonding at low temperature," *Micromach. Microfabr. Process Technol. X*, vol. 5715, no. Imm, p. 180, 2005, doi: 10.1117/12.590753.

[13] W. Rawicz, K. C. Olbrich, T. McIntosh, D. Needham, and E. A. Evans, "Effect of chain length and unsaturation on elasticity of lipid bilayers," *Biophys. J.*, vol. 79, no. 1, pp. 328–339, 2000, doi: 10.1016/S0006-3495(00)76295-3.

[14] L. Lu, W. J. Doak, J. W. Schertzer, and P. R. Chiarot, "Membrane mechanical properties of synthetic asymmetric phospholipid vesicles," *Soft Matter*, vol. 12, no. 36, pp. 7521–7528, 2016, doi: 10.1039/c6sm01349j.

Chapter V

5 Continuous and multiple trapping of biological and biomimetic objects: from GUVs to spheroids.

Traditional micropipette aspiration suffers from several limitations already discussed in chapter II. Mostly, several manual steps tend to prolongate the time of experiments, such as the preparation of the set-up, the calibration of both the hydrostatic pressure and the micropipette inside the GUVs chamber. Moreover, it requires searching manually the sediment GUVs. It thus lacks throughput because it is done only with one single object at a time.

In our first on-chip micropipette presented in the previous chapter, we tried to address some of these limitations, by creating a platform where GUVs arrive automatically to the chip using a pressure controller, and then due to imposed hydraulic resistance in the channels the GUVs get trapped in the micropipette channel. However, this chip also suffered from many limitations that were discussed in chapter IV.

In this chapter, we introduce a novel microfluidic chip involving a novel fabrication technique which allows us to fabricate on chip micropipette with cylindrical shape. The microfluidic chip is made of two pieces: a classical PDMS chip in which a sliding element, containing the main function (in this case the micropipette), is inserted. A determinant feature of this technique is the possibility to fabricate pipettes with any chosen shape in the cross section of a microfluidic channel, especially the cylindrical channel shape which is crucial for micropipette aspiration experiments. In addition, the technique allows us to fabricate multiple pipettes on the same element, possibly with different diameters, in order to quickly perform parallelized micropipette aspiration experiments. Finally, this technique allows generating this sliding element by hundreds whereas keeping the same PDMS chip design. Therefore, the system can be reconfigurable for many applications.

As a proof of concept of the chip, we first characterized the mechanical properties of simple lipid compositions such as DOPC, POPC and Brain SM. We then quantified the effect of cholesterol on DOPC membranes by increasing the concentration of cholesterol up to 50% in DOPC-cholesterol lipid mixture. Moreover, we characterized DOPC membrane challenged with co-polymers nanoparticles and gold nanoparticles, typically used for drug delivery, at two different concentrations of each type of nanoparticles. Finally, by adapting the chip design (size of the micropipette and PDMS channel), we showed that the approach could be extended to characterize the viscoelastic properties of spheroids, 3D cancer cells aggregate, which are used as a model for cancer treatment and drug screening.

5.1 Microfluidic design for an on-chip micropipette enabling continuous and high throughput trapping

5.1.1 Microfluidic design principle: the power of the sliding element

As discussed in the previous chapters, both traditional micropipette aspiration and our first microfluidic on-chip micropipette, based on standard planar fabrication techniques, suffer from many limitations. Most of the on-chip micropipettes developed over the years suffered from one important aspect: the square shape of the traps due to the microfabrication techniques used. Moreover, fabricating a 3D chip where the trap is hanging in the middle of two is feasible but very challenging and demanding using the traditional way of fabrication, as seen in the previous chapter. Consequently, we had to come up with a new original technique to address these limitations.

A new microfluidic concept combining a PDMS microfluidic chip and a sliding / removable element was developed in Curie Institute with Laurent Malaquin who then moved to our lab [1]. The technique was then strongly extended and adapted from one side by Morgan Delarue a researcher in our team who uses it to culture on-chip cancer spheroids. From another side, we optimized this technique to create a microfluidic chip for continuous trapping and high throughput on-chip micropipette experimentation.

The microfluidic platform is made of two main parts, as seen in ***(Figure V-1)***. First, a PDMS chip contains an inlet and an outlet for the fluidic connections, defining a large channel where the flow goes through. In the middle of the long PDMS channel, a deeper channel is opened to allow the insertion of the sliding element, which is the innovative part of this technique ***(Figure V-1 a-b)***. The idea of this approach is that this sliding element contains the main functions that the chip has to perform. In our case, it is the cylindrical micropipettes. The PDMS microfluidic chip can thus remain the same for all applications, and the changes come by changing only the functions in the sliding element ***(Figure V-1 c-d)***. Thanks to the fabrication technique, which will be described in the following paragraph, the shape of the pipette can be chosen to be cylindrical, but also in any other shape needed. Likewise, the positioning of the holes can also be chosen, as well as the diameters of the holes, which represent the diameter of the micropipette. In fact, we were able to fabricate pipettes going from 6 to 15 µm diameters. The high throughput experimentation is possible because we designed multiple traps on a single sliding element ***(Figure V-1 e-f)***, however, a single object characterization is also possible by designing one trap per sliding element. Interestingly, different diameters of micropipettes could be fabricated on the same sliding element to be used in the same

experiment. ***Figure V-1 g*** represents a sliding element containing pipettes with diameters of 8, 10, 12 and 15 µm.

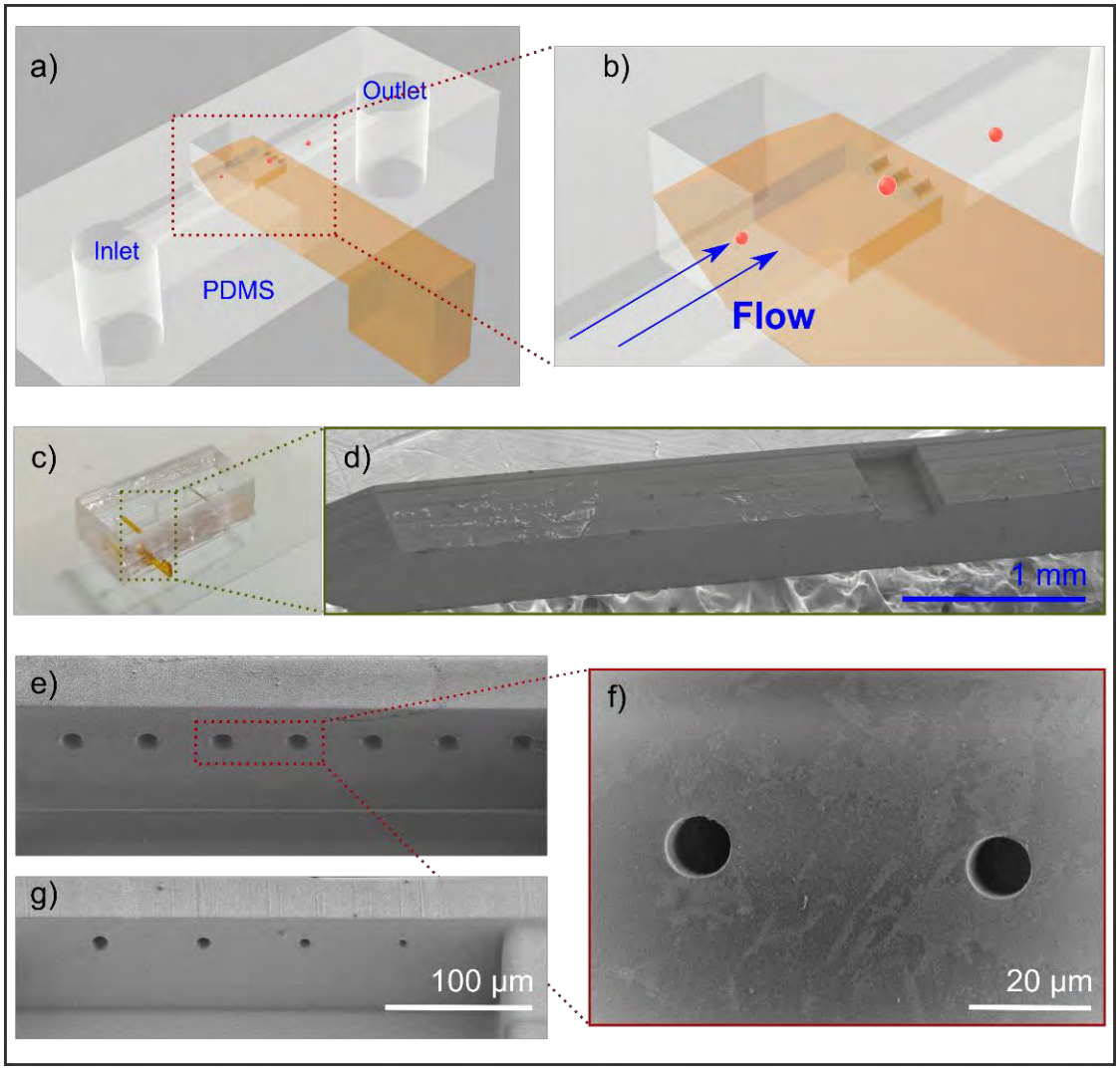

Figure V-1: Microfluidic new concept: combination of a sliding element and a PDMS chip. a) 3D scheme of the PDMS (white) microfluidic chip where a long channel is connected to an inlet and outlet which allows fluidic connections. In the middle of the channel, a deep opening in the PDMS is made for the sliding element (yellow), containing the cylindrical holes of the micropipette, to be inserted. b) Close up view of the 3D scheme, showing the flow inside the chip and how the GUVs (red spheres) are trapped inside the holes of the sliding element. c) Picture of the PDMS chip bonded on a glass side, with the sliding element inside it. d) Scanning Electron microscopy of the whole sliding element from far. e-f) Close-up SEM images of the holes in the sliding element which represent the micropipette aspiration. e) are holes with the same diameters (15 µm), whereas g) are holes with different diameters: 8-10-12 and 15µm

The chip works as follows: after the sliding element is inserted inside the PDMS main platform, the GUVs solution is injected thanks to a pressure controller which controls at the same time the pressure on the objects. Once the objects arrive to the micropipettes, they get trapped inside them. If multiple micropipettes are used (sliding element with multiple traps), we wait until all the traps are full, and the micropipette aspirations experiment is conducted. This offers high throughput experimentation.

Once the study is done, the pressure is increased to release the trapped GUVs to the outlet, while other GUVs arrive and more micropipette aspiration studies can be conducted.

5.1.2 Microfabrication technique of the sliding element and the PDMS chip

The sliding element and the PDMS chip are fabricated differently and separately before they are finally combined together to make the final microfluidic platform for the on-chip micropipette. The sliding element fabrication is new and very original. The PDMS chip fabrication is traditional and requires a SU8 or DF mold.

5.1.2.1 Fabrication of the sliding element

Tigettes Dimensions

The sliding element, which I will call from now on the "tigette", is made of Dry Film resist which I introduced in the previous chapter. Such element is made in the normal horizontal (XY) plane during its fabrication by photolithography; However, the tigette would be used turned 90° angle in the x-axis for its insertion in the microfluidic chip. Before I explain the fabrication, it is important to understand the final dimensions of the tigette shown in ***Figure V-2.*** The total length of the element is 10.5 mm, as seen in the **XZ view**. At the head of the tigette, we added a rectangle of 1.75 x 1.5 mm^2, to easily handle and manipulate the tigette using a tweezer (seen in the **XY view**). The total height of the sliding element beam is 500 µm (y-axis). This dimension was chosen in order to avoid breaking when inserting it inside the PDMS chip. In the **XZ view**, the total thickness of the tigette is 500 µm (z-axis): 50 µm of thickness of the micropipettes and 450 µm of opened chamber. Scaling down to the micropipette dimensions where the actual functions and flow are present (inset from **XY view**): a chamber of 100 µm x 400 µm x 450 µm is opened for the flow of the GUVs to cross through. On the other side of the chamber, we observe the cylindrical holes of the micropipette which diameters can vary from 6 to 15µm, with a length of 50 µm. In the rest of the chapter, the thickness of the pipette is referred to by the length of the pipettes.

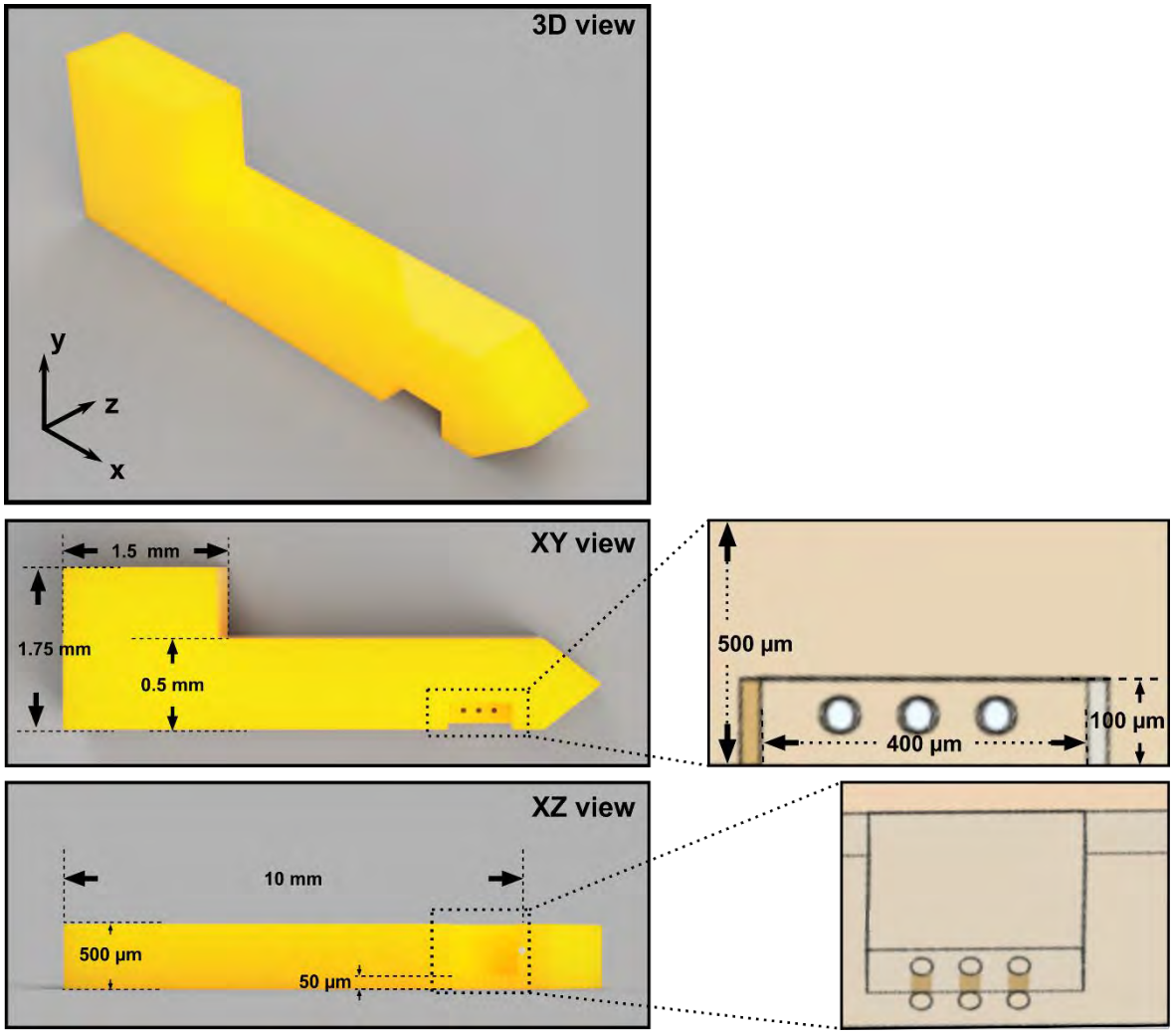

Figure V-2: 3D scheme of the sliding element showing the final dimensions after fabrication. The total dimension of the tigette is 10.5 mm x 500 µm x 500 µm. The images on the right, shows from one side the micropipette chamber of 100 x 400 x 450 µm³ and from the other side, the micropipette cylinder of 6-15 µm diameters and 50 µm depth.

Tigettes Fabrication

The fabrication of the tigettes is made by several steps of lamination of the Dry Film on silicon wafer followed by photolithography steps. It can be fabricated by hundreds per wafers (~300) ***(Figure V-4)***, and each sliding element can have a design different from the others, as the shape and diameters of the pipettes are imposed by the design and not by the fabrication technique. As already mentioned, it is a strong advantage of this approach. The general process is seen in ***(Figure V-3)*** and detailed as follows:

- A silicon wafer is plasma-activated and cleaned, before a first layer of DF is laminated. No additional adhesive coating is made on the silicon surface on purpose, for the tigette to detach after development. The first layer of lamination (50 µm-thick DF) is to determine first the length of the micropipette channels. This length of the cylinders permits to have enough length for the GUV to

deform inside it without escaping it sooner than it should. Since high aspect ratio structures are challenging to define in DF, 50 µm is a good compromise to fabricate 5 – 15 µm diameter pipettes. A thicker film, would generate longer pipettes, however it would not allow reaching such small openings. Moreover, longer pipettes are prone to clogging during microfluidic experiments.

- A photolithography step is then made in order to open the holes of the pipettes. No steps of Post-baking neither development are necessary for the moment, as it will be done once in the end.

The total height of the tigette, which is 500 µm, is determined by the design as it is represented in the (XY) plane of the design (mask). However, the width of the tigette, also 500 µm is determined by the total laminated DF thickness. Therefore, as 50 µm are already made for the pipettes, 450 µm of DF thickness is yet left to do, with a good alignment with the first 50 µm layer. This alignment is crucial for the microfluidic experiment. In fact, the (XY) plane of the tigette as represented in ***Figure V-2,*** would turn to the (XZ) plane during the microfluidic experiment. Any misalignment in the (XY) during fabrication, could lead to a leakage of the flow under the tigette in (XZ) plane of the microscope, and could cause possibly the loose of control over the pressure applied on the trapped GUVs.

- The lamination of 450 µm of DF is made in 5 steps, as the thickest DF film we have in the clean room is DF 100, which is 100 µm-thick. Therefore, to obtain 450 µm, we laminate 4 times DF 100 and 1 time DF 50.
- A photolithography step is made in order to a) open the fluidic chamber behind the micropipette cylinders and b) complete the total thickness of all the tigette which is 500 µm.
- A relatively long post-bake (~ 30 minutes) is made for all the DF films that had been deposit, followed by a very long development step (~ 3hours) to remove the part of the DF that is not needed. The development is long because of the total 500 µm thickness of DF present on the wafer. It is important to change the solutions every (30 – 40 minutes) to renew the developer and keep it efficient. During this step, and to facilitate the "lift-off" process of the tigette from the silicon wafer, it is recommended to develop the wafer in an upside-down position.
- Finally, the tigettes are "fished out" of the developer solutions, cleaned and dried. An additional step of *Perfluorodecyltrichlorosilane (FDTS)* molecule deposition to surface treat the tigettes and to make the surface hydrophobic, in order to avoid the lipid membranes sticking to its surface during the microfluidic experiments. This step is the same as the one made on silicon mold wafers and is explained in the materials and methods section.

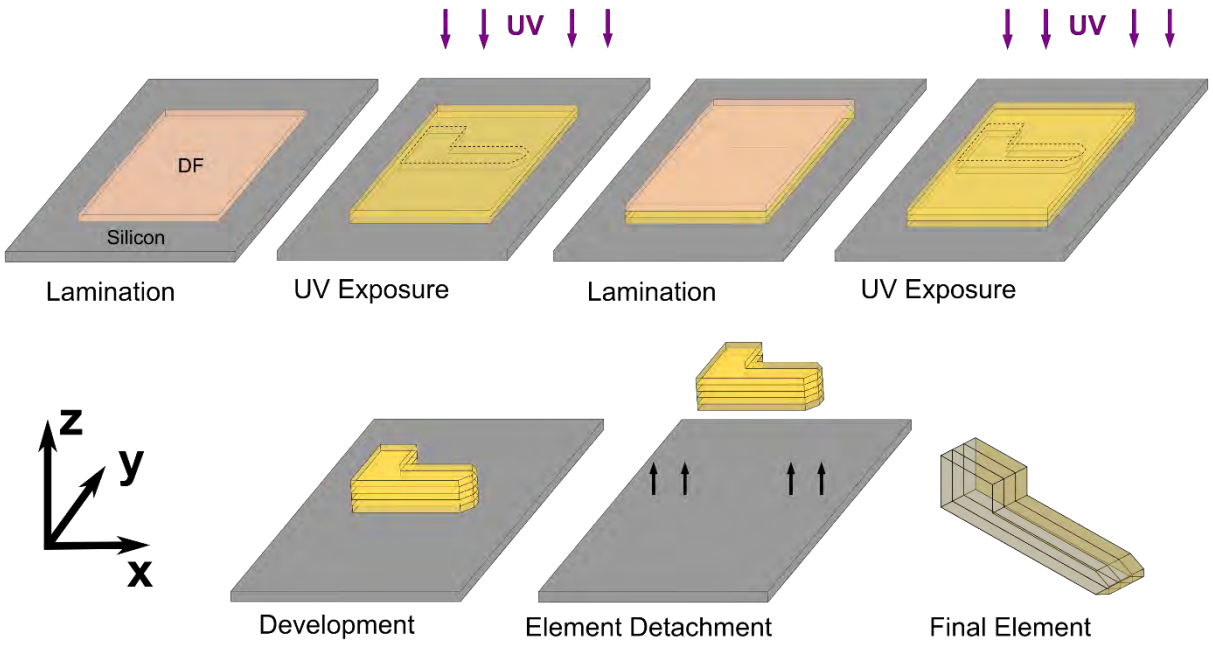

Figure V-3: Steps of the microfabrication technique of the sliding element. It is fabricated using several lamination steps of Dry Film on a silicon wafer with UV exposure after each step to pattern first the holes of the pipette and then the rest of the element. The fabrication is made in the (XY) directions. The development is made after the final step of exposure and postbake, where the elements detach from the silicon wafer. The element is then used by turning it 90° angle.

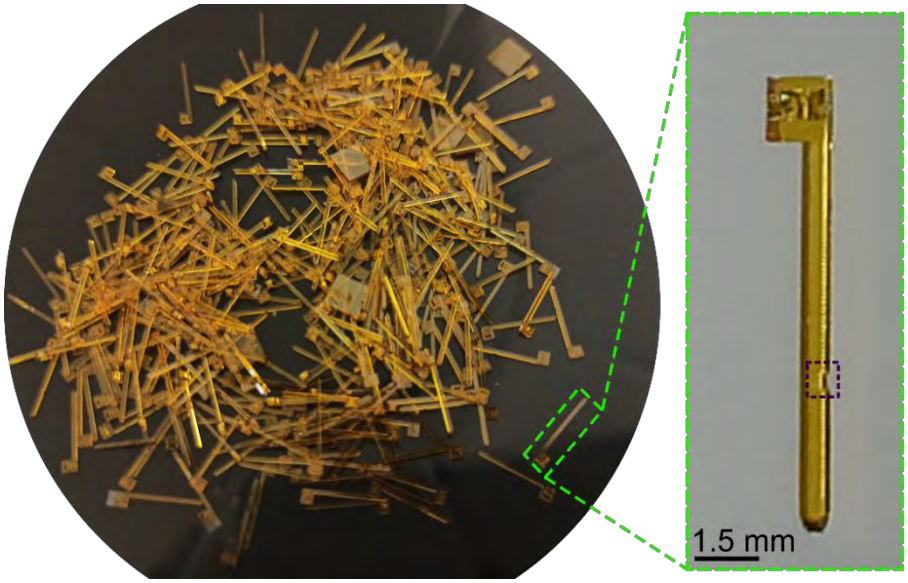

Figure V-4: Tigettes after "lift-off" process during the development . The tigettes can be fabricated in hundreds on the same wafer, and they are fished out after the developing step. On the right, a close up picture of the sliding element. The purple dashed rectangle shows the location of the opened chamber along the tigette.

5.1.3 Fabrication of the PDMS microfluidic chip

5.1.3.1 PDMS chip dimensions

The PDMS concept and dimensions are seen in ***Figure V-5.*** The final PDMS chip is made of two main channels (aside from the inlet and outlet for the fluidic connections). The first main channel is linked to the inlet and outlet and it is where the flow would be passing through. The channel is 100 µm height and 400 µm wide. These dimensions also correspond to the opening chamber of the sliding element. The length of the channel is 2.5 mm from each side of the second deeper main channel (as seen in ***Figure V-5).*** The deep channel in the middle of the two first main channels corresponds to an opening in which the sliding element would be inserted. The deep channel is 450 × 450 µm^2: it is 50 µm thinner and narrower from the dimensions of the tigette to ensure complete sealing when the element is inside it and therefore no leakage would be possible from the sides. The length of the deep channel is slightly smaller than the tigette one but long enough to ensure a good sealing also when the element is inserted.

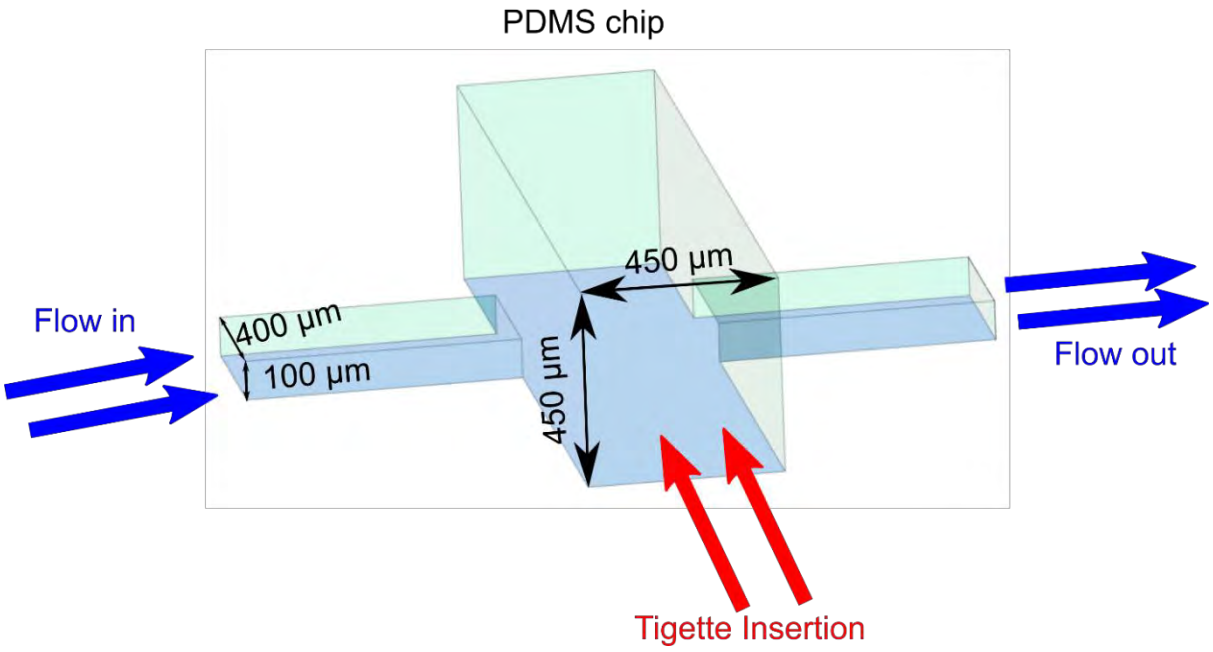

Figure V-5: PDMS final chip, showing the dimensions of the opened channels. The actual fluidic channels are 100 µm height × 400 µm width and a total length of 2.5 mm from each side of the deepest channel. The deep channel is where the tigette will be inserted and is 450 × 450 µm^2.

5.1.3.2 DF mold fabrication

PDMS chip is fabricated following the traditional processes. Briefly, a silicon mold is needed with the chips' patterns on it. Because of the 450 µm thickness needed for the deep main channel, we chose to fabricate the mold using lamination of Dry Film, as it is cheaper and way faster than SU8 mold fabrication. A first layer of DF 100 is laminated and insolated to fabricate the first main channels of 100 µm thickness. 4 other steps of lamination are made (3 × DF 100 and 1 × DF 50) to complete the

deep channel of 450 µm total thickness. The wafer is then developed to remove the unwanted DF parts and cleaned. Finally, same as for the SU-8 molds (seen in materials and methods), the DF wafer is treated to make it hydrophobic to allow further PDMS detachment easier.

5.1.3.3 PDMS chip fabrication

The PDMS chip is made in three different steps. First, in order to ensure a better sealing of the fluidics, the bottom part of the chip is made of PDMS instead of glass. In fact, we tried to insert it inside a PDMS bonded directly on glass and the chip leaked from the sides and under the tigette. Therefore, after degassing the PDMS, one part is poured on the DF/silicon mold and the other part is spin-coated on a pristine silicon wafer, treated with a hydrophobic surface treatment. Secondly, once the PDMS is reticulated, the PDMS chip is cut and the holes are opened with a PDMS puncher. A very important step here is to also cut and open the beginning of the second deeper channel, to allow later the insertion of the tigette. The two PDMS pieces (the chip and the thin layer) are then plasma-treated and bonded together. Finally, the whole PDMS chip is then cut and removed from the wafer, and it is bonded to an additional glass substrate to facilitate its handling and for optical microscopy.

5.1.4 Characterization of the sliding element

5.1.4.1 Design and characterization of the size and shape

As discussed in the previous chapters, the cylindrical shape of the micropipette is crucial in order to prevent residual leakage and shear on the membrane and ensures that the pressure difference to be considered is exactly the one imposed. Moreover, the formulas developed in chapter II to extract the area expansions and membrane tensions of the GUVs can be directly applicable. The circular shape of the pipettes is seen in ***Figure V-1***. Moreover, characterizing the size of the pipette is also important as it directly affects these formulas. Therefore, we characterized the tigette using Scanning Electron Microscopy, and optical microscopy. The diameters of the pipettes obtained are: 8.5 ± 0.3 µm , 10.8 ± 0.3 µm, 12.5 ± 0.28 µm and 15.7 ± 0.3 µm for respectively $8, 10, 12$ *and* 15 µm. As the diameter of the pipette ought to be around one third of the GUVs size, we tried to lower down the size of the pipettes to 6 µm. However, for a DF thickness of 50 µm (corresponding to the pipette length), the ratio of the thickness over the diameter is very high and the holes of the pipette wouldn't open all the way through the 50 µm thickness of the DF. Therefore, we lowered the length of the pipette to 25 µm instead of 50 µm, by changing the DF thickness to 25 µm instead of 50 µm. We fabricated pipettes with diameters 8, 6, and 4 µm. However, only the pipettes of 8 and 6 µm were able to open all the way through the 25 µm but not the 4 µm as the ratio 25/4 > 5:1 becomes high. In general, it was demonstrated that this material is able to perform aspect ratio of 5:1 for channel

structures [2]. Therefore, achieving the 4 µm pipette diameter is not easy and more optimization of the photolithography step is needed.

On the other hand, because the aspect ratio of the length of the pipette over the diameter of the pipette increases with the decrease of the diameter of the pipette, the cylindrical aspect of the pipettes is not preserved all over the length of the micropipette. A conical aspect is rather seen between the entrance and the exit of the pipette, and the percentage of decrease in the diameters between the entrance of the pipette and the exit is seen in ***Table V-1.*** However, this is not problematic for us as the trapping and the measurement are always made from the same side of the pipette (the entrance), and the deformation of the GUV is made in the first 25 % of the pipette before it escapes. Therefore, the decrease of the diameter of the pipette which corresponds to the location of the GUVs during the micropipette aspiration is divided by 4, decreasing therefore the effect of the conic shape in our studies.

Table V-1: DF aspect ratio effect on the cylindrical form of the pipettes seen by a decrease of the diameters at the exit of the pipette compared to the diameters at the entrance

DF thickness (µm) (Pipette length)	Pipette diameter (µm)	Aspect Ratio (Pipette length/pipette diameter)	Decrease (conic shape)
25	6	4.16	18 %
50	8	6.25	22 %
50	10	5	14 %
50	12	4.16	8 %
50	15	3.33	10 %

5.1.4.2 Characterization of the surface rugosity

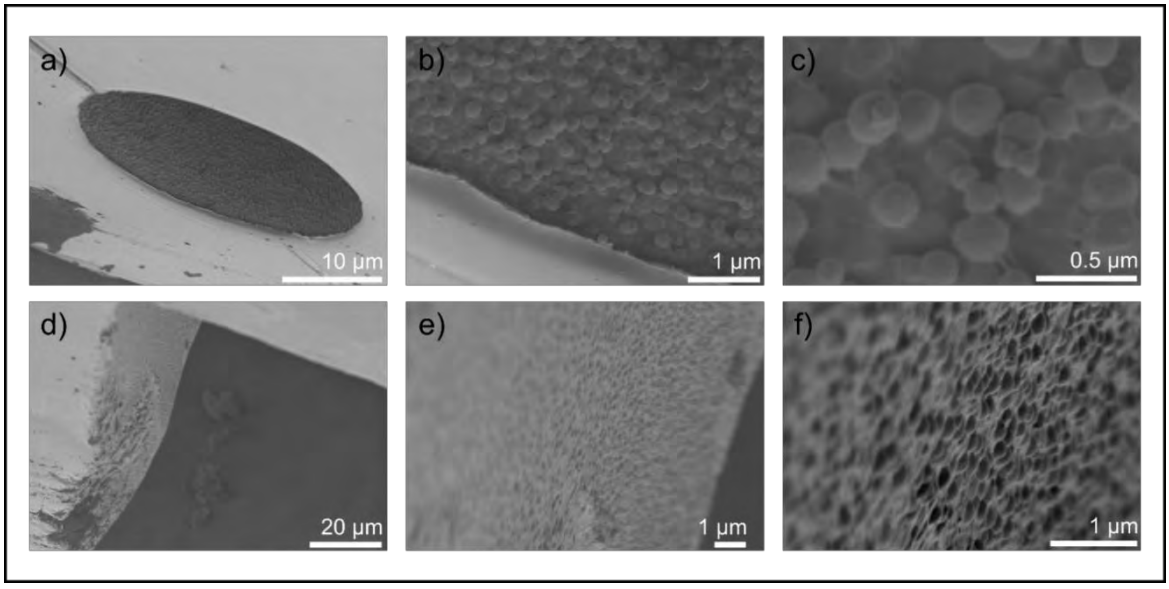

Figure V-6: SEM images of the pipette (a-c) and the chamber (d-f) in the sliding element. The images show bubbly structures on the surface of the walls of the pipette and on the walls of the chamber. This refers to the roughness of the material that has not been exposed to UV lights. The roughness was measured, and it's about ~ 300 nm.

The surface condition is very critical for the micropipette aspiration experiments. In fact, it is necessary to avoid adhesion of lipid membranes on the pipette's wall, which could cause damages to the thin lipid membranes (~5nm) and to not add additional area to the one considered in the computation. We characterized the surface of the holes and of the chambers. As seen in ***Figure V-6,*** the surfaces, which corresponds to the frontier between zones exposed and not exposed to UV light, present bubbly structures. The associated surface roughness was measured around 300 nm, with a typical lateral length scale of order 50-100 nm. This could be problematic for the micropipette aspiration experiments, as mentioned before.

5.2 Multiple parallelized trapping of GUVs and on-chip micropipette experiments

5.2.1 PDMS Microfluidic chip and sliding element operation

The general micropipette aspiration and image acquisition experiments are the same as the one explained in the second chapter for the traditional experiments and in the previous chapter in the first on-chip micropipette approach. However, the operation of this microfluidic chip is slightly different from the ones before. In fact, the total chip is made of an assembly of both the PDMS chip and the tigette.

5.2.1.1 Chip assembling

Once the PDMS chip is bonded on the glass substrate and the tigette element is cleaned and characterized, both parts are assembled in the following way: the PDMS chip is lubricated by injecting filtered ethanol or water solution using a syringe. The tigette is then inserted inside the deep channel of the PDMS chip, until the chamber of the tigette meets the main channels of the PDMS chip. The alignment can be visualized and manually fixed under microscopy. ***Figure V-7 a-c*** is a top view of the DF sliding element inside the PDMS chip, showing the alignment of the single or multiple micropipettes with the microfluidic channel. However, since the alignment is made manually and visually, a small and possible misalignment (roughly ~ 50 µm) can happen during the insertion, as seen in ***Figure V-7c.*** This misalignment is not problematic as long as the pipettes still face the main fluidic channel and are not blocked by the PDMS. A possible upgrade of the approach could be to have a motorized stage to do that, which would enable a ~10 µm alignment. On the other hand, a possible deformation of the PDMS chip can occur when inserting the tigette. In fact, the element is 50 x 50 μm^2 larger and deeper than the PDMS channel which is crucial to avoid leakage around and under the element, however this causes deformation in the PDMS of around 20 µm. Nevertheless, this small deformation (5%) is not problematic in our case, as long as the pipettes are still functional. A way to

avoid this is to lubricate the PDMS as mentioned above, and insert directly the tigette inside it before the evaporation of the ethanol solution.

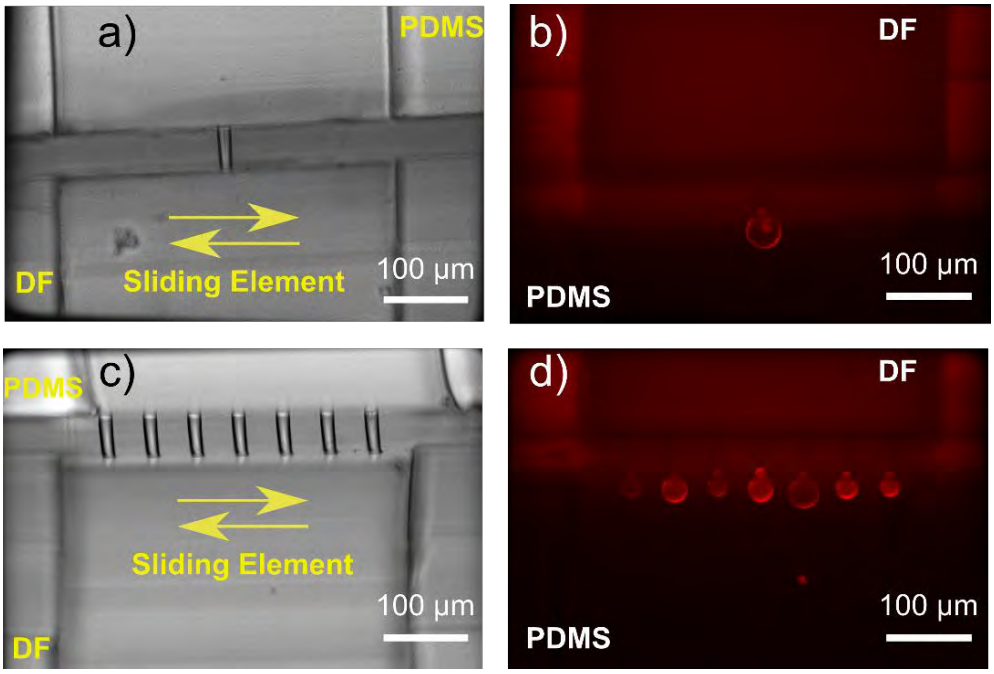

Figure V-7: Images of the PDMS microfluidic chip with the sliding element inside it. a-c) Bright-field microscopy images showing one and multiple parallel micropipettes aligned with the main channel of the PDMS chip. b-d) Confocal microscopy images of one or several DOPC GUVs trapped and deformed inside the micropipette upon applying a certain pressure. DOPC GUVs (in red) are stained with 16:0 Liss Rhod PE.

5.2.1.2 Chip operation

The microfluidic experiments follow the same protocol detailed in the previous chapter with minor differences that I will mention here. After inserting the tigette, the chip is put under vacuum for 20 minutes in order to degas it and avoid bubbles inside the chip during experiments. The chip is then functionalized using *β-casein* 0.5mg/mL, for 20 minutes. Because the dimensions of the main channels are very large compared to the dimensions of the micropipettes, the hydraulic resistance is mainly controlled by the pipettes. In fact, the hydraulic resistance of the pipettes corresponds to a circular cross shape and the resistance of the PDMS channels corresponds to a rectangular cross shape. The formulas are represented in chapter 3, in ***Table III-1***. Therefore, the hydraulic resistance of a pipette of 8 µm diameter is more than 2500 times bigger than the PDMS channels. This means that for any configuration possible (no matter how many traps are blocked), the pressure applied in the whole chip is restricted to the pressure applied on the entrance and exit of the pipettes. On the other hand, since the pipettes are in parallels, the pressure applied on one blocked object, is the ratio of the equivalent of the rest of the resistances and the total resistances, multiplied by the total pressure applied. This is seen in chapter III, equation ***3-13***. However, since the resistance of the PDMS main channels are negligible, the total resistances and the equivalent resistance are the same. Which means, the

pressure applied in the chip is almost the pressure applied to the object. This principal is applicable no matter how many objects are trapped. The consequence of such chip, is the need to have an accurate control over the applied pressure.

5.2.1.3 Pressure control and stability

The bending regime corresponds to membranes surface tension ranging between 0.001 and 0.5 mN/m, as seen in chapter II. This corresponds to a range of pressure between 0.004 and 0.4 mbar, for a micropipette of 8 µm diameter. Since the pressure applied on the object is directly the pressure applied by the pressure controller, it is necessary to have good stability of the pressure over the objects. Hence, we switched the pressure controller to a *Fluigent MFSC* – EZ, 0-25 mbar (instead of the 0-69mbar), with a minimum pressure step of 0.0075 mbar and stability of 0.02 mbar. Clearly it is difficult to be precise enough in the low pressure range however minimum surface tension reached by the minimum stability of this pressure controller is 0.005 mN/m. This means that the pressure operation in the chip, combined with the good stability of the pressure controller, allows us to characterize well the bending modulus. The characterization of the stability of the pressure controller is shown in materials and methods.

When using a single micropipette, the study of the deformation can start as soon as the object is trapped ***(Figure V-7b)***. However, when using the multiple micropipettes chip and in order to have high throughput experimentation, it is better to wait for the whole traps to be filled and perform the micropipette aspiration on all of them ***(Figure V-7d)***. Depending on the number and size distribution of GUVs (electroformation not being fully reproducible regarding these aspects), this step typically takes less than a minute. However, smaller objects might escape from the pipette at lower pressure than the larger one. As discussed, due to the repartition of hydraulic resistances this does not affect the pressure applied to the objects.

5.2.1.4 Leakage characterization of the chip

Because the chip is made of two assemblies, it is important to verify that no leakage is possible during the experiments. In fact, as discussed in the previous chapters, the control over the pressure during the micropipette aspiration is crucial as the deformation of the membrane depends on the pressure applied to the object, and its surface tension is directly linked to the pressure. If there is a leakage, the control over the pressure is lost. Before every experiment, there are two important points to check under the microscope: the lateral alignment of the tigette, which have to block the width of the deep PDMS channel completely in order to avoid leakage on the side of the tigette. Second, the tigette designs must be perfectly aligned in the XY plane to avoid leaks underneath the tigette chamber, as seen in paragraph ***A.2.α***. Any misalignment in the Y direction comes from the alignment step during

the photolithography process. These leakages can be observed under microscopy during the experiments. In fact, once the GUVs are trapped, the resistance in the micropipette becomes very high, and the flow should stop instantly. In case of a leakage, the flow will continue running even if all the micropipettes are completely blocked. We made a particle tracking analysis on one of the micropipette aspiration experiments using Image J to follow the movement of small vesicles right outside the pipettes ***(Figure V-8).*** Once all the GUVs are trapped inside the pipettes, the flow completely stops and the small particles seem to have a Brownian movement. This proved that there is no leakage from any side of the chip.

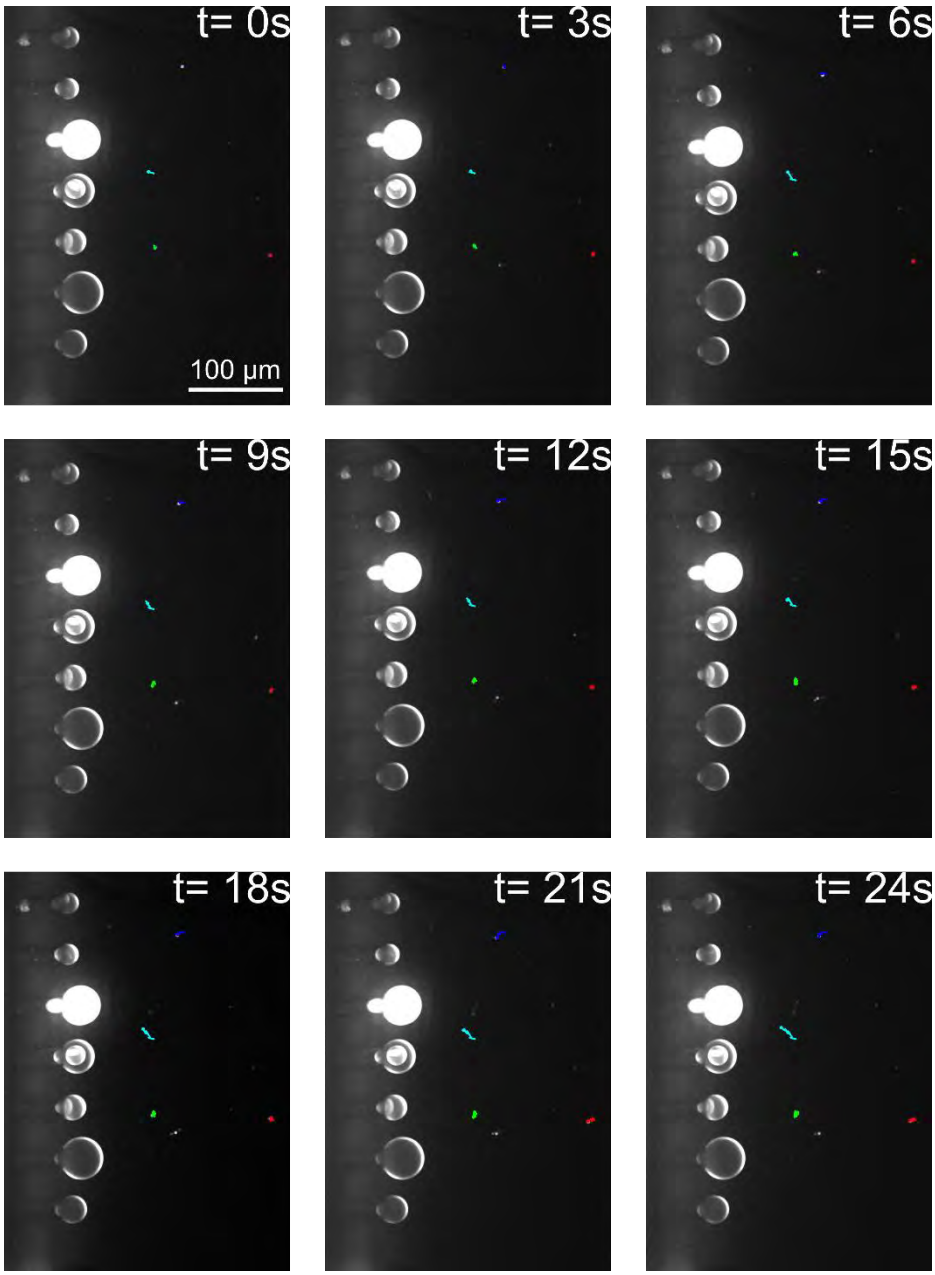

Figure V-8: Confocal microscopy images of a multiple micropipette chip where all the traps are filled. We characterized the flow outside the pipette to verify that there is no leakage. Using Image J, we made a particle tracking of small vesicles. The movement of these vesicles seems to be Brownian, and the flow is completely stopped.

5.2.2 Image acquisition and automation of the image treatment

5.2.2.1 Confocal microscopy image acquisition

During the micropipette aspiration experiment under confocal microscopy, a picture is taken for each pressure increase. In fact, once all the traps are filled with the GUVs, a first picture is taken to determine the minimal area of each GUV. Then, the pressure is increased every 3 seconds (to ensure the objects are in their equilibrium state) and a picture is taken corresponding to each pressure. Finally, once the study is done and the GUVs are out of the traps and before other GUVs arrive to refill the traps, a picture of the background is taken. In fact, as seen ***Figure V-7 (b-d)***, the DF material is fluorescent for a wide range of wavelengths. In most cases, the GUVs were stained with 16:0 Liss Rhod PE (λ_{ex} = 560 nm, λ_{em} = 583 nm). The background picture is used in the image treatment to remove the noisy fluorescent background of the material and keep only the fluorescent of the GUVs. Using a fluorimeter setup (Varioscan), we characterized the spectrum of excitation and emission of the DF material. The results are presented in Material and methods. A fluorophore emitting around 580 nm, where DF is not so bright, limits the fluorescence background.

5.2.2.2 Semi-automation of the image treatment

The multiple micropipette aspiration and the parallelized experiments generated a large amount of data, and analyzing these data couldn't be done anymore manually like in the previous chapter. Therefore, with Hajar Ajyel and during her Master 2 internship which I supervised, we worked on making the analysis of the micropipette aspiration semi-automatic, using Matlab software.

First, the images of the multiple pipettes are manually cropped to a single pipette each in order to facilitate the detection of the GUV. Then, the Matlab code is divided into three main steps. The main function of the code is the "find circles" process, which purpose it to find the circle of the GUV outside the pipette, which diameter is one of the vesicle, and the circle corresponding to the cap of the GUV inside the pipette. The radius of the cap corresponds to the micropipette one, and the position of its center permits to determine ΔL, the elongation of the vesicle inside the pipette. ***Figure V-9*** shows the images corresponding to the treatment and analysis. Note that a simpler detection of the position of the tip inside the micropipette, by finding the maximum intensity along the pipette, was tried. It appeared to be less precise and robust than the described circle-based detection.

The objective of the first part of the code is to determine the range of diameters of the vesicle inside and outside the pipette, and then to find them. In fact, the program reads the stack of images of the micropipette aspiration experiments and removes first the background to highlight only the vesicle. Secondly, the image is transformed to binary to focus only on the edges of the vesicle ***(Figure V-9A)***, and the range of the diameters is found and chosen in this step.

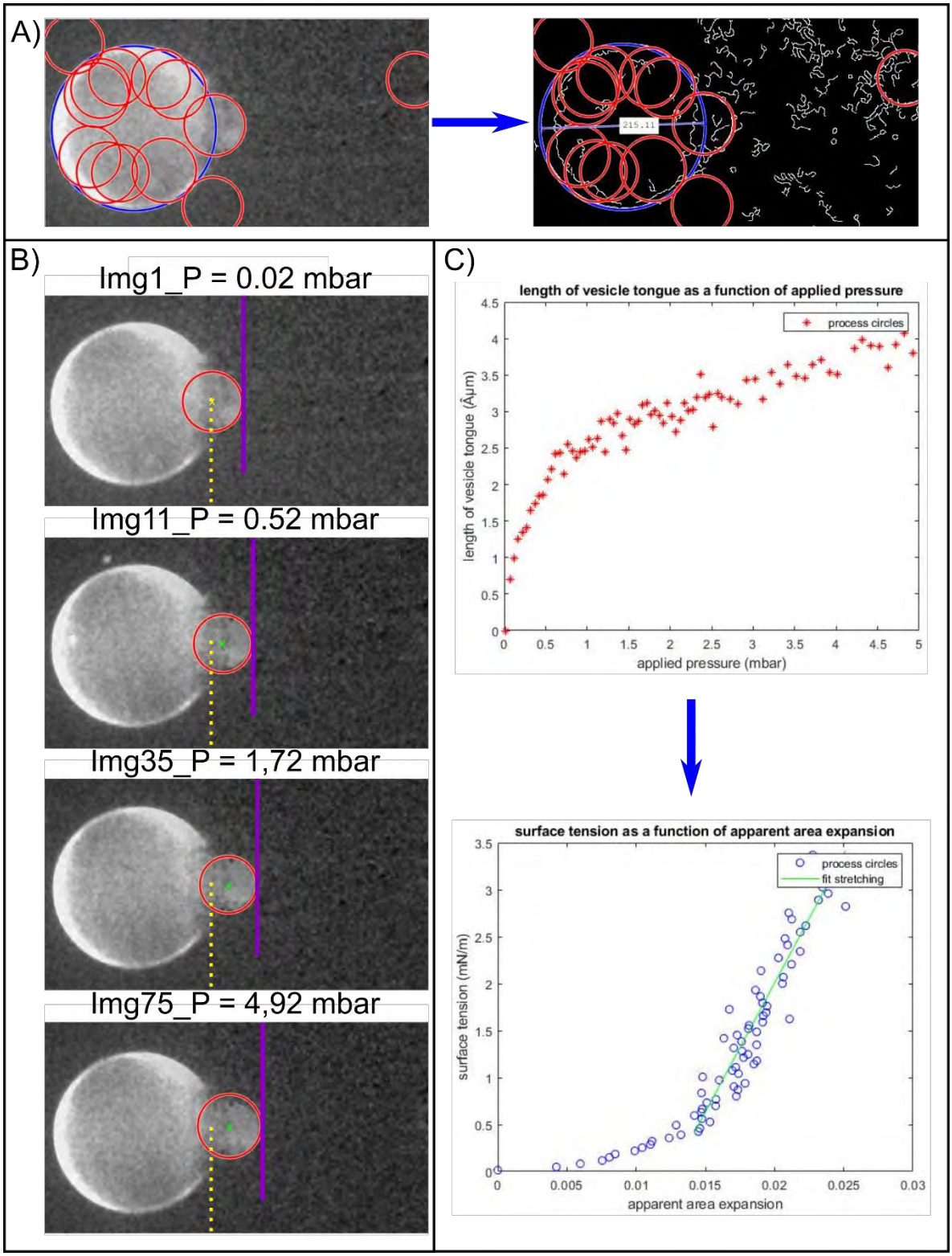

Figure V-9: Semi-automatic Image treatment and analysis using Matlab: A) The background of the images is removed, and using the find circles code, the vesicles diameter (Blue) and the vesicles cap diameter inside the pipette (red) are detected. The picture is then transformed to binary using edge detecting code, to focus only on the edges of the vesicle. B) The program then detects, for every picture, the position of the cap of the vesicle inside the pipette (purple line and red circles). Yellow and green marks were added to this picture only to show the advance of the center of the circles because of the progressive deformation of the GUV. The yellow dots line is to show the initial place of the center of the vesicle inside the Pipette. C) the program then records and plots the increasing length of the vesicle inside the pipette as function of the applied pressure. By using the equations introduced in chapter II, the tension and the area expansion are finally plotted.

The second part of the code is to determine the elongation of the GUV inside the pipette, which is necessary to determine the area expansion. To do so, the "find circles" process is also used to find the circle corresponding to the cap of the vesicle inside the pipette. However, as seen in ***Figure V-9A,*** the code can detect multiple circles which are in the same range of the cap. To eliminate the detections of all the other circles, the program allows to manually point out the area in which the circle of the CAP is present. This is done only once at the first picture of the stack, and it corresponds to the purple line shown in ***Figure Figure V-9B.*** After this detection, the code will only take into consideration the circles which centers are aligned with each other (the blue circle and the red circle). And then, for each image corresponding to increased pressure, a red circle is found to determine the red cap of the vesicle. In each picture, L_p is arithmetically obtained from the distance between the initial Lp (blue circle of the vesicle) to the center of the red circle plus the red radius. This value corresponds to the length of the vesicle inside the pipette. The code then draws the length of the GUV elongation inside the pipette as function of the pressure applied ***(Figure V-9C)***. The pressure array (list of pressure's value vs image number) is entered manually inside the code as it changes not only for each experiment but also for each study in each experiment. In fact, because the flow is always going from one side of the chip to the other, the hydrostatic pressure in both the inlet and outlet reservoir of the chip slightly changes during long experiments. Therefore, the pressure P_0 to be imposed at the inlet reservoir to cancel the flow by compensating differences in reservoir levels, also slightly changes during the studies. Next, the code saves the information in an excel sheet, which will be used in the third part of the Matlab code for data treatment, detailed in the next paragraph.

5.2.3 Data treatment to extract the mechanical properties of the lipid GUVs

The third and last step would be to plot and fit the necessary curves in order to extract the mechanical properties of the membranes. ***Figure V-10*** shows the successive graphs that the code generates, for seven POPC GUVs. The equations used in the data treatment are seen already in chapter II and IV, therefore I will not go through them again. In any case, the parameters extracted from the data analysis, such as the elongation of the GUV inside the pipette L_p, the diameter of the vesicle D_v, the diameter of the pipette, and the pressure applied on the GUVs are transformed, thanks to the equations (***2-6***, ***2-8*** and ***2-9***) detailed in the previous chapter, to the curves of the surface tension vs. the apparent area expansion. The apparent stretching moduli K_{app} is then extracted from the linear fitting of the curve. As seen in ***Figure V-10A left,*** the linear fitting to extract the apparent stretching modulus is made starting $\tau = 1$ mN/m and till the end of the curve, as this is characterized by the stretching regime (as seen in chapter II). The apparent stretching moduli (for all the GUVs) are then plotted as a function of the different GUVs diameters ***(Figure V-10A-right)***. The second step is to extract the bending moduli. To so to, the logarithm ln (surface tension) vs the area expansion is first

plotted. A linear fitting of the curve is made from the beginning of the curves until $ln(\tau = 0.5)$, which usually corresponds to the ending of the bending modulus and the beginning of the stretching modulus ***(Figure V-10B right)*** . The bending moduli is then extracted from the slope of the curve, following equation ***2-11*** from chapter II. The bending moduli (for all the GUVs) are then plotted as a function of the different diameters of the GUVs ***(Figure V-10B left)***. As mentioned in chapter II, the apparent stretching modulus is a combination of both the thermal fluctuations and the direct stretching modulus. Therefore, in order to correct the stretching modulus and to extract the direct area expansion, an average of the bending moduli of all the studied GUVs is calculated. Then, a correction of the area expansion is made by removing the effect of the bending modulus (chapter II, equation ***2-12***) and the surface tension vs. the direct area expansion is plotted. Finally, the direct stretching modulus K_{dir} is extracted from the linear fitting of surface tension vs. direct are expansion curves as seen in ***Figure V-10C left.*** The linear fitting is made starting $\tau = 1$ mN/m until the end of the curve (same as the apparent stretching modulus) and the direct stretching moduli are plotted as a function of the diameter of the vesicles ***(Figure V-10C).***

This semi-automatic process of image and data treatment has saved us a lot of time and allowed us to quantitatively analyze a large number of experiments. Nonetheless, there are some limitations of this program that could be worked on in the future to make it stronger, easier to use, and completely automatic. First, a preparation step of cropping and adjusting the rotation of the images is done in Image J before starting the image treatment. Second, the metadata such as the images' total numbers, the first image of the movie, and the background image, as well as the values of the pressure with the increasing steps (ΔP) are all manually entered in the code as they are different for each study. Third, if the quality of the images is a bit noisy the code can have difficulties finding the proper circles and therefore is unable to perform the image treatment using the "find circles" process. The process is unable to detect circles that are less than 5 µm. This was problematic when we used the micropipette of 6 µm diameter (3 µm radius). Finally, and overall, the detection of the cap was progressive and easily detected, however, sometimes the program detects non correct positions. These errors generate curves that are not perfectly linear, which makes the fitting wrong and therefore the values of the bending and stretching wrong. An example is shown in ***Figure V-10B:*** the blue and brown curves are more spread than the others and the bending moduli points are very low compared to the rest of the points, and this is due to a problem of detection and then of fitting. This could lead to an "error propagation" as the average values of the bending for example would be wrong and therefore the direct stretching modulus also. When this happens, the image treatment is still done in Matlab, however the data treatment is done manually as for the experiments described in the previous

chapters, using Origin Lab. It enables removing spurious points and choose more accurately the fitting region.

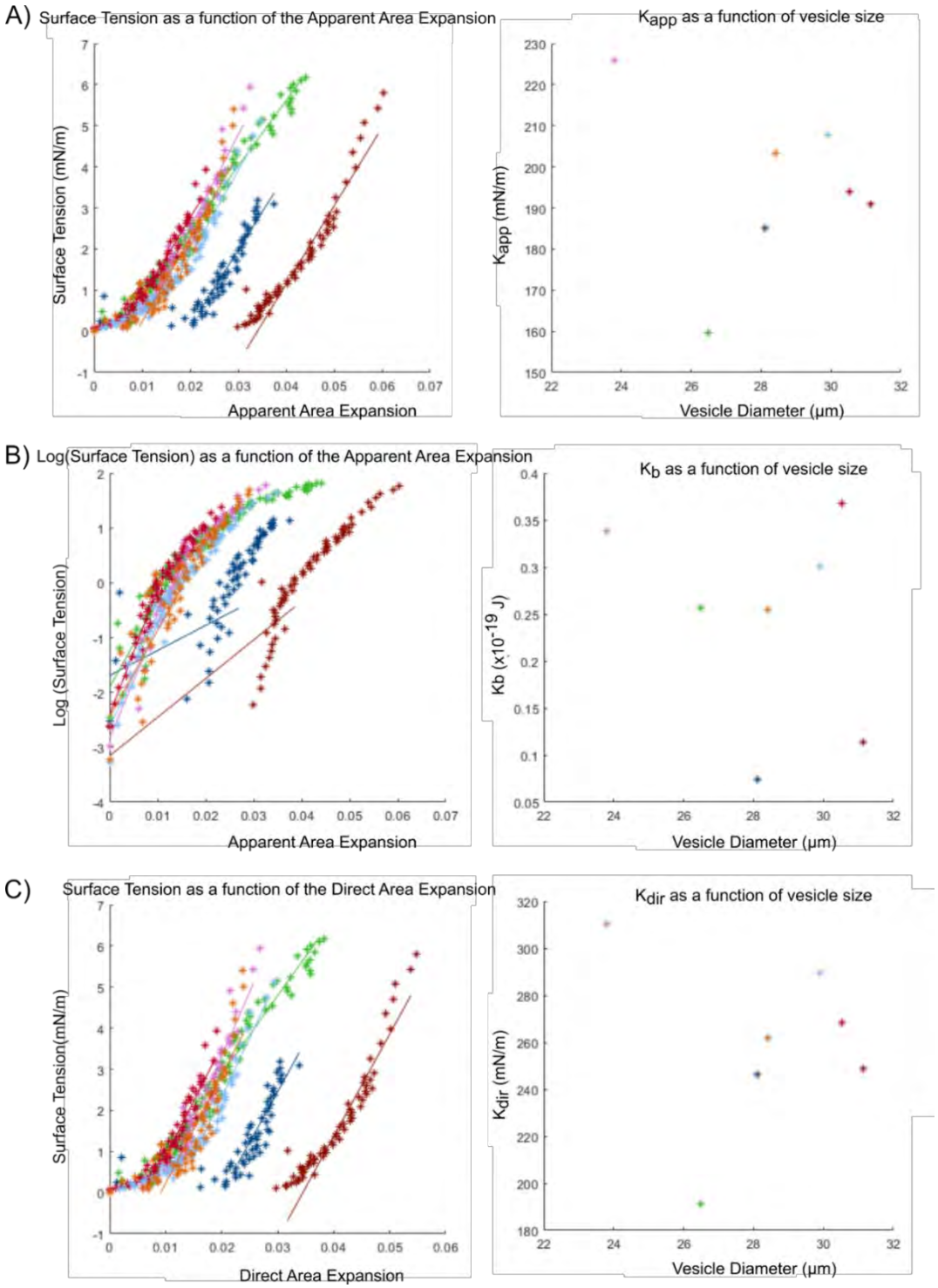

Figure V-10: Data treatment is done by Matlab for seven POPC GUVS membranes: A) The surface tension and Area expansion of all the GUVs treated is extracted from the analysis of the elongation of the vesicle and the pressure applied. The apparent stretching modulus is extracted by fitting the linear curves of the surface tension vs apparent area expansion and plotted as a function of the GUVs diameters. B) The bending modulus is extracted from fitting the linear curves of the ln (surface tensions) vs apparent area expansion. The average bending modulus is then calculated and is used to correct the area expansion, and the surface tension vs. the direct area expansion is plotted C). The direct stretching modulus is extracted from fitting the linear curves and is plotted as a function of the vesicles diameters.

5.3 Results and Discussion: on-chip micropipette aspiration

In order to characterize the effect of nanoparticles on the mechanical properties of the lipid membranes, which is one of the main objectives of my Ph.D project, we had to be sure first that our chip works well and is able to provide the necessary tools to do that. Therefore, as a proof of concept of the chip, we first tested with lipids that are well characterized in the literature, with mechanical properties extensively measured since the 2000s. Hence, we characterized first simple lipids such as DOPC and POPC, and lipid mixtures such as Brain SM with cholesterol which has higher moduli values compared to the two simple lipids. Since we were able to fabricate different diameters of pipettes, we also investigated if the pipette's diameters can affect the measured moduli of the lipids. Note however that, as discussed in Chapter 2, the quantitative values of moduli that can be found in the literature show significant differences between each other. This is true even for similar systems characterized with similar or different techniques, so that the data obtained by our method should bring useful information to the scientific community. The influence of composition on the moduli (cholesterol, sugar concentration) is also still debated in the community. Therefore, we investigated if the concentration of sucrose has any role in the low bending modulus as we studied the effect of cholesterol on DOPC lipid membranes. Finally, we investigated completely original situations: the effect of two types of nanoparticles on DOPC lipid membrane.

5.3.1 Characterization of the membranes' mechanical properties for simple lipids and simple lipid mixtures

As discussed, we first investigated first the mechanical properties of simple lipids such as DOPC and POPC and a mixture of Brain Sphingomyelin (SM) lipids and cholesterol. In chapter II, we saw that the length and saturation of the lipids' chains have an effect on the mechanical properties of the membrane, especially the bending modulus. Sphingomyelin lipids present around 6% of the lipids in the plasma membrane, and they have high affinity to cholesterol which together create microdomains in the membrane, which also affect the elastic properties of the membranes. The chemical structure of the lipids studied here as well as the lipids mentioned overall the manuscript are represented with the list of the abbreviations, at the beginning of the manuscript.

Electroformation

The phase transition temperature of DOPC, POPC, and Brain SM are respectively: -20°C, -2°C and -40°C. However, when SM is mixed with cholesterol, the temperature phase transition increases to 50°C. Therefore, for DOPC and POPC, the electroformation was made at room temperature, whereas for SM+Chol (1:1 molar ratio), it was done at 55°C. The concentration of sucrose used was 180 mMol/L in most cases, but we also investigated lower concentration to characterize a possible change on

moduli ***(chapter 2.3.2.2)*** [3], [4]. The lipids were stained with 0.1%mol 16:0 Liss Rhod PE ***(Figure V-11)***. In order for the GUVs to be easily deformed inside the micropipette, the GUVs have to be slightly floppy. It ensures that the pipette diameter controls the cap's curvature and thus that the applied tension is known (Laplace law). To do so, we imposed a small osmotic pressure difference on the GUVs by slightly increasing the concentration of the sucrose in the final medium where the GUVs are suspended. In fact, 50µL of GUVs obtained in a 180 mMol/L sucrose solution are diluted with 950µL of a 185 mMol/L sucrose solution. The total osmolarity outside the GUVs is 184.75 mOsm for 180 mOsm GUVs.

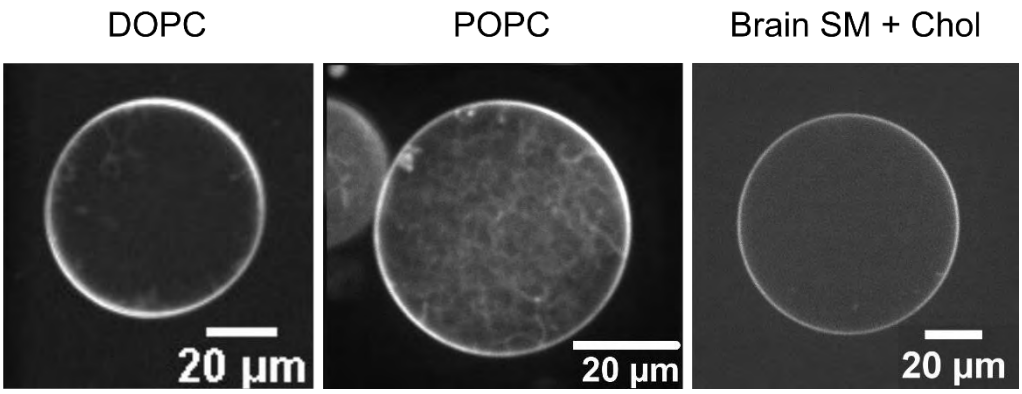

Figure V-11: Confocal microscopy images of DOPC, POPC and Brain SM + Chol GUVs stained with Liss-Rhodamine. POPC and DOPC were fabricated at room temperature whereas SM + Chol was fabricated at 55°C.

5.3.1.1 Effect of the diameters of the pipette and the GUVs on DOPC bending modulus

Before going through the results of the elastic moduli of all the lipids mentioned above, we characterized the effect of the diameters of the pipette and the GUVs, combined with the effect of sucrose on the DOPC lipid membrane. To do so, we performed micropipette aspiration using different pipettes of 6, 8, 12, and 15 µm diameters. Moreover, the different concentrations of sucrose used are 18, 105 and 185 mM. In fact, GUVs were electroformed using concentrations of sucrose of 15, 100 and 180 mM which was then diluted in sucrose of respectively 18, 105 and 185 mM final concentrations. The results of the bending modulus as a function of the GUVs diameters, for different pipette diameters and sucrose concentrations are shown in ***Figure V-12***. Considering the GUVs diameters and for each same concentration of sucrose, the bending modulus appears to not be affected by the diameters of the GUVs, which are aspirated by different pipette diameters. In fact, except for the blue circle point appearing in ***Figure V-12A***, the bending moduli appear to be in the same order of magnitude, with no systematic effect of either the pipette diamter or the GUV diameter . The blue point corresponds to a single measurement made by a micropipette of 6 µm diameter in 18 mM sucrose concentrations. This only single outlier point is most likely to be discarded, since it probably originates from an error in measuring the pipete actual diameter, or to its contamination during the experiment. Moreover, in ***Figure V-12C***, another single measurment made by micropipette of 6 µm

was analyzed and the bending modulus was in the same range as for the rest of the pipette diameter. Corresponding the pipette diameter and if the blue point of 6 µm is discarded, a small difference in the bending modulus values appear in ***Figure V-12B***, which is slighly higher for the pipette of 8 µm than the pipette of 12 µm. However, overall the results, the difference in the pipette diameters doesn't not seem to alter systematically the bending modulus.

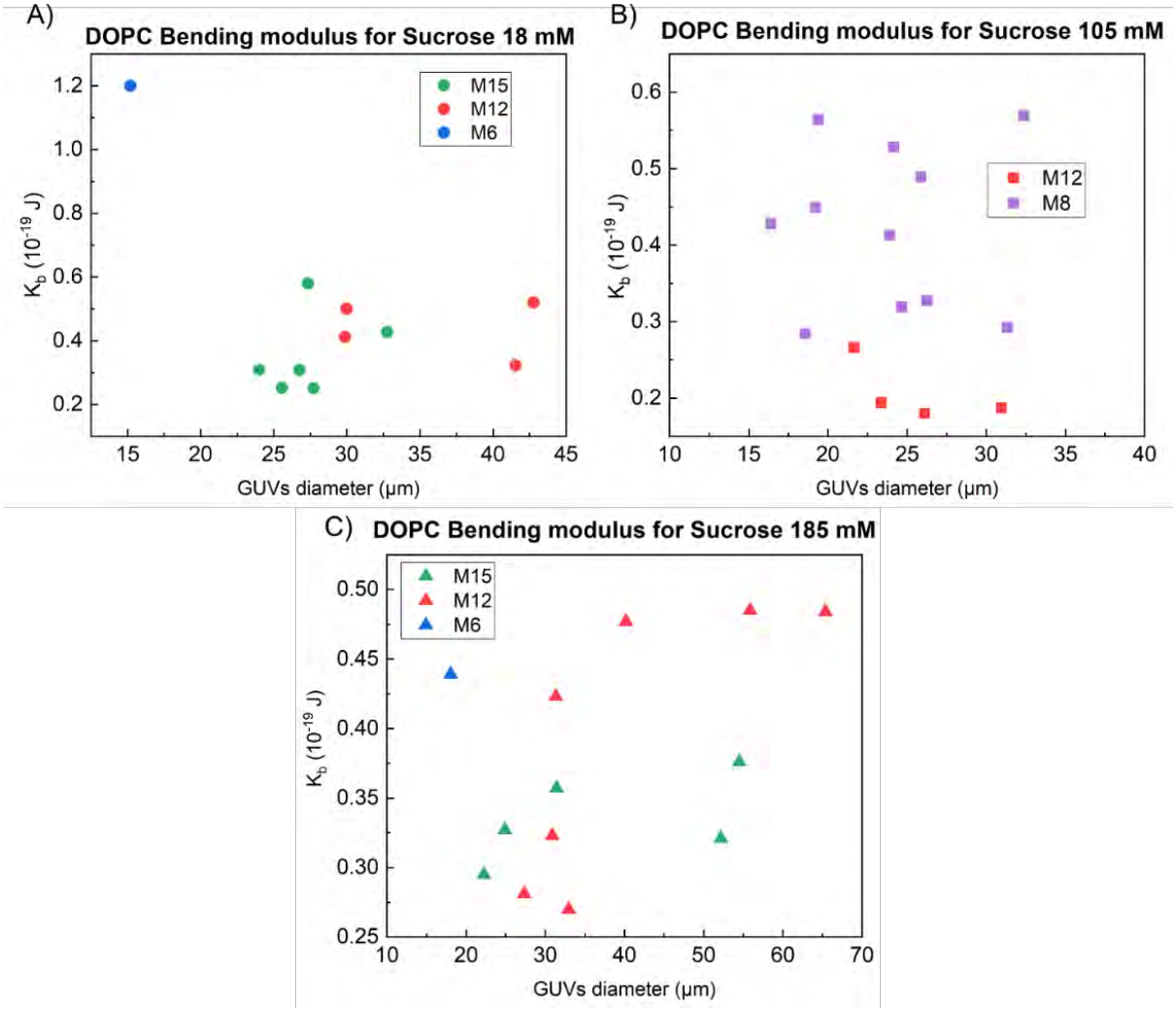

Figure V-12: DOPC bending modulus as function of the GUVs diameters trapped in different micropipettes diameters 6 µm (blue), 8µm (purple), 12µm (red) and 15µm (green). The micropipette aspiration experiments were also performed on different concentrations of sucrose of respectively A) 18 mM (circles), B) 105 mM (squares), C) 185 mM (triangles).

As the effect of the diameters of the GUVs alone on the bending modulus of DOPC membrane is not so clear, we normalized the GUVs diameter by the pipette diameter, and characterized the effect of the ratio of GUVs diameter and pipette diameter on the bending modulus. ***Figure V-13*** shows the combined results of all the DOPC GUVs that were characterized, normalized by the pipette diameter and for the different concentrations of sucrose. In fact, in the literature and as mentioned before, it is advised to have a pipette diameter that is 1/3 times the diameter of the GUV. The values of the bending modulus appear to be very dispersed compared to the ratio of the diameter of the vesicles

and the diameter of the pipette. The orange rectangle is to separate values of the bending which corresponds to a ratio that is lower than 2.5: if the pipette diameter is too close to the GUV diameter, the bending modulus tend to be slightly lower than the rest. This could be an error in estimating the area. However, because of the dispersion of the values, no clear results can be deducted of the effect of the ratio D_v/D_p. Note that, usually equation ***2-8*** (chapter II), which compute the area increase of the GUV is a simplified equation after using a Taylor approximation for $\frac{D_v}{D_p} \ll 1$. However, in our case and in order to avoid an error of estimation of the area for GUVs that have comparable size to the micropipette, the exact formula (equation ***2-7***) is used.

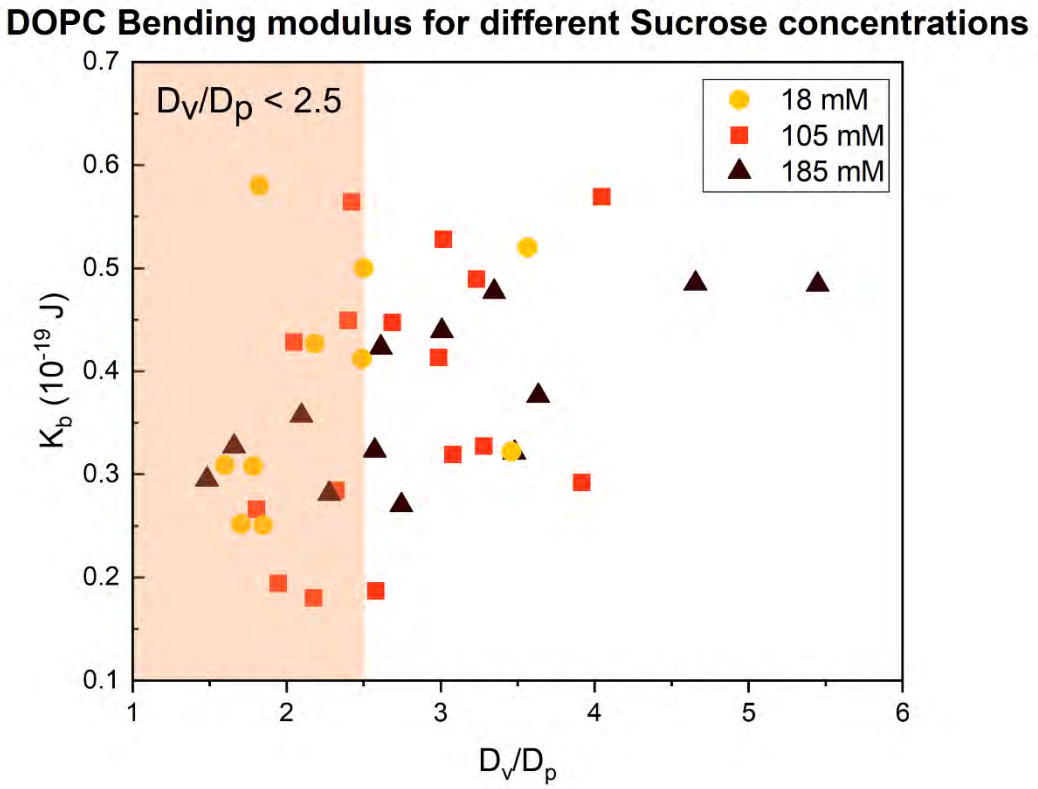

Figure V-13: Effect of the ratio of GUVs diameter over the diameter of the pipette on the bending modulus for different sucrose concentrations: 18 mM in yellow, 105 mM in orange and 185 mM in brown.

5.3.1.2 Effect of Sucrose concentrations on DOPC lipid membranes

Finally, since no clear or systematic change appear in the bending modulus values as a function of the diameter of the micropipette, as well as the diameters of the GUVs, we represented the average of all the bending and stretching moduli as a function of the different sucrose concentrations. The results are summarized in ***Table V-2***. Considering the bending modulus, the average values obtained for the different concentrations as very close to each other, suggesting that there is no effect of sugars on the bending modulus. Considering the stretching modulus, the average values obtained for sucrose concentrations of 18 and 105 mM are very close to each other. On the other hand, the stretching

modulus seem to increase for higher sucrose concentrations (185 mMol). However, this increase is still in the same range of the others and still in the margin of the estimated errors.

Table V-2: Effect of sucrose concentrations on bending and stretching modulus of DOPC lipid membranes

Sucrose concentrations (mM)	*Bending modulus K_b (10^{-19} J)*	*Stretching modulus K_A (mN/m)*
18	0.38 ± 0.11	235 ± 51
105	0.39 ± 0.13	232 ± 59
185	0.37 ± 0.07	294 ± 81

In conclusion of these measurements, the effect of the pipette diameter and the concentration of sucrose on the bending modulus of DOPC lipid membranes were characterized. The effect of the concentration of sugars on the bending modulus has been a debate in the membranes community as previous micropipette experiments showed a correlation between them, whereas X-ray experiments showed the opposite. It is thought that at high concentration, sugar is absorbed in the membranes, forcing the membrane to increase its area [5]. This could explain the slight increase in the average stretching modulus with the increase of sucrose concentrations. However, our results showed that there is no clear effect of the sucrose nor the pipettes diameters on the elastic moduli of the DOPC lipid membranes.

In order to extract the elastic moduli of DOPC, POPC, and Brain SM + Chol lipid membranes, micropipette aspiration experiments discussed hereafter were performed using a pipette of 8 µm and a sucrose concentration of 105 mM. The choice of 105 mM sucrose was to use a middle concentration between 15 mM (where the GUVs could not be totally stable) and 180 mM where an effect could happen on the stretching modulus. Considering the choice of the diameter of the pipette, even though there is no systematic effect of the pipette diameter on the elastic moduli, using a smaller pipette allows us to characterize larger range of GUVs size. Moreover, we could avoid altering the area measurement when using bigger pipettes. In fact, if the diameter of the vesicle is close to the diameter of the pipette, which is mostly the case of the 15 and 12 µm pipettes, the vesicle might slide inside the pipette and escape sooner than it is supposed to. ***Figure V-14***, shows the average release pressure at which the vesicle escapes from the micropipette as function of the diameter of the pipette. In fact, the GUVs escape at quite low pressure (around 4 mbar) when the pipettes are between 10 and 15 µm, which corresponds to a surface tension of 2 mN/m. On the contrary, in the smaller pipettes (6 and 8 µm) the GUVs have the time to reach up to 23 mbar before they escape, which corresponds to a surface tension of around 6 mN/m, thus permits to fully characterize the stretching (high tension) regime.

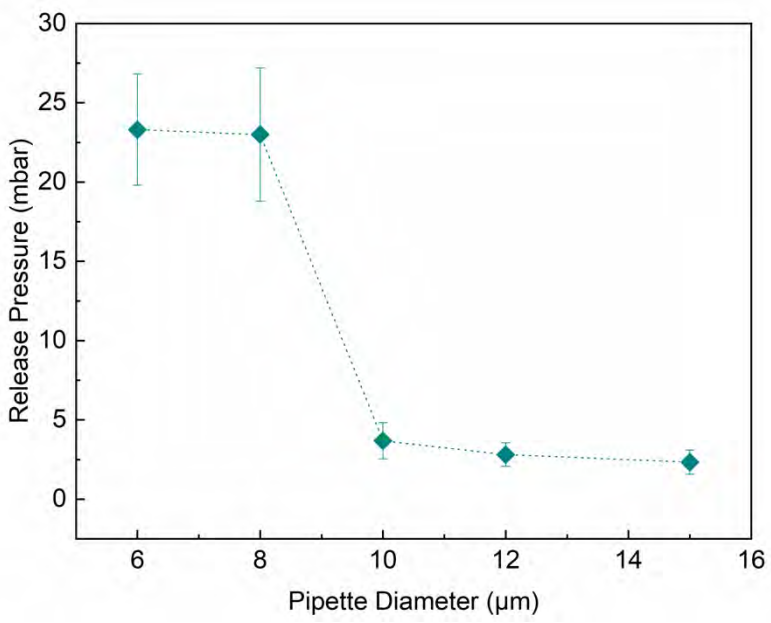

Figure V-14: Average release pressure of DOPC GUVs as function of the diameter of the micropipette.

5.3.1.3 Bending modulus of DOPC, POPC and Brain SM + Chol lipid membranes

The bending modulus of DOPC, POPC and Brain SM + Chol membranes obtained in our experiments are shown in ***Figure V-15*** and are respectively : $0.48 \pm 0.11\ x10^{-19}\ J$, $0.60 \pm 0.18\ x\ 10^{-19}\ J$ and $0.76 \pm 0.30\ x\ 10^{-19}\ J$. Note that for DOPC, the value obtained here corresponds only to the average values of the bending moduli obtained using a micropipette of 8 µm diameter and a sucrose concentration of 105 mM, in order to homogenize the parameters used for POPC and Brain SM + chol also. The values of the bending moduli of DOPC, POPC, and Brain SM + chol correponds to an average of respectively 5, 7 and 3 vesicles. For DOPC and POPC lipid membranes, the values are in the same range, but lower (around the half) compared to the literature values which are shown in ***Table V-3*** for DOPC lipid membranes. The value we obtain for Brain SM + Chol is 4 times lower than the only value found in the litterature ($3.1\ \pm\ 0.2\ x\ 10^{-19}\ J$). However, it was obtained using tube pulling technique though [6] and not micropipette aspiration as these data are missing from the litterature. As discussed in chapter II, the bending moduli measured with different techniques do not always show quantitative agreement. In addition, some parameters can affect the bending modulus of lipids membranes such as the temperatures and the concentration of sugars and salt (which is still debated). We do not fully explain why our results give lower bending moduli than most values found in the literature. However, these discrepancies between different measurements made on similar systems highlights the importance of developing robust methods for bending characterization of membranes, which are still not fully quantitive.

Table V-3: DOPC Bending modulus values taken from the literature as a function of the following parameters: the temperature, the sucrose concentration and the diameter of the pipette. The colored line represents our data.

	Bending (10^{-19}J)	Temperature (°C)	Sucrose concentration (mMol/L)	Pipette Diameter(µm)
DOPC	0.78 [4]	30	200	10
	0.85 [7]	18	200	10
	0.91 [8]	22.5	200	20
	0.48	22.5	105	8

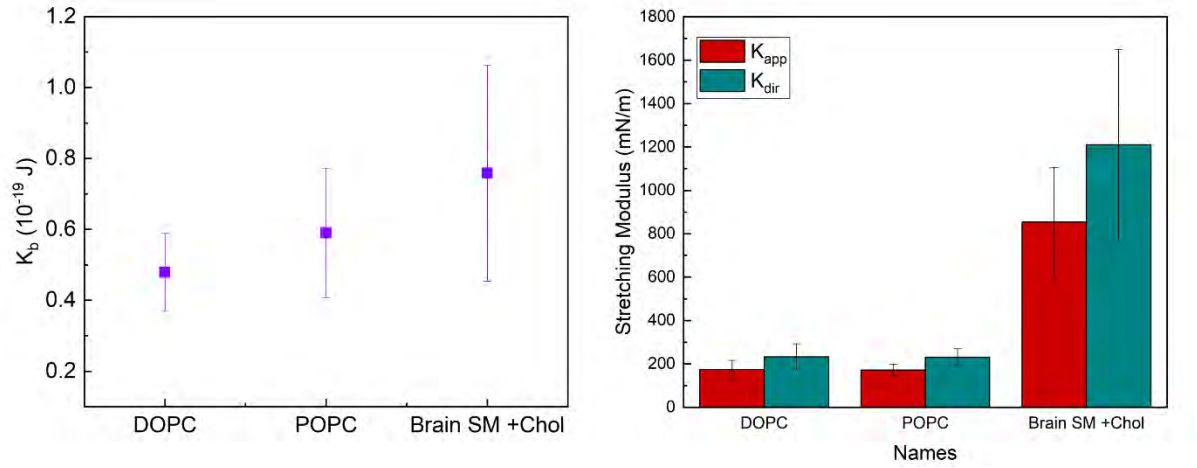

Figure V-15: Bending and Stretching modulus values for DOPC, POPC and Brain SM + Chol lipid membranes. Micropipettes aspiration were made using a pipette of 8 µm and a sucrose concentration of 105 mM.

5.3.1.4 Stretching modulus of DOPC, POPC and Brain SM + Chol lipid membranes

The measured average apparent moduli of DOPC and POPC membrane are respectively: $174 \pm 41\mathrm{mN/m}$ and $172 \pm 24\ \mathrm{mN/m}$. The stretching moduli were then corrected using the average bending modulus values (as seen in chapter II) and the direct stretching moduli were obtained: $232 \pm 59\ \mathrm{mN/m}$ for DOPC and $231 \pm 39\ \mathrm{mN/m}$ for POPC. These values are compatible with the values found in the literature. For DOPC membranes characterized by micropipette aspiration techniques, the values of the direct stretching modulus are between 198 mN/m and 310 mN/m [8],[9],[7],[10]. For POPC membranes characterized by micropipette aspiration, to our knowledge, there are much fewer data available: 213 mN/m in ref [11]. In order to understand the small difference in these values, I assembled, in ***Table V-4,***the values of the DOPC and POPC stretching modulus from the literature with the different parameters that were used during the traditional micropipette aspiration experiments: the temperature, the sucrose concentration, and the micropipette diameter. For DOPC, as sucrose concentration in all these experiments is the same (200 mMol/L), the differences could lie in the temperature and the pipette diameter. However, there is no systematic effect of the pipette diameters on the stretching modulus: the smallest pipette diameter (3 µm) gives an intermediate value of the stretching modulus compared to higher pipette diameters (10 and 20 µm).

Therefore, the only parameter that seems to affect the stretching modulus is the temperature. In fact, in chapter II, I discussed that the temperature has an effect on the bending modulus, especially close to the phase transition temperature. Here, the low temperature (15 °C) seems to give a higher value for the stretching modulus whereas the higher temperature (22.5°C) gives lower values of the stretching modulus. The reason for that could be that the low temperature can make the membrane more rigid, whereas high temperature can fluidify it, giving therefore a lower stretching modulus. In our experiments, under 22°C, the concentration of sucrose is 105 mM and the diameter of the pipette is 8 µm gave a stretching value of 232 mN/m. This value is in the same ranges as the rest of the values found in the literature. Considering POPC, our value fits perfectly with the only value found in the literature, using micropipette aspiration. In fact, the difference between the two experiments is the slightly higher pipette diameter that we used, and the slightly lower temperature at which we performed our studies. However, the concentration of sucrose we used was 2.5 times lower than in the other experiment, this did not seem to affect the stretching modulus of POPC lipid membrane

Table V-4: DOPC and POPC stretching modulus values taken from the literature as a function of the following parameters: the temperature, the sucrose concentration and the pipettes diameter. The colored lines represent our data.

	Direct Stretching modulus (mN/m)	Temperature (°C)	Sucrose concentration (mMol/L)	Pipette Diameter(µm)
DOPC	210 [8]	22.5	200	20
	198 [12]	22.5	200	3
	265 [7]	18	200	10
	310 [9]	15	200	10
	232	22.5	180	15
POPC	213 [11]	25	250	5
	231	22.5	100	8

Considering the Brain SM/cholesterol mixture, the molar ratio of cholesterol and the sphingomyelin is 1:1. It is a high concentration of cholesterol in a GUV lipid membrane; however, it is close to the plasma membrane's reality. The value of the apparent and direct stretching modulus obtained in our experiments are: $K_{app} = 853 \pm 250$ mN/m and $K_{dir} = 1210 \pm 440$ mN/m. These values are much higher than the one obtained for DOPC and POPC, showing that our method enables measuring wide ranges of stretching moduli. Only one example of micropipette aspiration to characterize such lipid mixture is found in the literature with the value of $K_{dir} = 2193 \pm 209$ mN/m [9]. A possible explanation for the lower value of stretching modulus obtained in our experiments, even if they are in the same range, could come from the low speed of loading the GUVs during the pre-stretching step to remove possible lipid reservoirs and defects (seen in chapters II and IV). In fact, it was shown that if the pre-stretching loading was fast, there is not enough time for the thermal undulation to smooth,

and therefore, as the deformation of the lipid membrane is the combination of both regimes, the stretching modulus gives high values compared to low-speed loading [9]. In the previous reference, the tension increase was 2 mN/m/s, which corresponds to a ΔP = 4 mbar, for a pipette of 10 µm and a vesicle of 20 µm. The applied pressure increase in this reference is 80 times faster than the increase pressure that we apply during our experiments which corresponds to 0.01 mbar for the bending regime, and 0.05 for the stretching regime.

5.3.2 Effect of Cholesterol on DOPC lipid membranes

Cholesterol is one of the main components of the plasma membrane, along with the phospholipids, and it is an important component for the membrane as seen in chapter I. Some studies demonstrated that cholesterol increases membrane's stiffening shown by the increase of the stretching modulus as seen in ***chapter 2-3-3-2*** [13], [9]. However, another study discussed by Nagle showed a decrease of the stretching modulus when adding cholesterol up to 40% [14]. The effect of cholesterol on lipid membranes is still debated and more studies are needed to understand it better. Therefore, we also investigated the effect of cholesterol on DOPC lipid membranes, which has 18 carbon chains with one unsaturation in each of the chains. To do so, we fabricated GUVs that are formed of DOPC and Cholesterol with different increasing molar concentrations: 30%, 40% and 50%. The micropipette aspiration studies were made using micropipettes of 15 µm diameters and a concentration of sucrose of 180 mMol/L. The stretching and bending moduli results of these lipid mixtures are shown in ***Figure V-16***. The stretching modulus of DOPC:Chol membranes increases from 294 mN/m to 521 mN/m when adding 50% of cholesterol, which corresponds to an increase of 77%. On the other hand, the bending modulus slightly changes, but the final increase corresponds to only 14 %. Our results confirm the many studies done before by micropipette aspiration and which also proves the increase of membranes stretching modulus in the presence of cholesterol, whereas no effect was seen regarding the bending modulus.

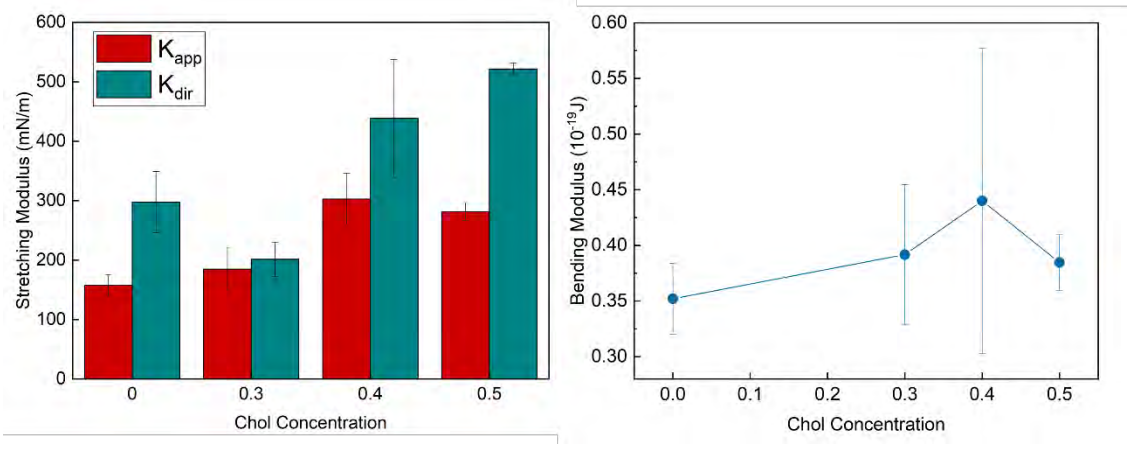

Figure V-16: Stretching and bending moduli of DOPC lipid membranes mixed with a different molar concentration of cholesterol.

5.3.3 Effect of nanoparticles on DOPC lipid membranes

As mentioned in the introduction, one of the project's objectives is to understand how different nanoparticles (NPs) are able to affect cell membranes. *Are they able to go through the membrane upon interaction? Or do they merge within the lipids bilayer? Do the mechanical properties change and how?* These are relevant questions for medical purposes, for example, in the case of drug delivery systems. As I mentioned in ***chapter 2-4***, the interaction of NPs with lipid membranes depends on the characteristics of the NPs, such as their size, their surface chemistry, and their type, but also on the lipid membranes properties, if it was in the liquid or gel phase for example. As we were able to characterize the mechanical properties of the DOPC membranes, we chose it as a case study to investigate the effect of nanoparticles on the mechanical behavior of biomimetic membranes. To do so, we chose two types of nanoparticles that have been used before in comparable studies (as seen in chapter ***2- 4***): self-assembled micelles made of block copolymers, and gold nanoparticles. The NPs were mixed together with the DOPC membranes before being sent to the microfluidic chip. The micropipette aspiration experiment was then performed to determine the mechanical properties of the membranes that have been in contact with the NPs. We changed the concentration of nanoparticles for each type and checked if the increasing amount of NPs can modify or even deteriorate the lipid membranes. The micropipette aspiration experiments for the GUVs that were challenged with NPs were performed using a micropipette of 15 µm diameter, and a concentration of sucrose of 185 mM. Therefore, note that the elastic moduli of pure DOPC lipid membrane, which will be mentioned later, corresponds to the average of the values of elastic moduli obtained only in micropipette of 15 µm and in sucrose of 185 mM.

5.3.3.1 Effect of PEO-PCL copolymer micelles on DOPC lipid membrane

We collaborated with the "Laboratoire des Interactions Moléculaires et Réactivité Chimiques et Photochimiques)"- IMRCP who provided us with the nanoparticles. These copolymer nanoparticles were developed for drug vectorization due to their ability to solubilize hydrophobic compounds [15]. The preparation of the NPs solution was done by the IMRCP lab, and the protocol is detailed in the materials and method part.

PEO-PCL nanoparticles dilution with DOPC lipid membranes

The concentration of the mother solution of PEO-PCL nanoparticles was unknown; therefore, we tested two different dilutions of NPs as follows: as mentioned in the electroformation paragraph, the electroformed GUVs are usually diluted 20 times in a total volume of sucrose of 1 mL (50 µL (GUVs) + 950 µL (sucrose) = 1mL). The dilution of the NPs was done compared to the total final volume of 1 mL. For a dilution of 1/150 times, 50 µL of GUVs solution was mixed with 6.6 µL of NPs and then a sucrose

solution was added to complete a total 1mL solution. The 1/20 dilution follows the same principle; however, this solution is 7.5 times more concentrated in NPs than the first one. ***Figure V-17A*** is a schematic representation of the dilution of both GUVs (red hydrophilic heads and black hydrophobic tails inside the membrane) and NPs (green hydrophobic heads and blue hydrophilic tails in the water). After dilution of the NPs with the DOPC GUVs for half an hour, a confocal microscopy image was taken to characterize any visual effect ***(Figure V-17C)***: DOPC GUVs seemed to be floppier, with some small changes in the shape leaning to a more oval shape. This indicated that the NPs might affect the DOPC membrane. The mixture was then sent to the microfluidic chip, and the micropipette aspiration experiment was performed. The results of the stretching and bending modulus are shown in ***Figure V-17D-E*** and are the average moduli of 5 vesicles for pure DOPC membrane, 7 vesicles for the dilution of 1/150 and 5 vesicles for the 1/20 dilution.

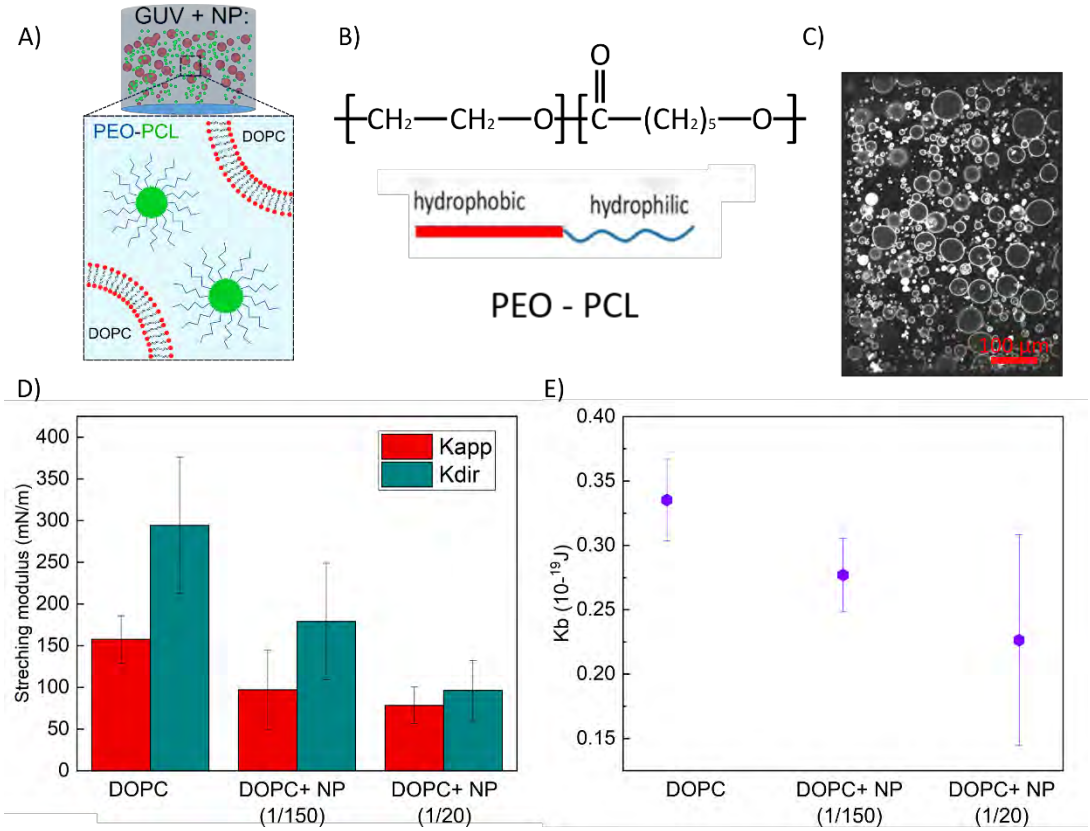

Figure V-17: Interaction of DOPC lipid membranes with PEO-PCL copolymer nanoparticles: A) representation schema of the GUVs and the NPs mixed together. The NPs are self-assembled micelles with a hydrophobic head and a hydrophilic tail, as seen in B). C) is a confocal microscopy image of the DOPC membranes after mixing them with the NPS (1/20 dilution). D) is the apparent and direct stretching moduli, and E) is the bending moduli of the DOPC membranes that have been in contact with different concentrations of NPs.

Stretching and bending modulus of DOPC lipids membranes in contact with PEO-PCL nanoparticles

Upon interaction of DOPC lipid membranes with PEO-PCL nanoparticles, both bending and stretching modulus decrease as seen in ***Figure V-17D-E.*** The direct stretching modulus values are 179 ± 70

mN/m and 96 ± 35 mN/m for 1/150 and 1/20 dilutions, respectively. This corresponds to a decrease of respectively 39% and 67%. Considering the bending modulus, the values are respectively $0.27 \pm 0.03\ x\ 10^{-19}$ J and $0.22 \pm 0.08\ x\ 10^{-19}$ J. This corresponds to a decrease of respectively 17% and 32%.

A possible origin of these decreased stretching and bending modulus of the DOPC vesicles is that upon interaction of the PEO-PCL micelles, the micelles (partly) merge with the lipid bilayer, which could lead to intermediate values of stretching modulus between that of DOPC and that of pure PEO-PCL vesicles. The fusion of copolymers liposomes with GUVs lipid membranes has been already demonstrated but in the presence of salt [16]. Typical values of the stretching modulus (K_A) of membranes made of the amphiphilic copolymer in the literature are indeed below 100 mN/m [12], for example, for pure PEO-PBD membrane, $K_A = 89\ \mathrm{mN/m}$ [17]. However, the bending modulus of such co-polymers are absent in the literature, making it difficult to compare it to other values. The decrease of both measured moduli could also originate from the fact that these nanovectors create defects in the membrane, modifying the effective stretching and bending modulus. This is consistent with experiments on Large unilamellar vesicles (LUV) in the absence or presence of polymer micelles where PEO-PCL micelles increased the permeability of DOPC LUV [18] as seen in ***chapter II-D-2-b***. This could play an important role in the potential of such NPS to interact efficiently with membranes, a key asset for drug carriers.

5.3.3.2 Effect of Gold nanoparticles on DOPC lipid membrane

We collaborated with the CSGI laboratory and the University of Florence who have developed expertise in model membranes and their interactions with nano-objects, as well as in synthesizing different nanoparticles. They also provided us with the nanoparticles. The preparation of the citrate gold NPs (NPs@Ct) solution was done by the CSGI lab, and the protocol is detailed in the materials and method part.

Citrate Gold nanoparticles dilution with DOPC lipid membranes

We tried two different concentration ratios of NPs compared to the GUVs. In the first one we diluted 50 µL of GUVs in 950 µL of sucrose solution obtaining 1 mL of GUVs solution and then we added 12.5 µL of 9 nM NPs@Ct nanoparticles, which corresponds to a final molar concentration of NPs in the solution of 112 pM (~ 0.1 nM). In the second one w diluted 50 µL of GUVs in 862 µL of sucrose solutions and then we added 100 µL of 9 nM NPs@Ct nanoparticles, which corresponds to a final molar concentration of NPs in the solution of 882 pM (~ 0.9 nM). The micropipette aspiration was performed after half an hour of incubation of the GUVs with the NPs. The results are shown in ***Figure V-18.***

Stretching and bending modulus of DOPC lipid membranes in contact with Citrate Gold nanoparticles (NPs@Ct)

In order to characterize an optimal time at which the interaction of the NPs with the DOPC lipid membranes is the most efficient, we kept track of the time after the incubation of the NPs and the GUVs in each micropipette aspiration study. In ***Figure V-18 A –B,*** the stretching and bending modulus are plotted as a function of the time since the incubation and for the different concentrations of NPs used. Our result of the moduli seems to be spread over the time, and we do not observe a very clear systematic temporal evolution of the values of the moduli. In fact, even if there seems to be variations of the moduli, it is difficult with just our data to quantify this evolution. Therefore, the average values over the incubation time of the bending, and stretching modulus are calculated and are plotted in ***Figure V-18 C-D*** for the different concentrations of NPs.

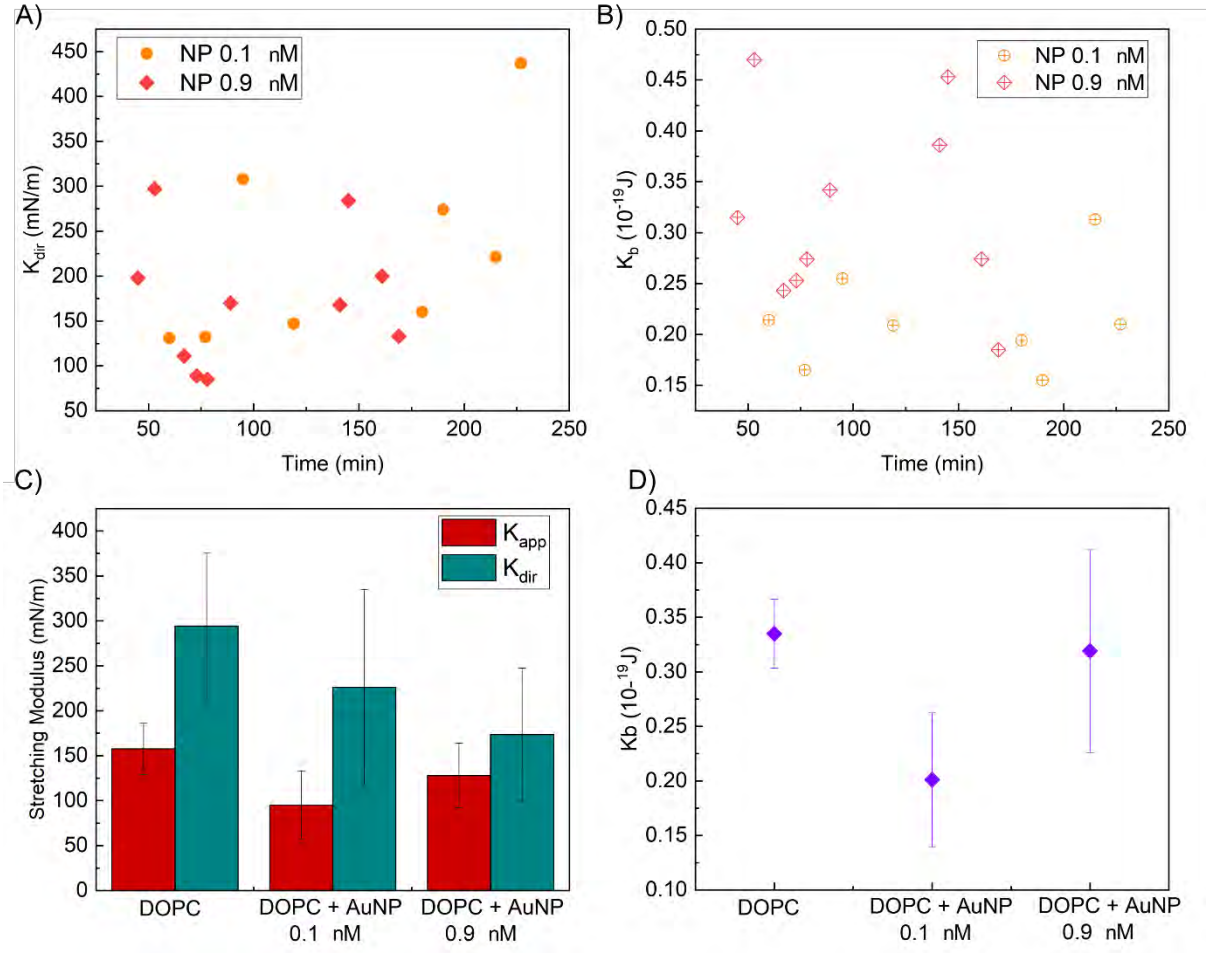

Figure V-18: Interaction of DOPC lipid membranes with Citrate Gold nanoparticles: A) and B) are the bending and stretching modulus of each vesicle respectively represented as a function of the time of interaction of the nanoparticles with the membranes, and for the different NPs concentrations used. C) and D) are respectively the average stretching and bending modulus of DOPC lipid membrane challenged with the different concentration of Citrate Gold NPs

The average stretching modulus for DOPC membranes challenged with 0.1 nM and 0.9 nM NPs are respectively 226 ± 108 mN/m and 173 ± 74 mN/m. This corresponds to a percentage of decrease

of respectively 23% and 40%. The average bending modulus for DOPC membranes challenged with 0.1 nM and 0.9 nM NPs are respectively $0.2 \pm 0.06\, x\, 10^{-19}$J and $0.32 \pm 0.09\, x\, 10^{-19}$J. This corresponds to a percentage of decrease of respectively 40% and 4.4%, 4.4% being in the range of the error bars and therefore a negligible decrease.

We propose a plausible scenario considering the behavior of the NPs: in fact, in ***Figure V-18 A-B,*** the last GUV studied for 0.1 nM concentration was upon 225 minutes of incubation. The bending modulus exhibits a value that is the same as the GUV which was characterized upon 50 minutes of incubation However, the stretching modulus exhibits a significant increase in its value. On the other hand, for the higher concentration (0.9 nM), the bending modulus shows an increase from the first GUV studied until 150 minutes of study and then a sudden decrease when the duration of the incubation reaches 170 minutes. Same for the stretching modulus, which exhibits an increase in its value up to 150 minutes of incubation and then a decrease after 170 minutes of incubation.

Our results could be explained as follows: for a high concentration of NPs, the bending modulus increase is caused by the aggregation of NPs at the lipid membranes and creating the raft-like domains which induce local rigidification in the membrane. After a certain time, the NPs cause defects and increase the permeation of the NPs inside the membrane, releasing them from the surface of the membranes. The defects and the permeation on the membranes causes the effective bending and stretching modulus to finally decrease. ***Figure V-19*** illustrate how this scenario would explain such results. On the other hand, for a lower concentration of NPs, the effect of the NPs is delayed and starts later compared to the 0.9 nM concentration. Therefore, the average values represented in ***Figure V-18 C-D*** can be incorrect to time-average if the process is still evolving and if the adsorption equilibrium is not respected. Finally, in order to prove our theory, more micropipette aspiration experiments are still needed to be done in order to characterize the evolution of the elastic moduli with the incubation time.

Another possible reason for the dispersion in the values of the moduli, could be the cause of a non-homogenous spread of the NPs around the GUV, causing non-homogenous aggregations of NPs on the different GUVs studied. We suggest that using microfluidics, we may mix the NPs-GUVs more efficiently and expose the GUVs to a shear stress, which could influence the process of interaction and permeation of the NPs. We proposed another microfluidic design, using the same technique of the element, to trap the GUV and allow the flow to continuously shear the GUV. This will be detailed in the end of this chapter, as a future perspective of this subject.

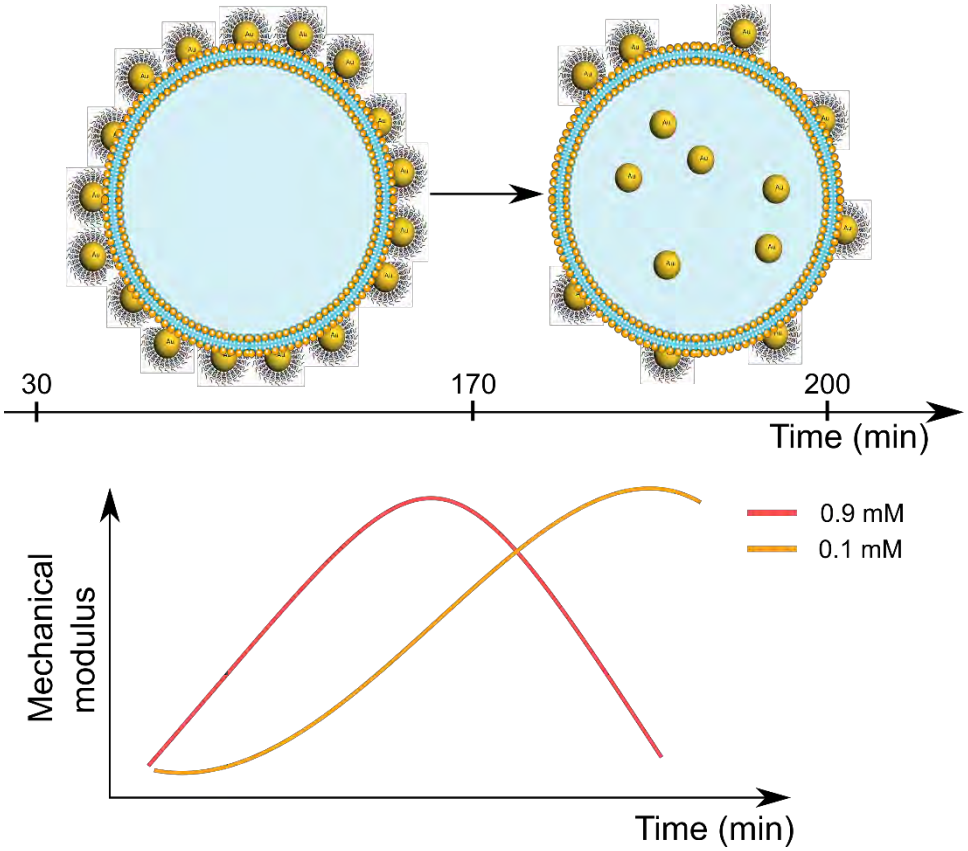

Figure V-19: Scheme representation of the Gold NPs interaction with a GUV lipid membrane. NPs aggregated on the lipid membranes first, which increases their bending modulus. After some time, the Gold NPs induce permeation in the membranes and cross the lipid barrier inside the GUV, which decreases their mechanical moduli

We have characterized the effect of both PEO-PCL copolymer micelles NPs and Gold nanoparticles on DOPC membranes. Both nanoparticles have been proven to be a great tool in biomedicine to deliver drugs or vaccines. Our study completes the picture by characterizing the effects of these NPs on the mechanical properties of the lipid membranes. PEO-PCL nanoparticles show a possible fusion of these particles with lipid membranes, which makes the membrane softer and therefore easier to deliver a drug inside the GUV. Gold NPs increase membrane permeability and create raft-like domains, however, their effect on the mechanical properties of lipid membranes is not so clear and more experiments are still needed, in particular to investigate the different temporal steps of the interaction.

5.4 On-chip micropipette for biological objects

Micropipette aspiration was first developed in 1954 to characterize the mechanical properties of cells and it was called back then “the Cell Elastimeter” [22]. Because this technique is powerful, theoretical models have been developed for many different objects: micropipette aspiration has been used on many kinds of single cells such as red and white blood cells, but also 3D aggregates of cells such as embryos [23], spheroids, tissues, and cells within tissues (cell-cell surface tension within a tissue).

5.4.1 General properties of Spheroids

In vitro studies of cells in 2D are used to study a range of biological processes because they are easy to culture under controlled conditions, however they do not represent the complex 3D environment that exists *in vivo*. Therefore, scientists have been culturing 3D models made of cell aggregates. An important dense 3D aggregate of cells model is the spheroid [24]. Spheroids are spherical shape 3D aggregates which sizes range from 100 µm to > 500 µm. Spheroids which derive from cancer cells can reach 1000 µm diameter ***(Figure V-20)***. They exhibit greater physiological relevance than 2D cell cultures, such as cell viability, morphology, proliferation, differentiation, metabolic activity, migration and gene expression [25].

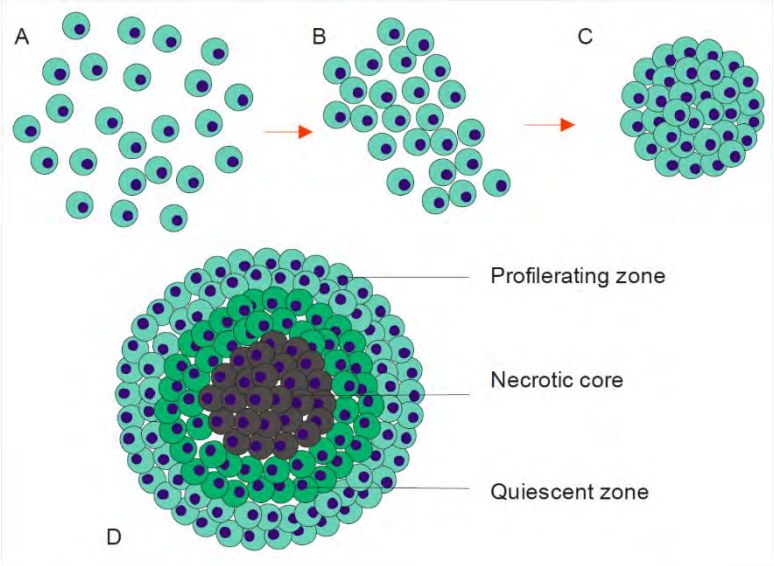

Figure V-20: Structure and formation of multicellular spheroid: (A-C) formation, and (D) structure [26]*. A tumor spheroid consists of sequential layers of proliferating cells, quiescent cells (dormant cells) and a pathophysiological necrotic core.*

With the same objectives as biomimetic membranes, *in-vitro* cell cultures are fundamental for observations and understanding all the biological behaviors that happen in our bodies and which are unreachable or very difficult to reach *in vivo*. Spheroids are the closest *in vitro* models to tissues and have properties that closely mimic *in vivo* tissues. Cell aggregates play an important role in many cellular processes such as tissue functionality, embryonic development and cancer metastasis. Studies have shown that the mechanical properties of cell aggregates and their interaction with

microenvironment have significant effects on functionality and biological behaviors. In fact, several pathologies, genetic mutations or even scarring can disrupt the architecture and the functions of tissues and thus result in changes in their mechanical properties.

Accordingly, spheroids have been used in cancer research and biomimetic *in vitro* models to study fundamental mechanisms in tumor biology [27], [28] . Moreover, they are widely used for drug discovery and toxicology screening [29]. Nevertheless, their overall physical properties are more complex than the properties of the cell's components. In fact, the mechanical properties of single cells are determined by the cytoskeleton and the membranes, whereas the mechanical properties of spheroids are averaged over a large number of cells and arise from complex associations of cell's adhesion with each other as well as the cytoskeleton and the extracellular matrix [30].

Many methods were used to characterize tissues; however, one of the most powerful tools to do so is the micropipette aspiration [31]. A comparison between other methods including the micropipette aspiration technique is made in reference [32]. The mechanical measurement tools will depend on many parameters; one of them is the lengthscale of the object under study as seen in ***Figure V-21***.

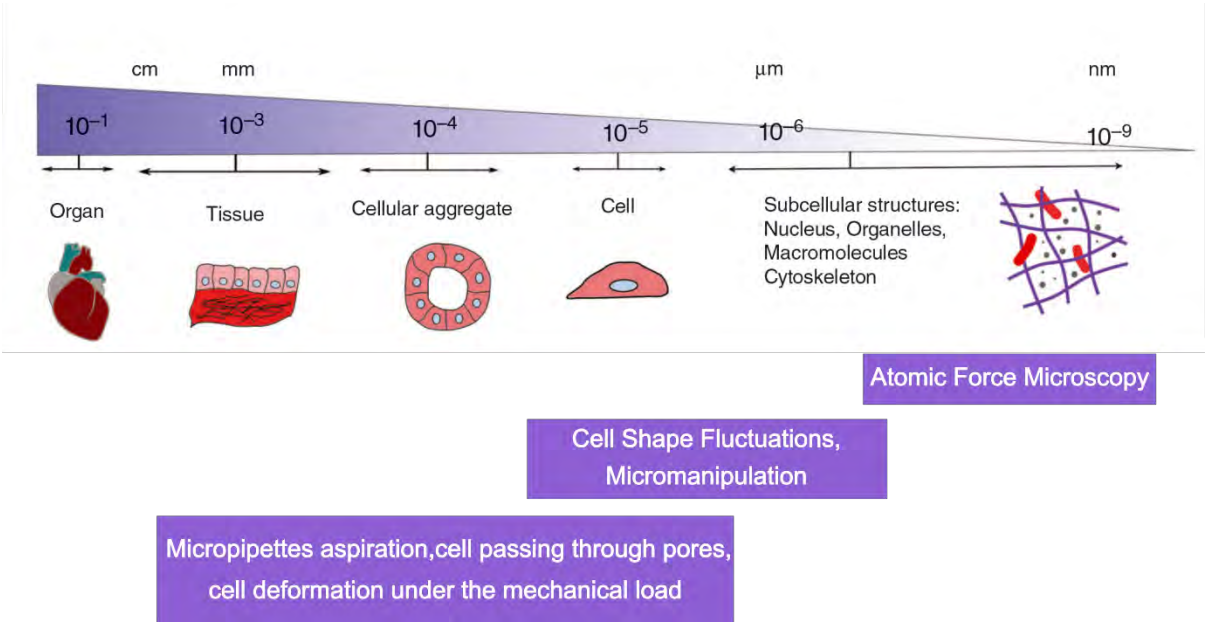

Figure V-21: Lengthscale of the objects under study which will determine the tool of mechanical characterization [33], [34].

Tissues are mainly considered as viscoelastic materials, which means they exhibit both elastic properties (characterized by the elastic moduli) and viscous properties (characterized by the viscosity): upon deformation, a viscoelastic material simultaneously stores and dissipates energy, and therefore mechanical stress relaxes and deformation increases over time. The two fundamental properties are Young's modulus (E), which determines the ability of a tissue to sustain its shape under mechanical stress, and viscosity (η), which is the rate at which the tissue flows under a defined load [33].

Until now, we have characterized the mechanical properties of some lipid membranes, which are close to the plasma membrane, however, without the proteins integrated into the membranes or a contractile cortex. The plasma membrane mostly exhibits elastic properties defined by its bending and stretching modulus. In parallel, we collaborated with Morgan Delarue, a biophysicist researcher in the Mile team in LAAS in order to characterize the mechanical properties of aggregates cancer cells. As our micropipette aspiration tool is very versatile, this technique was used to extract the viscosity and the elastic modulus of pancreatic cancer aggregates of cells. Micropipette aspiration on cells was considered as a parallel approach to characterize the mechanical properties of a biological system [35]. However, cells in general can be smaller than GUVs, and therefore small micropipette (~ 5µm) are required to perform the micropipette aspiration experiment. As seen previously in this chapter, the minimum diameter of pipette we could generate was 6µm, however the experiments were critical, as the pipettes were rapidly blocked during the microfluidic experiment. Therefore, for technical reasons, it was easier to start with bigger biological objects, such as spheroids. Nonetheless, this technique could be adapted for on-chip micropipette aspiration for cells, once the microfabrication and microfluidic experiments are both optimized.

5.4.2 Traditional micropipette aspiration for Spheroids

The micropipette aspiration set-up for spheroids is the same as the one used to characterize mechanical properties of GUVs lipid membranes seen in chapter II, but with minor adjustments due to the different sizes and properties of the objects under study. A major work of micropipette aspiration was presented by Guevorkian *et al.,* where an aggregate of cells forming a spheroid is aspirated at constant suction pressure into a micropipette and the length of the aspirated tongue inside the pipette is recorded over time [36]. Because spheroids are viscoelastic materials, their response to applied stress is a function of time. In fact, under stress and below a characteristic time T, a tissue behaves as an elastic solid. However, for t > T, the tissue behaves like a liquid with viscous properties. Nevertheless, the viscosity of the tissue η and the elastic modulus E are related by the following equation:

$$\eta \approx E\mathrm{T} \qquad 5\text{-}1$$

This equation could be deduced because the stress applied during the micropipette aspiration, in this case the aspiration pressure, stays constant while the tissue flows inside the pipette. However, for a tissue to be aspirated, the applied suction pressure has to be larger than a critical aspiration pressure P_c [32], which is related to the aggregate' surface tension γ given by:

$$\gamma = \frac{P_c}{2\left(\frac{1}{R_p} - \frac{1}{R_0}\right)} \qquad 5\text{-}2$$

Equation ***5-2*** is deduced from Laplace law, with R_p the pipette radius and R_0 the initial radius of the spheroid. The pipette diameter has to be 3-5 times bigger than a single cell diameter to ensure that the tissue can be treated as a continuum. The general protocol of micropipette aspiration of a tissue or a spheroid is as follows [37]: after the tissue is loaded, a small aspiration in the order of 0.2 – 0.3 mbar is applied in order to hold the spheroid far from the bottom of the dish. Then, a constant suction pressure ΔP is applied, larger than a critical pressure P_c at which the tissue starts to flow inside the pipette. The elongation is recorded over time by taking pictures every few seconds. When the elongation seems sufficient, the pressure is dropped again to P_0, and the retraction of the tongue inside the pipette is also recorded. The length of the aspiration and the retraction are plotted as a function of time as seen in ***Figure V-22.*** In fact, as seen in the figures, both aspiration and retraction experiments represent the viscoelastic properties in their curves: for the aspiration, after an initial fast deformation dominated by the spheroid's elasticity, the tissue continues flowing at a constant rate, which depends on the tissues viscosity η and is given by:

$$\dot{L}_{asp} = \frac{R_p}{3\Pi\eta}(\Delta P - P_c) \qquad 5\text{-}3$$

Where $\dot{L}_{asp}$ is the aspiration velocity rate extracted from the fitting of the viscous part of the curve of the elongation of the tongue inside the pipette. The retraction of the spheroid starts with a fast elastic dissipation and then continues to flow under the action of its surface tension γ limited by its viscosity, at a velocity given by:

$$\dot{L}_{ret} = \frac{R_p P_c}{3\Pi\eta} \qquad 5\text{-}4$$

where $\dot{L}_{ret}$ is the retraction velocity rate extracted from the fitting of the viscous part of the curve of the retraction of the tongue inside the pipette. The viscosity of the tissue is then deduced by summing equations ***5-3*** and ***5-4*** which eliminates P_c , and is given by:

$$\eta = \frac{R_p \Delta P}{3\Pi(\dot{L}_{asp} + \dot{L}_{ret})} \qquad 5\text{-}5$$

The critical pressure P_c can also be deduced from the aspiration and retraction velocity rates given in equations ***5-3*** and ***5-4*** and is given by:

$$P_c = \Delta P \frac{\dot{L}_{ret}}{\dot{L}_{asp} + \dot{L}_{ret}} \qquad 5\text{-}6$$

As mentioned above, the elastic modulus and the viscosity are linked together by a characteristic time crossing the elastic and viscous regimes. This characteristic time T is deduced experimentally from the

creep curve, by interpolating the linear curve with the time axis (as seen in ***Figure V-22f***) and is given by:

$$\mathrm{T} = -\frac{\delta}{\dot{L}_\infty} \qquad 5\text{-}7$$

where δ is the elastic deformation. The elastic modulus (Young's modulus) is then calculated following this equation:

$$E = \frac{3\Pi\eta}{\mathrm{T}} \qquad 5\text{-}8$$

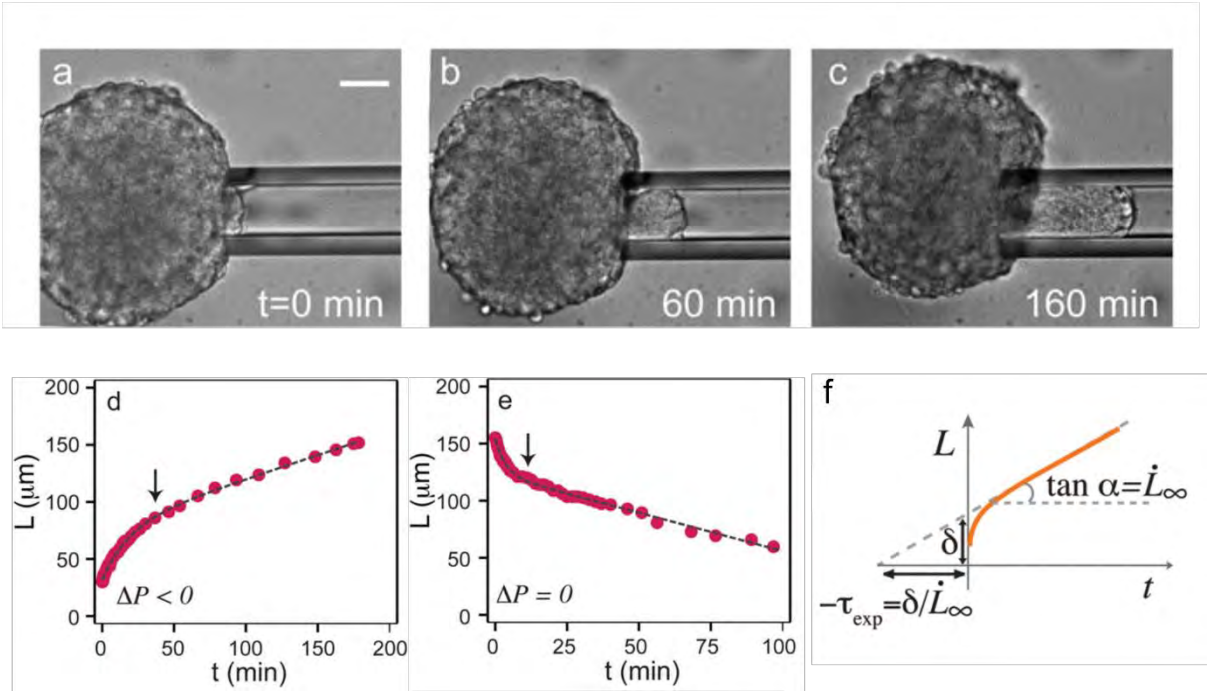

Figure V-22: Micropipette aspiration of spheroids: a-c) are progressive deformation inside the pipette upon aspiration at ΔP = 11,80 mbar. d-e) are respectively the aspiration length and the retraction length as a function of time [36].

The previous micropipette aspiration experiment was performed on aggregates of mouse sarcoma cell lines expressing E-cadherin, and which exhibited the following viscoelastic moduli: the viscosity was $\eta = 1.9 \pm 0.3\, x\, 10^5$ Pa. s, which is comparable to other types of mouse embryonal cell lines aggregates. The surface tension of the aggregates at rest is $\gamma_0 = 6$ mN/m, and the elastic modulus was calculated after extracting the characteristic relaxation time and the viscosity, $E = 700 \pm 100$ Pa. The values obtained are close to or at the same range of many embryonic tissues.

In order to characterize the mechanical properties of the spheroids made of cancer cells, we adapted our on-chip micropipette aspiration to trap such large objects. Moreover, the microfluidic set-up to manipulate these objects had to be adapted also. The following paragraph will elaborate all these details.

5.4.3 On-chip micropipette aspiration to characterize viscoelastic properties of aggregates of cancer cells

5.4.3.1 Microfluidic chip and sliding element adjustment

Our micropipette aspiration is versatile and adaptable for many applications because of the fabrication technique which allows almost any shape and size of the holes. Therefore, in order to use this tool to characterize the mechanical properties of spheroids, we had to slightly adapt the size of the channels of the PDMS microfluidic chip as well as the sliding element. In fact, we chose to fabricate spheroids that are between 150 and 300 µm size. It is a size that is easily visualized under microscopy and manipulated without the need to increase the size of the lateral channel of the chip; this way the same masks that were used to fabricate the PDMS chips for the GUVs are used for the spheroids. Therefore, the chip conserved its lateral dimensions and only the heights were changed during the DF mold fabrication. ***Table V-5*** shows the dimensions of the PDMS chip and the pipettes in the sliding element compared to the ones used for the GUVs experiments. Considering the PDMS chip: the height of the channels was changed to 300 µm instead of 100 µm in order to avoid squeezing of the spheroids with diameter ~ 100-200 µm, whereas the rest stayed the same (for example the large channel where the sliding element is to be inserted is still 450 x 450 µm^2). Considering the sliding element dimensions: the lateral dimensions were conserved (the length of the whole element and the width), as well as the thickness (500 µm x 500 µm^2). The changes occurred on the window of the micropipettes, and on the micropipettes. In fact, the window had to match the thickness and the width of the PDMS channel, so it was made 300 µm thick. Because the length of the deformation of the spheroids inside the pipettes can be very long, the length of the micropipette (which is defined by the thickness of the DF laminated) was 150 µm, which leaves 350 µm of DF lamination to complete the total width of the tigette of 500 µm. Finally, since the diameter of the pipette has to be 3-5 times the size of a single cell, we fabricated 3 different sizes of micropipette of 30, 50 and 70 µm. The dimensions of the sliding element's window and pipettes are shown in the SEM picture of **Figure V-23 *A-B.***

Table V-5: Dimensions of the PDMS microfluidic chips and the pipettes diameters and length used for the GUVs and the spheroids.

	Width (µm)	Height (µm)	Pipette diameters	Pipettes length (µm)
GUVs PDMS chip	400	100	8 – 15 µm	50
Spheroids PDMS chip	400	300	30 - 50 and 70	150

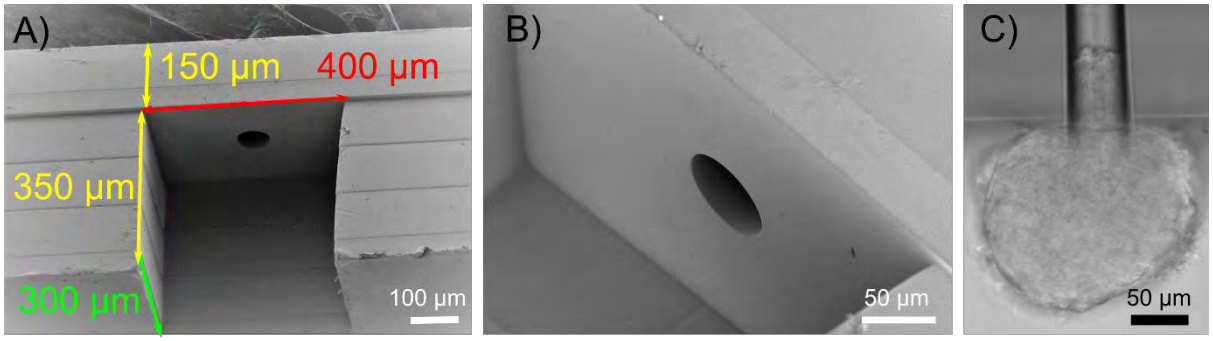

Figure V-23: A) SEM picture of the sliding element for the micropipette aspiration of spheroids, showing the dimensions of the window and the length of the pipettes. B) is a close-up SEM picture of the hole of a diameter of 50 µm. C) is a bright-field image of a spheroid aspirated in a 50 µm diameter pipette.

5.4.3.2 Spheroids fabrication

The cell line used is a murine pancreatic cancer cell line with oncogenic $Kras^{G12D}$ mutation, representative of > 95% of pancreatic cancer tumors. The method of fabrication of spheroids is based on the hanging drop cell culture method developed in reference [38]. This method presents several advantages to fabricate spheroids which are required to be loaded into a microfluidic chip. In fact, it is a fast, easy way to generate many spheroids without the need to add supplementary polymers or hydrogels such as agarose. Secondly, they are fabricated in droplet suspensions which avoid them to adhere or sediment at the bottom of a Petri dish. This is necessary for our application, as the spheroids are to be removed and loaded in the microfluidic chip. And finally, the size of the spheroids can be controlled by adjusting the number of cells added initially. On the other hand, this method does not allow to generate big size spheroids because of the low volume needed to hang a droplet without falling: the amount of culture medium present is not enough for the survival of big sizes spheroids.

48 hours before the micropipette aspiration experiment (time required for spheroids to aggregate), the cells are passaged and suspended in a tube and then counted. The volume of each hanging droplet is 10 – 15 µl, a volume that is small enough for the hanging droplet not to fall but also big enough to provide sufficient culture medium for the spheroids for a duration of 48 hours. Each spheroid will be formed in one of the droplets in the culture medium. To form 1 spheroid of around 150 µm diameter in each droplet of 10 µL, we need a total number of 500 cells/droplet which means a concentration of 50C/µL. After counting the initial concentration of cells present in the tube, and depending on the number of spheroids that we need to generate, the right dilutions are made. For example, in ***Figure V-24,*** there are 24 hanging droplets of 10 µL each. This means a minimum amount of 240 µL of 50C/µL concentration is needed to fabricate 24 spheroids. After making the right dilutions, the 10 µL droplets are deposited on the upper part of the Petri Dish. The bottom part of the Petri dish is then filled with PBS buffer solution (Phosphate-buffered saline) in order to avoid evaporation of the 10µL volume of

the culture medium containing the cells. When inverting the upper part of the Petri dish to close it, the droplets will be hanging in it. The spheroids in the Petri dish are then placed in an incubator under 37°C and 5% CO_2 (physiological conditions). Due to gravity in the hanging droplets, the cells start to aggregate together at the bottom of the droplet and form a spherical shape. After 48 hours, the spheroids formed have diameters between 100 and 300µm with an average of 150µm, as seen in ***Figure V-24.***

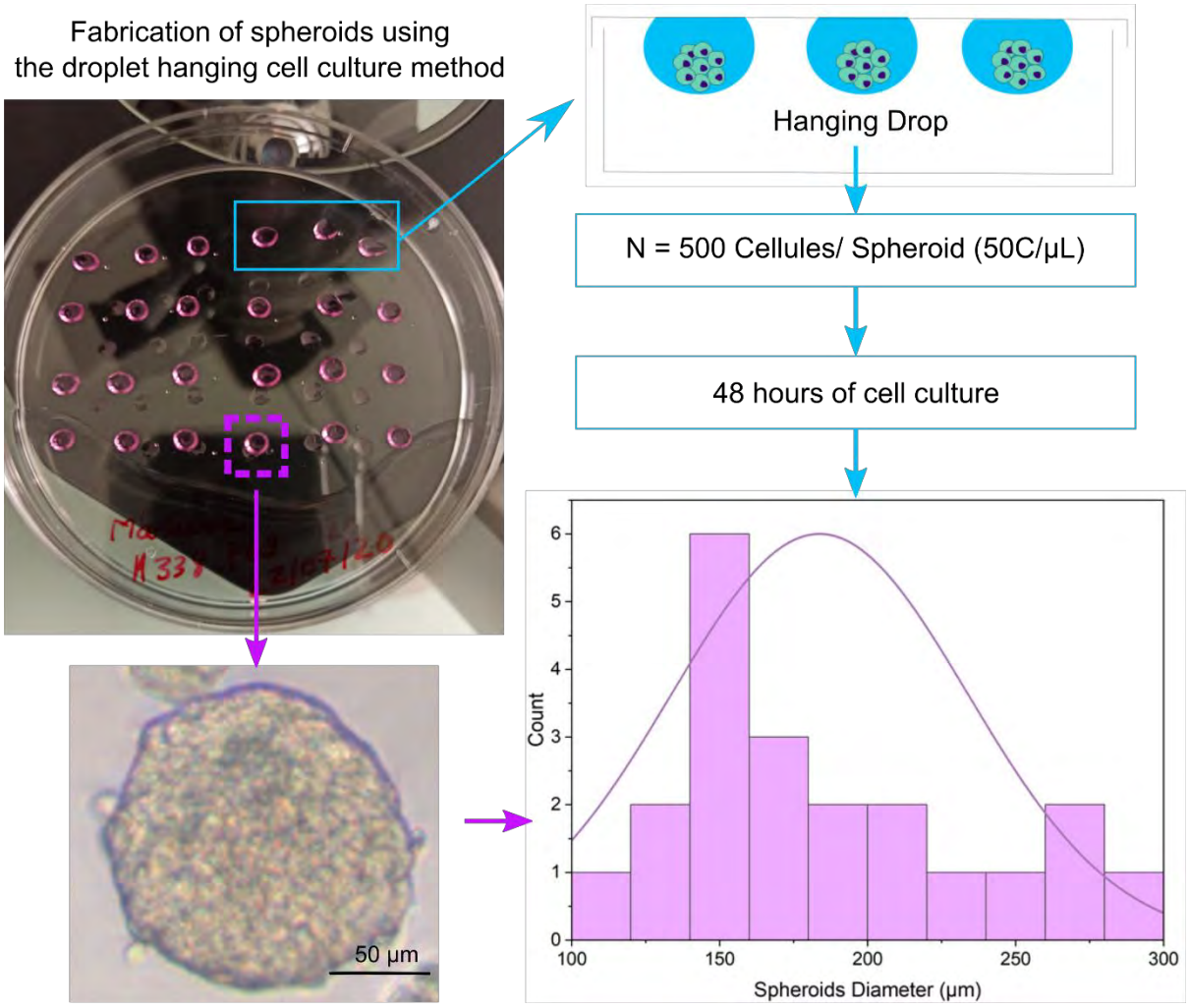

Figure V-24: Spheroids fabrication using the hanging drop cell culture techniques. The droplets (pink because of the medium culture) are hanging in a Petri dish and contain 500 cells/spheroid/droplet, which is cultured for 48 hours. The spheroids obtained have diameters ranging from 100 up to 300 µm.

Right before the microfluidic experiment, the spheroids are observed under the microscope and the ones with good shape (nicely spherical) and diameter are chosen to perform the micropipette aspiration experiment on. It is important to observe them as sometimes multiple small spheroids can be fabricated in a droplet instead of one big spheroid, and those small spheroids are to be eliminated.

5.4.3.3 Microfluidic experimental set-up: loading the spheroids

Loading the spheroids into the microfluidic chip is more critical than the GUVs for many reasons. First, even if the spheroids are generated in large numbers (a few dozens), this number is still limited compared to the GUVs. Second, the spheroids are heavy objects; therefore, they cannot be mixed or diluted in a solution as they will sediment at the bottom of the Petri dish or any tube. The best option is to keep the hanging droplet as they are until the end of the experiment. In fact, if the loading works perfectly from the first trial, only 1 spheroid will be needed per experiment as the experiments are very long (~ 6 hours). However, if the loading doesn't work directly, we might need to repeat several times, which is why generating several spheroids is necessary. Moreover, our chip could allow high-throughput experiments if the lateral size of the chip and the tigette are adjusted. For this reason also, large number of spheroids would be needed. A treatment of BSA 1% of the chip for 20 minutes is required to avoid spheroid adhesion on the surface. The chip is then rinsed with a culture medium before loading the spheroid. Note that the microfluidic experiment is performed in a closed heated chamber at 37°C, and under 5 % CO_2.

In any case, in order to load the spheroid inside the microfluidic chip, we use a 1 mL syringe connected to a very long tube. The tube and the syringe are first filled with a warm culture medium and all the bubbles are removed from them to ensure no bubbles are trapped inside the chip. The tube is then brought close to a droplet containing the spheroids, and the droplet with the spheroid is aspirated inside the tube. Directly after that, the tube is rapidly connected to the inlet of the chip while blocking the outlet in order to avoid an overpressure over the spheroid and losing it through the pipette then the outlet. The chip, still connected to the tube and the syringe, is placed under the microscope where the loading of the spheroid is observed and controlled. Once the spheroid arrives at the micropipette and before it gets trapped, the inlet is disconnected from the syringe and both inlet and outlet are connected to a pressure pump (Fluigent 69mbar), in order to control the pressure applied on the spheroid. Once everything is connected, a first step would be to find the pressure of equilibrium P_0: the pressure where the flux is at 0. The spheroid is then aspirated at a certain pressure ΔP, higher than P_c (introduced in the previous paragraphs). Because P_c is difficult to determine experimentally (due to the viscoelastic properties and the longtime of reaction of the system), ΔP aspiration corresponds to a pressure where the elongation of the spheroid inside the pipette is longer than the pipette radius (L > D_p). Bright-field images are taken every 15 seconds for a duration of almost 3 hours, to ensure the recording of both viscoelastic phases of the spheroids. After 3 hours, the pressure is dropped back to P_0, in order to record the retraction of the spheroids, and bright-field images are taken every 10 seconds as the retraction flow rate is faster than the aspiration one. However, sometimes when lowering the pressure to P_0, the spheroid retracts very rapidly and goes out of the

pipette. We do not fully understand this behavior, however this proves that our anti-adhesion treatment is very efficient the spheroid is not adhered on the walls of the pipette and the friction forces of the pipettes wall are negligible.

5.4.4 Results: Characterization of the viscoelastic properties of pancreatic cancer cells

When applying a constant pressure $\Delta P > Pc$ on the spheroid trapped inside the micropipette, the spheroid deforms progressively inside the pipette as a function of the time. ***Figure V-25*** shows an example of a micropipette aspiration study on a spheroid of 400 µm diameter (very large spheroid), under $\Delta P = 20$ mbar using a pipette of 50 µm diameter. The spheroid is a bit larger than our channels, but this is not crucial. After around 3 hours of aspiration, the pressure is dropped to $\Delta P = 3$ mbar. The spheroid starts to retract and the experiment is recorded for a duration of almost 3 hours. Using a homemade Matlab code, the elongation of both aspiration and retraction is analyzed and the graph of aspiration (in cyan) and retraction (in orange) as a function of time is plotted as seen in ***Figure V-25.*** Considering the aspiration, a fast elongation of the spheroid inside the pipette is noticed for the first 25 minutes, reaching a length of around 60 µm, followed by a linear elongation during the rest of the time (~ 2.5 hours), reaching a total length of 85 µm. Considering the retraction, same as the aspiration, a fast retraction is noticed for the first 10 minutes, going from 85 µm up to ~ 53 µm, followed by a linear slower retraction up until 2.5 hours. The retraction hits a plateau where the spheroid does not retract anymore, reaching a final length inside the pipette of 45 µm. The fast response of the spheroid during the aspiration and retraction corresponds to the elastic state of the cells where the spheroid is deforming under the action of its surface tension. The slow deformation corresponds to the viscosity of the spheroid and is characterized by the aspiration and retraction velocity rates, respectively $\dot{L}_{asp}$ and $\dot{L}_{ret}$. The velocity rates are extracted from fitting the linear part of the curves and which gives: $\dot{L}_{asp} = 0.137\ \mu\text{m/min}$ and $\dot{L}_{ret} = 0.08\ \mu\text{m/min}$. The critical pressure P_c can be then determined using equation ***5-6***, $P_c = 7.2$ mbar. Hence, the surface tension of the spheroid under its critical pressure can be calculated using equations ***5-2***, $\gamma = 9\text{mN/m}$. Moreover, the viscosity η can be calculated using equations ***5-5***, and which depends on both aspiration and retraction velocity rates, $\eta = 1.47\ x\ 10^6$ Pa.s. In order to extract the elastic modulus E of this spheroid, we need to extract first the characteristic relaxation time T as seen in equation ***5-7***. The relaxation time is deduced from the intersection of the extrapolation of the aspiration slope with the elongation and time axis (as seen in ***Figure V-22f)***, $\text{T} = 385.7$ min. Finally, the elastic modulus is calculated following the equation ***5-8***, $E = 600$ Pa.

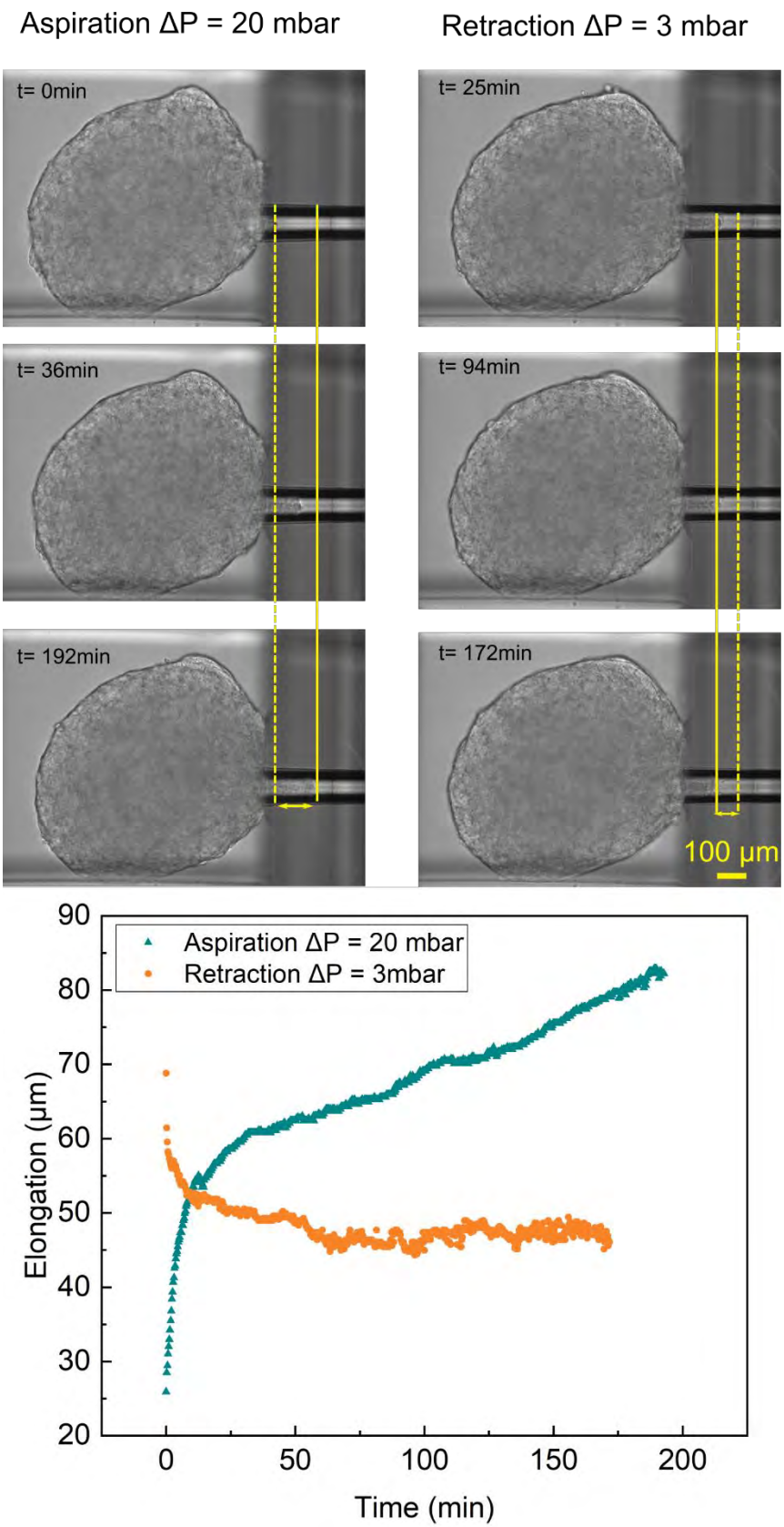

Figure V-25: Progressive deformation of the Spheroid inside a micropipette of 50 µm diameter. The aspiration is made under a pressure of ΔP = 20 mbar for almost 200 minutes; then, the pressure is dropped to 3mbar where the spheroid is retracting inside the pipette. The graph corresponds to the elongation of the spheroid inside the pipettes for the aspiration and the retraction as a function of time.

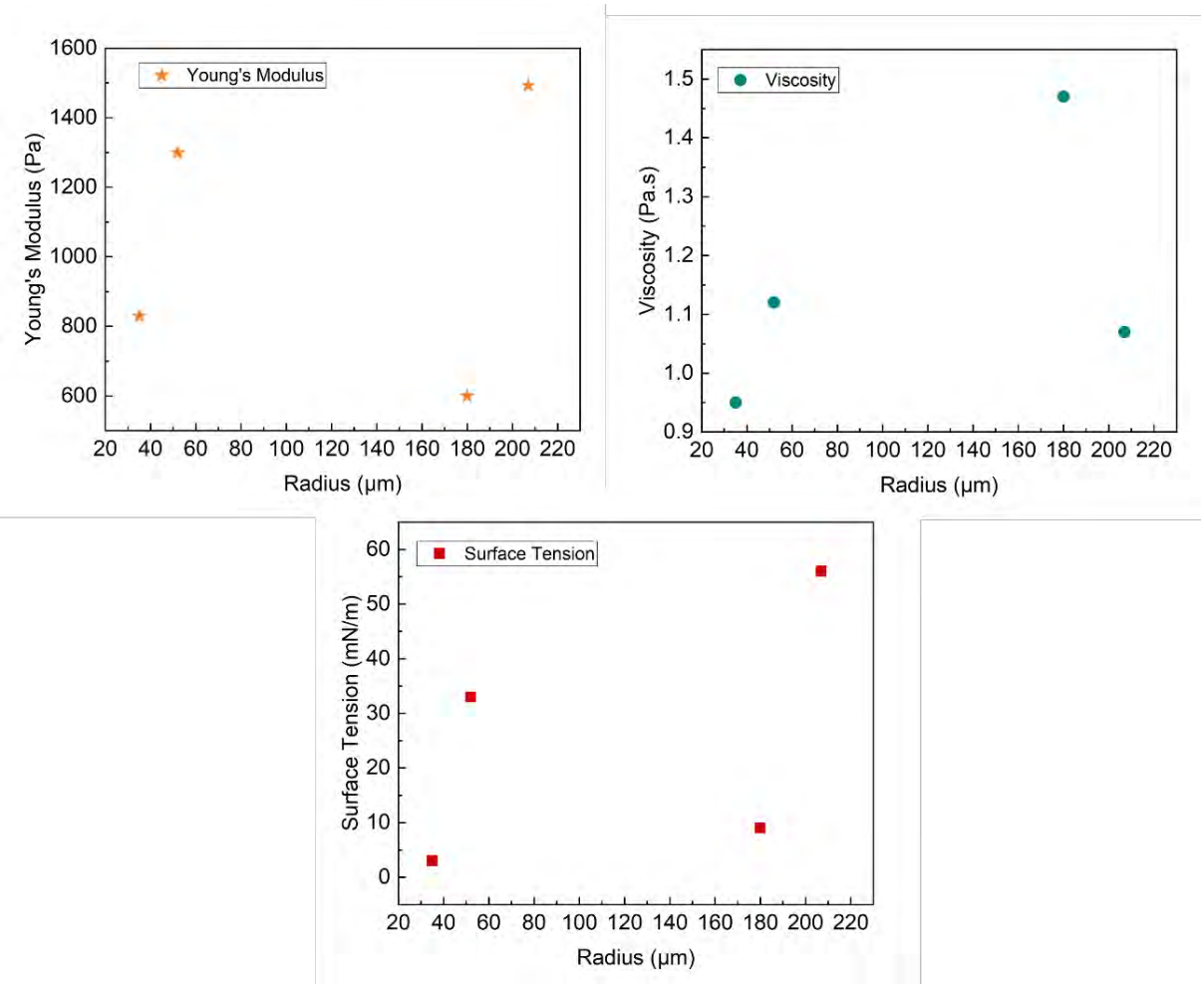

Figure V-26: Viscoelastic properties of pancreatic cancer cells aggregates as function of the radius of the spheroids

In order to characterize the reproducibility of the micropipette aspiration using our microfluidic technique, we repeated the experiment 3 more times, by also choosing different sizes of fabricated spheroids. The results of the elastic moduli, the viscosity and the surface tension as a function of the diameters are shown in ***Figure V-26.*** The viscoelastic moduli showed no systematic dependence with the spheroid diameter. The average elastic modulus (Young's modulus) is $E = 1060 \pm 357$ Pa and the average viscosity is $\eta = 1.12 \pm 0.2\, x\, 10^6$ Pa. s. The average surface tension is $\gamma = 25 \pm 19$ mN/m. The standard deviation of the surface tension is high, for two reasons. First, because of the experimental challenge to determine precisely the threshold pressure enabling a movement of the spheroid, for such a slow process. Secondly, because the surface tension of a cellular aggregate may depend on its history as discussed in the reference [36].

5.4.5 Discussion

Multicellular spheroids formed by transformed cells are widely used as tumor models for metastasis research and therapeutic screening. Characterizing the mechanical properties of cancer tumors is essential in order to evaluate the rigidity of such tissues in order to find suitable ways for treating

them. In our micropipette chip experiment, we fabricated spheroids made of pancreatic cancer cells of mouse, in order to model cancer tumors. Characterizing the deformation of the spheroids inside the pipette showed the viscoelastic behavior of such material. In fact, after a short time of applied pressure, the spheroid behaves as an elastic material: its short-term deformation is proportional to the applied pressure, and the tissue can quickly recover its initial shape once the pressure is released. Whereas, at a longer time, the spheroid undergoes cellular reorganizations, which lead to more persistent deformation and is characterized by a viscoelastic behavior [32]. The viscoelastic behavior is characterized by a surface tension, Young's modulus, and dynamic viscosity. Nonetheless, in our case, after hours of relaxation pressure, the deformation of the spheroid hits a plateau and do not come back to its original state. This could mean that the spheroid might behave as an elasto-visco-plastic, where at critical stress, the spheroid can still recover its initial shape; however, if this threshold is crossed, the spheroid can undertake a permanent plastic deformation and does not recover this shape. The elasto-visco-plastic behavior is characterized by Young's modulus, a dynamic viscosity and yield stress. However, this hypothesis is yet to be proven by doing more experiments.

The visco-elastic properties (the surface tension, the elastic modulus and the dynamic viscosity) of aggregates made of cancer cells were characterized. In micropipette aspiration, the spheroid undergoes a continuous traction force at constant stress, which generates motion between the aggregates and the surface of the pipette leading to its deformation. The surface tension is in general determined by both intracellular adhesion and cortical cell tension and is a key parameter to characterize long-term conditions. At the same time, the elastic modulus and the dynamic viscosity are rheological parameters, that characterize the dynamic evolution of the aggregates under pressure.

The values we obtained are hard to compare with other values from the literature for many reasons. First, it is mostly rare that other scientists have characterized the mechanical properties of the same cell line that we did. Second, the values of the different properties reported in the literature differ with the method of characterization. In fact, AFM studies usually show higher values than micropipette aspiration experiments as it targets different parts of the spheroid. And finally, not many micropipette aspiration experiments have been done on spheroids. However, our data are in the same range comparing to embryonic spheroids that have been characterized in reference [36].

5.5 Conclusion and Perspective

We presented a novel microfluidic chip that is able to reproduce the micropipette aspiration experiment but with several advances and advantages. Due to the innovative fabrication technique that we developed, we were able to reproduce the circular shape of the micropipette, in addition to the multiple pipettes that we can fabricate on the same element to be used in parallel in the same

experiment. This allowed us to parallelize the experiments, which is timesaving and very effective, while the fabrication technique remains low-cost. All these advantages allowed us to characterize the mechanical properties of numerous lipid mixtures, such as the bending and the stretching modulus.

As a proof of concept of the chip, we characterized first simple lipid mixtures: DOPC, POPC and Brain SM + cholesterol. The stretching moduli obtained were fully compatible with the literature, however, the bending moduli exhibited low values compared to most published results. We suggested that the difference could come from a combination of both pipette size (which is bigger than the ones usually used) and the concentration of sucrose inside the GUVs. In fact, the effect of sugars on lipid membranes is still debated between the community, but we finally observed no systematic influence of it on the bending modulus measured. However, one important constraint occurs when using the small micropipettes: because of the small diameters and the presence of debris inside the solutions, the small micropipettes are blocked very fast with dust which leads to changing the chip and sometimes it was even impossible to perform the experiments. Even if the protocol of pre-cleaning the chip was optimized several times by injecting ethanol or water solutions before inserting the sliding element, we have to admit that we are not working in a clean room environment and facing such problems is very common. We are thus still lacking quantitative results with small micropipette (6 µm diameter), and more experiments are still needed to reinforce our suggestions and our results.

Secondly, we characterized the effect of cholesterol on DOPC lipid membranes. Cholesterol effect is non-universal and depends on the lipid characteristic and the length and degree of unsaturation of the acyl chains. Cholesterol effect in lipid membranes is still somehow debated in the community. Nonetheless, we demonstrated that the Cholesterol stiffens DOPC lipid membranes by increasing its stretching modulus, but not its bending modulus.

Third, we characterized mechanical properties of DOPC lipid membranes that were challenged with co-polymer micelles nanoparticles and gold nanoparticles, which are used in drug delivery systems. Co-polymer micelles nanoparticles soften the membranes by decreasing both bending and stretching modulus. We hypothesize that this is due from one side to the fact that these copolymers might have fused with the lipid membranes, creating a hybrid lipid membrane, and from the other side, that these nanoparticles could create defects in the membrane which can alter the elastic moduli. The effect we observed for Gold nanoparticles is still blurry: we suggested that the Gold nanoparticle's effect is time-dependent, where the nanoparticles first aggregate on the lipid membrane causing it to rigidify first; however, when the NPs are released inside the membranes after around two hours, the membrane relaxes and softens again. Nonetheless, more experiments on the effect of gold nanoparticles on the membrane are still needed, especially for a longer time (more than two hours),

or with reduced data dispersion, in order to consolidate our suggestions. Both types of nanoparticles showed a strong effect on the mechanical properties of the lipid membrane which should be taken into consideration in the drug delivery systems.

Finally, by modifying the dimensions of the PDMS chip and the sliding element, we could adapt the setup to perform the micropipette aspiration on spheroids. We were able to characterize the viscoelastic properties of 3D aggregates of cancer cells, which are models of pancreatic cancer cells. Aside from extracting the elastic Young's modulus, the dynamic viscosity, and the surface tension of the aggregates, we suggested that these aggregates could exhibit plastic behavior, where the spheroids do not come back to their initial state before applying the stress. However, when characterizing the characteristic relaxation time, the value obtained was way higher than the time of the experiment. This means that longer relaxation time experiments are still needed to prove if the spheroids indeed exhibit plastic behavior, or if the spheroids needed more time to complete their relaxation.

Perspectives: Characterization of the shear stress effect on model membranes

The very unique and innovative way of fabrication allowed us to fabricate different shape of traps, such as cross shape or slit shape traps as seen in ***Figure V-27***, with the purpose of capturing a GUV but keeping the flow around it in order to characterize the effect of shear stress on the membranes. As seen in chapter III, microfluidics offers a great tool to characterize the effect of the flow on other properties of the model membranes. The cross shape is to model a symmetric flow around the trapped GUVs from four different places up, down, left and right. Whereas the slit models a symmetric flow only from the side of the GUVs. Same as the round shape traps for the micropipettes, these traps were fabricated as single ones on the sliding element or as multiples in order to parallelize the experiments. The traps were also fabricated in multiple sizes. For the cross shape traps, the diameters of the circles where the GUV would be trapped are 10, 15, 20 and 30 µm, and the rectangles around it are respectively 5 x 11, 7.5 x 11, 10 x 11 and 15 x 17 μm^2. For the slit shape, the squares in the middle where the GUV would be trapped are 10 x 10, 15 x 15, 20 x 20 and 30 x 30 μm^2.

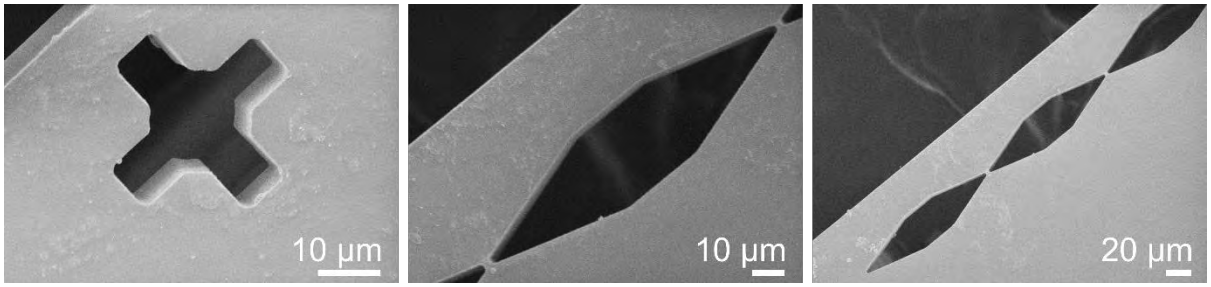

Figure V-27: SEM pictures of the cross shape and slit shape fabricated in the sliding element and used to characterize the shear effect in model membranes.

In order to visualize the mobility of the lipids on the GUVs membranes, we needed to fabricate a non-homogeneous membrane as it was done in reference [39]. Therefore, we fabricated GUVs which exhibit domains in the membranes due to a phase separation. To do so, we used a mixture of DOPC/DSPC/Chol, with a molar ratio of 32/40/28 and we added two different dyes: $DiIC_{20}$ (λ_{ex} = 551 nm, λ_{em}=566nm) which have a higher affinity for liquid-disordered phase, and BODIPY (λ_{ex} = 488 nm, λ_{em}=503nm) which have a higher affinity for liquid-ordered phase (introduced in chapter I and II). DSPC temperature phase transition is 55°C; therefore, the electroformation was done under 60°C for 2 hours and a half, and then the temperature was reduced 5°C/5min in order for the domains to assemble in circular shapes. If the temperature is rapidly reduced, the domains won't have time to rearrange and we won't be able to see them [12]. When the temperature is reduced to room temperature, DSPC would be in its gel phase, however cholesterol transforms it to a liquid disordered phase (as seen in chapter I). Therefore, the presence of both liquid-ordered and liquid disordered phase creates these domains in the membranes. ***Figure V-28*** shows the confocal images of the domains present in the GUVs. Note that the image on the right shows GUVs that are obviously separated into the two domains because of the budding that is caused by a strong difference in the osmotic pressure (inside and outside the GUVs) due to evaporation of the water from the sucrose solution during the observation under microcopy.

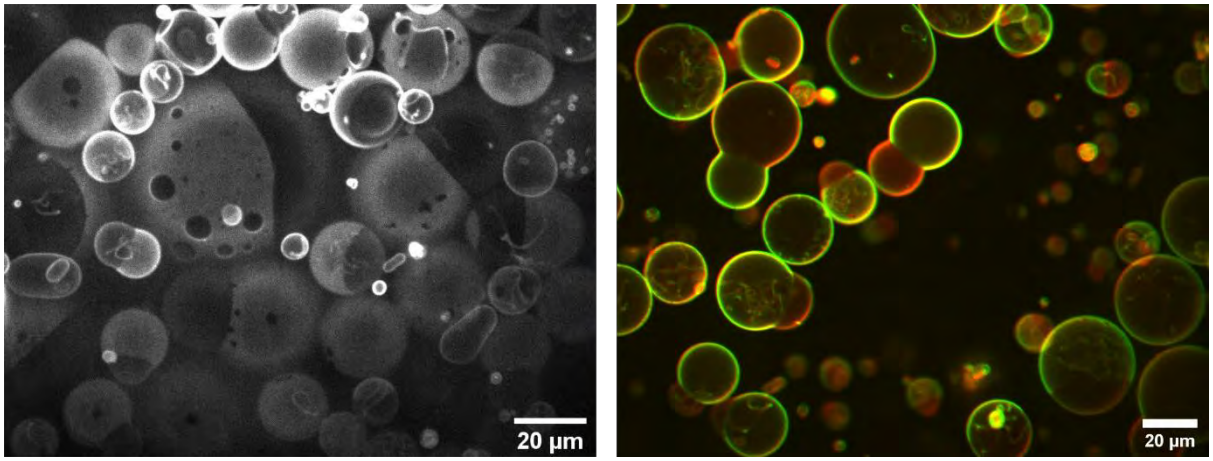

Figure V-28: Confocal microscopy images of lipid mixtures exhibiting domains made of DOPC/DSPC/Chol. Bodipy staining was used for the liquid-ordered phase (shown by the dark spot on the left and green spot on the right), and DiIC20 staining was used for the liquid disordered phase (shown by the light spot on the left and red spot on the right).

In order to characterize the movement of the domains in the GUVs under shear stress, fast imaging needed to be done in order to better construct the actions of lipids on the GUVs surface. However, when we tested this experiment first without any treatment to block the fluorescence of the material, the fluorophore present in the membrane bleached, while the fluorescence of the material remained the same. This caused to lower the resolution of the images, and we couldn't visualize the domains well anymore after a certain time of laser exposure on the GUVs. Therefore, we treated the sliding

element with different metallic coating in order to block the fluorescence of the material as seen in ***Figure V-29.*** We first tried a coating of 15 nm of a layered mixture of Gold and Palladium, and for the second treatment we coated a 25 nm layer of platinum. The images of the sliding element show the increasing dark color of the sliding element, which was yellow before treatment and which became very dark after metallic coatings. Confocal microscopy imaging shows the complete blockage of the fluorescence under λ_{em} = 503 (green) and λ_{em}= 566 (red).

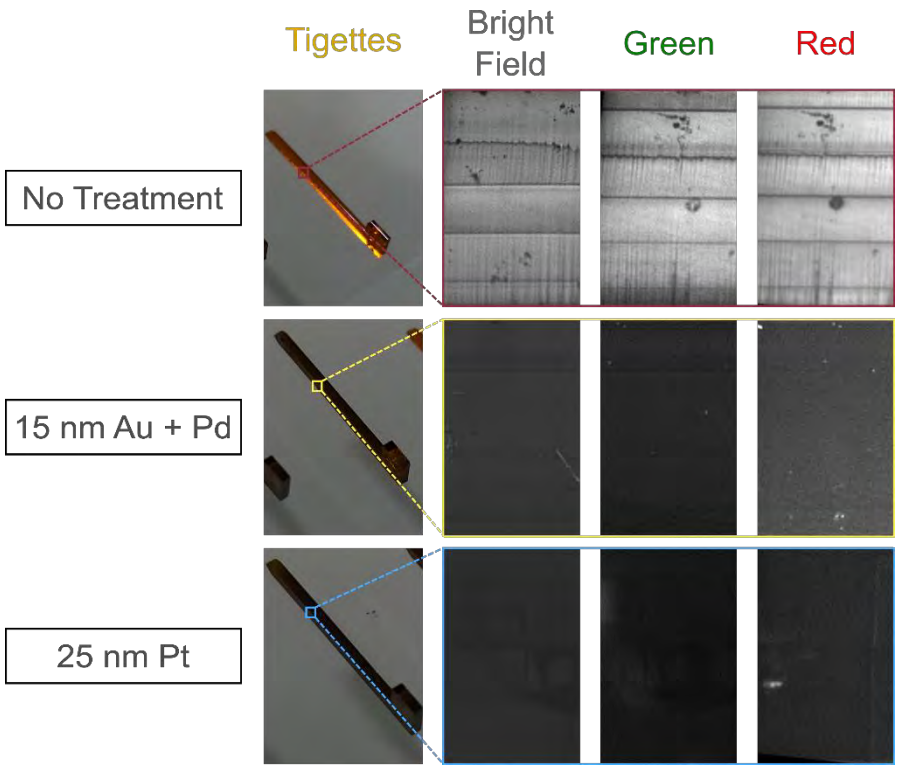

Figure V-29: Metallic treatment of the sliding element in order to completely block the fluorescence coming from the DF material to not disturb the GUVs studies. The sliding element was treated either with a 15 nm layer of a mixture of Gold and Palladium metals or with a 25 nm layer of Platinum metal. Confocal microscopy images were taken in Bright Field, green and red to compare the emitting fluorescence of the material. The coating blocked the fluorescence of red and green completely

In order to characterize the effect of the shear stress on model membranes, we first trapped the GUVs in a cross shape trap. We progressively increased the pressure, starting from zero, by steps of $\Delta P = 0.1$ mbar, and took a video for each pressure with an average of 40 pictures, by exposing the GUV for 200 ms, leading to a Δt = 500 ms between each picture. The interval time is slow, especially to this kind of experiment where the domains are merging at a certain fast speed. However, the high exposure time is needed in order to visualize well the florescence determining the domains The pictures were taken using an objective x63 with oil. Because of the fast imaging, we could not acquire two colors. In the following case, we exposed them in green (λ_{em} = 551 nm). In the following image examples, the light color presents the liquid disordered phase (DiIC20) and the black spots are the

liquid ordered phase. The blue and yellow color are only random chosen colors and do not express the real fluorescence color.

In the example seen in ***Figure V-30***, the GUV was trapped in a cross shape trap of 15µm diameter and exposed to an increasing flow controlled by increasing pressure from 0 to 0.6mbar. In the first two pictures, we realize that two domains in blue, which represent the liquid-disordered phase started to merge together after only an increase of 0.1 mbar. Upon a progressive increase of pressure, the domains in the same phase continued to merge together, however the two-phase domains were still differentiated and the GUVs is not homogeneous, which means that under a shear flow, the two states do not fully mix together.

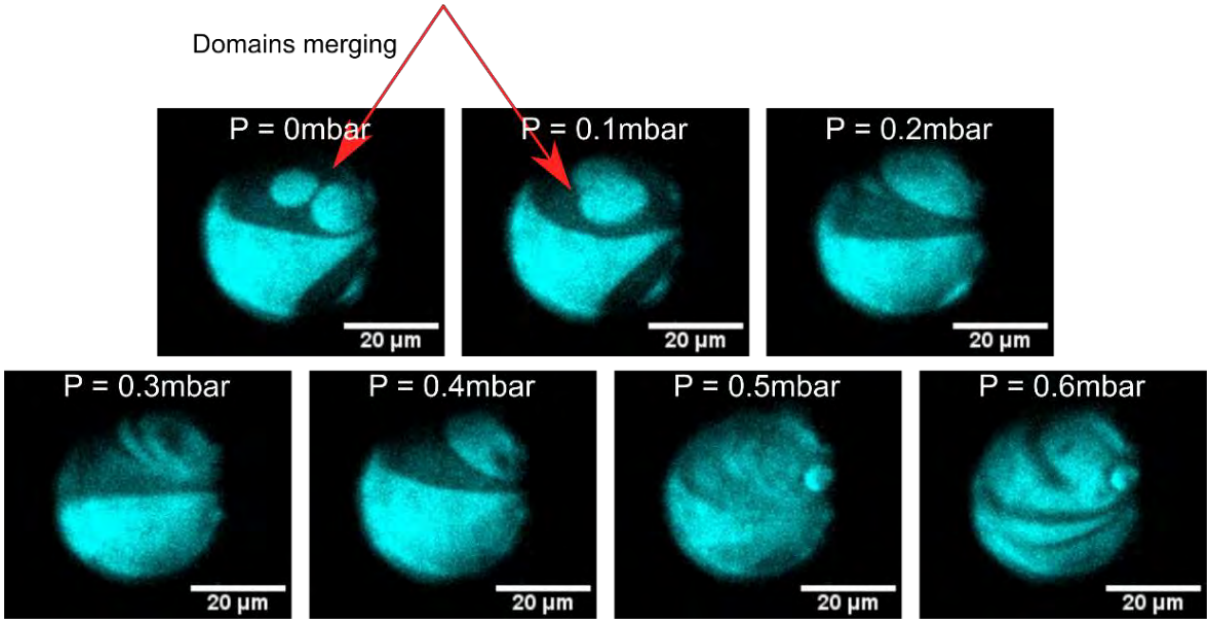

Figure V-30: Confocal microscopy images of a GUV trapped in a cross shape trap and exposed to increasing pressure from 0 to 0.6 mbar.

We repeated the same experiment as above, but with a vesicle that had from the beginning two large domains in the liquid disordered phase and many numerous small circular domains as seen in ***Figure V-31A.*** Upon increasing the pressure applied in the microfluidic chip from 0 to 0.9mbar, the shear flow around the GUV increased. The two large domains separated first into several smaller but still large domains. However, shortly after, the shear lead again to a mixing of the domains which are in the same phase only, while the two phases were still distinguishable. In fact, the flow shear allowed the domains to move and upon contact, the domains in the same phase, merged together. Moreover, upon shear stressing the GUV, the shape of the domains started to become elliptic instead of circular and the ellipse seemed to be in the same direction of the flow lines. Nevertheless, when the pressure

reached 0.3 mbar, the movement of the domains became difficult to track, because of the slow imaging compared to the fast movement of the GUV.

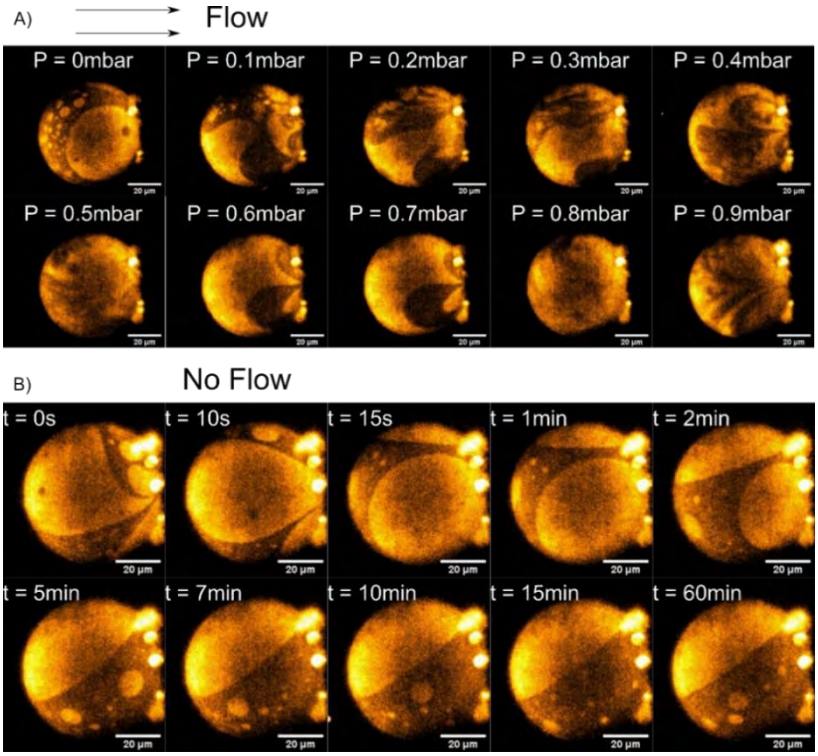

Figure V-31: Confocal microscopy images of GUV exposed to shear flow controlled by increasing pressure from 0 to 0.9 mbar. The GUV is excited by green laser (λ_{ex} = 551 nm, λ_{em}=566nm) which represents the liquid disordered phase. The flow is then stopped by decreasing the pressure to 0 mbar, and the relaxation of the domains is characterized up to 1 hour.

By the end of the first experiment where the pressure reached 1 mbar, we decreased instantly the pressure to ΔP = 0mbar, which instantly stopped the flow around the GUV and we characterized the relaxation of the domains up to 1 hour as seen in ***Figure V-31B.*** When the flow stopped around the GUVs, the domains started to relax. The two big domains in the liquid-ordered phases finally merged together to make one large domain between 2 and 5 minutes. Considering the small circular domains, some of them mixed together to make slightly bigger circular domains while others remained the same. Moreover, no more changes appeared in the size and shape of the domain after 5 minutes of domain relaxation. This could be a characteristic time for the domain's relaxation. However, we couldn't extract any quantitative data from these experiments because of the lack of resolution and the slow imaging which did not allow us to follow the movement of the domain at all times.

Therefore, for future experiments, it is necessary to combine confocal microscopy with fast imaging techniques which allows following the movement of the domains in order to characterize their speed of fusion and relaxing as function of the shear applied on GUVs. Moreover, the GUV is only seen in one plane due to the confocal microscopy, therefore, in order to follow the movement of the domains all over the GUV, we should combine the fast imaging with Z-stack imaging, which is really difficult to

do. Furthermore, due to the cross shape of the trap, extracting the shear flow on the GUV from the pressure applied was not easy as it was not easy to define the exact hydraulic resistance in the trap (chapter III), and also because the flow is not homogeneous. Therefore, for future experiments, we could consider working with a syringe pump which controls the flow instead of the pressure pump which controls the pressure. Moreover, image treatment to track the domains is also critical and requires the development of algorithms that can track them automatically and measure their surface and their movement to characterize their speed, for example. Finally, one interesting experiment that could be done, is to combine the effect of shear stress on vesicles that exhibit phase separations (with domains) with the effect of copolymers and gold nanoparticles. In fact, as demonstrated in this chapter, co-polymers nanoparticles and gold nanoparticles respectively soften and rigidify the membrane. If we can expose the membrane to shear stress and challenge it with NPs at the same time, do NPs adsorb preferentially on one domain? Do they induce phase mixing? Changes in the phase of the domains from the liquid-disordered to the liquid-ordered phase (or vis-versa) could occur. This could be an additional proof of the effect of the NPs on the mechanical properties of the membranes.

Furthermore, as our tool is very versatile and powerful, we could also test the effect of nanoparticles on the spheroids made of cancer cells, as a drug screening test. In fact, we could add small holes in the sliding element around the main micropipette aspiration of the spheroid in order to keep a flow running once the spheroid is trapped. Upon trapping the spheroids, the NPs could travel around it and come in contact with it. Multiple characterizations could be done: first, characterizing the effect of the NPs on the visco-elastic properties of the spheroids made of cancer cells. Second, characterizing the behavior of the NPs when in contact with the spheroids for example: if the NPs are able to cross it and if they are able to reach the cells that are deep in the middle of the spheroids and not just in the surface.

All these questions are essentials in drug delivery and drug screening tests, and we believe that our novel two parts microfluidic chip can offer the biophysicist and pharmacologist a great tool to perform their experiments.

References

[1] B. Venzac *et al.*, "Sliding walls: a new paradigm for fluidic actuation and protocol implementation in microfluidics," *Microsystems Nanoeng.*, vol. 6, no. 1, 2020, doi: 10.1038/s41378-019-0125-7.

[2] R. Courson *et al.*, "Low-cost multilevel microchannel lab on chip: DF-1000 series dry film photoresist as a promising enabler," *RSC Adv.*, vol. 4, no. 97, pp. 54847–54853, 2014, doi: 10.1039/c4ra09097g.

[3] R. Dimova, "Recent developments in the field of bending rigidity measurements on membranes," *Adv. Colloid Interface Sci.*, vol. 208, pp. 225–234, 2014, doi: 10.1016/j.cis.2014.03.003.

[4] J. F. Nagle, "Introductory lecture: Basic quantities in model biomembranes," *Faraday Discuss.*, vol. 161, pp. 11–29, 2012, doi: 10.1039/c2fd20121f.

[5] H. D. Andersen, C. Wang, L. Arleth, G. H. Peters, and P. Westh, "Reconciliation of opposing views on membrane-sugar interactions," *Proc. Natl. Acad. Sci. U. S. A.*, vol. 108, no. 5, pp. 1874–1878, 2011, doi: 10.1073/pnas.1012516108.

[6] A. Roux, D. Cuvelier, P. Nassoy, J. Prost, P. Bassereau, and B. Goud, "Role of curvature and phase transition in lipid sorting and fission of membrane tubules," *EMBO J.*, vol. 24, no. 8, pp. 1537–1545, 2005, doi: 10.1038/sj.emboj.7600631.

[7] W. Rawicz, K. C. Olbrich, T. McIntosh, D. Needham, and E. A. Evans, "Effect of chain length and unsaturation on elasticity of lipid bilayers," *Biophys. J.*, vol. 79, no. 1, pp. 328–339, 2000, doi: 10.1016/S0006-3495(00)76295-3.

[8] L. Lu, W. J. Doak, J. W. Schertzer, and P. R. Chiarot, "Membrane mechanical properties of synthetic asymmetric phospholipid vesicles," *Soft Matter*, vol. 12, no. 36, pp. 7521–7528, 2016, doi: 10.1039/c6sm01349j.

[9] W. Rawicz, B. A. Smith, T. J. McIntosh, S. A. Simon, and E. Evans, "Elasticity, strength, and water permeability of bilayers that contain raft microdomain-forming lipids," *Biophys. J.*, vol. 94, no. 12, pp. 4725–4736, 2008, doi: 10.1529/biophysj.107.121731.

[10] D. Chen and M. M. Santore, "Hybrid copolymer-phospholipid vesicles: Phase separation resembling mixed phospholipid lamellae, but with mechanical stability and control," *Soft Matter*, vol. 11, no. 13, pp. 2617–2626, 2015, doi: 10.1039/c4sm02502d.

[11] J. Henriksen *et al.*, "Universal behavior of membranes with sterols," *Biophys. J.*, vol. 90, no. 5, pp. 1639–1649, 2006, doi: 10.1529/biophysj.105.067652.

[12] D. Chen and M. M. Santore, "Hybrid copolymer-phospholipid vesicles: Phase separation resembling mixed phospholipid lamellae, but with mechanical stability and control," *Soft Matter*, vol. 11, no. 13, pp. 2617–2626, 2015, doi: 10.1039/c4sm02502d.

[13] R. S. Gracià, N. Bezlyepkina, R. L. Knorr, R. Lipowsky, and R. Dimova, "Effect of cholesterol on the rigidity of saturated and unsaturated membranes: Fluctuation and electrodeformation analysis of giant vesicles," *Soft Matter*, vol. 6, no. 7, pp. 1472–1482, 2010, doi: 10.1039/b920629a.

[14] J. C. Mathai, S. Tristram-Nagle, J. F. Nagle, and M. L. Zeidel, "Structural determinants of water permeability through the lipid membrane," *J. Gen. Physiol.*, vol. 131, no. 1, pp. 69–76, 2008,

doi: 10.1085/jgp.200709848.

[15] M. Demazeau, L. Gibot, A. F. Mingotaud, P. Vicendo, C. Roux, and B. Lonetti, “Rational design of block copolymer self-assemblies in photodynamic therapy,” *Beilstein J. Nanotechnol.*, vol. 11, pp. 180–212, 2020, doi: 10.3762/bjnano.11.15.

[16] I. M. Henderson and W. F. Paxton, “Salt, shake, fuse - Giant hybrid polymer/lipid vesicles through mechanically activated fusion,” *Angew. Chemie - Int. Ed.*, vol. 53, no. 13, pp. 3372–3376, 2014, doi: 10.1002/anie.201309433.

[17] J. Gaspard, L. M. Casey, M. Rozin, D. J. Munoz-Pinto, J. A. Silas, and M. S. Hahn, “Mechanical characterization of hybrid vesicles based on linear poly(Dimethylsiloxane-b-ethylene oxide) and poly(butadiene-b-ethylene oxide) block copolymers,” *Sensors (Switzerland)*, vol. 16, no. 3, pp. 1–12, 2016, doi: 10.3390/s16030390.

[18] L. Gibot *et al.*, “Role of polymer micelles in the delivery of photodynamic therapy agent to liposomes and cells,” *Cancers (Basel).*, vol. 12, no. 2, pp. 1–22, 2020, doi: 10.3390/cancers12020384.

[19] C. Montis, D. Maiolo, I. Alessandri, P. Bergese, and D. Berti, “Interaction of nanoparticles with lipid membranes: a multiscale perspective,” *Nanoscale*, vol. 6, no. 12, pp. 6452–6457, 2014, doi: 10.1039/C4NR00838C.

[20] A. Lesniak, A. Salvati, M. J. Santos-Martinez, M. W. Radomski, K. A. Dawson, and C. Åberg, “Nanoparticle adhesion to the cell membrane and its effect on nanoparticle uptake efficiency,” *J. Am. Chem. Soc.*, vol. 135, no. 4, pp. 1438–1444, 2013, doi: 10.1021/ja309812z.

[21] R. C. Van Lehn *et al.*, “Effect of particle diameter and surface composition on the spontaneous fusion of monolayer-protected gold nanoparticles with lipid bilayers,” *Nano Lett.*, vol. 13, no. 9, pp. 4060–4067, 2013, doi: 10.1021/nl401365n.

[22] B. Y. J. M. Mitchison and M. M. Swann, “The Mechanical Properties of the Cell Surface: I. The Cell Elastimeter,” *J. Exp. Biol.*, vol. 31, no. 3, pp. 443–460, 1954.

[23] M. von Dassow, J. A. Strother, and L. A. Davidson, “Surprisingly simple mechanical behavior of a complex embryonic tissue,” *PLoS One*, vol. 5, no. 12, 2010, doi: 10.1371/journal.pone.0015359.

[24] M. W. Laschke and M. D. Menger, “Life is 3D: Boosting Spheroid Function for Tissue Engineering,” *Trends Biotechnol.*, vol. 35, no. 2, pp. 133–144, 2017, doi: 10.1016/j.tibtech.2016.08.004.

[25] D. Anton, H. Burckel, E. Josset, and G. Noel, “Three-dimensional cell culture: A breakthrough in vivo,” *Int. J. Mol. Sci.*, vol. 16, no. 3, pp. 5517–5527, 2015, doi: 10.3390/ijms16035517.

[26] R. K. Vadivelu, H. Kamble, M. J. A. Shiddiky, and N. T. Nguyen, “Microfluidic technology for the generation of cell spheroids and their applications,” *Micromachines*, vol. 8, no. 4, pp. 1–23, 2017, doi: 10.3390/mi8040094.

[27] L. B. Weiswald, D. Bellet, and V. Dangles-Marie, “Spherical Cancer Models in Tumor Biology,” *Neoplasia (United States)*, vol. 17, no. 1, pp. 1–15, 2015, doi: 10.1016/j.neo.2014.12.004.

[28] F. Perche and V. P. Torchilin, “Cancer cell spheroids as a model to evaluate chemotherapy protocols,” *Cancer Biol. Ther.*, vol. 13, no. 12, pp. 1205–1213, 2012, doi: 10.4161/cbt.21353.

[29] C. R. Thoma, M. Zimmermann, I. Agarkova, J. M. Kelm, and W. Krek, “3D cell culture systems modeling tumor growth determinants in cancer target discovery,” *Adv. Drug Deliv. Rev.*, vol. 69–70, pp. 29–41, 2014, doi: 10.1016/j.addr.2014.03.001.

[30] A. Blumlein, N. Williams, and J. J. McManus, “The mechanical properties of individual cell spheroids,” *Sci. Rep.*, vol. 7, no. 1, pp. 1–10, 2017, doi: 10.1038/s41598-017-07813-5.

[31] W. Zhang *et al.*, “Advances in experimental approaches for investigating cell aggregate mechanics,” *Acta Mech. Solida Sin.*, vol. 25, no. 5, pp. 473–482, 2012, doi: 10.1016/S0894-9166(12)60042-1.

[32] J. B. Hall *et al.*, “Soft Matter Models of Developing,” vol. 82, no. November, pp. 910–918, 2012.

[33] E. Moeendarbary and A. R. Harris, “Cell mechanics: Principles, practices, and prospects,” *Wiley Interdiscip. Rev. Syst. Biol. Med.*, vol. 6, no. 5, pp. 371–388, 2014, doi: 10.1002/wsbm.1275.

[34] M. N. Starodubtseva, “Mechanical properties of cells and ageing,” *Ageing Res. Rev.*, vol. 10, no. 1, pp. 16–25, 2011, doi: 10.1016/j.arr.2009.10.005.

[35] R. M. Hochmuth, “Micropipette aspiration of living cells,” *J. Biomech.*, vol. 33, no. 1, pp. 15–22, 2000, doi: 10.1016/S0021-9290(99)00175-X.

[36] K. Guevorkian, M. J. Colbert, M. Durth, S. Dufour, and F. Brochard-Wyart, “Aspiration of biological viscoelastic drops,” *Phys. Rev. Lett.*, vol. 104, no. 21, pp. 1–4, 2010, doi: 10.1103/PhysRevLett.104.218101.

[37] K. Guevorkian and J. L. Maître, “Micropipette aspiration: A unique tool for exploring cell and tissue mechanics in vivo,” *Methods Cell Biol.*, vol. 139, pp. 187–201, 2017, doi: 10.1016/bs.mcb.2016.11.012.

[38] R. Foty, “A simple hanging drop cell culture protocol for generation of 3D spheroids,” *J. Vis. Exp.*, no. 51, pp. 2–6, 2011, doi: 10.3791/2720.

[39] F. Sturzenegger, T. Robinson, D. Hess, and P. S. Dittrich, “Membranes under shear stress: Visualization of non-equilibrium domain patterns and domain fusion in a microfluidic device,” *Soft Matter*, vol. 12, no. 23, pp. 5072–5076, 2016, doi: 10.1039/c6sm00049e.

General Conclusion

During this Ph.D project, we have successfully fabricated two different on-chip micropipette aspiration, which enables the characterization of the mechanical properties of Giant unilamellar vesicles, a lipid model membrane that mimics the cellular membrane, by size, shape and part of the composition. The first microfluidic platform consisted in a 3 level microchannels, with a hanging channel in the middle. The challenge of having a hanging channel was overcome by choosing etched silicon-glass as a final material for the chip. Silicon dry etching required few optimizations, however we successfully developed the etching process of non-pure glass wafer, starting by a dry etching step, followed by a wet chemical etching step which reduced the etched glass rugosity from microns to nanometers. The second on-chip micropipette aspiration was a very novel platform that is made by a combination of a traditional PDMS chip and a removable/sliding element which contains the micropipettes. The innovative fabrication technique, allowed us to first, reproduce the cylindrical shape of the micropipette aspiration, a crucial condition for successful measurements. Secondly, we were able to fabricate several pipettes per element which offered a high throughput trapping and micropipette aspiration experiments. And finally, the unique way of fabrication allowed us to fabricate different shape of traps (cross shape…), in order to characterize other properties of the membranes. The fabrication of such shape for the traps is almost impossible or very difficult using traditional microfabrication techniques.

We have properly measured the mechanical properties, such as the bending and stretching modulus of membranes made of simple lipid compositions, such as DOPC and POPC, and membranes made of binary mixtures such as DOPC /chol and SM/chol. We demonstrated that cholesterol increases the membrane's stretching modulus. In parallel, we also demonstrated that there is no systematic effect of the sucrose concentrations on the moduli of the lipid membranes. Moreover, we have demonstrated that NPs, such as copolymer micelles (PEO-PCL) and Gold NPS, usually employed as drug-delivery systems, have a strong effect on the mechanical properties of DOPC lipid membranes. The first one yielded lower bending and stretching modulus for the DOPC membrane suggesting a softening in the membrane, while the effect of Gold NPs could be time-dependent. And finally, because of the versatility of our microfluidic platform, we have successfully characterized the viscoelastic properties of spheroids made of aggregates of cancer cells, and we suggested that these types of spheroids could exhibit a elasto-visco-plastic behavior that is yet to be determined.

Our novel, adaptable and very functional microfluidic platform can be used for many other applications, some of them were discussed by the end of chapter 5. Some optimizations are however still needed, such as being able to successfully use small micropipettes, and reduce some of the dispersion in our data. Considering the lipid membranes, we can still reach many more properties, such as the membrane's permeability, as well as deepening the investigations considering the NPs effects. For example, combining the flow and the NPs to characterize their effect on the phase behavior of a membranes exhibiting both liquid-ordered and liquid-disordered phases. Our system could be extended to characterize spheroids made of other type of cells or cancer cells. Moreover, our platform could be used to characterize the effect of NPs (or drugs) on tumors spheroids, as a drug screening platform.

Materials and Methods

Clean room microfabrication processes for 3 level chip with the hanging structure in the middle (chapter 4)

SU-8 Molds fabrication for the PDMS-PDMS 3 levels chip

SU-8 molds fabrication

In order to fabricate the PDMS-PDMS three levels chip, two silicon wafers with SU8 photoresist were fabricated to be used as molds. The first wafer was made with a double layer of SU8: first layer of 10 µm thickness, to define mainly the layer of the trap and the rest of channels. The second layer was a 15 µm thickness layer of SU8 to draw the bottom layer of the inlet/outlet and bypass channels, which makes it in total 25 µm deep channels. The second wafer was made with one layer of SU8 of 15 µm thickness, mirror of the first mold.

The fabrication of the two SU8 molds were made in the clean room of LAAS following the steps below:

- Silicon wafers are first treated with plasma O_2 for 5 minutes, under 800W and 1000sccm, in order to remove possible hydration of the silicon wafers and to enhance adherence of the resist on the wafer.
- *SU8 3005 (10µm) and SU8 3025 (15µm)* negative resist were then deposited, baked, insolated and developed following these parameters:

	Spin coating (speed-acc-time)	Insolation (mJ/cm^2) (365 nm)	Development (min)
SU8 3005 (10µm)	900 – 4000 – 30	90	5
SU8 3025 (15µm)	4400 – 300 – 30	135	5

Soft bake, postbake and hard bake are made after spin coating, insolation and development steps respectively, as seen in the table below:

Soft Bake	PEB	Hard Bake
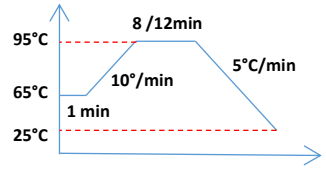	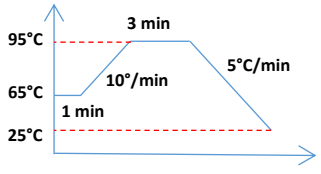	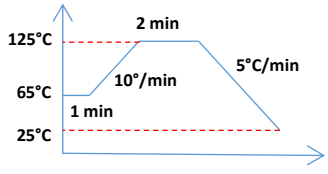

A characterization of the thickness of the SU8 resist for both wafers was made using a mechanical profilometer as shown in ***Figure 1*** **:** The first Si wafer has two SU8 levels (one for the main channels (15 µm thickness) and the other on for the micropipette channel (10 µm thickness), which gives a total

thickness of 25 µm ***(Figure 1*A).** The second Si wafer, which has 1 level of SU8, the main channels (15 µm thickness) **(*Figure 1*B).**

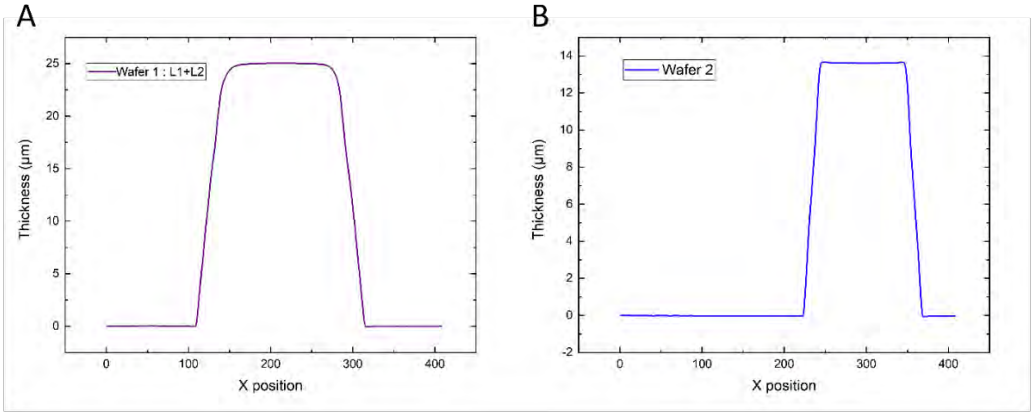

Figure 1: Profilometer characterization of the SU-8 thickness in the two wafers.

Fabrication of the SU-8 Poles on the silicon wafers

SU8 3050 was then deposited by gravimetric coating 5 layers of 100 µm each one, with a soft bake after each coat. After exposure of 2000 mJ/cm^2 and the post exposure baking, the wafer was developed for half an hour in SU8 developer. A final hard bake step was also made to smooth the SU8 structures by increasing the cross-linking and make sure the SU8 will not be damaged during PDMS fabrication steps.

Hydrophobic Treatment of SU-8 silicon molds

During the fabrication steps and due to oxygen plasma treatments and the resist surface chemistry, the surface of the wafers becomes hydrophilic. However, to be able to remove easily the PDMS from the wafer without having it attached on the wafer or breaking into small pieces, it is important to make a surface treatment to change it into hydrophobic. Therefore, using an *SPD MEMSSTAR* machine, we deposit first a 20 nm layer of SiO_2 that first attach on the Si wafer. We then graft and FDTS molecule *(1H,1H,2H,2H-perFluoroDecylTrichloroSilane)* which, with the SiO_2 layer makes a Teflon layer which is hydrophobic. The contact angle was than measured to ensure the hydrophobicity and the anti-adhesive surface: θ = 110°

PDMS 3 levels chip fabrication

Now that the molds are fabricated and treated, *polydimethylsiloxane* (PDMS), with a ratio 10:1 (1 is for the curing agent), is well mixed and degassed under vacuum. A thick layer (2 mm) of PDMS was poured over the first wafer and cured at 60 °C overnight. The second layer of PDMS was spin coated on the second wafer, in order to have a thin layer ~170 µm, in the bottom part of the chip. The parameters used for the PDMS spin coating are: 700 rpm, 300 rmp/s for 30 sec. Once both PDMS mold were cured, the thick layer was removed and the inlet/outlet were punched to ensure fluid access.

Depending on the alignment techniques used and seen in chapter IV, the two PDMS pieces were finally aligned and bounded together.

Dry Film process of fabrication for the DF microfluidic chip, in the 3 level chip design (chapter IV)

DF films are a negative image fry film photoresist, so what is exposed in UV light, is reticulated and therefore stays on the glass after development. In this case, the DF mold fabricated is directly the chip to be used.

Table 1: Parameters of the fabrication process of DF molds on glass wafers of 170 µm

DF 1005/1025		
Layer 1 (15µm)	Lamination: • 100°C • 2.5 bar • 0.5m/min Insolation: • 225 (mJ/cm^2)	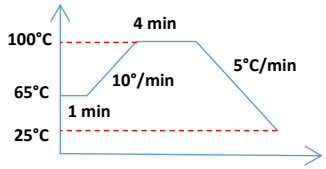
Development	Cyclohexanone	4 min
Layer 2 (10µm)	Lamination: • 65°C • 2 bar • 1m/min Insolation: 200 (mJ/cm^2)	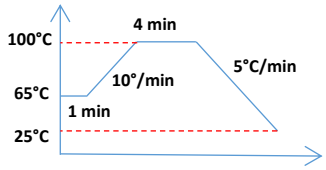
Development	Cyclohexanone	3 min 30 s
Layer 3 (15µm)	Lamination: • 65°C • 2 bar • 1m/min Insolation: • 225 (mJ/cm^2)	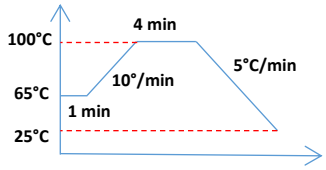
Development	Cyclohexanone	4 min
Layer 4 (25µm)	Lamination: • 65°C • 2 bar	

	• 1m/min Insolation: 275 (mJ/cm^2)	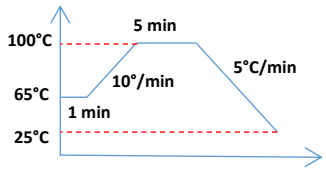
Development	Cyclohexanone	4 min 30 s

Bosch Process for Etching two levels in silicon wafer

First level etching:

- After treating the silicon wafer with plasma oxygen, to prepare the surface for resist adhesion, adhesion promoter *HMDS* was deposit to enhance resist adherence on the wafer.
- *ECI 3012* (1.1 µm) positive resist was spin coated (**3600 rpm, 5000 rpm/s, 30s**) and baked under **90 °C** for **60 s**.
- After exposure under **405 nm** UV wavelength, with **200 mJ/cm^2**, a PEB is made under **110°C** for **60s.**
- Finally, the resist was developed with a *MF-CD-26* developer for **15 s**.
- The plasma etching was done with **Bosh process**: The alternative flow of **SF_6/C_4F_8** was **700/250 sccm,** under **2800W/20W** power **and 0.1mb/0.06mb** pressure. The temperature of the chuck was **10°C**. Knowing that the etching rate of this process under these conditions is **3 µm/min**, we had to etch a total time of 3 minutes and 20 seconds in order to obtain **10 µm** deep channel.

Removing the resist was a bit tricky, as the resist was burnt due to the all the chemicals it had already seen. So we tried different ways to clean it, yet the best one: Acetone bath with ultra sound for 10 minutes, followed by 15 minutes of plasma oxygen which usually removes well the resists and finally a piranha cleaning for 5 minutes to make sure no small residue are still between the channels.

Second level etching:

After resist removal, a second photolithography/etching cycle was realized to etch the first part of the rest of channels (15 µm depth for inlet, outlet and bypass)

- A thicker resist *(AZ® 40 XT*, 20 µm) was needed in this step in order to fill the already etched trap and channels. In fact, after the first etching layer, a 10 µm etched channel is fabricated, and in order to cover the channel of the micropipette (the trap) a 10 µm resist are first needed to fill the 10µm etched channel plus the protective layer for the etching process. *BARC^{TM}* (Bottom Anti-Reflective Coatings) is used as adhesion promoter for its high efficiency for thick resist: (**3000 rpm, 4000 rpm/s, 30 s)** and baked for 1 minute under **200 °C.**
- *AZ 40XT* (20 µm) was deposit **(3200 rpm, 100rpm/s, 30 s)** by induction using the *EVG 120* machine.

- The resist is then soft baked for 1 minute under **65 °C** and then the temperature was linearly increased by **(10°C/min)** until **126 °C**. Then it stayed under **126 °C** for **150** seconds.
- The resist was then exposed under **405 nm** UV wavelength at **400 mJ/cm²** dose.
- The PEB is done for 1 minute under **65 °C** and then the temperature was linearly increased by **(10°C/min)** until **105°C**. Then it stayed under **105 °C** for 80 seconds.
- The resist was finally developed for 90 seconds with the *MF-CD-26* developer.
- Plasma etching was done under the same conditions as for the first layer. Only we increased the etching time to 5 minutes in order to obtain the 15 µm depth.

The etched silicon wafer was finally characterized with a mechanical profilometer. The total deepness of the main channels was 22.5 µm instead of 25 µm, as seen in ***Figure 2.***

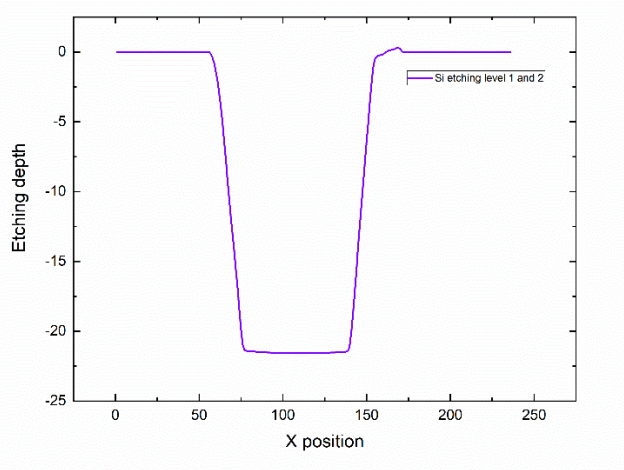

Figure 2: Profilometer characterization data of the total channels etched. Level one etched of 10 µm and the second one of 12.5 µm, giving a total depth of 22.5 µm

Borofloat Glass type etching process

The final process to etch 15 µm channels in Borofloat glass type is the following:

- *BARC™* was deposited before spin coating the photoresist and *AZ® 15nXT* (~17 µm thickness) negative photoresist was used as protective layer.
- In order to avoid cracks but reduce this roughness during the glass etching process, we worked at **-15 °C.** Knowing that the etching rate is **370 nm/min**, we divided the total time of etching in 9 cycles of 4 min 30 seconds each, in order to relax the resist constraints and clean the reactor for 5 minutes after each cycle. The cleaning of the reactor is absolutely necessary to avoid contaminating of the channels by reposition of resist during etching.
- The plasma process was realized using the following gases mix**: C_4F_8/CH_4/He**, **17/15/100 sccm**, under **4.8 10^{-3} mbar**, with source power and bias power respectively **2800 W** and **250 W**. **He** is used to cool down the chuck. **CH_4** is used to etch the glass, and **C_4F_8** to passivate the walls.

Removing *AZ 15nXT* resist after the plasma process is more difficult than the positive resist used during the silicon etching. The normal cleaning process was not applicable to this resist, so instead, we had to use a photoresist stripper, *TechniStrip® NF52*, which is a highly effective negative photoresist remover. An additional step of plasma O2 treatment was made to be sure the channels surface is well cleaned.

Experimental Set-Up

Electroformation protocol to fabricate GUVs

The GUVs were fabricated using electroformation protocol. For some lipids (DOPC, POPC), the temperature of the phase transition T_m from the gel phase to the liquid phase is very low [1], that the fabrication of the GUVs can be made on room temperature (~ 22 °C). However, other lipids have it around 40 or 50 °C or even higher. For those lipids, it is necessary to heat the glass substrate above their T_m during the electroformation. The electroformation protocol is as it follows:

1,2-dioleoyl-sn-glycero-3-phosphocholine (DOPC) lipid in powder was dissolved in Chloroform at 0.5 mg/mL concentrations. Lissamine rhodamine B sulfonyl (1,2-dimyristoyl-*sn*-glycero-3-phosphoethanolamine-N-) dye at 0.1% concentration of molecular number was added to the DOPC lipid solutions for fluorescence imaging (λ_{exc} = 560 nm and λ_{em} = 583 nm). Before the experiment, a 10 µL droplet of this solution was added in the center of two Indium tin oxide (ITO) covered glasses. The two cover glasses were then placed under vacuum for two hours, using *Welch™ vaccum pump MPC 101 Z* with a maximum pressure or 8mbar. We fabricated a homemade glass holder to fabricate the GUVs using the traditional electroformation technique. Once the glasses were removed, one of them was placed in the holder, with an O-ring around the film. 200 µL of 3 mM (or 15, 100 and 180mM) sucrose in water were added in the O-ring, before it was temporarily sealed with the second one. A sinusoidal voltage (peak-peak amplitude 2 V, frequency 10 Hz) was applied for 3 hours on the film in order to fabricate the GUVs. The GUVs were then diluted 5 times in a 3 (or 18, 105 and 185) mMol sucrose water solution**.**

Nanoparticles preparation

PEO-PCL nanoparticles preparation

The NPs were self-assembled polymer micelles made of PEO-b-PCL like follows: Poly(ethylene oxide)-*block*-poly(caprolactone), PEO (5000 $g.mol^{-1}$)-PCL (5400 $g.mol^{-1}$) which are amphiphilic block-copolymers. They formed micelles with a hydrodynamic diameter of 25 $\pm$ 5 nm when prepared using a nanoprecipitation method: 20 mg of the copolymer were dispersed in 400 µl of acetone, and this solution was slowly added to 5 ml of a 180 mMol sucrose solutions under stirring. The concentration of sucrose solution was chosen to match the solution of the GUVs, in order to avoid osmotic pressures

on the GUVs membranes. Acetone was left to evaporate for 48 hours. Dynamic Light Scattering measurements were performed at 25 °C and 173° angles using a *Malvern* (Orsay, France) *Zetasizer NanoZS* to characterize the micelles' size. Data were analyzed using the general-purpose non-negative least squares (NNLS) method.

Gold citrate nanoparticles preparation

The gold nanoparticles were provided to us by the CSGI laboratory and were fabricated following the classical Turkevich method. Briefly, 2 mL of 1 wt% trisodium citrate aqueous solution were rapidly injected into 20 mL of $HAuCl_4$ 1 mM boiling solution under vigorous stirring. The formation of NPs is indicated by the color of the solution, which turns from the original pale yellow to burgundy. After 15 minutes, the solution was cooled down by means of a water-ice bath. NPs@Ct were stored at 4 °C. NPs@Ct dispersion were centrifuged (5 min @ 500 rcf) at 15°C in order to remove aggregates prior to use. Nanoparticle size distribution was evaluated by AFM measurements which gives an average size of 15 nm. The molar concentration of gold nanoparticles is 9 nM and it was determined via UV-Vis spectroscopy. The chosen concentration is selected because it not toxic for cells, and yet ensures GUV surface saturation.

3D printing chip holder for DF and silicon-glass chips (chapter IV)

In order to connect the chip to the GUVs solution, we designed a chip holder with all the connectors integrated inside it. Having the connectors on the side, avoid any disturbance from the microscope like when the connectors are on the top. The two piece holders were first 3D printed, using a high-resolution 3D printer *(Dilase 3D, Kloe).* The material used was a commercial resin, ***DS3000.*** However, the layer of the down part of the holder, where the opening for the microscope light is, was thin (300µm). This lead to breaking it once we tightened the 2 pieces together. So we decided to change the bottom part to an aluminum holder, much harder than the resist used ***(Figure 3A – B).***

To characterize the efficiency of the 3D printed chip holder as well as the anodic bonding, we sent fluorescent beads of 1 µm diameters inside the channels through the chip holder. As shown in ***Figure 3C***, the beads are circulating inside the channels showing no leakage. This proved that the anodic bonding worked very well, and the chip holder works well also.

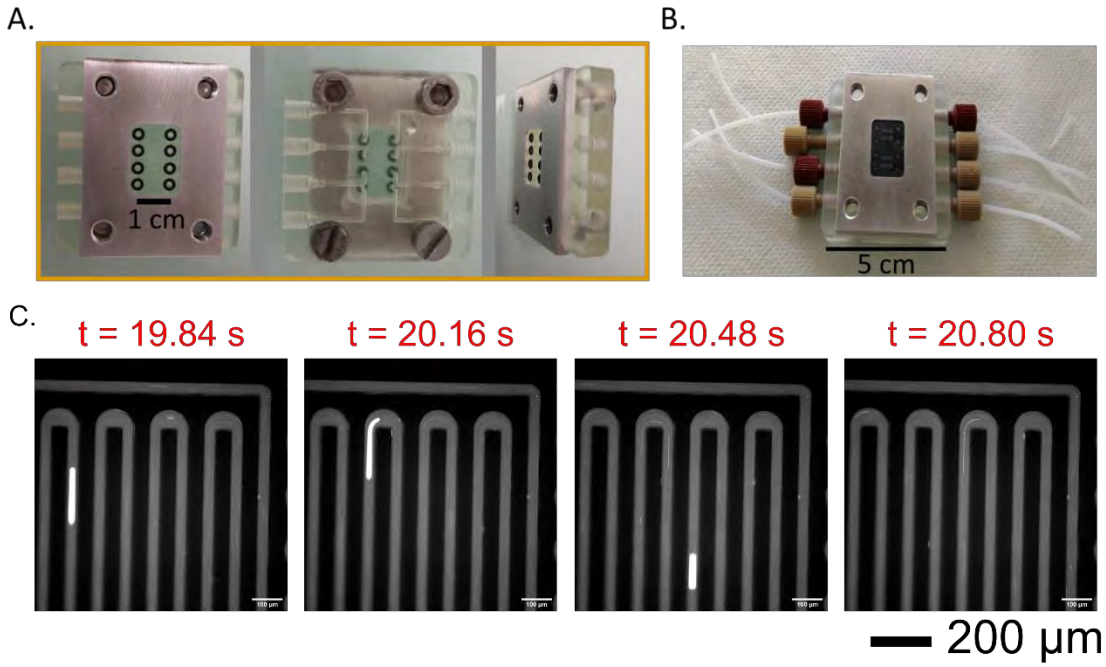

Figure 3: Pictures of the 3D chip holder. A) shows the down part opening to be able to see from the microscope. The opening had to be wide enough in order to see all the channels, even the holes, but not too wide for the chip no to fall from it. The second and third pictures show the integrated opened channels and connectors leading from one side to the chip and the other side to the microfluidics tube. B) is the holder with the connectors and the connected microfluidics tube, with the silicon-glass chip inside it. C) Confocal microscopy images of fluorescent beads circulating inside the channels showing that there is no leakage.

Fluorescence Characterization of the sliding element made of DF material (chapter V)

We characterized the excitation and emission spectrum of the sliding element made of DF material in order to choose a staining for the GUVs that is not in the same range of the fluorescence of the DF. This was important especially when fabricating GUVs with phase separation which exhibits domains, and in order to visualize the different domains, two different staining is needed. To characterize the fluorescence response of the DF, we used a Varioscan, which has multimode reader and equipped with a range of measurement technologies, especially the absorbance and the fluorescence intensity, which we will be measuring. To characterize the emission spectrum of the DF, we excited with several wavelengths (375, 488, 560 and 650 nm) and recorded the emission response, as seen in ***Figure 4.*** A pic of emitted fluorescence appeared around λ_{em} = 567 nm and another one around λ_{em} = 622 nm, when excited with λ_{ex} = 375 nm. The rest of the excitation wavelengths did not give high values of emission. In order to characterize the absorbance, we fixed the emissions at the wavelength found before (567 nm and 622 nm), and excited with the different excitation wavelength (375, 488, 560 and 650 nm). The pic of fluorescence at fixed emissions corresponded to the two pic of excitations under 375 nm and 560 nm. Therefore, any fluophore with λ_{ex} = 375 nm was discarded. **β-BODIPY™ FL C_{12}-**

HPC, which λ_{ex} = 500 and λ_{em} = 510 was a candidate. However, the GUV stained with it bleached quiet fast compared to other dyes we used. Therefore, BODIPY was only used for the GUVs with domains. For all the other studies, 16:0 Liss Rhod PE (λ_{ex} = 560 nm and λ_{em} = 583 nm) was used. Even though the DF presented a pic of fluorescence under these wavelengths range, the pic was still smaller than the one of 375nm. Therefore, it was a good compromise between the material's fluorescence and the stability of the GUVs.

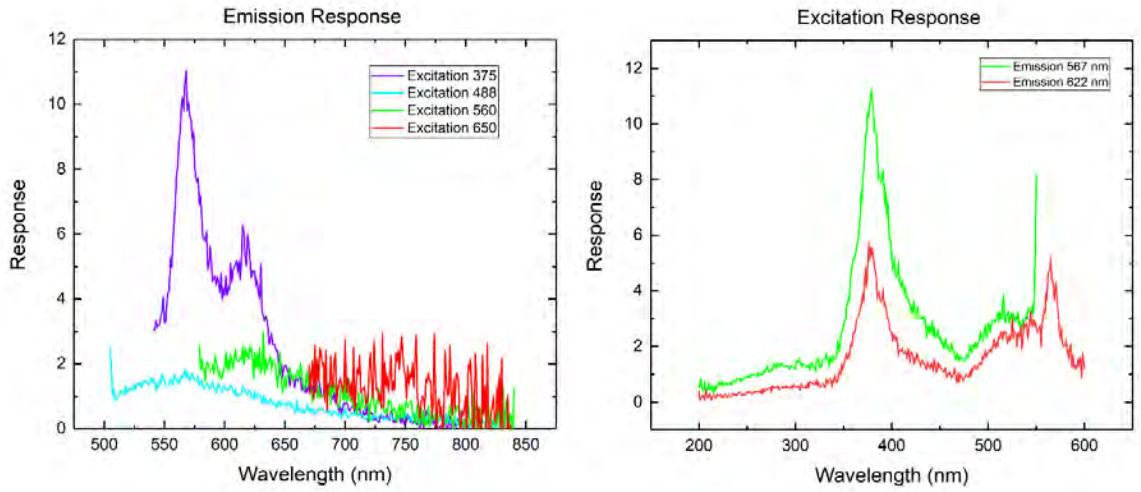

Figure 4:Excitation and Emission spectrum of the sliding element made of DF material.

Characterization of the stability of Fluigent MFCS-EZ 25 mbar (chapter V)

Characterizing the mechanical modulus of biomimetic membranes using micropipette aspiration technique requires a good control over the pressure applied on the object under study. Since the values of the bending modulus, which is characterized at very low suction pressure, were low compared to the literature, we characterized the stability of the pressure controller used during the micropipette aspiration on chip experiments. To do so, we used a pressure sensor for pressure ranges of 0 – 6 mbar. The bending modulus is usually measured under suction pressure of 0.1 Pa and 500 Pa (0.001 mbar and 0.5 mbar) as seen in chapter II. At low pressure (0 – 0.5 mbar), we increased the pressure of 0.01 mbar each and noted the tension value given by the sensor. For intermediate values (0.5 – 1 mbar), we increased the pressure of 0.05 mbar each, and finally for higher values we increased the pressure of 0.1mbar, until 3 mbar and then 0.5 until 7mbar. The results of the measured tension as function of the pressure applied by the pressure controller, for two different channels is given in ***Figure 5***. The linearity of the curve validates the accuracy of the pressure controller.

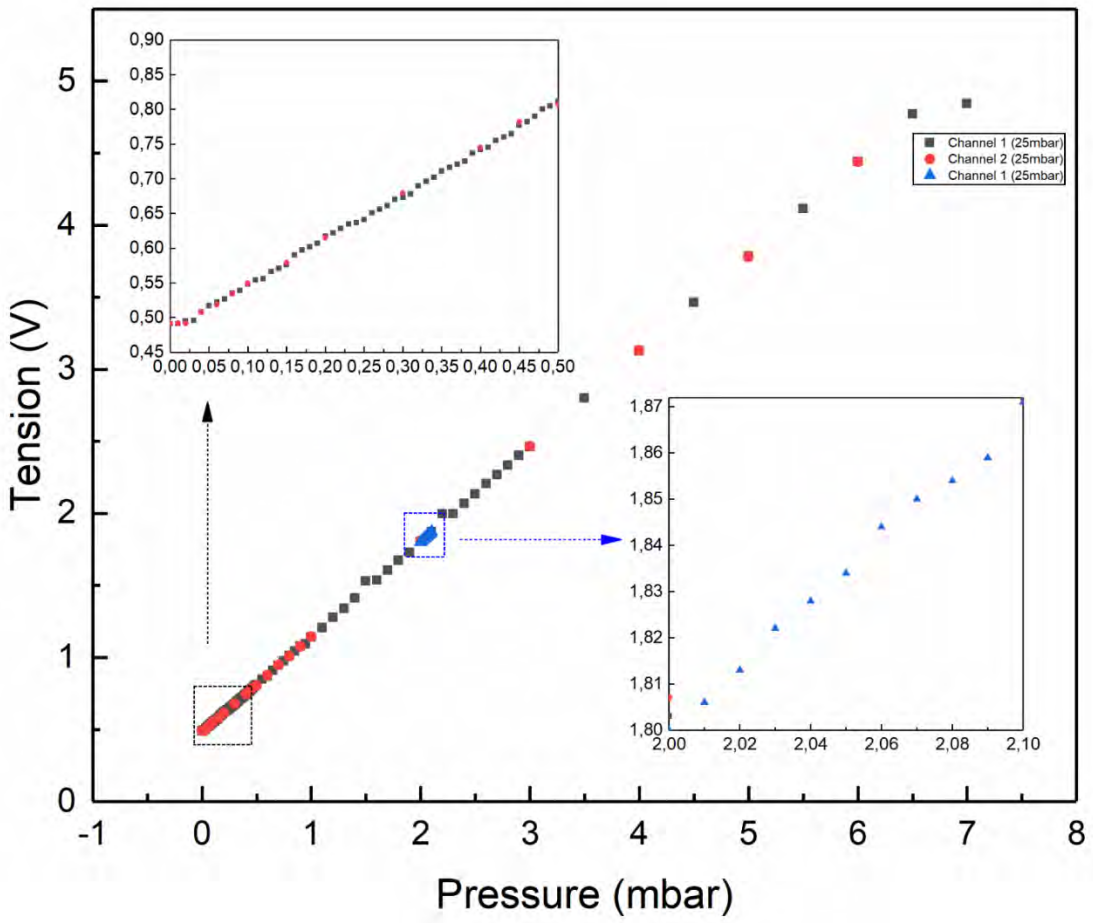

Figure 5: Characterization of the pressure controller stability using a pressure sensor.

Résumé

Les propriétés mécaniques de la membrane cellulaire contrôlent de nombreux processus biologiques. Les vésicules unilamellaires géantes (GUV) sont une approche facile pour reproduire la membrane cellulaire. L'aspiration par micropipettes est une technique bien connue utilisée pour caractériser leurs propriétés mécaniques, bien qu'elle implique une expérimentation de longue durée pour une mesure et une configuration complexe. Nous avons développé des plates-formes microfluidique visant à intégrer l'aspiration par micropipettes. Un avantage crucial de l'approche la plus avancée que nous avons mise en place est la flexibilité en termes de forme que nous pouvons fabriquer (en particulier forme de piège cylindrique). Cette approche permet également de multiplexer des micropipettes, offrant des mesures à haut débit, et enfin la possibilité de fabriquer les éléments composant la micropipette par centaines à la fois.

Nous avons d'abord pu caractériser des compositions lipidiques simples telles que DOPC, POPC et Brain SM, dont les modules de courbure et d'étirement étaient en très bon accord avec les valeurs rapportées dans la littérature. Nous avons également caractérisé l'effet du cholestérol sur les membranes DOPC : le cholestérol augmentait le module d'étirement de la membrane DOPC mais n'affectait pas son module de courbure, rendant ainsi la membrane plus rigide. De plus, nous avons caractérisé la membrane DOPC contestée avec des nanoparticules de copolymères, généralement utilisées pour l'administration de médicaments. Ces nanoparticules ont induit un ramollissement de la membrane, qui pourrait être dû à l'effet de perméabilisation des NP sur la membrane, ou à leur insertion dans les membranes provoquant des défauts.

Cette méthode étant polyvalente, en changeant la forme de la micropipette cylindrique en une section transversale permettant de piéger les GUV avec un écoulement résiduel autour d'elle, nous avons pu avoir une caractérisation préliminaire de l'effet de l'écoulement sur la fluidité des membranes.

Enfin, nous avons adapté la taille de la micropipette afin de caractériser les propriétés viscoélastiques des sphéroïdes, agrégats de cellules cancéreuses 3D. Nous avons caractérisé la viscosité des cellules cancéreuses du pancréas et démontré qu'elle est indépendante de la taille des sphéroïdes.

Mots clés : Microfluidique, membrane lipidiques, nanoparticules, aspiration par micropipette, vésicule géantes unilamellaires.

Abstract

The mechanical properties of the cell's membrane control many biological processes. Giant Unilamellar vesicle (GUV) are an easy approach to reproduce cells membrane. Micropipette aspiration is a well-known technique used to characterize their mechanical properties, though it involves long time experimentation, and huge set up. Here we present a microfluidic platform that reproduce micropipette aspiration especially by its cylindrical trap form. The main advantage is the flexibility in terms of the shape we can fabricate, as well as the multiplexing micropipette, offering high throughput measurements and finally the ability to fabricate the elements composing the micropipette by hundreds at a time.

We were able first to characterize simple lipid compositions such as DOPC, POPC and Brain SM, whose bending and stretching moduli are in very good agreement with the values reported in the literature. We also characterized the effect of cholesterol on DOPC membranes: cholesterol does increase the stretching modulus of DOPC membrane but does not affect its bending modulus, making therefore the membrane stiffer. Moreover, we characterized DOPC membrane challenged with co-polymers nanoparticles which are usually used for drug delivery and which showed a softening in the membrane which could be due to the permeation effect of the NP on the membrane.

As this method is versatile, by changing the shape of the cylindrical micropipette to a cross section which allows the GUVs to be trapped with a residual flow around it, we were able to have a preliminary characterization of the effect of flow on the membranes' fluidity properties.

Finally, we adapted the size of the micropipette in order to characterize the viscoelastic properties of spheroids made of cancer cells. We characterized the viscosity of pancreatic cancer cells and demonstrated that it is independent on the spheroids size.

Keywords: Microfluidics, Lipid membranes, nanoparticles, micropipette aspiration, Giant unilamellar vesicles,